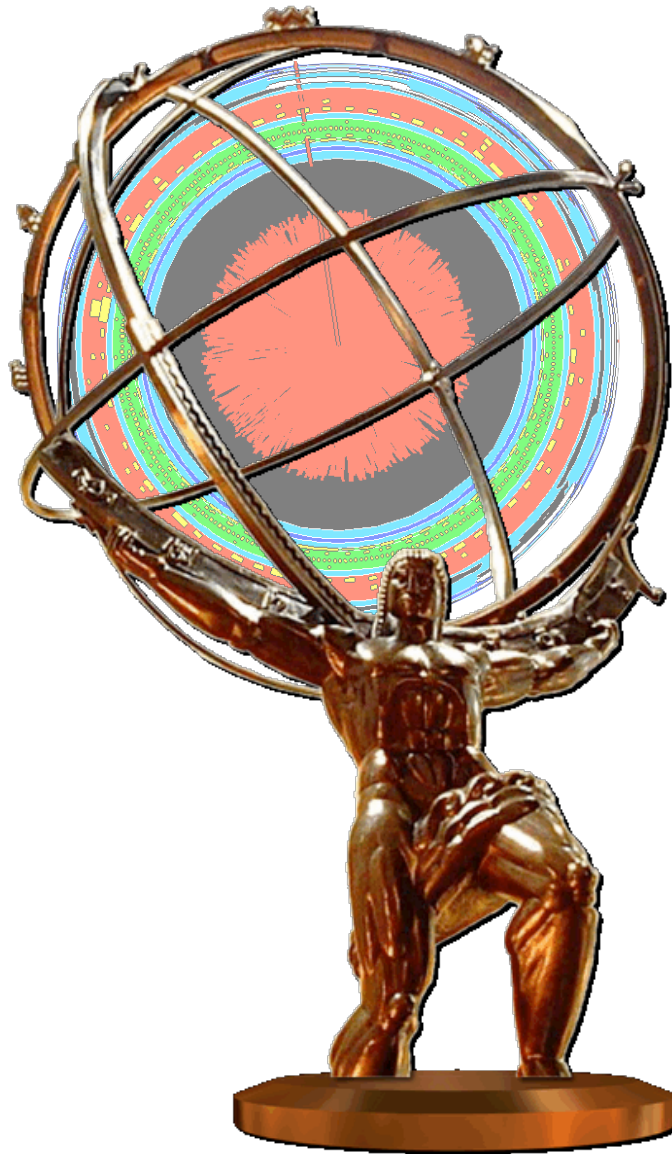# Heavy Ion Physics with the ATLAS Detector at the LHC

Heavy Ion Physics with the ATLAS Detector at the LHC

ATLAS Heavy Ion Working Group

M.D. Baker, R. Debbe, P. Nevski, P. Steinberg, H. Takai, F. Videbaek, S. White

Physics Department, Brookhaven National Laboratory, Upton, NY 11973

J. Dolejsi, M. Rybar, M. Spousta

Physics Department, Charles University, Prague, Czech Republic

A. Angerami, B. Cole, N. Grau, W. Holzmann

Physics Department, Columbia University and Nevis Laboratories, Irvington, NY 10053

L. Rosselet

Physics Department, University of Geneva, Switzerland

D. Derendarz, A. Olszewski, B. Toczek, A. Trzupek, B. Wosiek, K. Wozniak

Department of the ATLAS Experiment, IFJ PAN Krakow, Poland

J. Hill, A. Lebedev, M. Rosati

Physics Department, Iowa State University, Ames, IA 50011

V. Pozdnyakov

Physics Department, JINR, Dubna, Russia

H. Santos

LIP, Portugal

S. Timoshenko

Physics Department, MePHI, Moscow, Russia

S. Bathe

RIKEN/BNL Research Center, Brookhaven National Laboratory, Upton, NY 11973

W. K. Brooks, S. Kuleshov

Physics Department, Santa Maria University, Valparaiso, Chile

M. Leite

Physics Department, University of Sao Paulo, Brazile

A. Ajitanand, P. Chung, J. Jia[1], R. Lacey

Chemistry Department, Stony Brook University, Stony Brook, NY 11794

S. Milov, I. Tserruya

Physics Department, Weizmann Institute, Rehovot, Israel

G. Atoian,V. Issakov,A. Poblaguev, M. Zeller

Physics Department, Yale University, New Haven, CT

(November 20, 2009)

---

[1]Also *Physics Department, Brookhaven National Laboratory, Upton, NY 11973.*

Abstract

The ATLAS experiment will participate in the Heavy Ion program at the Large Hadron Collider (LHC) and will use its large acceptance, high granularity calorimeters, silicon tracking detectors, and muon spectrometers to study hard scattering processes and jet quenching, Z's, quarkonia production and suppression, and global observables in Pb+Pb collisions. The longitudinal and fine transverse segmentation of the ATLAS electromagnetic calorimeter gives ATLAS unique capabilities for measuring complete jets and photons. The simulation studies of the ATLAS performance and physics reach for a variety of observables necessary to characterize the properties of the dense and hot system formed in heavy ion collisions are presented. These studies show how ATLAS can be used to effectively study the physics of high-energy parton interactions with the quark-gluon plasma (QGP), the physics of Debye screening of Q-$\bar{Q}$ states in the QGP, and the physics of initial particle production and thermalization.

Contents

Chapter 1

Heavy Ion Physics at the LHC

1.1 The Quark Gluon Plasma

Heavy ion physics is the systematic study of a hot, dense, and strongly coupled system that holds out the possibility of extending our understanding of Quantum Chromodynamics (QCD), the theory of the strong interaction. The primary goal is to elucidate the phase structure of hot nuclear matter, something generally thought to be inaccessible in the collisions of single hadrons. It has long been thought that QCD should exhibit two distinct phases, a hadronic phase at lower temperatures where the degrees of freedom are composite bound states of quarks and gluons, and a "partonic" phase where the fundamental degrees of freedom are asymptotically-free quarks and gluons. This is the concept of "deconfinement", where the quarks are allowed to move quasi-freely over distances larger than hadronic scales (1 fm), which is generally precluded by gauge invariance in QCD. A deconfined system is thought to be equivalent to a plasma of quarks and gluons, and was thus given the name of "Quark Gluon Plasma" (QGP) [2]. These ideas have been primarily supported by lattice QCD calculations, which show a distinct change in the number of degrees of freedom (e.g. as expressed by ϵ/T^4 shown in the left panel of Fig.1.1) going through a critical temperature found to be $T_c \sim 170-190$ MeV at zero baryochemical potential. More general considerations, especially at finite baryon density, suggest a phase diagram along the lines as that shown in the right panel of Fig.1.1.

The experimental study of the QGP is expected to provide insight into the relevant degrees of freedom of the QCD Lagrangian, something typically quite difficult to assess in strongly-coupled systems. This is of great interest to subatomic physics and cosmology. The non-perturbative sector remains a major open question in particle physics, and insight is needed in order to justify the claim that the Standard Model provides a useful description of all natural phenomena. It is also essential to understand the many-body aspects of the theory to get a sense of what the early universe was like several microseconds after the Big Bang, at temperatures sufficiently high to prevent the existence of individual hadrons (especially protons and neutrons). In this regime, there remains a gap of understanding between nuclear physics (the low energy interactions of protons and neutrons), and the perturbative interactions of quarks and gluons at asymptotically high energies probed in particle physics experiments. The community is optimistic that the interplay between theory and experiment will be able to both validate the existing approaches to QCD, as well as isolate new phenomena that should give even deeper insight.

These discussions have dovetailed with theoretical ideas which pointed to the intriguing pos-
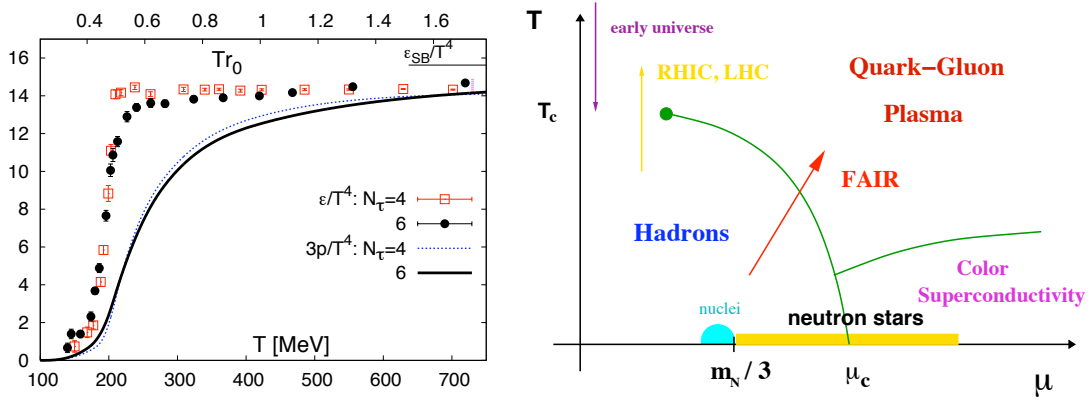
1

Figure 1.1: (left) Lattice calculations showing the sudden jump in the effective number of degrees of freedom (ϵ/T^4) at T_c [1]. (right) Schematic phase diagram of hot nuclear matter.

sibility of novel effects in the wave functions of high energy hadrons and nuclei, due to gluon recombination. In the case of nuclei, the nuclear wave function is currently understood as manifesting a "Color Glass Condensate" (CGC). For a review, see Ref. [3]. This is a high-density configuration of the predominantly low-x gluons which are produced at large beam energies. The interplay between the standard perturbative splitting diagrams are balanced by recombination diagrams at high enough densities, leading to the generation of a "saturation scale" Q_s (usually specified as Q_s^2) which characterizes the local gluon density. The CGC is primarily a model of the very initial state of the nuclear collision, predicting various aspects of the initial phase space distributions of partons just after the nuclear collision. An extension of these ideas to the decay of the initial coherent color fields leads to the concept of the "Glasma", a precursor state to the QGP [4].

One approach which has gained substantial attention in the last few years is the application of string theory techniques to strongly coupled theories similar to QCD, via the "AdS/CFT" correspondence [5]. The essential insight was Maldacena's discovery of duality between $N = 4$ supersymmetric Yang-Mills (SYM) theory in 3+1D and string theory in 9+1D (particularly in a supergravity approximation). This allowed the study of a QCD-like theory (albeit with no running coupling, as in full QCD) in a non-perturbative regime, by the use of a weakly coupled string theory. An important further insight for the study of hot QCD was made in 2001 by Kovtun, Starinets, and Son (KSS) [6], who performed a landmark calculation of the shear viscosity of the hot Yang-Mills plasma in $N = 4$ SYM and found that taking the ratio of that to the entropy density leads to a constant value $\eta/s = \hbar/4\pi$, independent of different background geometries and assumptions. As the thermal QCD system is mapped onto a black hole with a horizon located deep in the "radial" dimension of AdS space, the well-known Bekenstein upper bound on the entropy translates directly into a *lower* bound on the ratio of shear viscosity to entropy density. All known laboratory systems (e.g. water and liquid helium) fall far short of this bound, as shown in Fig.1.2 and so any system sitting at the bound, or even violating it, could give insight into the relevance of string theory to strongly coupled QCD.

Intriguingly, at the time the KSS bound was proposed, it was already understood that the medium formed in heavy ion collisions had extremely low viscosity, and could perhaps be con-

2
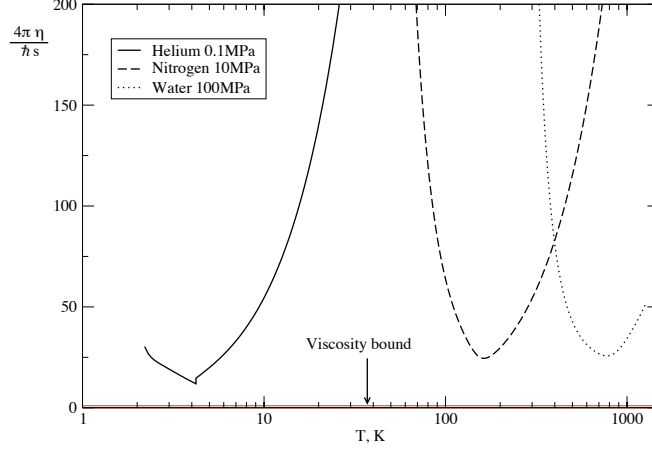
Figure 1.2: The shear viscosity to entropy ratio (η/s), normalized to put the bound at unity, compared to a variety of macroscopic physical systems.

sidered a "perfect" fluid with zero viscosity. By showing that viscosity of a fluid could never be arbitrarily small, the bound redirected efforts toward quantitatively estimating deviations from perfect local equilibrium. Early estimates of the viscosity estimated from charm production in heavy ion collisions suggest that RHIC collisions produce a nearly-perfect fluid, only a factor of two above the bound [7]. This has led to an explosion of activity, both experimental and theoretical, related to indirect and direct measurements of shear viscosity in heavy ion collisions. This in turn has galvanized efforts to understand viscous hydrodynamics, which has led to tangible technical progress and several new codes. It has also dovetailed with studies of QCD energy loss, which can now be used to estimate the viscosity directly using microscopic scattering processes. Both of these major topics (viscous hydrodynamics and energy loss codes) are being tested and validated by the TECHQM collaboration [8]. At the same time, the string theory community is working to find robust observables to compare to heavy ion measurements. Clearly, input of new and better experimental data, particularly at higher energies, plays an essential part in these developments.

1.2 The experimental search for the Quark Gluon Plasma: from SPS to RHIC

From the very early days of collider and detector design, the world-wide heavy ion physics program has had as its goal to identify the QGP predicted by both perturbative and lattice QCD and to study its properties. The idea is to use the high energies and high densities provided by the collider environment to induce large momentum transfers between nucleon constitutents, leading to weaker interactions, and thus a deconfinement of hadronic constituents. This was orig-
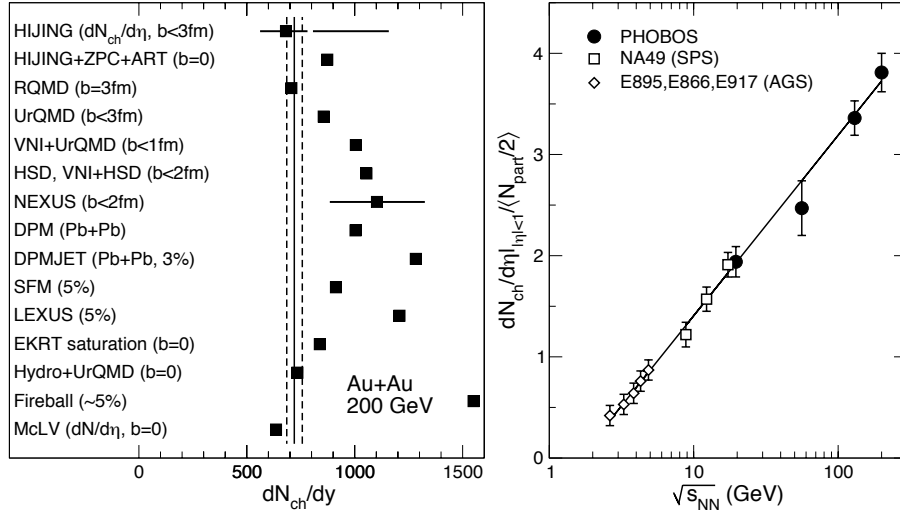
Figure 1.3: (left) The predictions for charged particle multiplicity at RHIC compared to "Day 1" PHOBOS measurements, shown by the vertical line (with systematic uncertainties indicated by the dotted lines). (right) Particle density as a function of nucleon-nucleon (NN) center of mass energy.

inally thought to lead to an enormous jump in entropy (e.g. via a first-order phase transition) with observable consequences, e.g. large multiplicities, large source sizes, and changes in thermal properties of observed particle distributions. At the same time, knowledge of hadronic structure functions and perturbative cross sections led to the prediction that jets could be produced, even at the "low" (on collider scales) RHIC energies, but would be subsequently quenched by the presence of a deconfined medium. Thus, the experimental studies have generally been of two types: "soft" observables, which are sensitive to changes in the medium properties or degrees of freedom, and "hard" observables, which are produced in the very early stage of the collision and are sensitive to the subsequent space-time evolution of the system.

After pioneering experiments covering collisions of smaller nuclei at the CERN SPS and BNL AGS established reference versions of many of the baseline measurements used in future experiments, the SPS program with truly heavy ions (Pb+Pb) began in 1994. While the experiments were overall quite successful in data-taking, no clear consensus emerged from the various data sets. Rather, intriguing new phenomena (strangeness enhancement, J/ψ suppression, low-mass dilepton enhancement) were observed, but no overarching dynamical scenario emerged in the first phase of these experiments (1994-1999). A summary of these findings was released by CERN in 2000 [9]. The RHIC program was carefully planned to avoid non-overlapping experiments, by cover as much of the available phase space as efficiently as possible, all the while focussing on the much higher rates of high-p_T processes opened up by the higher energies.

Figure 1.4: (left) Azimuthal modulation of charged particle production relative to the reaction plane at 130 GeV from PHOBOS. (right) Flow as measured by PHOBOS in 130 and 200 GeV collisions [10].
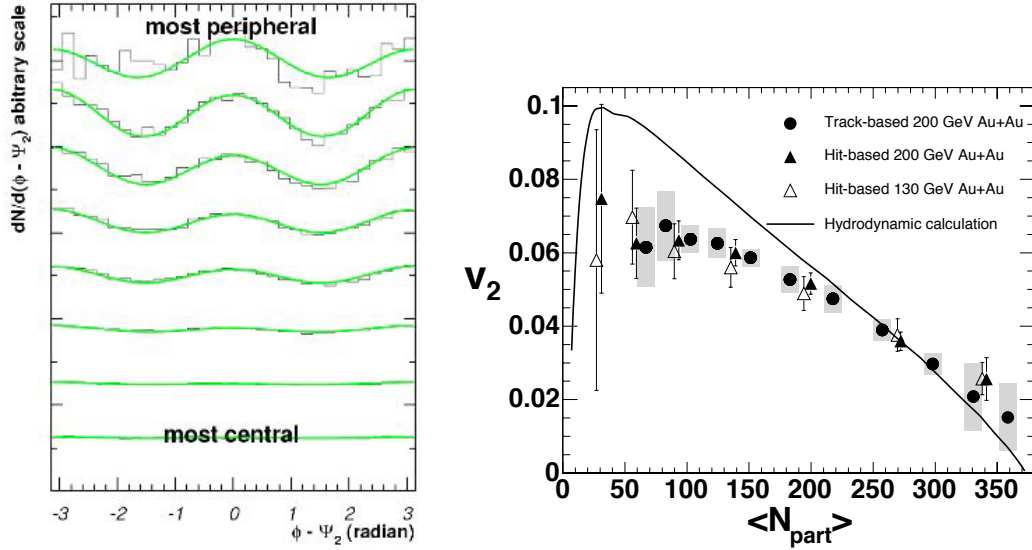
1.3 Bulk properties of heavy ion collisions through RHIC energies

"Bulk" observables are inclusive measurements, integrating over transverse momentum and rapidity, and reflect the particle and energy density of the system. They become particularly relevant to the understanding of heavy ion dynamical evolution if the viscosity is in fact small, as in that case the entropy is conserved and the final state multiplicity is linearly related to that in the initial state. The system also should show "elliptic" flow, which can be calculated in a hydrodynamic approach augmented by the equation of state from lattice QCD. These measurements are covered in detail in Chapter 5, but are discussed briefly here for context.

The RHIC data appeared very rapidly after the machine started providing physics events in 2000, with the PHOBOS measurement of the charged-particle multiplicity at mid-rapidity, shown in the right panel of Fig.1.3. The left panel shows that this was found to be on the low side of the range of predictions available at the time, as characteristic of models with a limited role of hard processes as contributing to the total entropy, and has been cited as evidence of the relevance of the CGC initial conditions. The inclusive measurements were quickly complemented by identified particle spectra and interferometric measurements, which found the particle source to be surprisingly similar to that found at lower energies. However, global measurements which characterized the collective flow of the system indicated that it was expanding as rapidly as ideal hydrodynamics would predict, suggesting that the system was in fact strongly-interacting, rather than weakly. These moreover established that the produced particles were not simply the result of a superposition of independent proton-proton collisions, but rather reflected collective behavior [11]. At the same time, measurements of particles originating in hard processes (e.g. high-p_T hadrons) showed that these were not produced according to binary collision (N_{coll}) scaling, characteristic

5

of the small scales probed by large momentum transfers. Rather, they were strongly suppressed by a factor of five. This supported the interpretation that the medium was dense and absorptive, an interpretation further confirmed by two-particle correlations showing the disappearance of back-to-back hadrons.

The role of the initial state wave function is connected with the dynamics of energy deposition and thermalization in the nuclear collision. If heavy ion collisions indeed form a collective system which is in local thermal equilibrium then the details of microscopic dynamics will not be important for the development of the system. Rather the "bulk" of the system (by which is meant the average behavior of typical particles) will reflect only macroscopic features of the collision. It is a major outstanding question exactly to what extent the system thermalizes, although the relevance of statistical-thermal models applied to the final state hadrons (e.g. in Ref. [12]) strongly suggests the system was in fact thermal throughout most of its evolution. Once the system is thermalized, then lattice QCD calculations are thought to be the relevant theoretical tool to understand the bulk properties of the medium, especially the equation of state (EOS) shown previously in the left panel of Fig.1.1. The details of the equation of state, both in terms of degrees of freedom, and especially in terms of the evolution of bulk quantities like energy density and pressure, are expected to have quantifiable effects on the dynamical evolution of the system.

The azimuthal distributions of inclusive charged particles (as well as transverse energies) have been found to show a strong event-wise modulation, shown for PHOBOS data in the left panel of Fig. 1.4. This is characterized by the second Fourier coefficient $v_2 = \langle \cos(2[\phi - \Phi_{RP}]) \rangle$, where Φ_{RP} is the angle of the reaction plane or event plane. The measurement of v_2 as a function of the number of participants (N_{part}) is shown in the right panel of Fig. 1.4 [10]. The data are compared with hydrodynamical calculations assuming zero viscosity (i.e. a perfect fluid). The value of v_2 at RHIC is about three times larger than achievable with hadronic models, already suggesting that the flow must be built up when the system is decidedly pre-hadronic in nature. Even with this simple measurement, which requires only a choice of energy density (ϵ) at a chosen thermalization time τ_0, one can test to see how far down in collision centrality (or volume) the assumption of early local equilibirium extends. With more differential measurements, it is possible to test various hypotheses about the degree of thermalization as well as the equation of state, either phenomenological or derived from lattice calculations. It is also possible to quantitatively extract estimates of the η/s ratio using the elliptic flow data from different channels (e.g. heavy flavor) [7].

It should be emphasized here that the applicability of hydrodynamical models is not a trivial outcome. Perturbative physics is predicated on the possibility of small cross sections when the coupling between degrees of freedom is weak. The fact that hydrodynamics seems to be the appropriate starting point for RHIC physics suggests the opposite, that strong coupling dominates the dynamics all the way back to the first instants of the collision. This led to the announcement in 2005 by all four RHIC collaborations that the medium formed there was not a weakly-coupled plasma, as originally envisioned, but a strongly-coupled medium [13, 11, 14, 15]. This state of matter, generally referred to as the "sQGP", is still not understood in microscopic detail, but the entire RHIC program is now dedicated to elucidating its properties. Given this context, the continuing relevance of hydrodynamics may well be the first major discovery from the LHC heavy ion program, and will be a major step forward in our understanding of the sQGP.
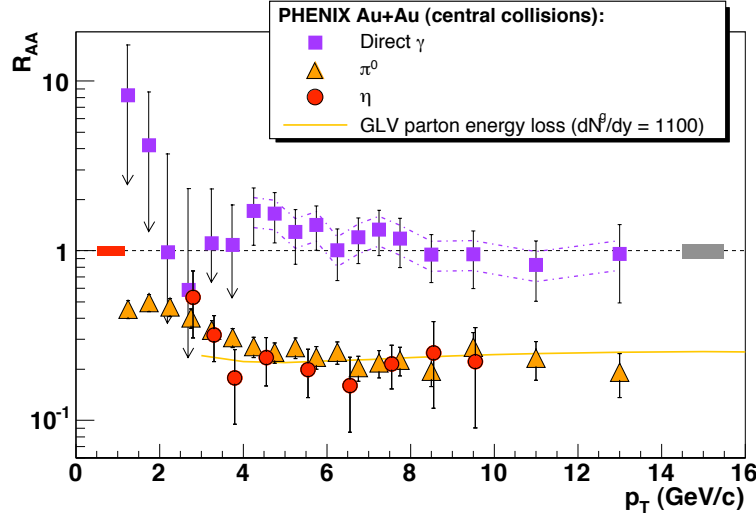
Figure 1.5: Nuclear suppression factor R_{AA} measured by PHENIX for photons, π^0 and η particles, from Ref. [16].

1.4 Jet Suppression in Heavy Ion Collisions

Another means to probe the microscopic origins of the bulk dynamics is to study "hard probes," physics processes resulting from large momentum transfers of quarks and gluons, to see if the nuclear environment produces different results than nucleon-nucleon systems. In this context, the latter is treated as a "null hypothesis", where it is assumed that no medium effects are present. QCD factorization theorems predict that every binary collision of two nucleons has an equivalent chance of inducing a hard process. Under this assumption, one can calculate the nuclear modification factor:

$$R_{AA} = \frac{dN/dp_T|_{AA}}{\langle T_{AA} \rangle d\sigma/dp_T|_{pp}} = \frac{1}{N_{coll}} \frac{dN/dp_T|_{AA}}{dN/dp_T|_{pp}} \tag{1.1}$$

where T_{AA} is the nuclear overlap function. This quantity was proposed in order to study the phenomenon of "jet quenching" in nuclear collisions, where jets produced in the original hard processes are attenuated as they pass through the medium. However, at this point it is used for suppression phenomena of all types (e.g. heavy quarks and photons as well). Theoretical energy loss schemes are able to relate the measured value of R_{AA} to transport properties of the medium, e.g. the transverse momentum transfer per unit length $\hat{q}$ or the gluon density dN_g/dy.

PHENIX data for identified π^0 and η have measured this quantity out to $p_T = 13$ GeV, which is shown in Fig.1.5 for central Au+Au events at $\sqrt{s_{NN}} = 200$ GeV. It is observed that R_{AA} is approximately constant at ~ 0.2 above 5 GeV both for π^0 and η. As a comparison, PHENIX also presents the normalized yield of direct photons, which should be unaffected by the strongly-interacting medium and simply reflect the incoming parton flux. As expected, the direct photons (out to 12 GeV) scale approximately with the number of binary collisions, ruling out substantial initial state effects. Calculations based on perturbative energy loss, an example shown by GLV [17], are able to quantitatively predict the magnitude of the suppression.
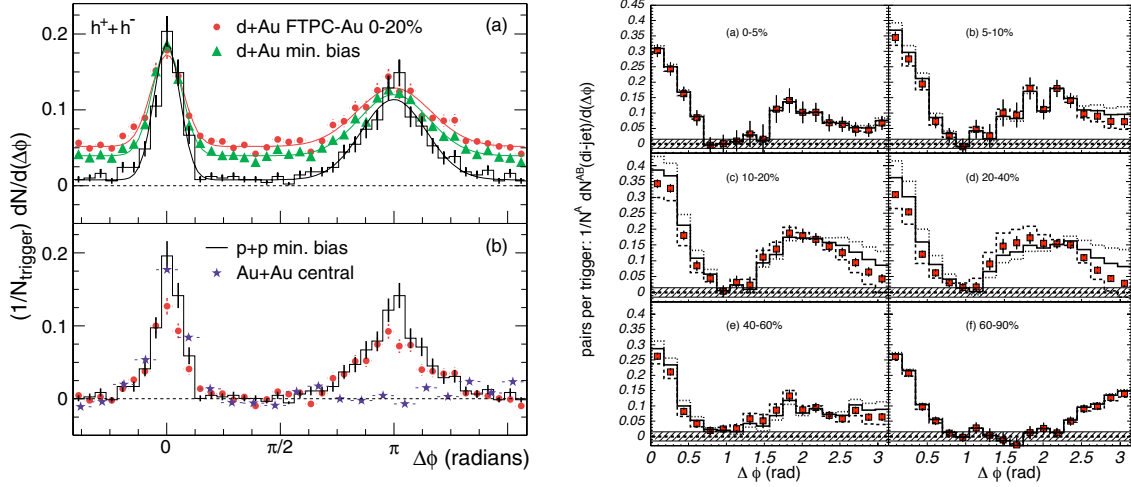
7

Figure 1.6: (left) Back-to-back suppression measured by STAR for trigger particles of 4 GeV and associated particles of 2 GeV [18]. (right) Away side modification measured by PHENIX in Au+Au reactions [19].

Although calculations explain it as a complicated interplay of various physics effects, the constancy of R_{AA} at high-p_T suggests a geometric origin for the suppression phenomenon. This has been explored by studies of correlations between high-p_T hadrons, which utilize the fact that energetic hadrons are typically produced back-to-back, e.g. in proton-proton and deuteron-gold collisions, simply as a result of local energy momentum conservation. STAR found a dramatic disappearance of the "away side" ($\Delta\phi \sim 180^0$) for trigger hadrons of 4 GeV and associated hadrons of 2 GeV [20]. They also observed, as shown in the left panel of Fig.1.6, that the "near side" ($\Delta\phi \sim 0^0$) was essentially unmodified in yield or width, as compared to the p+p or d+Au data. Together, these suggested that high-p_T hadrons came from jets that fragmented near the surface of the collision region, while the jets that point inwards are completely absorbed. This is a straightforward way to explain the constant R_{AA} value at approximately the value expected by N_{part} scaling, since $N_{coll} \propto A^{4/3}$ and dropping one radial dimension ($R \propto A^{1/3}$) leads to $A^{4/3}/A^{1/3} \sim A \sim N_{part}$.

Subsequent studies of hadron correlations found an interesting effect when considering the correlation of low-p_T associated particles with the high-p_T trigger particle, shown in the right panel of Fig.1.6. While peripheral events show a clear "back-to-back" recoil of the soft particles against the hard trigger particle, more central events find a relative minimum at $\Delta\phi \sim \pi$ and two peak structures $60 - 80^0$ off axis [21]. Using three particle measurements, this double hump structure has been interpreted as a "Mach Cone" structure, reflecting the difference between the speed of sound in medium and the speed of light (typical of hard probes) [22]. In any case, it shows a non-trivial interaction of the recoiling parton with the medium, modifying its fragmentation properties, perhaps so much that all that is predominantly observed is the conservation of energy and momentum.

A major outstanding issue remaining from these studies is a quantitative determination of the
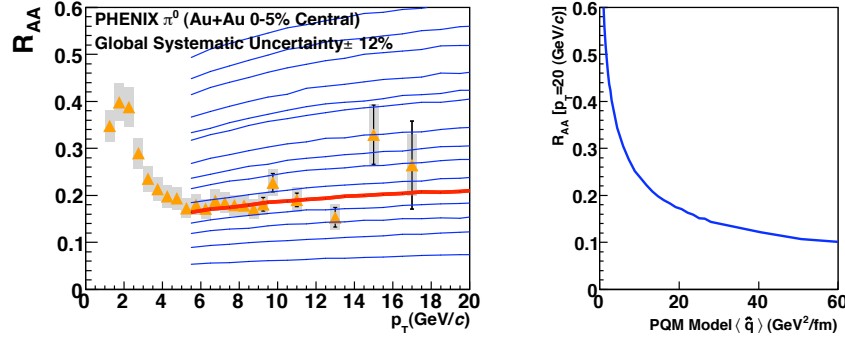
Figure 1.7: (left) Comparisons of PQM calculations for different $\hat{q}$ with high-p_T suppression data from PHENIX, from Ref. [23]. (right) R_{AA} at high p_T as a function of $\hat{q}$ [23].

transport coefficient $\hat{q}$ which reflects the energy broadening of a fast probe via radiating gluons. The jet energies probed at RHIC so far appear to be low enough that jets pointing into the bulk are completely absorbed. This occurs in some calculations for a very large range in $\hat{q}$, meaning that R_{AA} measurements in themselves offer limited sensitivity to information about the local density. What sensitivity remains has been fully exploited by the RHIC experiments, in particular an analysis by PHENIX using several existing jet quenching calculations [23], an example of which is shown in Fig. 1.7. In the left panel, it is shown that they extract a value for $\hat{q}$ of $13.2^{+6.3}_{-5.2}$ GeV^2/fm at the 95% confidence level, a large value well above perturbative estimates. It is shown in the right panel that R_{AA} as a function of $\hat{q}$ is quite flat at high p_T, which contributes to the large uncertainty. Given this, it is an interesting question whether the return of back-to-back correlated hadrons at very high trigger *and* associated p_T, shown in Fig. 1.8 is indicative of a "punch-through" phenomenon (i.e. no interaction while going through medium) [24]. However, it is found that the forward- and away-side fragmentation properties are both consistent with hadronization in vacuum, which suggests minimal passage through matter. This may be the result of tangential emission, where the primary hard process is formed on the edge of the reaction zone and neither parton is aimed directly into the bulk. Clearly, access to substantially higher-energy jets will clarify the situation, either by revealing a real punch-through effect, or showing such extreme quenching (or disappearance) that current pictures of jet production and evolution may be shown to be inadequate.

1.5 Prospects for the LHC

The start of the LHC Heavy Ion program (planned for 2010) will surely produce as dramatic a revolution in the study of the QGP in the laboratory as RHIC produced when it first started operation in 2000. Pb+Pb collisions at the LHC are expected to produce a QGP with initial energy density roughly an order of magnitude larger than at RHIC [25, 26], with larger initial temperatures (by a factor of two) and longer lifetimes (by a factor of 1.5) than achieved at RHIC [25]. The increase in the collision energy from RHIC to the LHC will provide a critical test of the application of saturation-inspired models in the description of $A + A$ particle multiplicities. Measurements of
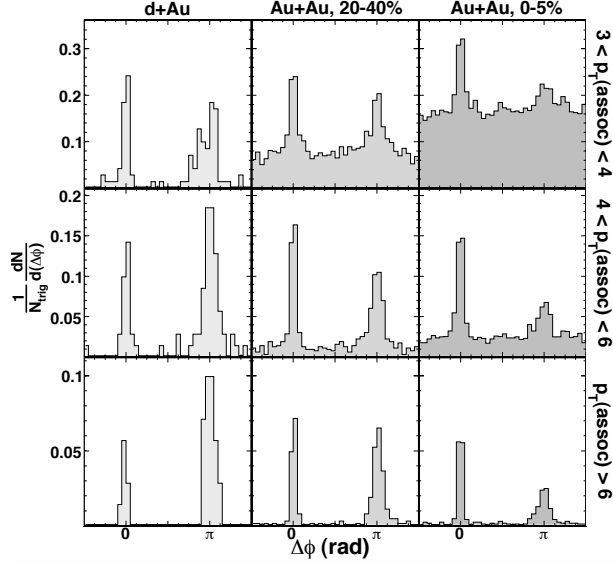
Figure 1.8: Return of back-to-back emission at high p_T measured by STAR.

elliptic flow resulting from the higher initial energy densities will test our interpretation of elliptic flow results from RHIC.

Arguably, the most important component of the LHC heavy ion program will be the measurements of jet quenching and the use of jets as a tomographic probe of the medium. The increase in hard scattering cross-sections between the top RHIC energy ($\sqrt{s_{NN}} = 200$ GeV) and the LHC ($\sqrt{s_{NN}} = 5.5$ TeV for Pb+Pb) will extend the p_T range accessible in quenching measurements by at least a factor of 10 [27]. For example, a single Pb+Pb run at design luminosity will produce nearly a million jets with $E_T > 100$ GeV [27]. As a result of the copious production of high-energy jets at the LHC, full jet measurements will be possible in Pb+Pb collisions, and these measurements should dramatically improve the understanding of jet quenching mechanisms. The energy loss bias will be reduced to the extent that a high-energy quenched jet should still be reconstructed, even if radiative energy loss produces a re-distribution of energy within the jet [28]. Direct measurement of the modified fragmentation functions of the jets [29] will provide more detailed tests of energy loss calculations, thereby reducing the current theoretical ambiguities and improving the utility of quenching measurements as probes of the QGP. Measurement of the inclusive jet E_T spectrum will, in principle, provide sensitivity to collisional energy loss [30, 31] as well as exhibit effects from non-perturbative energy loss that might transfer radiated energy to the medium [32]. The statistics for bottom and charm jets will be sufficient to perform detailed measurements of heavy quark quenching at high E_T. The rate for hard photon-jet processes will be sufficient to allow measurements of photon-tagged jet quenching for photon and jet transverse energies up to 100 GeV. Measurement of the acoplanarity of di-jet pairs at the LHC should provide sensitivity to the expected angular diffusion of high-p_T partons in the medium – an unavoidable consequence of radiative and collisional energy loss [33] that has, so far, eluded detection at RHIC. The large rates for jets will make possible the measurement of all of the above observables as a function of collision centrality, angle with respect to the event plane, and pseudo-rapidity. Taken together,

these measurements will provide a degree of sensitivity to the physics of jet quenching that will be difficult to achieve at RHIC. Hard-scattered quarks and gluons may be the only probes that we have that are directly sensitive to the nature of the interactions in the medium. Thus, an improved understanding of the physics of quark and gluon interactions with the medium is essential; full jet measurements at the LHC are the most likely means to accomplish this goal.

The LHC will also provide a new opportunity to explore the physics of deconfinement through the measurement of both charm and bottom quarkonium states. In particular, the ability to measure $b\bar{b}$ quarkonia states has the potential to dramatically improve the current confused situation with experimental probes of deconfinement. Bottom production requires a Q^2 roughly a factor of ten larger than that required for charm production so the production process is harder and, in principle, more amenable to pQCD calculation though theoretical uncertainties in how $b\bar{b}$ pairs evolve into Upsilon (Y) states persist. The relative yield of the Y and Y' states is expected to be closer than the yields of ψ and ψ' [34] making comparison of states with different nominal screening scales easier. Also, recent analyses of the temperatures at which the different quarkonia states melt [35] show that the Y is the only state that survives to $2T_c$. The relatively low multiplicity of $b\bar{b}$ pairs in Pb+Pb collisions at the LHC is expected to give little recombination contribution to production of Y states [34]. Thus, while it would be naive to assume that Y measurements will be completely free of complications, there is good reason to expect that the measurement of Upsilon production and suppression at the LHC will significantly advance the understanding of Debye screening/deconfinement in the QGP. Certainly, the Y states provide the first new experimental tool for studying Debye screening in the QGP since the advent of J/ψ suppression measurements in NA38 nearly two decades ago [36].

It should also be added that the LHC program has a good mix of a wide variety of measurements as well as the possibility of robust cross checks from experiments with similar (but not identical) capabilities, similar to that found in the RHIC program. There are three experiments with dedicated heavy ion groups: ALICE, ATLAS and CMS. ALICE is a large collaboration whose overall focus is heavy ions, with a large volume TPC and electromagnetic calorimetry covering mid-rapidity and a forward muon spectrometer. ATLAS and CMS have been optimized for proton-proton physics, particularly to find the Higgs and supersymmetric particles. And yet, this requires hermetic detectors with precise tracking and full calorimetry (EM and hadronic). The latter is particularly relevant to continuing progress in high-p_T physics, both to extend coverage in p_T via high level triggering, and in x via acceptance out to large rapidities.

1.6 Connection with RHIC and RHIC II programs

The scientific programs at the upgraded RHIC II and the LHC will be complementary and, together, will provide a comprehensive study of the properties of the QGP over an estimated initial temperature range $T_c < T < 5T_c$. Results from both programs will be required for the development of a systematic understanding of how the QGP is formed from initial semi-hard partonic scattering and emission, how it thermalizes, how it evolves dynamically, and how it hadronizes. Results from the LHC and RHIC will surely influence the thinking about results from the other program. In particular, measurements from the LHC that test concepts developed using RHIC results will certainly have an immediate and important impact on the future RHIC program.

The interaction between the RHIC and SPS Heavy Ion programs provides a good model for

the positive impact that the LHC Pb+Pb program will likely have on the RHIC program. In many places, but especially in the area of jet quenching, results from RHIC stimulated analysis of SPS data that would otherwise never have been performed – often with surprising and interesting results. A good example is provided by the strong distortion of the di-hadron correlation seen at RHIC [19]. This result from RHIC stimulated similar investigations by the CERES experiment which found similar features [37, 38] in their data. The fact that a similar modification of the di-jet shape is observed at SPS energies, where the p_T range of hard processes is extremely limited and where quarks dominate, necessarily constrains theoretical interpretations of the effects. The synergy between the SPS and RHIC programs has provided a substantial net benefit for the field as a whole. In a similar way, it will be fascinating to have a parallel program at lower energies to look for phenomena more easily seen at the higher LHC energy.

1.7   Report structure

The remainder of this document is structured as follows: Chapter 2 discusses the capabilities of the ATLAS detector for heavy ions, simulations of HIJING events in the ATLAS detector, with discussions of detector occupancies. Chapter 3 describes the ATLAS Zero Degree Calorimeter and the contribution of the calorimeter to the ATLAS Heavy Ion program. Chapter 4 discusses the particular issues related to charged-particle tracking in heavy ion events, and how they are addressed. Chapter 5 describes in more detail the physics impact of global measurements and shows results from studies of $dN_{ch}/d\eta$, $dE_T/d\eta$, event plane reconstruction and v_2 measurement. Chapters 6 provides the physics motivation and goals of complete jet measurements at the LHC and summarizes the ATLAS performance in carrying out full jet measurements in a heavy ion background. Chapter 7 describes ATLAS quarkonia measurements using dimuons and the physics impact of these measurements as well as similar techniques applied to the measurement of Z bosons in heavy ion collisions. Chapter 8 describes the physics motivation for direct photon and photon-jet measurements and shows the results of studies of background rejection and direct photon efficiency in heavy ion collision along with reconstructed photon-jet correlations. Chapter 9 discusses the importance of triggering in heavy ion collisions, and its implementation in ATLAS, Chapter 10 summarizes the main features of the ATLAS heavy ion program, and describes the outlook for the next several years.

Chapter 2

The ATLAS Detector in the Heavy Ion Environment

2.1 ATLAS as a heavy ion detector

The ATLAS detector [**?**, 39] provides several important capabilities essential for a robust heavy ion program:

- large acceptance, high quality electromagnetic and hadronic calorimeters with fine transverse segmentation and longitudinal segmentation;

- nearly hermetic external muon spectrometers;

- high precision silicon inner detector;

- high-rate trigger and data acquisition system designed for triggering on rare, high-p_T particles/jets.

Figure 2.1 provides a schematic view of the ATLAS detector showing all major detector components. The detector can be viewed as having three largely independent detector systems: the inner detector, the calorimeters, and the muon spectrometers. The inner detector consists of silicon pixel (Pixel), Semiconductor Tracker (SCT), and transition radiation tracker (TRT) detectors. The calorimeter system consists of barrel and end-cap liquid argon electromagnetic calorimeters, a traditional hadronic calorimeter (Tile Calorimeter), end-cap liquid argon hadronic calorimeter, and forward EM and hadronic calorimeters. The muon spectrometers consist of toroidal magnets and tracking detectors covering both the barrel and end-cap regions of the detector.

The pseudo-rapidity coverage of the ATLAS detector broken out into its various detector components is shown in Fig. 2.2. The ATLAS calorimeters allow measurement of jets over the pseudo-rapidity interval $|\eta| < 5$ and identified photons over the interval $|\eta| < 2.4$. In the inner detector charged particles are measured over the interval $|\eta| < 2.5$. The muon spectrometers, covering $|\eta| < 2.7$ allow measurement of Y states over a broad $|\eta|$ range. A forward luminosity monitoring detector (LUCID) will provide $dN_{ch}/d\eta$ measurements over $5.4 < |\eta| < 6.1$. The ATLAS Zero Degree Calorimeters (ZDCs) provide coverage of the region $|\eta| > 8$ for neutral particles, both neutrons and photons.
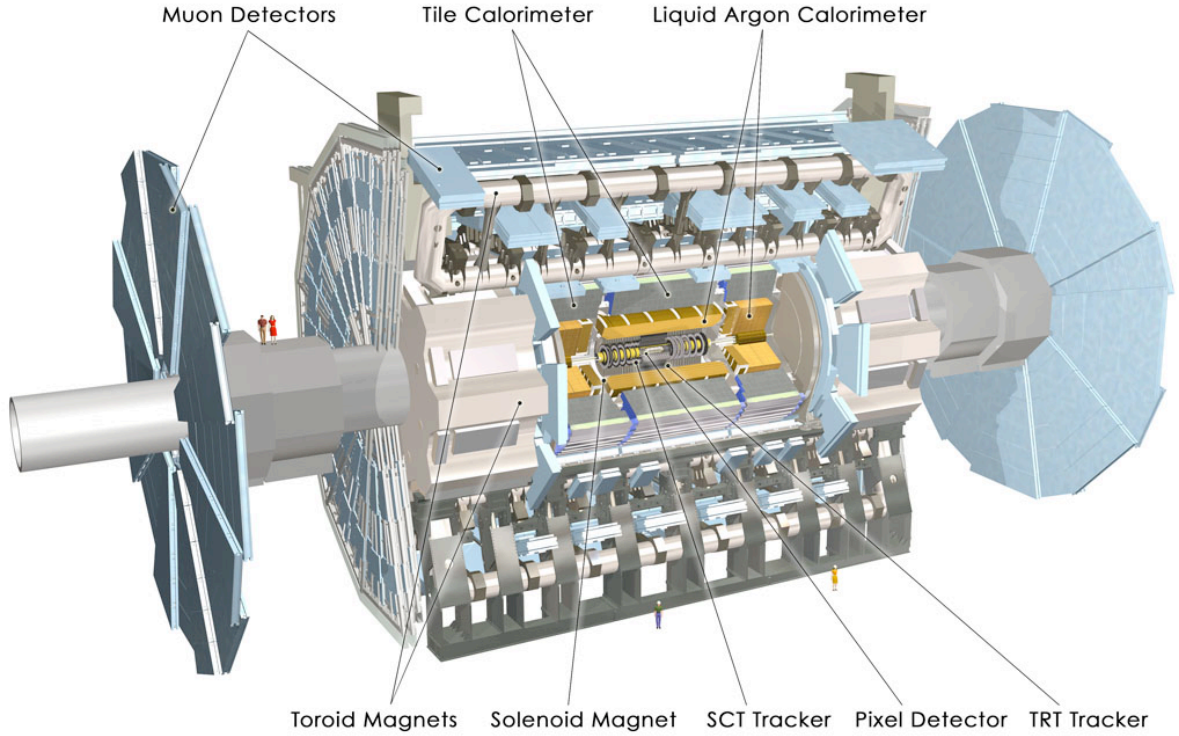
Figure 2.1: The ATLAS detector at the LHC

One of the unique components of the ATLAS detector relevant to this proposal is the liquid argon electromagnetic calorimeter shown in a diagram of the full ATLAS calorimeter system in Fig. 2.3. The electromagnetic calorimeter, broken into separate "Barrel" and "End-cap" sections as shown in Fig. 2.3, is radial segmented into three layers with the first layer consisting of "strips" that are finely segmented in the η direction ($\Delta\eta \approx 0.003$). This fine segmentation of the first EM sampling layer extends over $|\eta| < 2.4$ and provides valuable separation between single photons and photon pairs produced in neutral hadron (primarily π^0 and η) decays. Because of the fine segmentation of the first sampling layer, this separation can be utilized for neutral hadron transverse momenta as large as 100 GeV (see Chapter 8). The radial segmentation of the EM calorimeter allows for improved compensation and provides the best intrinsic jet energy resolution of the detectors at the LHC. The clear advantages of the ATLAS calorimeters for performing jet, di-jet, γ-jet, etc. measurements and the importance of the jet quenching measurements at the LHC provide a clear motivation for the ATLAS participation in the LHC heavy ion program.

The ATLAS heavy ion group will take advantage of the unique strengths of the ATLAS detector to pursue a focused study of hard processes in heavy ion collisions at the LHC with the goal of using jet quenching and quarkonia measurements to provide detailed, quantitative information about the properties of the QGP created in heavy ion collisions at the LHC. To accomplish this goal, the group will also perform measurements of global observables in Pb+Pb collisions as these will be essential for constraining bulk properties of the medium and providing reaction plane measurements that will be essential for performing differential measurements of quenching as a
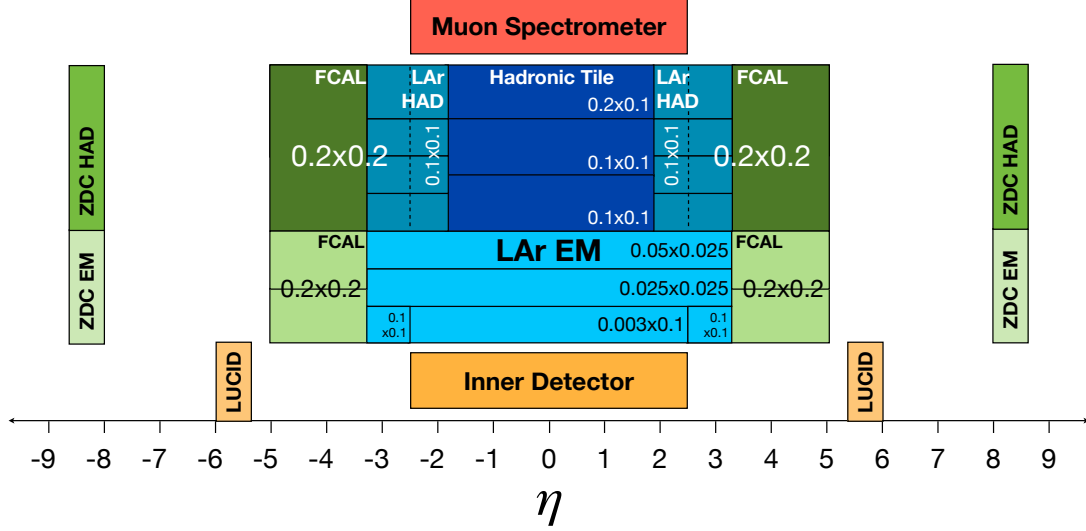
Figure 2.2: The pseudo-rapidity coverage of various components of the ATLAS detector by layer.

function of path length in the medium [40]. It will also participate in p+p measurements as needed to provide the necessary baseline measurements for the Pb+Pb program.

The program will first focus on "Day 1" physics, both in proton-proton and heavy on collisions, to establish the global features of these reactions, particularly in the context of data from a range of energy and system sizes. We plan to participate in first measurements of charged particle pseudorapidity density, $dN_{ch}/d\eta$, the transverse energy flow, $dE_T/d\eta$, and charged particle elliptic flow (v_2) in Pb+Pb collisions. The $dN_{ch}/d\eta$ measurements will be performed over the range $|\eta| < 2.5$ and $5.4 < |\eta| < 6.1$. The $dE_T/d\eta$ measurements will be performed over the range $|\eta| < 5$. Charged particle v_2 measurements will be made over the pseudo-rapidity interval $|\eta| < 2.5$ while calorimetric v_2 measurements will be performed over the range $|\eta| < 5$.

After the initial baseline studies, which can be performed on relatively small data sets (as even several hours of data can be used productively), the program will progress quickly to the study of high-p_T processes. We will measure jet energy spectra, jet charged particle fragmentation functions, jet charged particle j_T (transverse momentum relative to the jet direction) distributions, jet shapes, and di-jet angle and energy correlations to separately quantify collisional and radiative energy loss of hard-scattered partons in the QGP. We will use a combination of muon tagging and displaced vertex tagging to separately measure bottom and charm quark energy loss. A combination of direct photon identification and photon isolation will be used to perform high-statistics measurements of prompt photon production and γ-jet pairs to calibrate and further improve the precision of the jet quenching measurements and to extend jet measurements to low E_T. We propose to use the unique capabilities of the ATLAS electromagnetic calorimeter to statistically measure prompt photons down to and possibly below 10 GeV with the goal of detecting jet-conversion photons and medium-induced photon bremsstrahlung associated with jets. The wide calorimetric
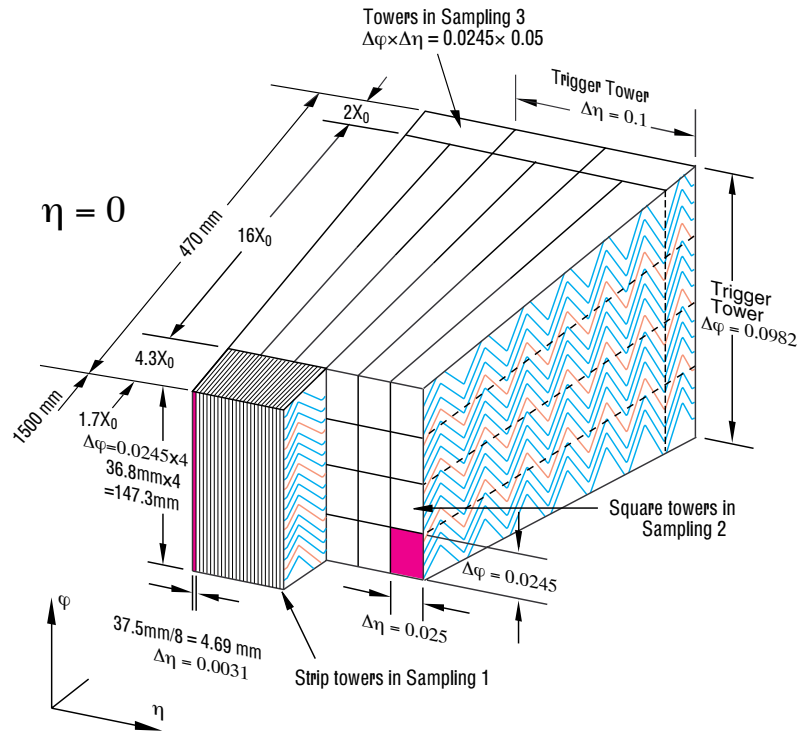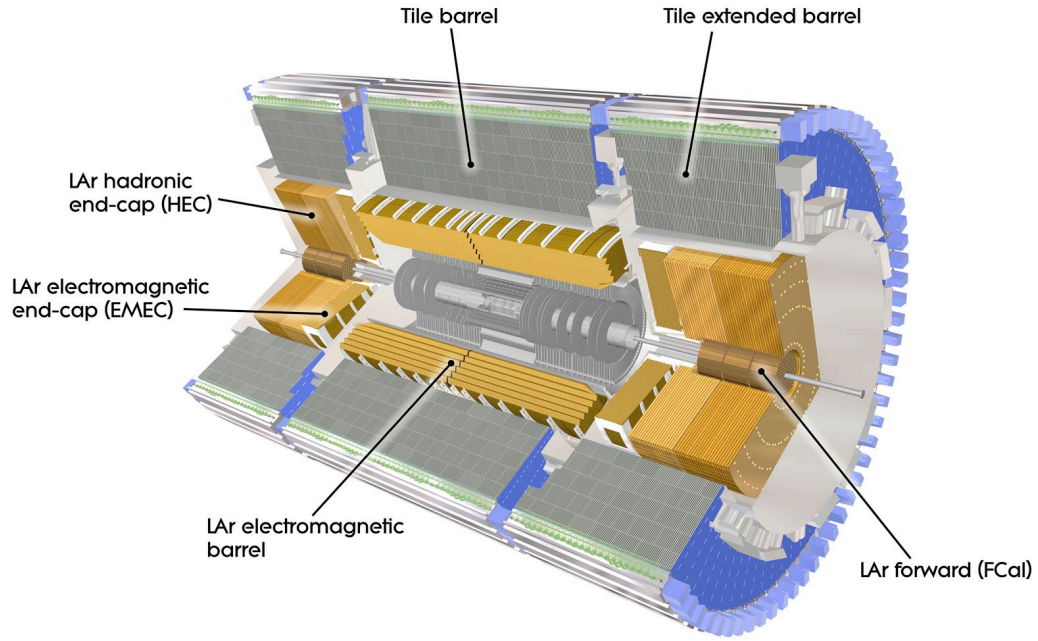
15

Figure 2.3: (top) Diagram of the ATLAS calorimeter system. (bottom) Diagram showing segmentation of ATLAS electromagnetic calorimeter.

16

coverage and tracking coverage of the ATLAS detector will be used to study the medium response to the passage of high energy jets with the goal of clarifying the exciting, but poorly understood jet modifications observed at RHIC. We will make all of the above measurements as a function of collision centrality, angle with respect to the event reaction plane, and pseudo-rapidity. We will measure jets over the pseudo-rapidity range $|\eta| < 5$, photons over the range $|\eta| < 2.4$, and charged hadron fragmentation over the range $|\eta| < 2.5$.

The quarkonia portion of the program focuses on measurement of Upsilons (Y) over the pseudo-rapidity range $|\eta| < 3.5$ with sufficient mass resolution to resolve the Y and the Y$'$ states. The Y and Y$'$ measurements will, by themselves, provide a direct probe of Debye screening of quarkonium states. Direct photon, Z bosons, single muon, and muon tagged jet measurements will provide benchmarks for Y suppression within the Pb+Pb measurements and will be used to assist in the interpolation of full energy p+p Y measurements to $\sqrt{s_{\mathrm{NN}}} = 5.5$ TeV.

2.2 Simulation tools

The HIJING model (Version 1.38) [41] is the primary event generator used for heavy ion events at the LHC. All generated events have been processed through a full GEANT4 [42] simulation of the detector response. The simulations in this Report have been performed with release 12 of the ATLAS Athena software and an "as built" detector geometry (ATLAS-CSC-01-02-00), the same as used for the Computing System Commissioning (CSC) [43] studies for p+p collisions. It includes a complete description of the active detector elements, and also a realistic description of the detector material, including supports, services and other passive elements.
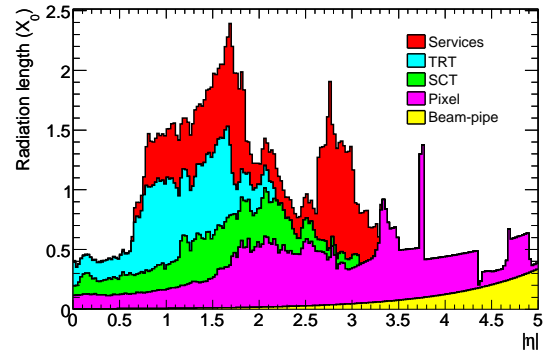
Figure 2.4: Amount of the material in radiation lengths in different subsystems of the ATLAS Inner Detector.

Figure 2.4 shows the distribution of the material in the Inner Detector. This detailed description allows us to correctly predict fluxes of all particles in active elements, including contributions from secondary interactions in the detector materials.

The fully simulated samples of Pb+Pb collisions at $\sqrt{s_{NN}} = 5.5$ TeV have been used to study the ATLAS capabilities for measuring the global characteristics of heavy-ion collisions (see Chapter 5). They have also been used as a generator of the soft particle background for embedding rare physics processes like quarkonia, Z bosons (Chapter 7), jets (Chapters 6 and direct photons (Chapter 8). For these studies, both PYTHIA [44] and single particle generation are used. When possible we make use of the ATLAS events generated during the ATLAS Computing System Commissioning, although some sets with merged signals have been generated privately.

The HIJING model was developed to study particle production in high-energy p+p, p+A and A+A collisions. It is based on a perturbative QCD description of multiple mini-jet production in hard parton scattering processes. For soft processes, with small transverse momentum transfers

17
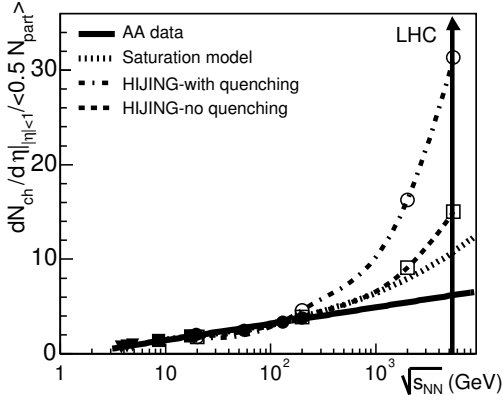
Figure 2.5: Average number of charged particles at mid-rapidity, normalized to the number of participant pairs, as a function of the center-of-mass energy for experimental data and various models. Lines show extrapolation of data and model predictions to the LHC energy.

(below 2 GeV), a string description of soft-gluon exchanges between valence quarks or di-quarks is adopted. The Lund JETSET fragmentation scheme [45] is used for jet and string hadronization. A nucleus-nucleus collision is decomposed into a sequence of binary collisions involving participant and excited nucleons. The Glauber model [46] is used to describe the collision geometry and to compute the number of binary collisions and the number of participant nucleons. Additional nuclear effects are also incorporated, including nuclear shadowing and final-state energy loss (jet quenching). Nuclear shadowing is the suppression of the effective number of partons at low values of x, leading to a decrease in the multiplicity of produced particles. This is implemented by suitable parameterizations of the quark and gluon structure functions in the small and medium x region, evolved by DGLAP evolution. Jet quenching occurs via gluon radiation with an assumed average energy loss of partons traversing the dense medium. In HIJING's implementation, the process of energy loss is stopped when p_T of a parton falls below 2 GeV. It should be noted that HIJING does not incorporate any final state re-interactions among the produced particles (partons or hadrons), and thus does not experience anisotropic particle flow.

The HIJING model has been tested against experimental data from p+p, p+A and A+A collisions over a wide energy range. While it roughly agrees with RHIC data at 130 GeV, it deviates from measurements both as a function of energy and centrality. That said, it is generally suitable as a source of particles for studies of detector performance. Figure 2.5 shows HIJING predictions (both with jet quenching switched on and off) for the charged particle density at mid-rapidity ($|\eta| < 1$) in central heavy-ion collisions. They are compared with experimental data from the AGS center-of-mass energy (about 4 GeV) up to the highest RHIC energy of 200 GeV. A logarithmic extrapolation of the experimental data (assuming average number of participants $< N_{part} >$ of about 380 for central Pb+Pb collisions) gives an expected charged particle density $dN_{ch}/d\eta \sim 1300$. The saturation model of Ref. [47] reproduces the data reasonably well, and predicts charged particle multiplicity at the LHC energy of about 2000. HIJING with jet quenching predicts a much higher density (up to about 6000) consisting mainly of soft particles with $p_T < 1$ GeV, while switching off parton energy loss reduces this density to about 3000. For the studies presented in this report we use HIJING without jet quenching, which still gives a much higher particle density than other models or generic trends observed in the experimental data. Thus, the results presented in this

report should be considered as rather conservative, since the level of soft background will likely be lower.
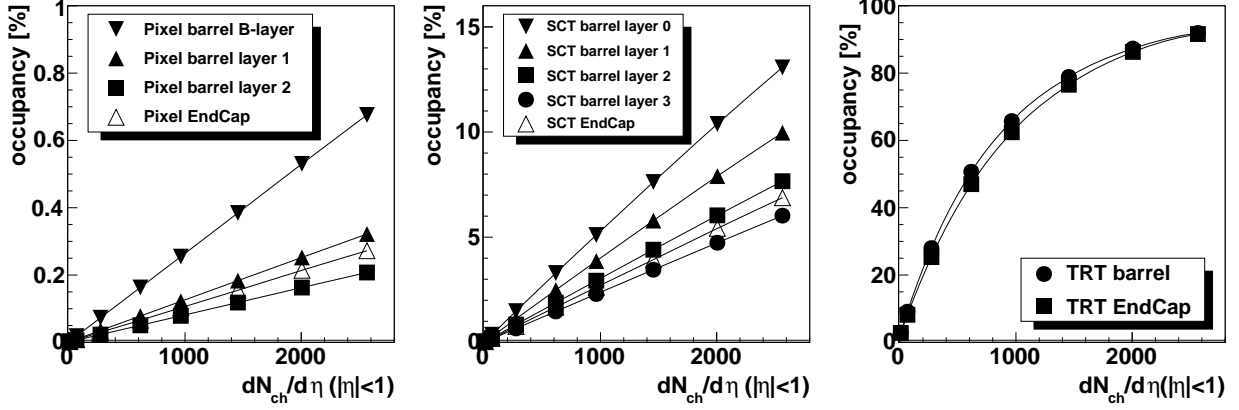
Figure 2.6: Occupancy in the Pixel, SCT (strips) and TRT detectors for minimum bias Pb+Pb collisions at 5.5 TeV/nucleon.

2.3 Detector occupancies

This section presents simulation results for detector occupancies assuming particle densities from HIJING without jet quenching. All three main systems: the inner detector, the calorimeter system, and the muon tracker, are shown.

2.3.1 Inner Detector

The occupancy in the inner detector has been evaluated for Pb+Pb collisions with different centralities. Due to high granularity, the precision layers (Pixel and SCT detectors) are expected to experience acceptable occupancies even in central collisions and will be capable of tracking in nucleus-nucleus collisions, as will be demonstrated in Chapter 4. The occupancies for the Pixel, SCT and TRT systems are shown in Fig.2.6 as a function of the generated charged particle density at mid-rapidity, $dN_{ch}/d\eta(|\eta| < 1)$. The Pixel detector occupancy does not exceed 1% while in the SCT the occupancy, although significantly larger, stays below 14% even for the most central collisions. The occupancy of the Transition Radiation Tracker (TRT) is quite large (nearly 100%) for central HIJING events, making it less useful for Pb+Pb analysis. However the TRT detector can be used for less central Pb+Pb and p+Pb collisions ($dN_{ch}/d\eta(|\eta| < 1) < 500$).

2.3.2 Calorimeters

In central Pb+Pb collisions most of the calorimeter towers will have signals. Figure 2.7 shows the amount of energy deposited in a typical $\Delta\eta \times \Delta\phi = 0.1 \times 0.1$ tower in the electromagnetic and hadronic calorimeter systems for central Pb+Pb collisions with impact parameter of 2.3 fm. The average transverse energy flow as a function of η is also shown in Fig. 2.7. Most (about 60%) of the
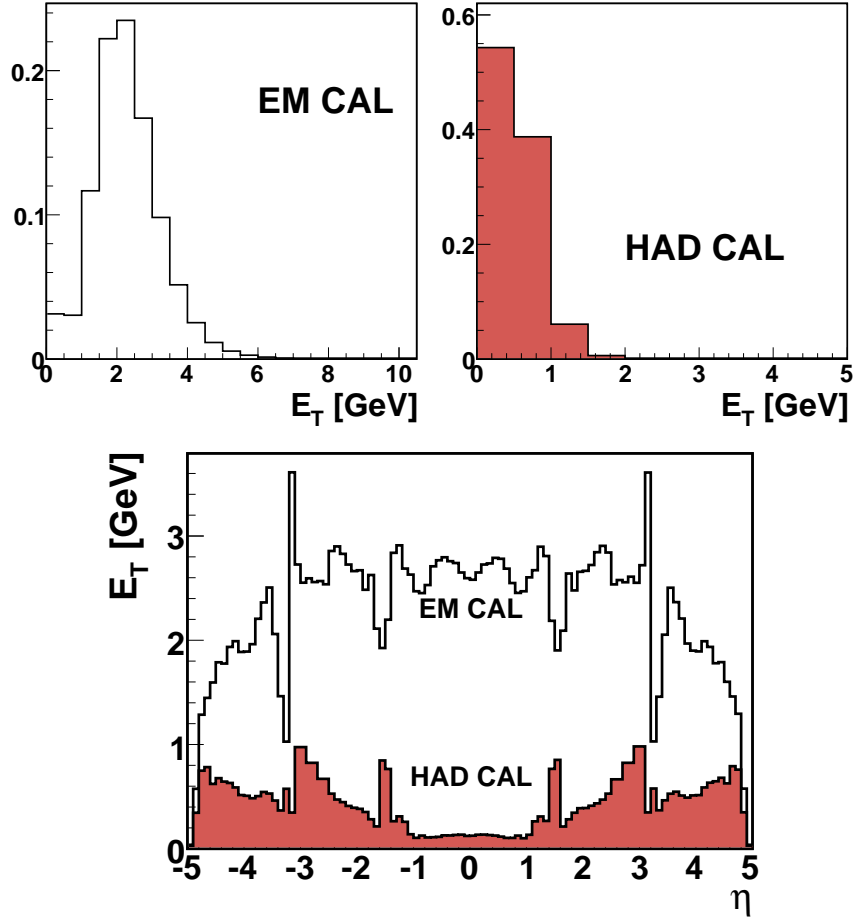
Figure 2.7: (upper) Distribution of energy deposited in a $\Delta\eta \times \Delta\phi = 0.1 \times 01$ tower, for electromagnetic calorimeter (left) and for the hadronic calorimeter (right). (bottom) The average energy per tower as function of η.

1 incident energy is deposited in the electromagnetic section of the calorimeter. The distribution of
2 energy within the electromagnetic calorimeter shows that the energy is predominantly deposited
3 in the first layer of the calorimeter.

2.3.3 Muon Spectrometer

5 The muon spectrometer will show very little activity in heavy ion collisions due to the negligible
6 background induced by thermal neutrons, produced by the interactions of primary and secondary
7 particles with the detector and accelerator elements. The level of this background is proportional
8 to the machine luminosity and to the neutron production cross-section. The luminosity is fore-
9 seen to be significantly lower ($\sim 10^{27}$ cm^{-2} s^{-1}) for Pb+Pb runs than the design luminosity of
10 10^{34} cm^{-2} s^{-1} for p+p collisions, whereas the neutron production cross-section should increase
11 only up to two orders of magnitude. In addition most of the soft particles originating from Pb+Pb

collisions will be absorbed by the calorimeters. As a consequence, the number of hits in the muon chambers will be much lower than that expected during p+p running. For the Monitored Drift Tube chambers [**?**], average number of hits per chamber for Pb+Pb central collisions ($b = 2.3$ fm) is correspondingly 0.185, 0.20 and 0.38 for the inner, middle and outer station in the barrel region ($|\eta| < 0.3$). Larger number of hits is expected to be recorded in the end-cap region ($1.6 < |\eta| < 2.0$), 2.16 in average for the inner station.

2.4 Summary

- The ATLAS Detector is shown to have excellent capabilities for heavy ion collisions at the LHC, with particular attention paid to its fine-grained electromagnetic calorimetry.

- A physics program is outlined which takes particular advantage of ATLAS strengths.

- Generation and simulation tools are discussed, especially the HIJING 1.38 model used for most of the studies in this Report.

- Detector occupancies are calculated for the three major ATLAS subsystems (Inner Detector, calorimeter, muon tracker) in heavy ion events over a range of impact parameters.

Chapter 3

The ATLAS Zero Degree Calorimeter

The Zero Degree Calorimeters (ZDCs) have played a crucial role in the heavy-ion physics program at RHIC, and we expect the same to be true for the LHC program. The ATLAS Zero Degree Calorimeters are the primary hardware contribution to the ATLAS detector by members of the ATLAS heavy-ion program. At LHC startup in September 2008, the two ATLAS ZDCs, one in each beam direction, were mechanically assembled and installed in the LHC tunnel. As of Spring 2009 both ZDCs are integrated with the Trigger and Data Acquisition (TDAQ) and Detector Control (DCS) systems and were operational during the recent cosmic data taking runs.

This chapter summarizes the physics role of the ZDCs and provides a brief description of their design and implementation. Further details on the ATLAS ZDC, its design and performance studies may be found in the original Expression of Interest [48].

3.1 Physics motivation

The ATLAS Zero Degree Calorimeter has been designed to provide precise measurements of energy and position of neutral particles emitted in the forward region, $|\eta| > 8.3$. Together with the ATLAS central detector and the other forward detector systems (FCAL, LUCID [**?**]), it thus allows us to address a broad spectrum of interesting physics topics in nuclear as well as in p+p collisions.

The primary motivation for building the ZDCs for the ATLAS heavy-ion program is to serve as a high-efficiency, low-background trigger for Pb+Pb events, as a means to characterize the centrality and determine the orientation of the reaction plane in nuclear collisions, and potentially to measure the absolute luminosity via coincidence measurements.

Ultra-peripheral heavy-ion collisions (UPC), where the impact parameter b is larger than the sum of the nuclei radii, offer the possibility of studying high-energy photon-nucleon collisions, that are competitive with the studies of Deep Inelastic Scattering processes (DIS) at HERA.

A unique aspect of UPC, particularly in photon-photon collisions is their strong fields that can approach the QED critical field limit. Also, they are interesting technically since $Z\alpha \sim .6$. Certain processes, such as pair creation and recapture which is significant for the LHC beam lifetime, must be treated non-perturbatively.

A general feature of ultra-peripheral collisions is that in heavy ions the electromagnetic cross-sections are larger than in p+p because they are roughly proportional to Z^2 (Z^4 in gamma-gamma processes). With the ZDC it is relatively straightforward to trigger and tag different processes in
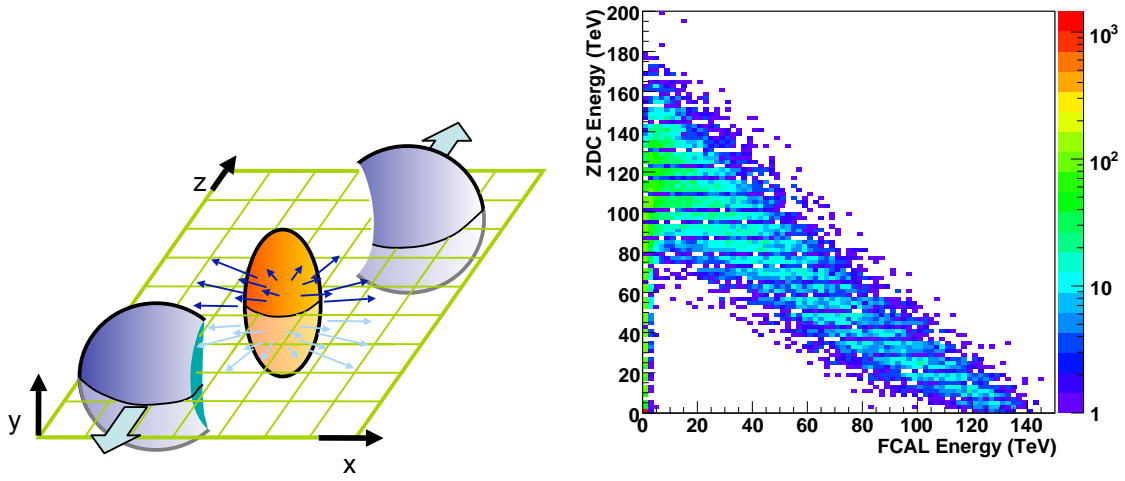
Figure 3.1: (left) Schematic of a nuclear collision, showing the participants in the overlap region and the spectator matter on the sides. In this plot the impact parameter, b, is parallel to the x-axis. (right) Correlation of simulated ZDC response with the forward energy emitted into the ATLAS Forward Calorimeters, illustrating the anti-correlation between collision centrality and number of forward spectator neutrons.

ultra-peripheral collisions.

Although the ZDC has been designed for measurements with heavy ions, there are a number of topics in p+p physics that could be addressed with early data even at low luminosity. Some of these are also of interest to the cosmic ray community since they provide valuable constraints on modeling high energy showers. Considering that the p+p program will get underway ahead of the heavy-ion program the study of these topics will be the first major application of the ZDC in ATLAS, and thus essential preparation for the heavy ion program.

3.1.1 ZDC in Pb+Pb collisions

The primary role of the ZDC in heavy-ion physics is in characterization of collisions. The collision centrality reflects the event-by-event change in the impact parameter between the colliding nuclei. The impact parameter, b, is the transverse distance between the centers of the colliding heavy ions. As illustrated in the left panel of Fig. 3.1, at a given impact parameter, the participating nucleons reside in the overlap region, while the rest of the nucleons continue forward as "spectators". The energy of the spectator neutrons as measured by the ZDC allows us to determine their number. Central events, with the smallest impact parameters, have the largest number of participants, but yield the fewest spectator neutrons in the far forward region. Peripheral events with large impact parameter yield a far larger number of spectators. This phenomenon is illustrated in the right panel of Fig. 3.1, which shows the strong anti-correlation between the ZDC neutron multiplicity

and energy observed in the forward hadron calorimeter. It should be noted that a lack of spectator neutrons can be a result of central collisions or very peripheral collisions in which many neutrons remain bound in larger charged nuclear fragments. It is through observation of the central particle multiplicity in the inner detector or the energy in calorimeters that this ambiguity can be resolved and the centrality of the event determined. Since free neutrons are produced at essentially all centralities, and there is negligible probability for the number of spectator neutrons to fluctuate to zero, a ZDC coincidence is an ideal minimum bias trigger, efficient also for the most peripheral collisions. These peripheral data can serve as a baseline reference for characterizing nuclear effects, in some cases preferable to p+p data because they are taken at the same energy and under the same run conditions as central heavy-ion events.

The spectator neutrons are also sensitive to the direction of the reaction plane, which is the plane defined by the beam direction and the direction of the impact parameter. Since the ZDCs also can measure the transverse position of the spectator neutrons, they can determine the orientation of this reaction plane. This is an important method used alongside the other methods discussed in Chapter 5, but which gives the reaction plane angle least distorted by non-flow correlations [49], and thus minimizes contamination by non-flow. Coordinate readout has been implemented in the PHENIX and STAR ZDCs at RHIC by means of a shower-maximum detector mounted following two interaction lengths. Data from these detectors at RHIC (see e.g. Ref. [50]) demonstrate that event-by-event energy flow of forward neutrons exhibits "directed flow," that is, a $\cos(\phi)$ dependence relative to the reaction plane measured by produced particles. It is expected to have similar or better performance at ATLAS since the ZDC has been designed from the ground up to provide position sensitivity.

3.1.2 Ultra-peripheral Pb+Pb and p+Pb collisions

Ultra-peripheral Pb+Pb collisions, large impact parameter ($b = 25 - 30$ fm) events where the very strong electromagnetic fields of the Lorentz-contracted nuclei may dissociate the nucleus in the opposite beam, provide an intriguing way to probe the low-x structure of nuclei with real photons, complementary to traditional DIS techniques. The detection of large numbers of forward neutrons in one direction with the ZDC, in tandem with no or possibly one (from additional photon exchange) neutron from the nucleus that emits the high energy photon, is the only known way to trigger on this kind of event. In this way, the ZDC in ATLAS opens up entirely new tools for studying the partonic structure of nuclei. These present an opportunity to make measurements of nuclear (in Pb+Pb) and even nucleon (in p+Pb) Parton Distribution Functions (PDFs) at very small x (down to $x = 10^{-6}$), as well as to study diffractive dissociation off nuclei by photons.

The signature of diffractive dissociation is that one nucleus exchanges a color neutral object (e.g., two gluons). Therefore it is separated by a rapidity gap from the rest of the event. Diffractive interactions are expected in about 50% of the di-jet photo-production sample for Pb+Pb collisions and 10% in the p+Pb case. It would be interesting to test this prediction as was discussed in detail in Ref. [51].

Aside from providing important insights into the initial conditions of heavy-ion collisions by testing models of the nuclear wave function, e.g. based on the Color Glass Condensate, these measurements are of interest in their own right. Similarly, in p+Pb collisions, the density distribution of partons inside the proton can be measured in a kinematic regime similar to HERA. Ref.[51] includes specific calculations based on realistic luminosities and an example of this is shown in
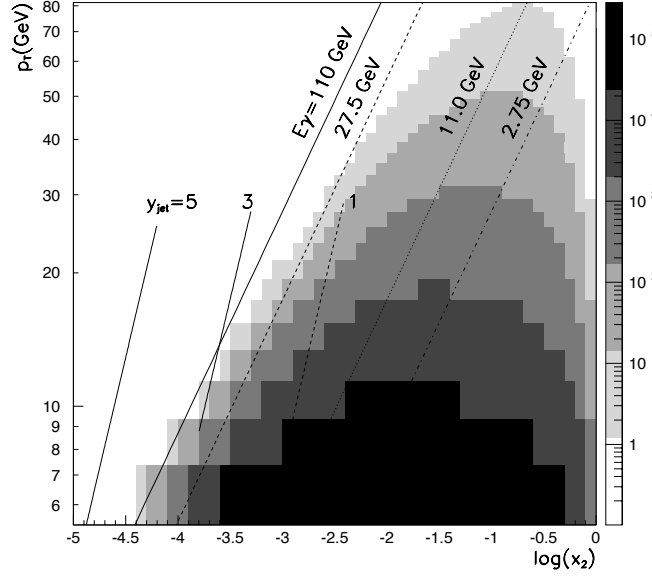
Figure 3.2: Rates of di-jet production in ultra-peripheral collisions at the LHC for an integrated luminosity of 0.42 x 10^{33} cm^{-2}, from Ref. [51]. The calculation assumes the dominance of the photon-gluon fusion process; in this picture, x_1 is the momentum fraction per nucleon carried away from one nucleus by the photon, while x_2 is the momentum fraction per nucleon carried away from the other nucleus by the gluon; $y_{jet} \approx -0.5 ln(x_1/x_2)$ and $x_1 x_2 \approx 4p_T^2/s_{NN}$.

Fig. 3.2 where rate of jet production in UPC collisions is shown as a function of x and photon p_T for a nominal one month Pb+Pb run. The predicted rate is substantial. For these measurements the ZDC (1 arm) together with jets in the central detector will be used for a trigger. An additional rejection of background due, primarily to inelastic nucleus-nucleus collisions will be obtained by requiring a rapidity gap. Since background events are likely to have particles in $3 < \eta < 5$ a veto on FCAL energy would be effective.

Another aspect of the trigger we are studying is: what is the minimum p_T jet trigger we can use in low activity events selected by the rapidity gap trigger? In this event sample we will have two classes of events: events with one isolated nucleus or two isolated nuclei. Isolated nuclei emit at most one neutron and have a rapidity gap extending to FCAL. In the first class of events, ZDC multiplicity can be used to determine which nucleus emitted the photon since the other nucleus will emit many neutrons. In events with both nuclei emitting one or zero neutrons, the nucleus emitting the photon cannot be identified.

Other processes of interest, such as quasi-elastic J/ψ or Y production $\gamma + A \rightarrow J/\psi(Y) + A(A^*)$ also can be studied with the triggering on forward neutrons and rapidity gap along one or both beam directions. In some fraction of the photo-production events, additional photon exchange occurs, exciting one of the nuclei, which then emits a neutron. This two-photon interaction reduces

25

the cross-section by a calculable amount, typically 50%, but is easier to trigger on. In the case of quasi-elastic J/ψ or Υ photo-production, one ion emits a spectrum of photons - usually calculated using the Weizsacker-Williams method - followed by the usual processes involved in photon-hadron interactions. For example, the photon may fluctuate into a heavy-quark $q\bar{q}$ pair which exchanges a two gluon 'ladder' with the target ion, subsequently materializing as a vector meson. In this connection, at least three processes are of interest: coherent quarkonium production, production of quarkonium with break-up of the nucleus, and large p_T quarkonium production with a rapidity gap between the quarkonium and the produced hadronic system.

(i) Coherent production. The four momentum transfer (t) distribution is steep, as expected for coherent production off a heavy target. In the leading twist approximation the coherent cross-section is expressed through a generalized gluon distribution function in the nucleus - providing sensitivity to gluon shadowing effects. As a result the coherent cross-section integrated over t is $\propto A^n$, where nominally $n = 4/3$. However, gluon shadowing may reduce this value to $n = 1.1$ [52], and in the "black disk regime" of complete absorption a more dramatic reduction is expected, to $n = 2/3$. The technical problem with this study is that for coherent processes it is hardly possible to determine which of the nuclei emitted the photon, which effectively limits the range of energies probed. The two other processes allow one to avoid this problem.

(ii) Incoherent quarkonium production In this process a two gluon ladder is attached to one nucleon of the nucleus which receives a substantial transverse momentum and is knocked out of the nucleus. This process is accompanied by emission of several neutrons (~ 4) [52]. Hence detection of these neutrons allows one to determine which of the nuclei emitted the photon, and hence perform studies of quarkonium production at larger γp center-of-mass energy ($W_{\gamma p}$) than in (i) above. This process is also very sensitive to the onset of the black disk regime as in this case transition from the regime of color transparency $\sigma \propto A$ to the regime of strong absorption $\sigma \propto A^{2/3}$ corresponds to a strong change of the A-dependence as in the case of (i).

(iii) Large p_T quarkonium production This process is expected to be dominated by an exchange of a two gluon ladder with one parton of the target leading to production of hadrons in the nucleus fragmentation region followed by a rapidity gap. Neutron production in the nucleus decay allows one to trigger on such diffractive events and determine which of the nuclei fragmented, thus resolving the ambiguity mentioned above. The detector acceptance for J/ψ particles produced through this mechanism is expected to be good. These processes provide a direct approach to tracking fast small color dipoles through strong gluonic fields at the LHC and would allow one to determine the onset of the black disk regime for dipoles of the transverse size of the order 0.25 fm [53].

Experimentally, the measurement with Υ is most likely to be useful due to the limited acceptance in p_T for J/Ψ. The trigger requirements would include two high p_T muons, at least one neutron in either ZDC, or rapidity gaps which could potentially be determined using the FCAL. To optimize the experimental conditions, a more detailed study of the rapidity and p_T acceptance and accessible trigger rates needs to be performed.

In ultra-peripheral p+Pb collisions, the dominant process is photo-production off the proton since the photon coupling is much stronger. Quasi-elastic production off the proton is also of general interest, and it was previously a focus at HERA. ATLAS would extend the data to the highest energies and resolve many open issues such as the $W_{\gamma p}$ dependence of the cross-section. Also it may help to separate quasi-elastic $\gamma + p \rightarrow J/\psi + p$ and inelastic processes $\gamma + p \rightarrow$
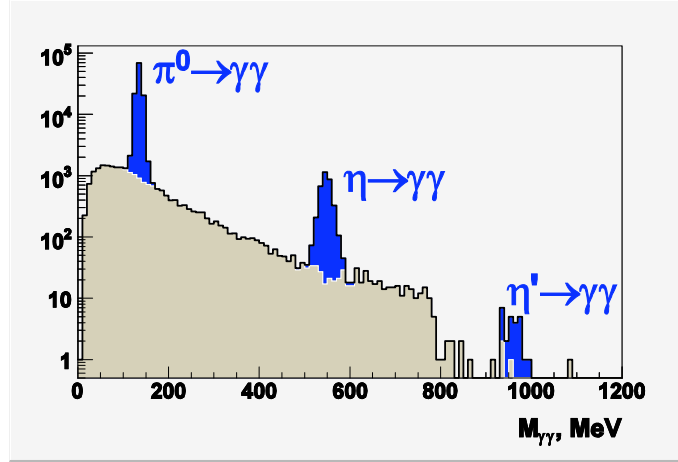
Figure 3.3: Reconstructed neutral meson decays in the ZDC acceptance for p+p collisions at full LHC energy.

$J/\psi + X$, since a significant fraction of inelastic final states ($\sim 40\%$) will contain leading neutrons. It will allow one to produce more reliable measurements of the t dependence of the quasi-elastic process (which for large t becomes a correction to the inelastic process) and also to determine the ratio of inelastic to quasi-elastic rates at small t which measures fluctuations of the gluon density in protons at small x [54]. In the case of large momentum transfer quarkonium photo-production in ultra-peripheral collisions it will be possible to measure the energy dependence of the cross-section up to $W_{\gamma p} \approx 1$ TeV, thus extending the HERA reach in energy by a factor of 10 [55].

Other processes in p+Pb scattering where forward neutron tagging would be useful are hard diffractive processes with production of di-jets, $\gamma + p \rightarrow$ di-jet $+X + n$. For this process it would be possible to study the probability of removing a gluon from the proton (the so called fracture function) [56, 57] and test the validity of factorization in hard diffractive processes [58]. p+Pb collisions with production of di-jets will allow the measurement of nuclear parton distribution functions down to small x.

3.1.3 Capabilities for p+p collisions

In addition to forward going neutrons, the ZDC can detect and reconstruct π^0 and η mesons decaying into $\gamma\gamma$ and measure their production cross-section as a function of x_F and p_T. The ATLAS ZDC has a large acceptance in these parameters as shown in Ref. [48] and therefore should provide useful empirical information needed to constrain parameters of models describing particle production in the fragmentation region. Fig. 3.3 shows the invariant mass distribution of di-photons from a sample of 1 million PYTHIA simulated p+p events at $\sqrt{s} = 14$ TeV with a parameterized response of the detector as simulated by GEANT.

With forward neutron tagging it will be possible to study several topics of interest both for p+p and cosmic ray physics.

The interest in the measurement of the inclusive neutron production cross-section, has recently been renewed due to the disagreement in the measurement of $\frac{d\sigma}{dx/dp_T^2}$ from both H1 [59] and ZEUS

[60] at HERA and earlier results on leading baryon spectra measured in hadronic reactions at lower energy from CERN-ISR [61], when all results are scaled by the corresponding inelastic cross-sections. It is also observed at HERA that for most of their data the spectrum of neutrons produced when a gluon was removed from the target was practically the same as for the quark removal which indicates dominance of the fragmentation processes over the triple Regge processes. At the same time for the leading neutrons with x_F very close to one, pion exchange may give the dominant contribution as suggested by several authors, see e.g. [62]. The complication of the hadronic processes as compared to DIS is that the colliding protons can be involved in multiple soft and hard collisions which will screen production of the leading baryons. This effect is likely to be enhanced at the LHC. Hence it would be very interesting to study to what degree Feynman scaling is violated for neutron production when energies are increased from ISR/RHIC energies to LHC energies. On the other hand by applying a veto for production of leading baryons, one can study very violent p+p collisions which are characterized by very high gluon densities at small x [63].

Overall, detection of neutrons provides a unique tool for the study of super long-range correlations in rapidity - on the scale of 20 units! Global issues that can be addressed include:

- correlations between leading neutrons produced in two fragmentation regions which should be strongest at large $|x_F| \geq 0.7$;

- di-jet production at mid-rapidity when one can expect a decrease of leading neutron multiplicities in both fragmentation regions;

- dependence of the leading neutron multiplicity and spectra on the mid-rapidity charged particle multiplicity.

One would also be able to use neutrons in the studies of the photo-production of Y in p+p collisions. Similar to the A+A case, one would be able to use them to select diffractive dissociation and resolve the forward- backward photon ambiguity. In addition, it would allow one to measure processes of inelastic diffraction with production of Y. Experimentally, the trigger could simply be either ZDC with, e.g., at least 10% of the beam energy combined with a central interaction trigger like MBTS. The trigger rate will be high- but still only a fraction of the ~ 2Hz bandwidth assigned to the ZDC in ATLAS. Measuring the p_T distribution - over which we have to integrate to get the cross-section - is an issue.

The forward distribution of neutrons in p+p interactions reflects the event-by-event inelasticity. This is of great importance for cosmic ray physicists trying to calibrate data for air showers above 10^{16} eV using hadronic models. While some data exist on the x_F distribution of neutrons between $0.2 < x_F < 1.0$ at the CERN-ISR, and preliminary results are in preparation from RHIC-PHENIX, this would be a very important measurement at the LHC.

A second topic, that of $\pi \pi$ elastic scattering, can also be addressed. As mentioned above, inclusive neutron production at very large x_F and small p_T proceeds by pion exchange. For this reason, if we observe two leading neutrons as well as pions in the central detector we are really measuring the $\pi \pi$ elastic cross-section at very high energy and potentially out to high momentum transfers. This is a unique and very interesting measurement. Experimentally, it is not yet clear whether this is possible. The trigger would have to be a ZDC coincidence with rapidity gaps since it would be hard to trigger on the pions. This is under study.

Finally, topics in hard diffraction can be addressed. In diffractive collisions one of the beam protons often leaves the collision intact. A fraction of the time it is excited to a system with additional pions. The N*(1400) is the lowest lying state and there is a continuum falling off as $1/M^2$. The spectrum is reasonably well known at the Tevatron, though extrapolations to the LHC are strongly model dependent. Very little is known about double diffraction when both nucleons are excited to higher mass states, leaving a large rapidity gap in-between. Measurement of neutrons in both ZDCs provides a nearly model independent method of studying these cross-sections. First, one measures multiplicity of neutrons in single diffraction, and next uses a factorization approximation - independence of neutron multiplicity in two diffractive clusters (an assumption valid in all current models) to determine the ratio of double and single diffraction. Interesting information on the mechanism of diffraction may also be provided by a study of the correlation of the transverse momenta of the neutrons. Indeed, it is usually expected that the t-dependence of double diffraction is very broad $\sim \exp(B_{dd}t)$, $B_{dd} \sim 2\,\mathrm{GeV}^{-2}$. If so, the relative transverse momentum of the two clusters is, on average, of the order of ~ 1 GeV, which may be reflected in a nonzero value of $\langle \vec{p}_{n1t} \cdot \vec{p}_{n2t} \rangle$. One can consider this quantity both for the case of fixed or varying $\vec{p}_{n1t}$. Also, one can study it for different masses of the produced hadronic systems provided one gets information on the rapidity interval filled by hadrons from other components of the detector.

There are still some open questions about the theoretical uncertainty on the cross-section for the Central Exclusive Production (CEP) of di-jets, which CDF at the Tevatron is trying to constrain [64]. At the LHC the central exclusive dijet production is very important because of its implication for Higgs production using CEP. With the neutron there is the possibility of accessing directly the question of what fraction of the exclusive di-jet cross-section is really exclusive.

3.2   ZDC design

The ZDCs are located in the TAN absorbers, 140m in both directions from the nominal interaction point, as shown in Fig. 3.4, thus they are only sensitive to spectator neutrons. The size of the TAN dictates the dimensions of the calorimeter, and thus the detector acceptance, which effectively covers $|\eta| > 8$.

The ZDC module and detector design is shown in Fig. 3.5. The modules consist primarily of a sandwich of tungsten radiator and quartz rods that are used to collect Cherenkov light generated by the electromagnetic and hadronic showers. Each ZDC detector consists of four modules, all of which are similar and have the same intrinsic energy resolution but several have particular capabilities. The three module types are described below.

- **EM X-Y Module** This is the first module which has been provided with X-Y coordinate readout by means of quartz rods which also penetrate the tungsten plates longitudinally allowing the position location of EM showers in an 8x8 grid.

- **Hadronic X-Y Module** This is similar to the EM X-Y Module, but has 24 channels, since the showers will be much wider in this module.

- **Hadronic Standard Module** This module is comprised of quartz rods sandwiched between the tungsten plates. There is no position sensitivity in these modules, which are the rear two modules in each arm, and thus give a single energy measurement per module.
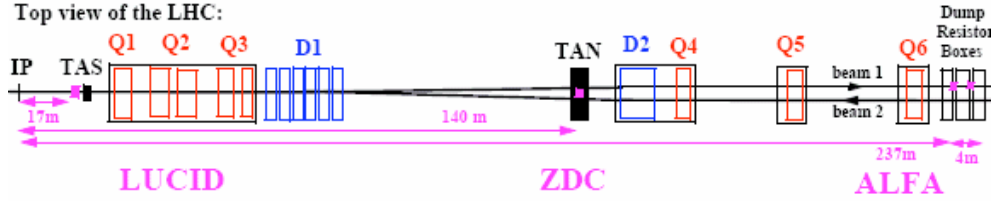
Figure 3.4: Schematic of the ATLAS beam line, showing the position of the ZDC in the far forward region.

While the energy measurement is essential for event triggering and centrality selection, the position sensitivity of the front two modules provide two additional functions that are well motivated by physics issues in Pb+Pb, p+Pb, and p+p.

- **Directed Flow:** In heavy-ion collisions the transverse coordinate measures the net p_T of the particles hitting the front face of the ZDC. This net p_T is directly related to the directed flow and the reaction plane angle.

- **Neutral Meson Reconstruction:** In p+p and p+Pb interactions, where the detector occupancy is low, the first ZDC module has impressive capability for reconstructing neutral particles which decay electromagnetically near the interaction point (IP).

3.3   Triggering in Pb+Pb

The two main triggers are expected for heavy-ion running.

- **Minimum-bias Trigger:** The ZDC minimum-bias trigger is straightforward, requiring a coincidence of energy $E > 0.1 \times E_{beam}/A$ in both arms. The purpose of the trigger is to indicate an inelastic nuclear collision, either via strong or electromagnetic interactions. Similar triggers have been successfully implemented at RHIC, with high efficiency and low fake rate.

- **UPC quarkonia production:** This trigger is based on detecting a J/Ψ or Y produced in coincidence with a ZDC signal above threshold. In PHENIX, one electron candidate in the central detector was required (corresponding to one J/Ψ decay) in coincidence with one or more ZDC clusters. A similar strategy should be appropriate for ATLAS where the calculated fraction of events with one or more neutrons (due to an additional photon exchange) is roughly 50%.

Of course, trigger development and commissioning is highly contingent on experimental and physics working conditions, and it might be found that the final running conditions are somewhat different from RHIC. Thus, it is crucial to have the flexible ATLAS multi-level trigger system which can allow the integration of ZDC triggers with other ATLAS triggers.
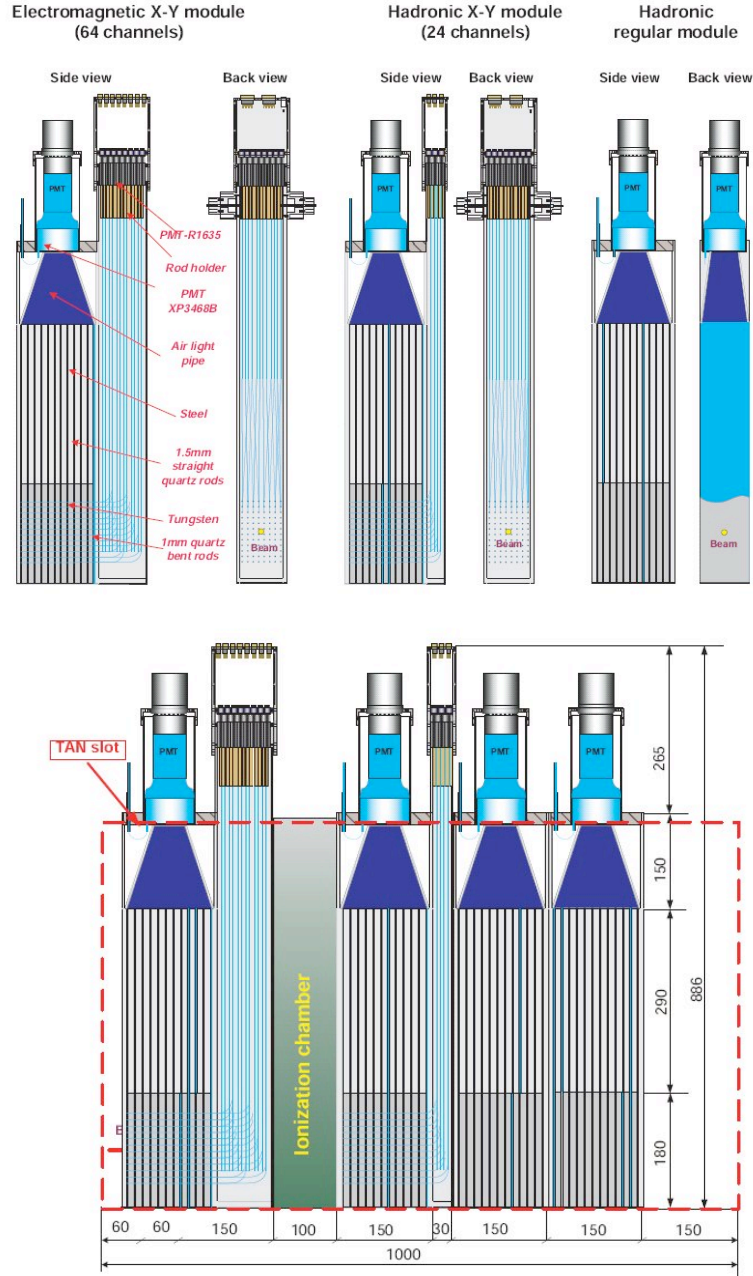
Figure 3.5: (top) ZDC module types and their designs, (bottom) ZDC configuration planned for standard running with the TAN absorber, from Ref. [48].

3.4 Operations issues

The ZDC is an extremely radiation-hard calorimeter. It has been tested up to $\sim$ 5 GRad absorbed dose and will have an essentially infinite lifetime during the Pb+Pb operation of the LHC. Unfortunately the detector is not expected to survive more than a few months of operation at the ultimate LHC p+p design luminosity. The light attenuation in the optical systems will become significant in the visible wavelengths and as a result the resolution of the device will deteriorate. This is a possible way to operate the ZDC but it will substantially limit the usefulness for a long term heavy-ion program. Therefore, once the p+p luminosity of the LHC reaches 10^{33} cm^{-2}s^{-1} the ATLAS ZDC will be removed for high luminosity runs and replaced for heavy ions or for special low luminosity p+p runs.

During the first period of 43 bunch operation, the ATLAS ZDC will have its first module replaced by a module from the LHCf detector ($\sim$ 30 cm long). This allows the LHCf experiment to carry out its program during the first few weeks of operation of the machine. When their program is completed, the corresponding ATLAS ZDC module will then be re-inserted and the full program of measurements will continue.

3.5 Summary

The Zero Degree Calorimeters (ZDCs) will play a crucial role in the Heavy-ion physics program at the LHC.

- The ATLAS Zero Degree Calorimeters (ZDCs) are the main hardware contribution to the ATLAS detector from Brookhaven National Laboratory and the US ATLAS heavy-ion program.

- The ZDC will provide an event trigger, centrality characterization, reaction plane determination, and access to ultra-peripheral collisions in Pb+Pb collisions

- It also provides unique capabilities for forward neutron and hadron production in p+p collisions, of great interest to cosmic ray physics

- The two ATLAS ZDCs, one in each beam direction, have been mechanically assembled and installed in the LHC tunnel.

- Operations issues are known and being addressed in collaboration with ATLAS management.

Chapter 4

Tracking Performance

4.1 Tracking heavy ion events

The ATLAS Inner Detector (ID) has been designed to track charged particles in 5 units of pseudo-rapidity centered around mid-rapidity [65] The detector combines three technologies, closest to the beam, tracking is done with silicon pixel detectors (Pixel) arrayed in a barrel with three layers (B-layer, Layer 1 and Layer 2) and 3 end-cap disks on each side of the barrel. The Pixel end-cap disks are mounted on disks perpendicular to the beam axis and placed on both sides of the nominal interaction point. The Pixel detector is followed by the Semiconductor Tracker (SCT) consisting of double-sided silicon strip detectors arranged in four layers in the barrel, and two sets of 9 end-cap disks located on both sides of the nominal interaction point. The third tracking detector is a Transition Radiation Tracker (TRT) based on drift tubes interleaved with the X-ray radiators (polypropylene foils or fibres) and arranged in a barrel and 2 endcaps. Figure 4.1 is an artist rendition showing in detail, the actual location of each component of the ID detector. The ID was designed with high granularity to cope with the high luminosity expected in p+p collisions, which leads to multiple p+p collisions in each LHC bunch crossing. The granularity turns out to be essential for tracking charged particles produced in the high-multiplicity environment of heavy ion collisions in a wide pseudo-rapidity window.

Starting with the first heavy-ion collisions at LHC, tracking of charged particles in the ID acceptance will be used to extract information about particle production in transverse momentum and rapidity space. Such information will be used to infer properties of the gluon distributions in the initial state as derived from the charged particle pseudorapidity density. Comparisons of transverse momentum distributions of charged particles emerging from heavy-ion collisions with the corresponding distributions measured or estimated for p+p collisions at the same energy, will also be used to extract nuclear effects such as the formation of a strongly-coupled QGP similar to the one found at RHIC. Azimuthal correlations between charged particles will also be used to study the presence of asymmetries in the flow of matter formed by the collisions. Such flow studies of the hydrodynamical expansion of the system after the collision can be used to characterize its properties such as its equation of state, viscosity, speed of sound, etc. Matching the particle trajectory and its momentum with the energy deposited in the calorimeters will allow the detailed study of how jets are modified in heavy ion collisions. We plan to study the distribution of the transverse momentum of charged particles within jets (j_T distributions), we expect to able to identify modifications related to gluon emmission induced by the medium formed at the colli-
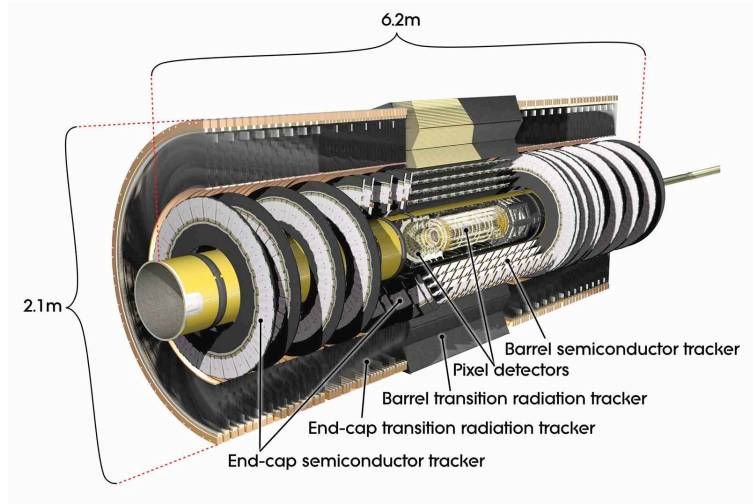
Figure 4.1: Layout of the ATLAS Inner Detector, with the Pixel detector, SCT detector, and TRT indicated.

sion. Studies will be performed as well with fragmentation functions extracted from tracking and calorimeter information. These studies will focus on the possible attenuation of leading particles (i.e. as described in Chapter 6).

4.2   Inclusive charged particle spectra

The ATLAS Inner Detector can be used to estimate the momentum spectrum of inclusive charged particles, which can contribute to measurements of charged particle multiplicity, transverse energy (via the mean p_T), and elliptic flow. The results presented in this chapter were obtained with the previous ATLAS tracking algorithm xKalman [66] run in version 12 and higher of the Athena framework. Work is ongoing to fully commission the default tracking NewT [67] for the tracking reconstruction of heavy ion events. An invariant distribution of the transverse momentum of charged particles is produced as an example of the capabilities of the algorithm. In the heavy ion environment, the occupancy in the TRT sub-detector is high (see Chapter 2). The TRT hits are not used in the present studies, but we will, in a near future, explore their use for tracking in less central events. The NewT algorithm evolved out of the xKalman and they share many aspects of their strategy, both algorithms start by translating information recorded by the detectors into clusters and then define space points. Track candidates (seeds) are formed with combinations of space points. For this particular analysis these seeds are formed from combinations of hits in the Pixel and SCT detectors. In p+p events these combinations are built from hits previously sorted into regions along the beam axis (in z) and the azimuthal angle ϕ. The topology of the heavy-ion collision, with its single collision per bunch crossing favors the sorting of track candidates in polar angle regions as well as ϕ. The actual pattern recognition and track fitting is done by propagating a trajectory already suggested by each seed, starting at its inner most point. The propagation is done using the Kalman filter-smoother method [68]. Every step of this propagation includes in-

formation about the local value of magnetic field and the amount of material that would distort the motion of a charged particle by multiple scattering. Once the outer edge of the Inner Detector is reached, the process can be repeated backwards to propagate the full pattern recognition information to all detector surfaces included in a particular track. The backward propagation is also designed to recover tracks that did not start on the primary vertex (conversions or V_0). From the set of tracks reconstructed so far, both xKalman and NewT proceed to select tracks according to predefined quality factors. As expected, NewT has a much more efficient and sophisticated approach to this task, for details please refer to: [67]. For our work on heavy ion events with the xKalman algorithm we used the following constraints on the tracks:

	Value	Comment
Reconstruction Strategy	3	Seeds from pixel+SCT
Selectivity	9	Heavy ion specific; seeds constrained with event vertex and defined in θ bins
MinNumberOfUniqueSilClusters	2	
Xi2for PresicionClusters	10.	
MaxNumberHoles	11	Max. 1 hole pixel and 1 hole in SCT
MinNumberofSilClusters	9	

Table 4.1: Track conditions and constraints used by the xKalman algorithm when precessing heavy-ion events.

The set of tracks reconstructed in heavy ion events with the xKalman algorithm has a substantial number tracks that appear as copies of each other; having only small differences and matching to the same generated particle with the procedure described further down in this section. Besides those "ghost" tracks, the algorithm can also produce tracks that will not be matched to generated particles. By imposing the condition on all reconstructed tracks that requires that the extrapolated track intercept a calorimeter element with a recorded energy deposit, the number of these "fake" tracks is drastically reduced even before any matching to generated particles is attempted. Before the tracking efficiency of the xKalman algorithm is extracted, an additional set of quality cuts and further conditions on extrapolated tracks is applied as described below: This particular set of cuts may evolve as we repeat the excercise using the NewT algorithm and finally, once actual data are available.

- A track has to be formed with at least 10 hits (from a total of 11 and 12 active layers in the Pixel and SCT barrel and end-cap disks, respectively).

- Poor quality tracks are rejected by imposing a momentum-dependent cut that rejects the upper 5% of the χ^2/NDF distribution in each momentum bin.

- The normalized distance from the perigee of the track (defined with respect to the nominal Atlas interaction point (x=y=x=0)) to the reconstructed event vertex is defined as

$$R_{vtx} = \sqrt{((d_0 - d_{vtx})/\sigma_{d_0})^2 + ((z_0 - z_{vtx})/\sigma_{z_0})^2},$$

where d_0 is the distance between the point of closest approach of the track projection to the plane normal to the beam direction and the nominal interaction point (x=y=0), z_0 is the z

coordinate of the point of closest approach, and σ_{d_0} and σ_{z_0} are the errors associated to these track parameters. All tracks have to satisfy a cut of $R_{vtx} < 3$.

- All tracks are extrapolated to the calorimeter, and have to match a tower with signal above a pre-determined threshold. The matching threshold starts from a value of 0 at 4.0 GeV in transverse momentum and grows linearly to reach a value of 6 GeV at $p_T = 24$ GeV. Beyond that transverse momentum, the threshold is constant and equal to 6 GeV.

- The difference in θ and ϕ at the perigee of all track pairs is used to eliminate all but one copy from the sets of tracks that can be generated from signal deposited by a single generated particle; for each pair with $\Delta\theta < 0.005$ and $\Delta\phi < 0.01$ the track with the best quality factors (χ^2, number of Si hits, number of missing planes, etc) is kept.

The reconstructed tracks that satisfy the above conditions are then matched to the generated particles. The matching can be done by using two methods. The first one makes use of the difference between the pseudo-rapidity and the azimuthal angle at the perigee of reconstructed tracks and generated particles (the azimuthal angle at the track perigee is defined as the angle of the tangent at the point of closest approach in the plane transverse to the beam direction. The pseudo-rapidity is defined as $\eta = -ln(tgt(\theta/2))$ where θ is the angle between the z axis (beam direction) and the track projection in the (y,z) plane). A reconstructed track is compared to all generated particles and a match is declared for the pair that has the smallest value of $R = \sqrt{(\Delta\eta)^2 + (\Delta\phi)^2}$ which in turn is required to be smaller than a pre-defined value, i.e. $R < R_{cut}$. A second method matches reconstructed tracks to generated particles using the fraction of hits in the reconstructed track that are common to the generated particle. Each particle generates a set of hits and one hit can have contributions from several particles. The correspondence of a track to a generated particle is established when the track shares 50% or more of its hits with the particle. The latter method is used by the developers of the tracking algorithm and is the standard approach used throughout ATLAS. Accordingly, we use this method to define the tracking efficiency in this Report. Tracks that can not be matched to any of the generated particles, e.g. nearly straight tracks formed from random hit patterns, are then declared as fakes.

Within a pseudorapidity window, the p_T-dependent tracking efficiency is defined as the ratio of the number of matched reconstructed tracks that satisfy all quality cuts divided by the number of generated charged primary particles in the same p_T bin. Primary particles are selected as generated particles that originate at the same z coordinate as the primary vertex. It is also required that the particles do not decay in the detector volume. Note that these studies have been done with a lower limit in the transverse momentum of the generated particles set at 400 MeV.

The filled circles in the left panel of Fig. 4.2 show the tracking efficiency in the pseudo-rapidity window $|\eta| < 1$ extracted from a sample of central Pb+Pb collisions simulated with HIJING events produced with quenching turned off (with $dN_{ch}/d\eta = 2650$). The two track matching methods used in this study have been found to provide compatible results when applied to particles with $p_T \leq 10$ GeV. The tracking efficiency for particles with $p_T > 10$ GeV was extracted from a special sample of events where ten negative pions, with flat distributions in η and p_T, are simulated and merged with central HIJING events. The matching of reconstructed tracks with generated particles in this sample of embedded pions was done using the perigee difference method. The filled triangles in the bottom part of Fig. 4.2 show the rate of fake tracks found in the central sample. The benefit obtained from the matching extrapolated tracks and the corresponding calorimeter
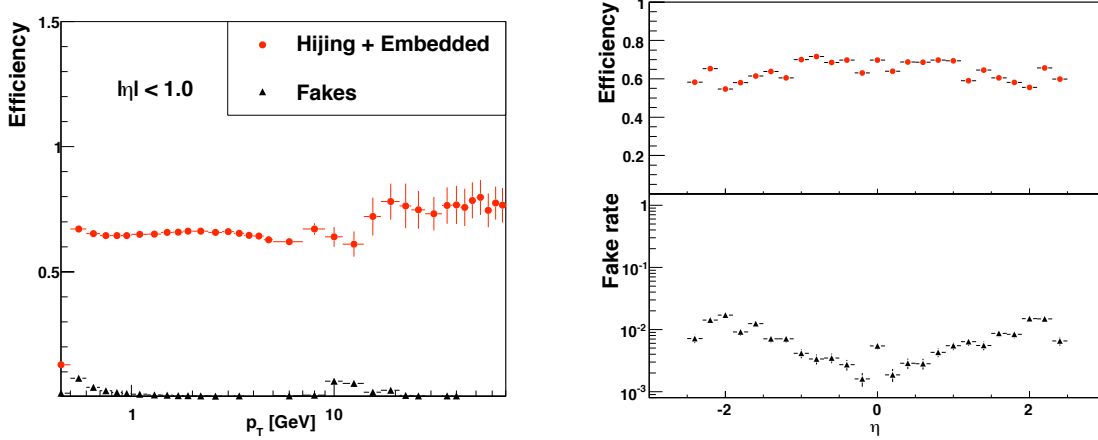
36

Figure 4.2: (left) Tracking efficiency and fake rate in $|\eta| < 1$ extracted from a sample of central (b=2 fm) HIJING events produced with quenching effects turned off and above 10 GeV, from negative pions embeded in central HIJING events. The ATLAS track reconstruction algorithm xKalman was used to reconstruct the tracks. (right, top). Tracking efficiency as a function of pseudo-rapidity for tracks with $3 \leq p_T \leq 8$ GeV extracted from the same central sample of HIJING events. (right, bottom) Fake rate as function of pseudo-rapidity for the same tracks as in the top panel.

tower information is most pronounced for tracks with p_T above 15 GeV where the fake rate falls well below the value of 5%. (Above 10 GeV, the fake rate produced by tracking alone grows fast with transverse momentum and can reach values greater than 30%). The tracking efficiency has a dependence on pseudo-rapidity that tracks the amount of material traversed. The top-right panel of Fig. 4.2 shows that the efficiency is 70% near midrapidity, and drops to about 55% at $|\eta| \sim 2$. The bottom panel of that figure shows the fake rate as a function of pseudo-rapidity for tracks with $3 \leq p_T \leq 8$ GeV. The increase of the fake rate with pseudo-rapidity is present at all values of p_T but it only reaches values that exceed 2.5% for $p_T \leq 1$ GeV (not shown in the figure).

The detector was designed to have low mass in order to minimize the effects of multiple scattering and the spatial resolution of each detector module is high (10 μm in the Pixel detector and 17 μm in the SCT along the Rϕ bending direction) [69]. Together these two features produce an overall good momentum resolution (defined as $\Delta p_T / p_T = |p_T^{rec} - p_T^{gen}|/p_T^{gen}$). The momentum resolution around mid-rapidity shown in Fig. 4.3 reaches an almost constant value around 2.5% for transverse momenta up to 10 GeV. This resolution, extracted from heavy ion events with high multiplicity ($dN_{ch}/d\eta = 2174$) is $\sim 30\%$ worse that the one extracted for p+p events in the same rapidity window [69]. This difference is mainly due to the fact that we do not include information from the TRT detector to reconstruct heavy-ion events. The resolution deteriorates slightly at high η where it reaches values of 4% for intermediate $p_T \sim 3$ GeV. At high momentum, the design momentum resolution is 30% for 500 GeV tracks.

The spectrum shown in Fig. 4.4 has been extracted for tracks reconstructed from hits in the Pixel and SCT sub-detectors within a narrow pseudo-rapidity window ($|\eta| < 0.5$). The same quality cuts as used in the definition of the tracking efficiency were imposed on the tracks used to
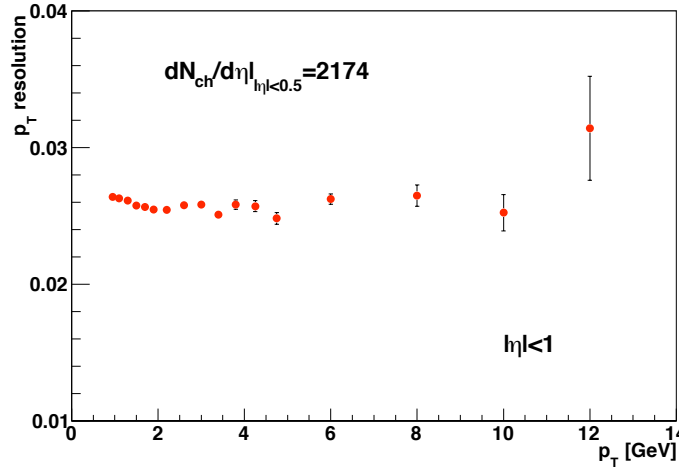
Figure 4.3: Transverse momentum resolution around mid-rapidity ($|\eta| < 1$).

generate this distribution. The yields were then corrected for tracking efficiency to calculate the final spectrum. There is no correction for fake tracks, but their contribution to the measured cross section has been estimated to be on the order of a few percent below 5 GeV and can be kept below 10% at 10 GeV and 1% at 30 GeV. One can see that the reconstructed spectrum agrees well with the input spectrum for generated primary charged particles.

It should be noted that while most of the tracking studies performed for heavy ions so far are for particles with $p_T > 400$ MeV, this is not due to limitations of the ATLAS detector itself. The tracker has sufficient size compared to the bending power of the main 2 T dipole field such that particles below $p_T < 400$ MeV leave full tracks in the silicon detectors. Development to extend the work done with simulated p+p events to heavy ion collisions is ongoing.

4.3   Vertex reconstruction

Primary vertex reconstruction in the ATLAS framework is done with a robust algorithms based on tracks reconstructed in the Inner Detector. The algorithms are capable of identifying the 20 or so primary interactions along the beam that will be recorded per bunch crossing in high luminosity p+p collisions. The high precision measurements performed in the first three layers of the ID, together with their short distance from the beam pipe, make possible the high resolution measurement of the primary vertex coordinates. Simulations of p+p events find resolutions of ~ 40 μm along the z axis (beam) and ~ 10 μm in the plane transverse to the beam [70] depending on the luminosity and topology of signal events. The ATLAS vertex finding is also capable of identifying displaced vertices in the vicinity of the primary vertex. Such vertices may be produced by the decay of long-lived particles, photon conversions, vertices within jets, and decay chains. The rate of heavy ion collisions is much lower than the one for p+p collisions. Only a single primary vertex is expected in each recorded event.

The software design of the vertex finding is modular and object oriented with interfaces that
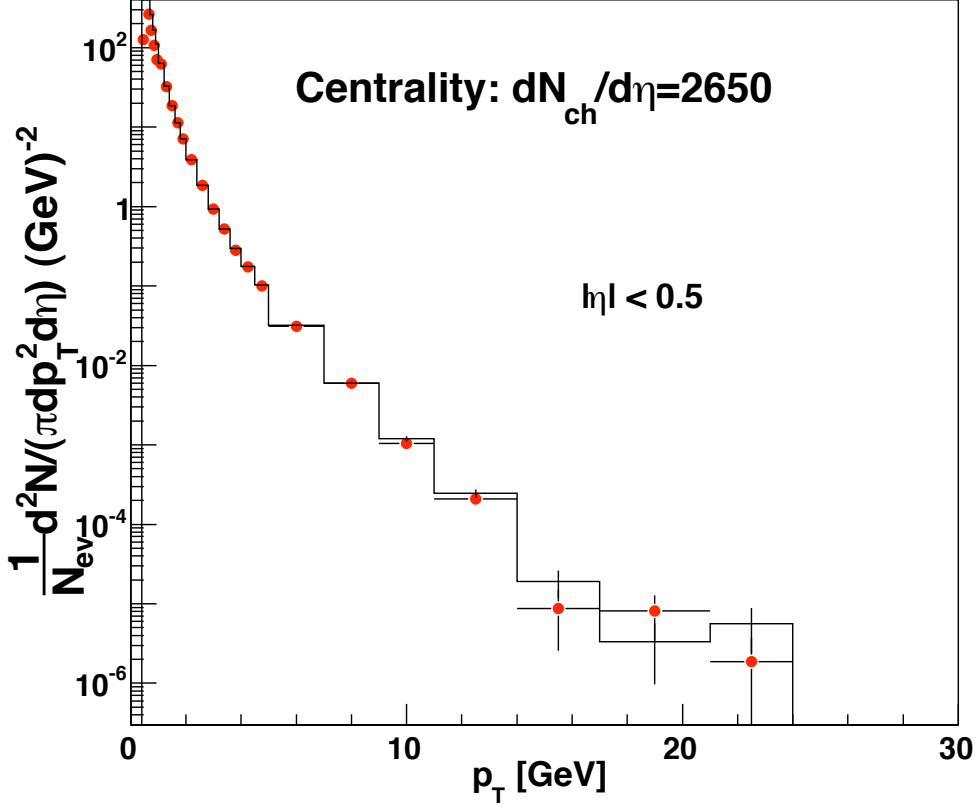
Figure 4.4: Reconstruction of the invariant yield of charged particles in $|\eta| < 0.5$ for a sample of central HIJING events with quenching effects turned off (b=2 fm with $dN_{ch}/d\eta = 2650$). Red circles show the extracted yield and the histogram corresponds to the generated input distribution.

provide different strategies that the user may apply depending on the nature of the problem at hand. The package can be set to find a vertex using tracks previously reconstructed and then proceed to a fitting procedure that optimizes the vertex coordinates and produces a covariance matrix that quantifies the dependence of the extracted coordinates on the tracks' quality. At this moment, we are focusing on the reconstruction of the primary vertex in the so called SingleAdaptive mode, where a single primary vertex is reconstructed. Figure 4.5 (left) shows the residual of the primary vertex x coordinate. This residual distribution can be well described with a Gaussian with an RMS equal to 8.6 μm. The same figure shows the residuals of the primary vertex z coordinate in the middle panel, where the distribution shows non-Gaussian tails but can be well described overall by a Gaussian with an RMS equal to 20 μm.

As expected, the resolution of the vertex reconstruction improves with the number of tracks available. Figure 4.5 (right) shows the RMS of Gaussian fits to distributions of z coordinate residuals as function of the number of reconstructed tracks used to find the primary vertex. The res-
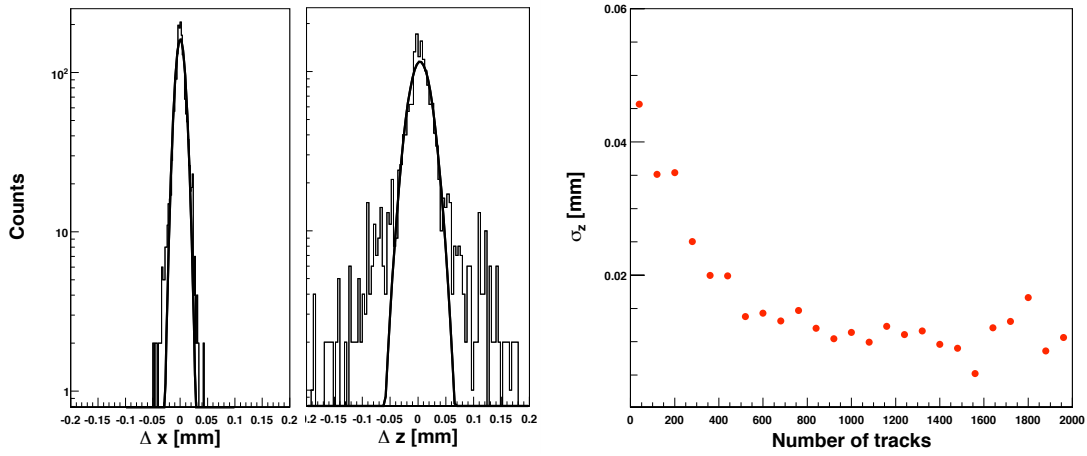
Figure 4.5: (left) Distribution of vertex x coordinate residual reconstructed with SingleAdaptive method using tracks produced with xKalman tracking algorithm from a sample of minimum biased HIJING events produced with quenching effect turned off. (middle) Distribution of z coordinate residuals for the same reconstructed vertices as in the left figure. (right) The resolution of the vertex finding algorithm as a function of the number of tracks used to construct the vertex averaged over events with different centrality from HIJING minimum bias sample.

olution of the vertex finding algorithm ranges from 45 μm when the event has tens of tracks to a low, and apparently stable, value of 10 μm for events with thousands of tracks.

4.4 Summary: Tracking Performance

The ATLAS tracking algorithms xKalman used for this report, has been shown to be well suited to reconstruct charged particles in five units of pseudo-rapidity of heavy ion collision at LHC. The xKalman algorithm is not the default ATLAS tracking algorithm. The use of NewT, the new default algorithm is a work in progress and all work done so far indicates similar performance. We have shown that among other tasks, we will be able to deliver:

- charged particle distributions as a function of transverse momentum for $|\eta| < 2.5$;

- the primary vertex of the event with high precision and full efficiency;

- integrated p_T distributions as another measurement of the charged particle pseudo-rapidity density;

- the jet structure and its expected medium modifications, through fragmentation functions or j_T distributions measurements with tracks assigned to jets.

Chapter 5

Global Observables

This chapter will discuss the ATLAS capabilities for measuring several "global" observables, by which are meant: charged-particle multiplicities, transverse energy, and elliptic flow. Of course, a precise estimation of event centrality is an essential part of measuring any of these variables, and so will also be discussed. Global variables have the paradoxical role of being integrals of particle number and energy in the final state, but which appear to reflect dynamical quantities (e.g. entropy, transverse energy) established much earlier in the system evolution. Most importantly, they provide access to aspects of the system relevant to understanding the nature of the strongly coupled fluid. The particle multiplicities should be directly relevant to the initial state entropy. The elliptic flow reflects a combination of the equation of state (EOS) as well as the shear and bulk viscosities.

Global variables will certainly be the focus of Day-1 physics activities at the LHC, when heavy ion collisions are delivered to the experiments at the end of 2010. Even with low to moderate luminosity, 50 Hz taken to tape will amount to 2 million Pb+Pb events per day, providing sufficient data within a few days to test extrapolations of RHIC data to LHC energies. As part of this process, the measurements of similar variables in proton-proton collisions (which will most likely be the first data published from the ATLAS detector) will be essential preparation for heavy ion data taking, trigger preparation, and analysis – and work on this is already underway.

5.1 Global physics at the LHC

While it is difficult to calculate features of soft particle production from first principles in the complicated environment of a heavy ion collision at high energies, it is found that global observables follow relatively simple patterns which may eventually give some insight into the bulk (and generally non-perturbative) sector of QCD. At the same time, measurements of inclusive charged particle density will be essential for an empirical understanding of particle production in these collisions, and will help constrain the gluon densities that will be needed for jet quenching calculations.

Various predictions for inclusive particle production at the LHC have been made, that test the applicability of different theoretical approaches already applied at RHIC. Three of these predictions for $\rho(s) = (dN_{ch}/d\eta)/(N_{part}/2)$ are shown in Fig. 5.1, overlaid on data from p+p and A+A collisions. The first is the simple $\log(s)$ trend that is often invoked as a description of data from
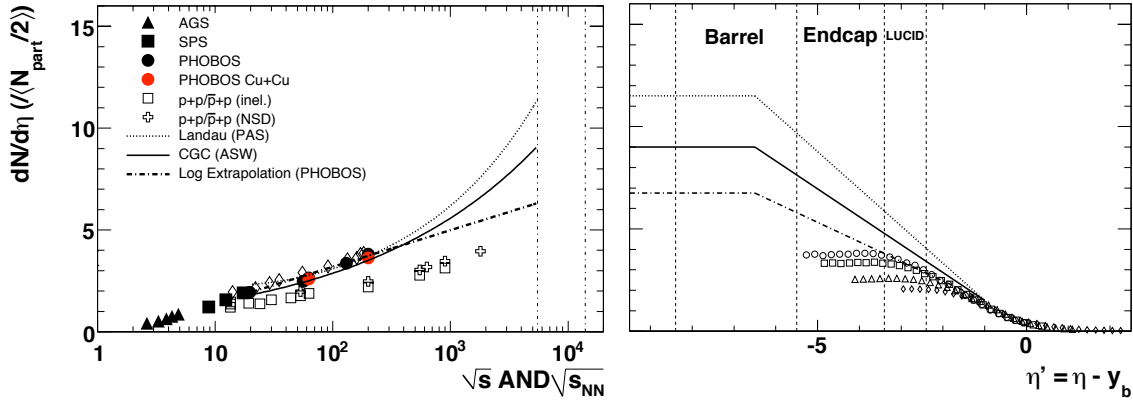
41

Figure 5.1: (left) Data for $dN_{ch}/d\eta(|\eta| < 1)$ vs $\sqrt{s}$ for A+A and p+p collisions, compared with three theoretical extrapolations [71, 72, 73]. The rhomboids are e^+e^- data for dN/dy_T, relative to the thrust axis. (right) Capabilities of ATLAS detector, in the rest frame of one of the projectiles, compared with RHIC data. The lines show how extended longitudinal scaling behavior might appear, given the mid-rapidity predictions of the three models in the left panel.

1 AGS to RHIC energies, and thus may well be relevant at the LHC [74]. This extrapolates to a
2 value of around 6.5 at $\sqrt{s_{NN}} = 5520$ GeV, which is the lowest value considered. The second is a
3 functional form suggested by Color Glass Condensate-based models, $\rho(s) = N_0 s^\lambda$, with λ being
4 extracted from scaling violations measured at HERA [71]. With parameters taken from Ref. [71],
5 which misses the RHIC data by about 10%, one gets $\rho(s) \sim 9$, corresponding to $dN_{ch}/d\eta \sim 1600$.
6 Finally, Carruthers' version of Landau's hydrodynamical model gives a functional form propor-
7 tional to $s^{1/4}/\sqrt{\log(s)}$ with no free parameters [72]. Tuned to the RHIC data, as was done in
8 Ref. [73], this function extrapolates to $\rho(s) \sim 11.5$. Clearly, within a few days of first LHC running,
9 entire classes of models may be excluded, and new data will be added to this compilation. This
10 example illustrates that many measurements of global variables will contribute rather rapidly to
11 our understanding of heavy ion collisions, particularly if the ramp-up of the machine involves
12 small data sets with a range of beam energies.

At RHIC there was a general expectation that particle production and transverse energy would arise from a combination of soft processes and semi-hard process, each with a distinct scaling with the nuclear geometry. Soft processes are thought to deal with long wavelength excitation processes and thus scale linearly with the number of excited (or "wounded") participant nucleons, N_{part}. Semi-hard processes, or mini-jets, while at a lower energy scale than usually considered for isolated jets, are thought to scale with the number of binary collisions, N_{coll} (which exceeds the number of participant pairs $N_{part}/2$ by a factor of ~ 10 for the most central Au+Au collisions). These assumptions are the basis for the "two-component" model for inclusive particle production (e.g. Ref. [?]):

$$\frac{dN}{d\eta} = n_{pp} \left[(1-x)\frac{N_{part}}{2} + xN_{coll} \right]. \tag{5.1}$$

13 At the same time, RHIC data on ratios of $\rho(s)$ at different N_{part} and different $\sqrt{s}$, have shown that
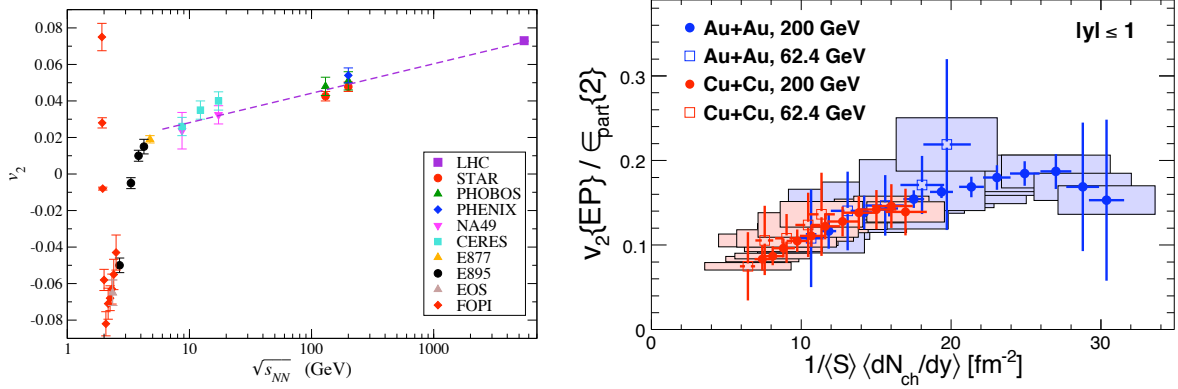
42

Figure 5.2: (left) Compilation of data on v_2 vs. $\sqrt{s}$ in heavy ion collisions, from Ref. [71]. (right) Data for v_2/ϵ vs. the areal density of charged particles, for two energies and two colliding systems, from Ref. [77].

$\rho(s)$ "factorizes" as $f(s)g(N_{part})$ [75]. This is apparently at odds with the two-component model, even at RHIC, since the semi-hard contribution should rise with energy, leading to an increase in the extracted value of x, something which is not observed. However, much of the community still uses the two component model in its original formulation. It is thus fortunate that the LHC will provide a definitive test of the role of semi-hard processes in the initial state of the strongly-coupled QGP. The expected copious production of jets and minijets should lead to a substantial increase in the fraction of inclusive particle production that scales with N_{coll}, which will lead to a larger value of x, and thus a manifestly different centrality dependence than has been seen over the measured energy range at RHIC. The E_T measurements as a function of centrality will also provide additional insights into whether there is an increase in transverse activity due to the larger fraction of hard and semi-hard processes.

While the previous discussion involved the inclusive charged particle multiplicity near mid-rapidity, the large acceptance will also play a crucial role in the elucidation of global properties. One key observation away from mid-rapidity at RHIC was that of "extended longitudinal scaling" [76]. This phenomenon, shown in the right panel of Fig.5.1, by plotting yields as a function of $\eta' = \eta - y_b$, where y_b is the beam rapidity, is characterized by the fact that the normalized inclusive yields are invariant with energy when viewed in the rest frame of one of the projectile. It is also observed that while the scaling is obeyed at all centralities, the invariant yield vs. η' varies with centrality. The same figure also shows how the various ATLAS sub-detectors are situated in η' space, illustrating the dramatic extension to large negative η' as well as the overlap in the forward region. While the silicon and tracking detectors only extend to $\eta = 2.5$, the calorimeters provide measurements out to $\eta = 5$, and the LUCID detector (Cerenkov tubes) should provide multiplicity measurements of primaries out to $\eta = 6$, overlapping the RHIC data.

Elliptic flow, which is manifest as a significant anisotropy in the event-by-event azimuthal angle distribution of inclusive particles, is one of the more striking phenomena observed at RHIC. The azimuthal modulation is typically characterized by the second Fourier coefficient, v_2, of the azimuthal angle distribution measured with respect to the reaction plane. This quantity has been measured over a wide range of energies, collision systems, and centralities by all of the RHIC

43

heavy ion experiments and several AGS and SPS experiments. A compilation of v_2 vs. $\sqrt{s}$ for minimum-bias heavy ion collisions, is shown in the left panel of Fig. 5.2, from Ref. [71]. While there is a non-monotonic behavior observed below $\sqrt{s} = 4 - 5$ GeV, above this energy (including the AGS, SPS, and RHIC data) a logarithmic rise is observed. The further energy dependence is difficult to predict from first principles, as it depends on the details of the initial state and on the equation of state (EoS). It has been suggested by some authors that the logarithmic rise could continue to higher energies (reaching $v_2 \sim 0.07$ at LHC energies for minimum-bias samples), while others have suggested that the "hydro limit" may already have been reached at RHIC, implying no further rise in v_2 [34]. This hypothesis has been tested by correlating v_2/ϵ (where ϵ is a measure of the spatial eccentricity of the initial state) with $dN_{ch}/dy/S$ (where S is the area of the nuclear overlap region), shown in Fig. 5.2 from Ref. [77]. This plot seems to show a constant rise of elliptic flow as the areal density of charged particles increases, but some still see a flattening at large value of $dN_{ch}/dy/S$. Finally, some authors predict that elliptic flow at the LHC may even decrease [78]. As with the multiplicity predictions, only the LHC will provide enough of a lever arm to really test these hypotheses.

5.2 ATLAS capabilities

The ATLAS detector has acceptance and hermeticity for the measurements of global variables superior to RHIC experiments. Whereas at RHIC, experiments have had to make serious choices optimizing acceptance vs. capability (e.g. choosing large aperture tracking and limited calorimetry, or vice versa), the ATLAS detector has a full 10 units of rapidity coverage for calorimeter, both electromagnetic and hadronic, and 5 units of rapidity for tracking (as described in detail in Chapter 4. There is also substantial forward coverage beyond the central detector, with the LUCID counter being staged in from $5.3 < |\eta| < 6$ and especially the ZDC being built by the ATLAS Heavy Ion group, which detects neutral particles with $|\eta| > 8$ [76]. The ZDC also has a position-sensitive front face that can be used to estimate directed flow (v_1), as discussed in Chapter 3.

5.3 Determination of the collision centrality

The event-by-event characterization of centrality is a fundamental observable in heavy ion physics, since most global observables closely track the event geometry as controlled by the impact parameter (the distance b between the centers of the two colliding nuclei). A simple example is the charged particle multiplicity which, as RHIC data showed [79, 80], predominantly scales proportionally to the number of participating nucleons (N_{part}), but has sub-dominant contributions that seem to scale proportionally to the number of binary collisions (N_{coll}). This simple fact implies that the total energy will correlate very tightly with any of the three standard event centrality observables (N_{part}, N_{coll} and b). Figure 5.3 shows the correlation between the energy deposited in electromagnetic (EMCAL, $|\eta| < 3.2$), hadronic (HCAL, $|\eta| < 3.2$) and forward calorimeters (FCAL, $3.2 < |\eta| < 4.9$) and the collision centrality as measured by N_{coll}, N_{part} and b for HIJING Pb+Pb collisions at $\sqrt{s_{NN}} = 5.5$ TeV.

The energy is particularly large in the FCAL due to the longitudinal boost of forward-going particles ($E \sim m_T \cosh(y)$). A monotonic correlation between the energy deposited in various
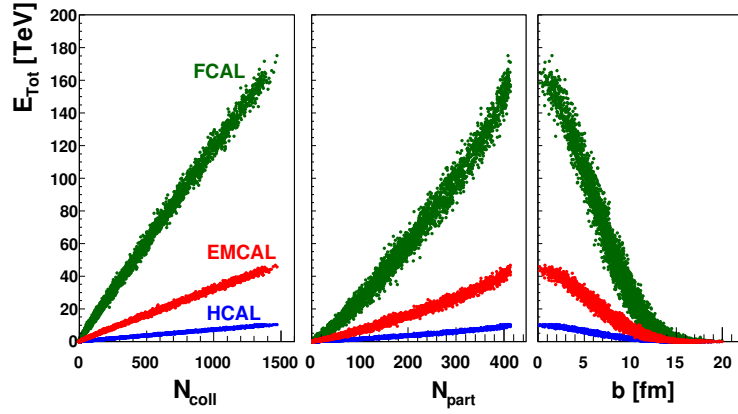
Figure 5.3: Correlation of the total energy measured by the FCAL, EMCAL and HCAL calorimeters with N_{coll} (left), N_{part} (middle) and impact parameter, b (right).

calorimeter systems and the centrality parameters can be seen. Similar strong correlation with centrality is observed for silicon clusters recorded in the pixel and strip detectors ($|\eta| < 2.5$).

The strong correlation implies that one can bin each of these variables into percentile bins, each corresponding to e.g. 5% of the total cross-section (i.e. the most central 0-5% events, 5-10%, etc.), and relate these to similar percentages of events of the N_{part}, N_{coll} and b distributions. This is a standard technique used by all heavy ion experiments [46], which only requires the multiplicity or energy depositions to vary monotonically with the impact parameter. Ultimately the limiting factor in a precise estimation is the uncertainty in knowing what fraction of the total inelastic A+A cross section is sampled by the experimental trigger. However, if one assumes this can be determined precisely, then one can bin the HIJING variables and extract the mean and width of the centrality variable distributions in each bin, as shown in Fig. 5.4 for the bins in the energy deposited in FCAL. One can see that for a wide centrality range, the mean values of the centrality parameters are correctly determined with an accuracy of the order of 10%. The similar behaviour is observed by using bins in energy deposited in EMCAL and HCAL.

The Zero Degree Calorimeter (ZDC), discussed in Chapter 3, will also be an important contributor to the characterization of event centrality. Most importantly, it can provide a high efficiency minimum bias event trigger for Pb+Pb collisions as it was demonstrated at RHIC energy [81], which will be important for reducing the systematic errors on centrality observables. It will also provide the total spectator energy, which should anti-correlate with the energies in the other AT-LAS calorimeters, thus verifying the assumption that the multiplicity or energy deposition varies monotonically with the impact parameter.
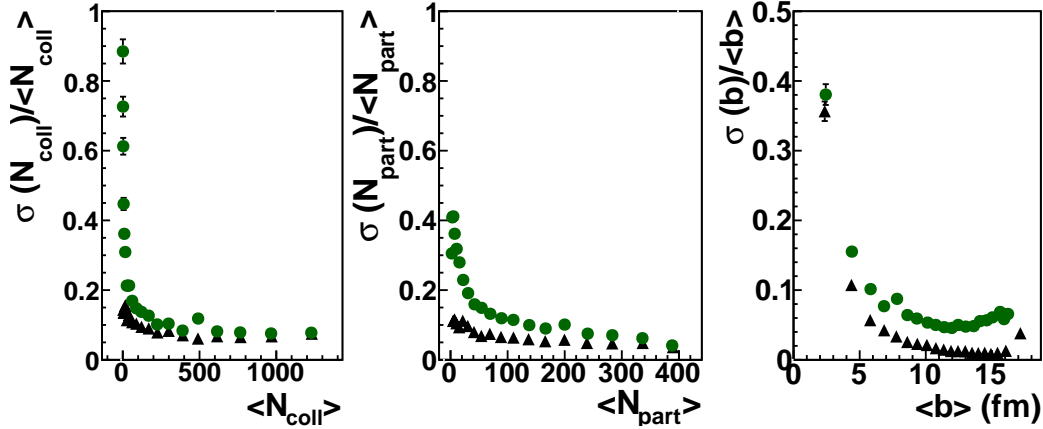
45

Figure 5.4: Normalized width of distributions of N_{coll}, N_{part} and b, corresponding to bins in the energy deposited in FCAL (circles). Filled black triangles correspond to the cuts made directly on the centrality variable (N_{coll}, N_{part} or b).

5.4 Charged particle multiplicity measurements

The measurements of the primary charged particle pseudo-rapidity density, $dN_{ch}/d\eta$, as a function of the collision centrality will be performed at the start of the LHC running with heavy-ion beams. These measurements will provide crucial information on the underlying physics and determine the initial energy and entropy densities. In addition charged particle multiplicities are in principle also sensitive to dynamical effects like jet quenching and nuclear shadowing [41] (see also Fig. 2.5).

The measurement of $dN_{ch}/d\eta$ can be performed with the silicon tracker of the ATLAS detector, covering pseudo-rapidity range $|\eta| < 2.5$. While it would be desirable to use the standard ATLAS tracking algorithms to estimate the total yield of charged particles, two issues arise. The first is simply that the algorithms have not yet been optimized for tracks lower than $p_T < 400$ MeV. The second is that while tracks can be reconstructed, as shown in Chapter 4, there is a substantial fake rate, which will have to be tuned using detailed Monte Carlo simulations. Beyond this, it is desirable to have a method which requires fewer choices than the standard tracking, in order to rapidly measure the track densities in real data under the tight time constraints of early minimum bias running. The limits of the tracking system to register particles at low values of transverse momentum (see Chapter 4) suggest the use of different approaches, of varying redundancy.

One approach which can be used to reduce the complexity of the problem is the "tracklet" method, most notably used in heavy ion collisions by the first PHOBOS paper [82]. As shown in the left panel of Fig. 5.5, the idea is to use the event vertex (determined by whatever means are available, e.g. with higher p_T tracks), and use this to seed vectors based on correlated hits in the first two Pixel layers (B layer and Layer 1). A tracklet is thus a three point track characterized by the event vertex, the η and ϕ of the hit in the inner-most pixel layer, and residuals $\Delta\eta$ and $\Delta\phi$ between that hit and a hit in Layer 1. The residuals are used both to cut away non-correlated hits (in this case $\Delta\eta < 0.08$ and $\Delta\phi < 0.8$), as well as to estimate the track momentum in low-multiplicity events. The set of tracklets selected by this method can then be used to estimate the particle density, with very little background. A distribution of the uncorrected number of tracklets integrated over $|\eta| < 1$ compared with HIJING truth is shown in the right panel of Fig. 5.5. This
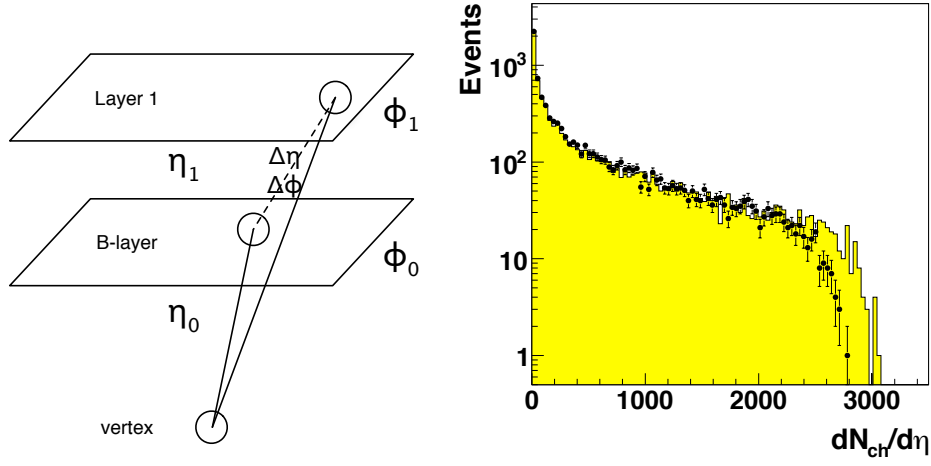
Figure 5.5: (left) Schematic diagram showing how tracklets are defined. (right) Distribution of $dN_{ch}/d\eta$ from HIJING events (histogram) and reconstructed using the tracklet method event-by-event, but without efficiency corrections (points with error bars).
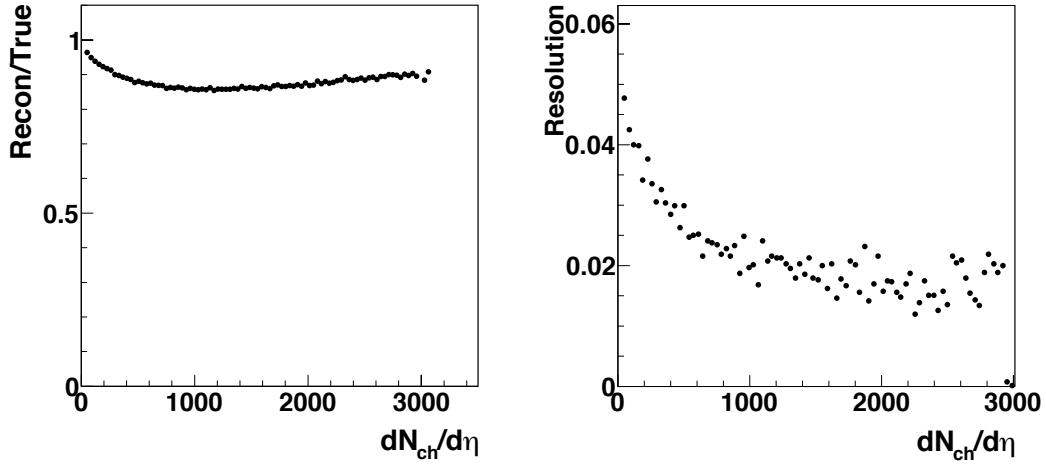
Figure 5.6: (left) Tracklet reconstruction efficiency at $|\eta| < 1$ for raw MC and reconstructed simulation data. (right) Resolution of the event-by-event charged particle multiplicity measurements.

shows that even without efficiency correction, the tracklet method gives a good estimate to the event-by-event multiplicity, allowing the study of mean values as well as fluctuations.

Efficiency is largely controlled by the efficiency of the silicon detector, which is very high. However, although using three hits in addition to the primary vertex provides some redundancy, a large occupancy (e.g. as one might expect in heavy ion collisions) can lead to fake tracks, especially when choosing only the closest hit in Layer 1 for each hit in B layer. To estimate this, an equivalent

47

sample of truth tracks is extracted by looking at charged hadrons (protons, pions and kaons). The η, ϕ and p_T are all relevant for this study. Comparisons of the total yield (integrated over all p_T and within $|\eta| < 1$) relative to the MC truth are shown in Fig.5.6. It can be seen that, over wide range of event multiplicities, the efficiency of 90% is achieved with the resolution of 2%.

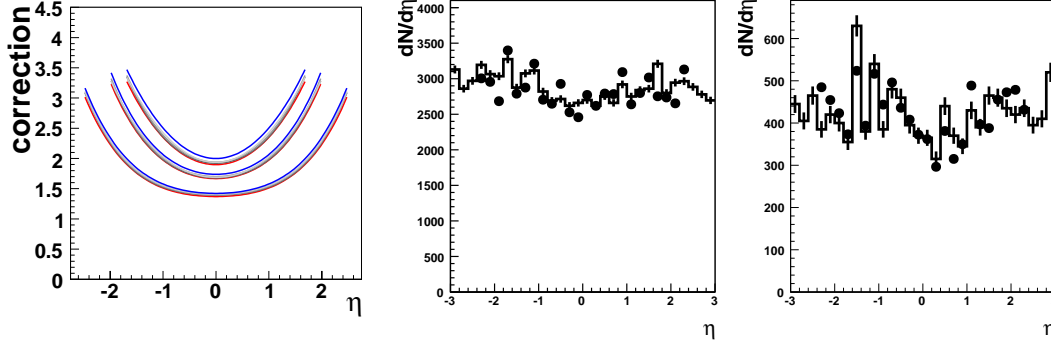Figure 5.7: (left) Correction functions for the three pixel layers (for B layer, lower band to Layer 2, upper band) from samples of Pb+Pb collisions with different centralities. For each band, corresponding to the pixel layer, the low curve is for the most central sample ($b = 2.3$ fm), and the upper curve is for the most peripheral sample ($b = 10.7$ fm), while functions derived for all other samples fall in the area between these two curves. Comparison of the reconstructed charged particle density distribution obtained from the first pixel layer clusters (dots) with the true distribution (histogram) for a central event with $b = 2.3$ fm (middle) and peripheral event with $b = 10.7$ fm (right).

The another approach was to use the clusters reconstructed in the silicon pixel layers. The clustering procedure accounts for the fact that a charged particle traversing the detector usually leaves signal in more than one pixel. The pseudo-rapidity distribution of the clusters shows a significant excess as compared to the generated distribution of the primary charged particles. This excess can be attributed to particles originating in secondary interactions and the effects of the magnetic field. Therefore, in order to extract pseudo-rapidity distribution of the primary particles, the Monte Carlo based correction factors had to be applied. These correction factors are defined as

$$C(\eta) = \frac{(dN_{ch}/d\eta)_{rec}}{(dN_{ch}/d\eta)_{true}}. \tag{5.2}$$

They have been calculated for each of the three pixel layers for samples of simulated HIJING Pb+Pb collisions with different centralities. A smooth functional dependence was fitted to the calculated $C(\eta)$. The shape of the correction function reflects the distribution of the material in the detector, indicating that secondary particle production gives the dominant contribution to the observed excess in the $dN_{ch}/d\eta$ distribution of pixel clusters. Thus-determined correction functions weakly depend on centrality (variation within less than 5%), as illustrated in Fig. 5.7 (left).

The correction functions determined in this way were then used in the reconstruction of $dN_{ch}/d\eta$ distributions on an event-by-event basis for events with different centralities. Examples for the

two such events with impact parameters $b = 2.3$ and $b = 10.7$ fm are shown in Fig. 5.7 together with the comparison to the true distribution for primary charged particles. The estimated reconstruction errors are of the order of 10-15%. Previously [83], we have also shown that with this reconstruction method we can correctly reproduce much higher particle densities as well as variations in the shape of the $dN_{ch}/d\eta$ distribution.

5.5 Transverse energy measurements

The transverse energy flow as a function of pseudo-rapidity is related to the energy density attained in nucleus-nucleus collisions [84]. The hermetic and granular calorimetric system of the ATLAS detector allows for measuring energy depositions in a wide range of pseudo-rapidity, out to $|\eta| = 5$, including both electromagnetic and hadronic energy. The simplest method for extracting $dE_T/d\eta$ uses sum of calibrated transverse energies deposited in calorimetric cells calculated as a function of η. The correction factors for acceptance cracks and energy deposits from particles produced in interactions with the detector material should be applied. They can be calculated as $(dE_T/d\eta)_{rec}/(dE_T/d\eta)_{true}$, thus in a similar way as correction factors used to derive $dN_{ch}/d\eta$ (see Section 5.4). They have been calculated for samples of events with different centralities and were found to be independent of centrality. The final corrections, averaged over all centralities, are then applied in the reconstruction of $dE_T/d\eta$ for single events. Figure 5.8 (left) shows as an example the comparison of the corrected reconstructed $dE_T/d\eta$ with the generated one for a single Pb+Pb event with $b = 2.3$ fm. A good agreement can be seen over the pseudo-rapidity range $|\eta| < 4.9$.
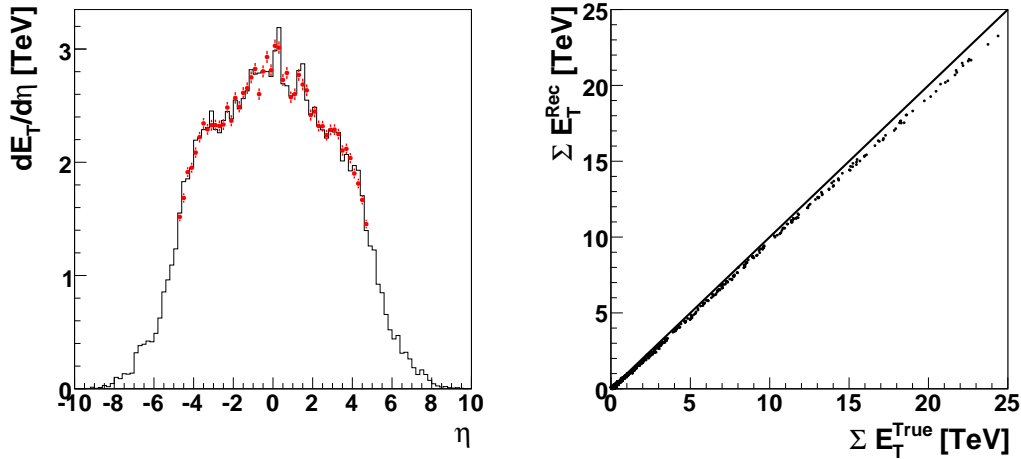
Figure 5.8: (left) Comparison of the reconstructed $dE_T/d\eta$ distribution (points) with the true distribution (histogram) for a central event with $b = 2.3$ fm. (right) The reconstructed total transverse energy in $|\eta| < 4.9$ (dots) versus the true one.

We have applied also another method which is independent of the Monte Carlo corrections and is based on the use of the algorithm developed to reconstruct the missing transverse energy in p+p collisions [85]. With this algorithm the total transverse energy (ΣE_T) is calculated summing

calibrated energy deposits of all calorimeter cells that survive the noise cut. The energy of the reconstructed muons in the muon spectrometer is also accounted for and the corrections for the energy loss in the detector material are applied. With this method we can reproduce the total transverse energy in $|\eta| < 4.9$ with an accuracy better than 5%, see Fig. 5.8 (right).

5.6 Elliptic flow

When two nuclei collide with non-zero impact parameter, the initial spatial anisotropy of the overlapping region leads to a momentum anisotropy in the final state, providing that the system evolves collectively with significant re-interaction between produced particles. This anisotropy arises due to the pressure gradients built in the initial stage of the system evolution. The stronger pressure gradients in the direction of the reaction plane (shorter axis of the overlap almond-like region) lead to a preferential in-plane particle emission. This final state momentum anisotropy can be quantified by studying the Fourier decomposition of particles' azimuthal angle distribution:

$$E\frac{d^3N}{dp^3} = \frac{1}{2\pi}\frac{d^2N}{dp_T^2 dy}\left(1 + 2\sum_{n=1}^{\infty} v_n(p_T, y)\cos\left[n(\phi - \Phi_{RP})\right]\right), \qquad (5.3)$$

where ϕ is the azimuthal angle of the particle and Φ_{RP} denotes the azimuthal angle of the reaction plane defined by the impact parameter, $(\vec{b})$, and the beam axis (z). The second Fourier coefficient, $v_2 \equiv \langle\cos\left[2(\phi - \Phi_{RP})\right]\rangle$, referred to as elliptic flow, measures the elliptical shape of the distribution of particles' momenta in the transverse plane.

The most widely used method [86] of measuring the final state azimuthal anisotropy requires the estimation of the azimuthal angle of the reaction plane, Φ_{RP}, which is not directly measurable. The knowledge of the reaction plane is also important for other than elliptic flow studies, like e.g. jet quenching. Therefore, in the next sub-section we discuss the procedure to estimate the reaction plane. Then, the methods used to reconstruct elliptic flow signal are described.

The analysis is based on the HIJING generated events with implemented flow effects via redistribution of the particles' azimuthal angles in order to get the desired elliptic flow signal. Several fully simulated event samples with different flow effects have been produced. These include samples with the flow signal dependent on centrality, pseudo-rapidity and transverse momentum as deduced from the RHIC data extrapolated to the LHC energy. For this input flow signals five centrality selections were applied by fixing the impact parameter values within the range from 2.3 fm up to 10.7 fm. In addition several samples with constant flow values of 3%, 5% and 10% have been also simulated for different centralities of Pb+Pb collisions.

5.6.1 Reaction plane reconstruction

Anisotropic effects are due to a truly collective motion which means that the emission of every produced particle in a given event is correlated with the reaction plane of that event. This multi-particle correlation gives rise to the inter-particle correlations providing the basis for the estimate of the reaction plane. For each event we determine the angles, conventionally called event plane angles:

$$\Psi_n = \frac{1}{n}\tan^{-1}\left(\frac{\sum w_i \sin(n\phi_i)}{\sum w_i \cos(n\phi_i)}\right), \qquad (5.4)$$

where the sums run over all particles in an event. The weights, w_i, are introduced to account for some acceptance biases and to get the best estimate of the Φ_{RP}, e.g. for calorimetric measurements the weights are taken as $w_i = E_{T,i}$. The flow signal, v'_n, measured using the nth harmonic event plane, Ψ_n, is then given as: $v'_n = < \cos n(\phi_i - \Psi_n) >$, where the brackets denote average over all particles in all events. An event plane angle of each order fluctuates around the true reaction plane angle, Φ_{RP}, due to the finite particle multiplicity. Thus, the flow value, v'_n, has to be corrected by the reaction plane resolution, $\langle \cos n(\Psi_n - \Phi_{RP}) \rangle$. The correction is found by calculating an event plane angle in two distinct sub-event regions, N and P, in every event, where for example sub-event N (negative) covers $\eta < 0$ while sub-event P (positive) covers $\eta > 0$. The following relation between the two event plane angles, Ψ_n^N and Ψ_n^P and the reaction plane resolution holds if any correlations not due to flow are assumed to be negligible:

$$\left\langle \cos[n(\Psi_n^N - \Psi_n^P)] \right\rangle = \left\langle \cos[n(\Psi_n^N - \Phi_{RP})] \right\rangle \left\langle \cos[n(\Psi_n^P - \Phi_{RP})] \right\rangle. \tag{5.5}$$

When the two sub-events have similar multiplicity then the resolution correction for each sub-event is

$$R \equiv \left\langle \cos[n(\Psi_n^N - \Phi_{RP})] \right\rangle = \left\langle \cos[n(\Psi_n^P - \Phi_{RP})] \right\rangle = \sqrt{\langle \cos[n(\Psi_n^N - \Psi_n^P)] \rangle}, \tag{5.6}$$

and the resolution corrected flow signal (v_n/R) is:

$$v_n = \frac{v'_n}{\sqrt{\langle \cos[n(\Psi_n^N - \Psi_n^P)] \rangle}}. \tag{5.7}$$

For the subsequent study of the elliptic flow the order n in the above equations should be substituted by $n = 2$.

With the ATLAS detector, the reaction plane angle and its resolution can be determined using different detector sub-systems since all of them have a complete azimuthal angle coverage. Table 5.1 shows the reaction plane resolution obtained with different detector sub-systems for the sample of simulated Pb+Pb collisions with constant flow of 5% for the three centrality classes selected by the impact parameter cuts: peripheral, $b = 10 - 12$ fm, semi-central, $b = 6 - 8$ fm, and central, $b = 2 - 4$ fm. One can see that resolution corrections are small (not very different from unity) particularly for central collisions. The resolution worsens for more peripheral events due to smaller event multiplicities.

For illustration Fig. 5.9 shows the distribution of the difference between the true reaction plane and the event plane angle, $\Delta\phi = \Psi_2^N - \Phi_{RP}$, for the sample with constant flow of 5% and the impact parameter $b = 6 - 8$ fm, where the event plane angle is determined from the different detector sub-systems.

The systematic study of the event plane resolution have been performed for all simulated samples. The best resolution (correction close to unity) is obtained, as expected, for the samples with stronger flow signal, i.e. 10% constant flow or using the sample of central events with a flow signal extrapolated from RHIC data.

5.6.2 Elliptic flow reconstruction from the event plane method

As discussed in the previous section, the elliptic flow parameter, v_2, is obtained from Eq. 5.7 with $n = 2$:

Sub-system	η - coverage for sub-events	Resolution correction		
		$b = 10 - 12$ fm	$b = 6 - 8$ fm	$b = 2 - 4$ fm
EMCAL-Barrel	$0.2 < |\eta| < 1.5$	0.29 ± 0.06	0.70 ± 0.02	0.81 ± 0.01
EMCAL-EndCaps	$1.5 < |\eta| < 3.2$	0.57 ± 0.03	0.88 ± 0.01	0.93 ± 0.01
HCAL-EndCaps	$1.6 < |\eta| < 3.2$	0.25 ± 0.07	0.59 ± 0.03	0.74 ± 0.02
FCAL0 (first layer)	$3.1 < |\eta| < 4.8$	0.60 ± 0.03	0.89 ± 0.01	0.93 ± 0.01
Pixel, B layer	$0.2 < |\eta| < 2.6$	0.56 ± 0.03	0.87 ± 0.01	0.92 ± 0.01
SCT, 1st layer	$0.2 < |\eta| < 1.6$	0.36 ± 0.05	0.71 ± 0.01	0.76 ± 0.01
Reconstructed tracks	$0.2 < |\eta| < 2.0$	0.45 ± 0.04	0.85 ± 0.01	0.92 ± 0.01

Table 5.1: Resolution corrections calculated for different sub-systems for the simulated events with different centralities and with the constant flow of 5%.

$$v_2 = \frac{v_2'}{\sqrt{\langle \cos[2(\Psi_2^N - \Psi_2^P)] \rangle}}. \tag{5.8}$$

.

As mentioned before, two separate sub-event regions, N and P, are used to find the event plane angles, Ψ_2^N and Ψ_2^P (see also Table 5.1). In order to avoid autocorrelations, the flow signal, v_2' is measured for signals recorded in the $P(\eta > 0)$ hemisphere with respect to the event plane angle determined from the $N(\eta < 0)$ hemisphere and vice versa. With the suite of detectors possessing the full azimuthal symmetry, we can reconstruct the flow with different combinations of the detectors used for the event plane estimate and the flow signal measurement.

As an example we show the analysis in which the flow is calculated from azimuthal angles of pixel clusters from the innermost pixel layer while the event plane angle is calculated from the energy weighted azimuthal angles of the calorimetric cells in the first layer either of the electro-magnetic barrel or of the forward calorimeter. Fig. 5.10 shows the azimuthal angle distributions of the silicon clusters measured with respect to Ψ_2 for peripheral ($b = 10 - 12$ fm) data samples with input v_2 of 3%, 5% and 10%. A clear flow signal can be visible, more pronounced for the samples with stronger input flow. For the samples with the constant flow values, the reconstructed flow signal was correctly found to be independent of the event multiplicity, pseudo-rapidity, and transverse momentum.

Method		Input v_2		
		0.03	0.05	0.10
pixel clusters (ϕ)	v_2^{rec}	0.018 ± 0.003	0.034 ± 0.002	0.070 ± 0.002
FCAL0 (Ψ_2)	v_2^{rec}/v_2^{true}	0.60 ± 0.10	0.68 ± 0.04	0.70 ± 0.02
tracks (ϕ)	v_2^{rec}	0.031 ± 0.004	0.047 ± 0.003	0.100 ± 0.002
FCAL0 (Ψ_2)	v_2^{rec}/v_2^{true}	1.00 ± 0.10	0.94 ± 0.06	1.00 ± 0.02

Table 5.2: Resolution corrected v_2 averaged over $|\eta| < 2$ obtained from pixel clusters and reconstructed tracks.
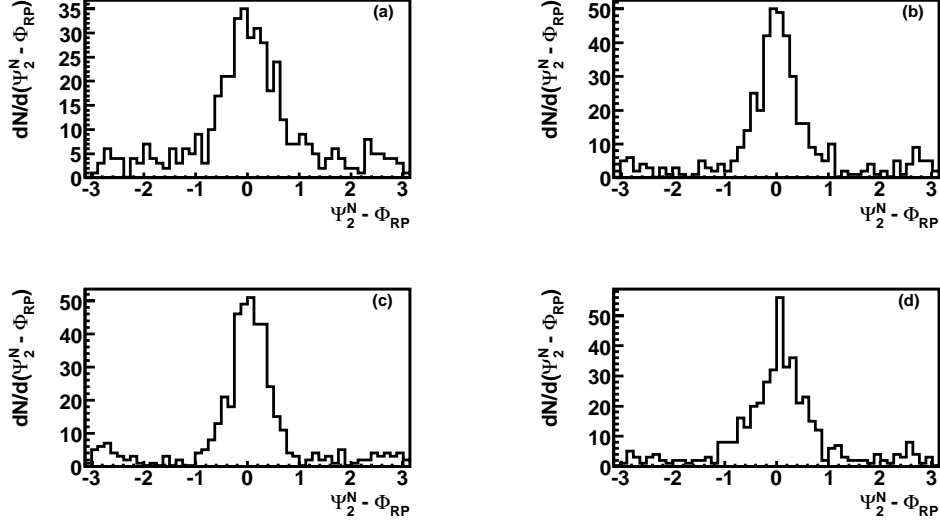
Figure 5.9: Distribution of the difference, $\Delta\phi = \Psi_2^N - \Phi_{RP}$, where Ψ_2^N is obtained from EMCAL-Barrel (a), FCAL0 (b), pixel B layer (c) , and from the reconstructed tracks with $p_T > 0.5$ GeV (d).

Figure 5.10: Distribution of $\phi - \Psi_2$, where ϕ is the azimuthal angle of pixel clusters and Ψ_2 is obtained from the first layer of EMCAL-Barrel (upper panel) or FCAL0 (lower panel) for the simulated data with 3% (left column), 5% (middle column) and 10% (right column) constant input flow.

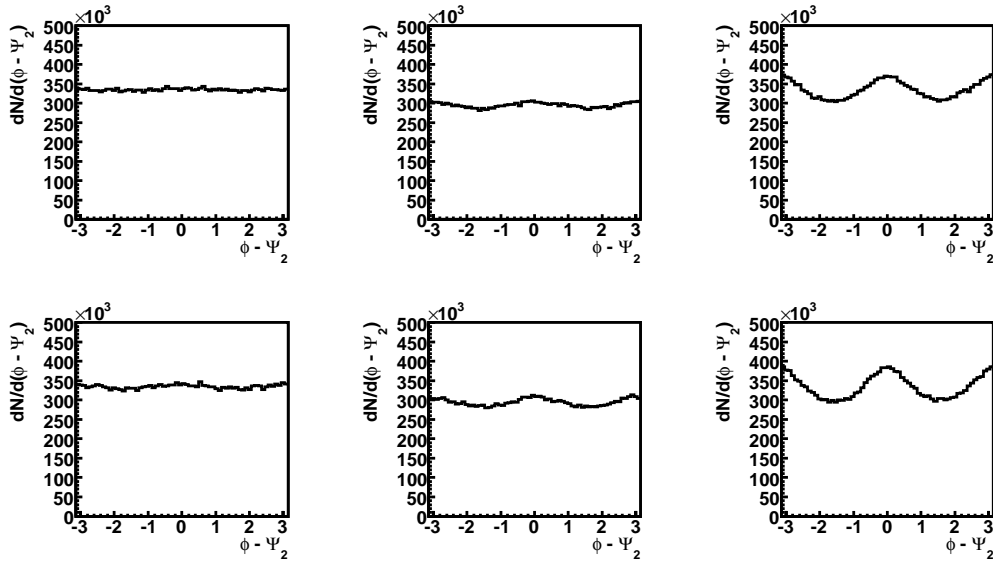In Table 5.2 we show the resolution corrected reconstructed flow signal from this analysis, v_2^{rec}, averaged over $|\eta| < 2$. The ratios of the reconstructed to the true flow value are also listed. One can see that using silicon clusters we underestimate the flow signal, by about 30%. This underestimation is approximately independent of the magnitude of the flow signal. The Monte Carlo corrections are needed to account for this suppression. The dilution of the flow calculated with pixel clusters is due to the signals not correlated with the reaction plane.

The elliptic flow can be also studied with the reconstructed tracks. The current tracking software imposes the limit on the lowest transverse momentum of 0.5 GeV. Lower part of Table 5.2 shows the resolution corrected elliptic flow signal calculated from the azimuthal angles of the reconstructed tracks, averaged over $|\eta| < 2$ for the three samples of simulated events with constant flow. One can see that the input flow signal is well reproduced (within 10%), and there is no need for corrections beyond the event plane resolution.

Fig. 5.11 shows the comparison of the reconstructed and the true v_2 values as function of pseudo-rapidity for a sample of peripheral Pb+Pb collisions with generated flow of 5%. A good agreement between the generated and reconstructed magnitude of the flow signal calculated from the reconstructed tracks shows our capability of measuring differential flow effects with a very good accuracy in peripheral collisions. Using pixel clusters and energy depositions in the forward calorimeters results in underestimation of the flow magnitude, a similar effect to that observed for the integrated flow studies (see Table 5.2).

Transverse momentum dependence was also studied for samples with different centralities and with the generated flow in agreement with the extrapolation of RHIC data. Results are shown in Fig. 5.15 (see Subsection 5.6.4), in comparison to the input flow signal and results obtained from other analysis methods. For peripheral collisions the event plane method correctly reproduces the generated flow in a wide range of particle transverse momenta. For central collisions, we observe that the reconstructed flow signal is larger than the generated one, especially for low transverse momenta. This effect is likely due to the large contribution of fake tracks among the reconstructed tracks in central Pb+Pb collisions as shown in Fig. 4.2. Fake tracks may associate with the correctly reconstructed tracks forming pairs close in $\Delta\phi$, thus leading to the autocorrelation effect distorting the event plane determination as well as the flow measurement. The ongoing work on the optimization of the tracking algorithm should result in the reduction of fake tracks, and consequently a better agreement between the true and reconstructed flow signals for low-momentum particles (below 1.5 GeV) produced in central collisions.

5.6.3 Elliptic flow from two-particle correlations

A method, alternative to the event plane method, uses the Fourier decomposition of the distribution in the azimuthal angle difference, $\Delta\phi = \phi_1 - \phi_2$, between pairs of charged particles [87, 88]:

$$\frac{dN_{ch}}{d\Delta\phi} \propto (1 + \sum_{n=1}^{\infty} 2v_n^2 cos(n\Delta\phi)). \tag{5.9}$$

The method allows the determination of the elliptic flow without event-by-event estimation of the reaction plane and can be used even for incomplete azimuthal coverage, e.g. in PHENIX at RHIC [88]. In this analysis the reconstructed charged particles tracks, with $|\eta| < 2$ and $p_T >$
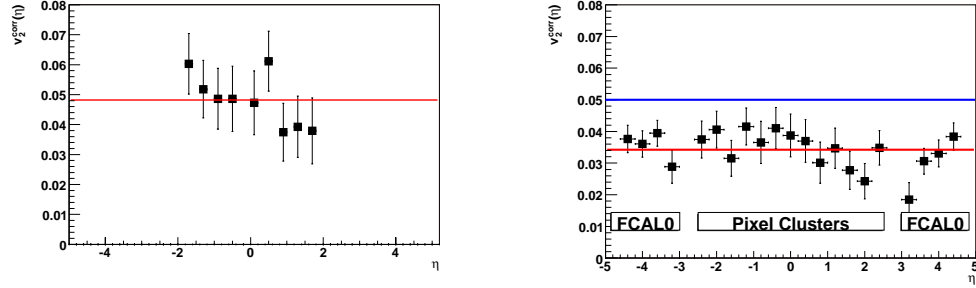
Figure 5.11: Pseudo-rapidity dependence of the reconstructed elliptic flow signal calculated from reconstructed tracks (left) and from pixel clusters and forward calorimetric cells (right) for a sample of peripheral events ($b = 10 - 12$ fm) with input flow of 5%. The reaction plane was estimated from signals in the first layer of forward calorimeters.

0.5 GeV, are used to form pairs. A two-particle azimuthal correlation function is defined as

$$C(\Delta\phi) = \frac{N_{corr}(\Delta\phi)}{N_{uncorr}(\Delta\phi)}, \tag{5.10}$$

1 where $N_{corr}(\Delta\phi)$ is the $\Delta\phi$ distribution for charged particle pairs observed in the same event, and
2 $N_{uncorr}(\Delta\phi)$ is the $\Delta\phi$ distribution for particle pairs which are formed from the two tracks selected
3 from different events. The magnitude of the elliptic flow, v_2, was extracted from the fit $C(\Delta\phi) \propto$
4 $[1 + 2v_2^2 \cos 2\Delta\phi]$. Centrality dependence of the two-particle correlation function is illustrated in
5 Fig. 5.12 for samples with input flow of 5%. The reconstructed magnitudes of the elliptic flow
6 signal, obtained from fits to $C(\Delta\phi)$ are listed in Table 5.3. One can see that the input flow is
7 well reconstructed in peripheral collisions, although with large statistical errors. Obviously much
8 higher statistics is needed for the study of two-particle correlations. For more central collisions
9 ($b = 6 - 8$ fm) the reconstructed v_2 is significantly larger than the input value of 5%. An even
10 stronger effect is observed for collisions with impact parameter ranging from 2 to 4 fm. Clearly,
11 the two-particle correlation method is very sensitive to autocorrelations induced by high level of
12 falsely reconstructed tracks.

b range [fm]	Input v_2	Reconstructed v_2 [%]
10 - 12	3%	4.0 ± 4.0
10 - 12	10%	9.0 ± 2.0
10 - 12	5%	5.0 ± 3.0
6 - 8	5%	7.1 ± 0.4
2 - 4	5%	9.2 ± 0.1

Table 5.3: Elliptic flow obtained from the two-particle correlation method for different samples of Pb+Pb collisions.
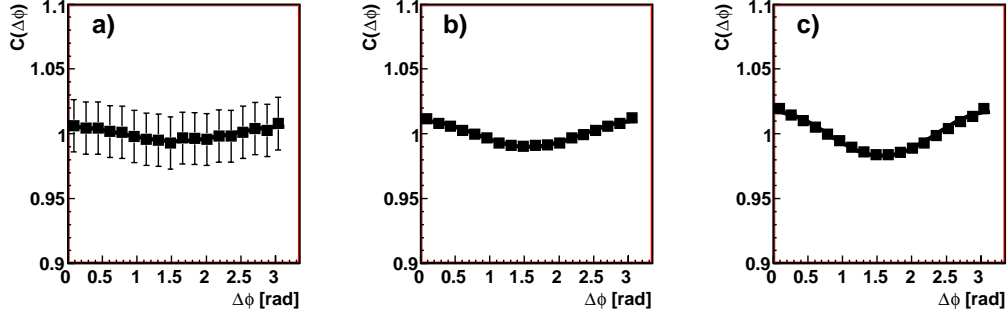
13   .

Figure 5.12: Correlation functions for samples with input flow of 5% and impact parameter range (a) $b = 10 - 12$ fm, (b) $b = 6 - 8$ fm and (c) $b = 2 - 4$ fm.

The two-particle correlation method was also used to study the p_T dependence of the flow magnitude for samples of events with different centralities and with the generated elliptic flow as extrapolated from RHIC data. Results are shown in Fig. 5.15. Similar conclusions as those related to the event plane method can be drawn. For peripheral collisions the two-particle correlation method well reproduces the generated p_T dependence of the elliptic flow, while for more central collisions the reconstructed flow signal is larger than the true one, particularly at low transverse momenta due to autocorrelation effects induced by fake tracks.

5.6.4 Elliptic flow with the Lee-Yang Zeros method

The standard method for analyzing anisotropic flow, described above, is to correlate particles with an estimate of the reaction plane angle Φ_{RP}, where this estimate is obtained also from correlations among the produced particles. So essentially the global collective behavior is studied via two-particle correlations, which are sensitive to various non-flow correlations induced by quantum interference effects, resonance decays or mini-jet production. The Lee-Yang Zeros method [89, 90] was proposed in order to extract flow effects from the correlations between a large number of particles, not influenced by non-flow correlations. The method is based on searching for minima in the complex plane of a generating function of azimuthal correlations, defined as:

$$G^\theta(ir) = \prod_{i=1}^{N_{ch}} [1 + irw_i cos(2\phi_i - 2\theta)], \tag{5.11}$$

where r is a real positive variable, θ is an arbitrary angle in the range from 0 to $\pi/2$ and w_i are weights (in this study assumed to be equal 1). N_{ch} is the charged particle multiplicity measured either over the whole acceptance or as a function of pseudo-rapidity or transverse momentum. $|G^\theta(ir)|$ is plotted as a function of r for different θ values. The elliptic flow is directly determined by the location of the first minimum, r_0:

$$v_2 \equiv \frac{j_{01}}{N_{ch}r_0}, \tag{5.12}$$

56

where $j_{01} \approx 2.405$ is the first root of the Bessel function $J_0(x)$. Fig. 5.13 shows the dependence of $|G^\theta(ir)|$ on r for samples of peripheral events and with constant input flow of 3, 5 and 10%. Similar dependencies, but for samples with different centralities and input flow of 5% are depicted in Fig. 5.14. Table 5.4 summarizes the elliptic flow values calculated from Eq. 5.12. In most cases the generated elliptic flow is well reproduced. Only for the sample of most central events the reconstructed v_2 is larger than the input v_2, indicating that the method is not able to remove autocorrelations. For the sample of peripheral events ($b = 10 - 12$ fm) and low input v_2 (3%), the output v_2 is determined with a large error, but in this case we reach the limits of the applicability of the Lee-Yang Zeros [90]. Nevertheless, the performance of the Lee-Yang Zeros method is clearly superior as compared to the two-particle correlation method (Table 5.3).
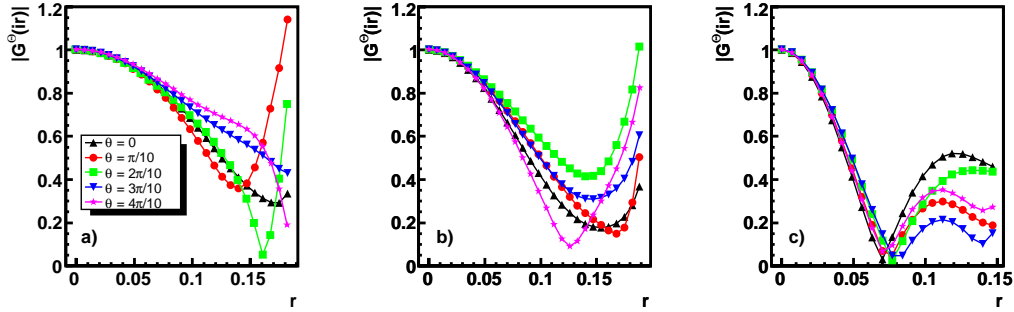

Figure 5.13: $|G^\theta(ir)|$ versus r for peripheral samples ($b = 10 - 12$ fm) with the generated v_2 of 3% (a), 5% (b) and 10% (c). In each plot the curves are calculated for different θ values as indicated in the legend.
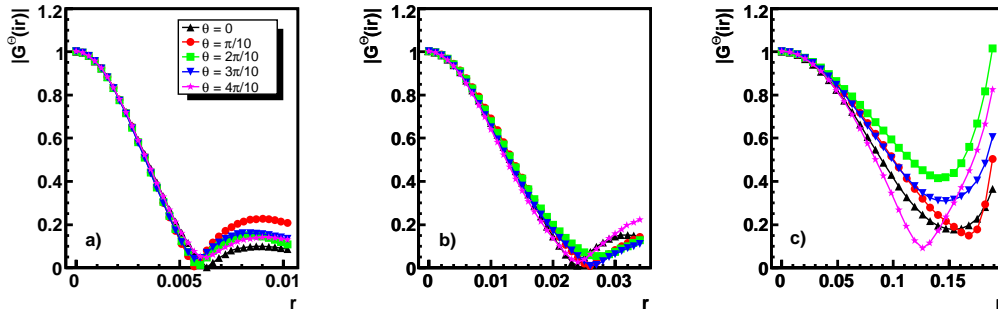

Figure 5.14: The same as in Fig. 5.13 for samples with constant input flow of 5% and different centralities: $b = 2 - 4$ fm (a), $b = 6 - 8$ fm (b) and $b = 10 - 12$ fm (c).

The Lee-Yang Zeros method was also used to study the p_T-dependence of elliptic flow. The simulated data samples with different centralities and with the generated flow obtained from ex-

b range [fm]	Input v_2	Reconstructed v_2 [%]
10 - 12	3%	4.0 ± 1.0
10 - 12	10%	10.0 ± 0.3
10 - 12	5%	5.0 ± 0.9
6 - 8	5%	5.4 ± 0.2
2 - 4	5%	7.7 ± 0.2

Table 5.4: Elliptic flow obtained from the Lee-Yang Zeros method for different samples of Pb+Pb collisions.

trapolation of RHIC measurements were used in this study. The elliptic flow values obtained from this method are presented in Fig. 5.15, together with the results from the event plane method and from two-particle correlations, and compared to the generated $v_2(p_T)$ dependence. All methods give consistent results which reasonably agree with the generated data for peripheral and mid-central Pb+Pb collisions. For the most central collisions all methods consistently overestimate the elliptic flow values in the range of $p_T = 0.5 - 1.0$ GeV. This discrepancy, as already discussed, is due to the autocorrelation effect caused by tracking algorithm imperfections. It has to be noted that the event plane and the two-particle correlation methods are equally sensitive to the non-flow effects, but have different requirements on the data statistics (much larger low-multiplicity event samples are needed for the two-particle correlation method). In addition, a good event plane res-olution which can be achieved with the ATLAS detector makes the event plane method superior to the two-particle correlation one. On the other hand, the Lee-Yang Zeroes method should be the best in eliminating non-flow contributions. Indeed, even at low transverse momenta, this method gives the results closest to the generated flow magnitude, in agreement with the generated values down to p_T of about 0.8 GeV. However, it is clear that even with this method it is not possible to eliminate the autocorrelation effects at still lower p_T.
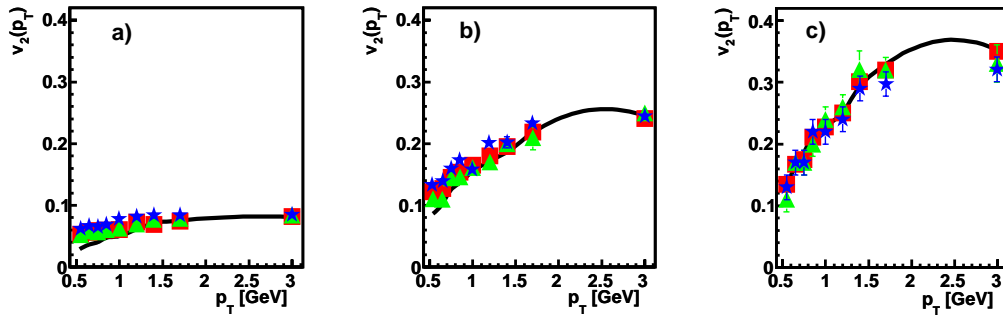

Figure 5.15: Transverse momentum dependence of the reconstructed v_2 from the event plane method (squares), two-particle correlations (stars) and the Lee-Yang Zeros method (triangles) for Pb+Pb collisions with (a) $b = 2.3$, (b) 7.0 and (c) 10.7 fm.

5.6.5 Elliptic flow studies: Outlook

The ATLAS detector offers an excellent capability of measuring azimuthal anisotropies in the transverse momentum distributions of produced particles. As have been shown here, various analysis methods can be applied, characterized by different efficiencies, dependency on Monte Carlo corrections and sensitivity to non-flow correlations. It is also planned to apply the method based on a cumulant expansion (up to the 4th order) of multi-particle correlations [91]. This method, as the method of Lee-Yang Zeros, does not require the estimate of the reaction plane and, to a large degree, allows the elimination of low-order non-flow correlations. A systematic comparison of various methods will provide a reliable estimate of the non-flow contribution and the measure of elliptic flow directly comparable to the hydrodynamic model calculations. An attractive possibility, not yet studied in detail, is to measure the elliptic flow of photons, which can be separated from hadrons thanks to the fine segmentation of the electromagnetic calorimeter. Another possibility, left for future studies, is the measurement of elliptic flow fluctuations, although these are complicated by the irreducible presence of non-flow correlations.

5.7 Summary

We have shown that the ATLAS detector is well suitable for studying global observables in heavy ion collisions. Notice that most of the discussed analysis techniques can be also applied for minimum-bias p+p collisions and thus tested on real data before the start of heavy-ion runs.

- The centrality parameter for heavy-ion collisions can be estimated using the energy deposited in the central and forward calorimeters as well as by using hits or reconstructed tracks in the silicon tracker.

- The charged particle pseudo-rapidity density can be determined by various technigues, with an accuracy of about 10% on an event-by-event basis, in the η range from -2.5 to 2.5.

- The transverse energy flow $dE_T/d\eta$ and the total transverse energy can also be precisely measured in single events over the broad η range.

- Measurements of collective flow can be performed using various analysis techniques and different detector sub-systems.

Chapter 6

Jet Reconstruction

3 This chapter describes the physics motivation for complete jet reconstruction and measurements
4 in heavy ion collisions at the LHC extending the discussion from the introduction, and shows
5 results for ATLAS jet reconstruction performance in Pb+Pb collisions. It also shows results on
6 measurements of jet fragmentation properties, di-jet correlations, and heavy-flavor tagged jets.

6.1 Physics motivation

8 As emphasized in Chapter 1, a major aspect of the heavy ion physics program at the LHC is the
9 extension and clarification of the understanding of the effects of hot, dense QCD matter on hard
10 probes, specifically jets. Prior to RHIC startup, several groups predicted the energy loss of a fast-
11 moving, colored parton traversing a colored medium via perturbative gluon bremsstrahlung and
12 multiple elastic scattering, leading to "jet quenching" [92, 93].

Evidence for this pQCD energy loss has been established through the measurement of high-p_T
single particle suppression [94]. The suppression is quantified by the nuclear modification factor,
R_{AA}, defined as the ratio of single particle yields in A+A collisions, $dN/dp_T|_{AA}$, compared to p+p
single particle rates, $dN/dp_T|_{pp}$, scaled by the number of binary nucleon-nucleon collisions (N_{coll}):

$$R_{AA} = \frac{1}{N_{coll}} \frac{dN/dp_T|_{AA}}{dN/dp_T|_{pp}} \qquad (6.1)$$

13 The nuclear modification factor for three different particle species, measured by PHENIX, is shown
14 in the left panel of Fig. 6.1: direct photons, which do not strongly interact in the nuclear medium,
15 are not suppressed while a factor of 5 suppression is measured in π^0 and η production. The level
16 of π^0 suppression is apparently consistent with a particular pQCD energy loss model [95]. How-
17 ever, it has been argued, many models of energy loss can describe this data even when the details
18 of the mechanism and implementation differ greatly between those models [96].

Further evidence for jet quenching comes from the azimuthal correlation of two high-p_T par-
20 ticles. These serve as a proxy for direct jet reconstruction, which is difficult at RHIC due to the
21 high-multiplicity underlying event which overwhelms the low-energy jets with fragments at com-
22 parable momentum as particles in the underlying event. Two-particle correlations in p+p suggest
23 that high-p_T particle production is dominated by hard scattering [20, 97]. Two high-p_T particles
24 from the trigger jet are correlated at $\Delta\phi \sim 0$ while two high-p_T particles at $\Delta\phi \sim \pi$ are fragments
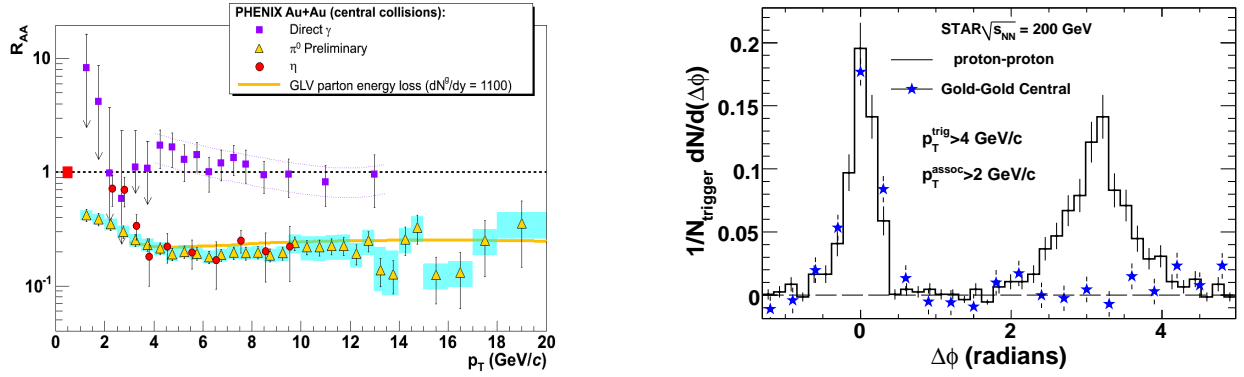
Figure 6.1: (left) Nuclear modification factor for direct photons, π^0, and η [16]. $R_{AA} < 1$ is evidence of jet energy loss. (right) Azimuthal angle ($\Delta\phi$) correlations of two high-p_T charged hadrons [18] with trigger hadron $p_T > 4$ GeV and associated hadron $p_T > 2$ GeV. The recoil jet (at $\Delta\phi \sim \pi$) is strongly suppressed in central Au+Au compared to p+p correlations [20].

from a di-jet pair. Such correlations are seen in the histogram on the right panel of Fig. 6.1. Measurements of these correlations in Au+Au indicate a substantial suppression of the recoil jet at $\Delta\phi \sim \pi$ while the trigger jet is essentially unmodified, as shown by the blue stars. These results suggest that the trigger jet originates from the surface of the interaction region and is unaffected by the nuclear environment while the recoil jet traverses a significant length in the medium and appears to be largely absorbed [20].

In addition to the suppression of light quarks and gluons, a quantitatively similar suppression
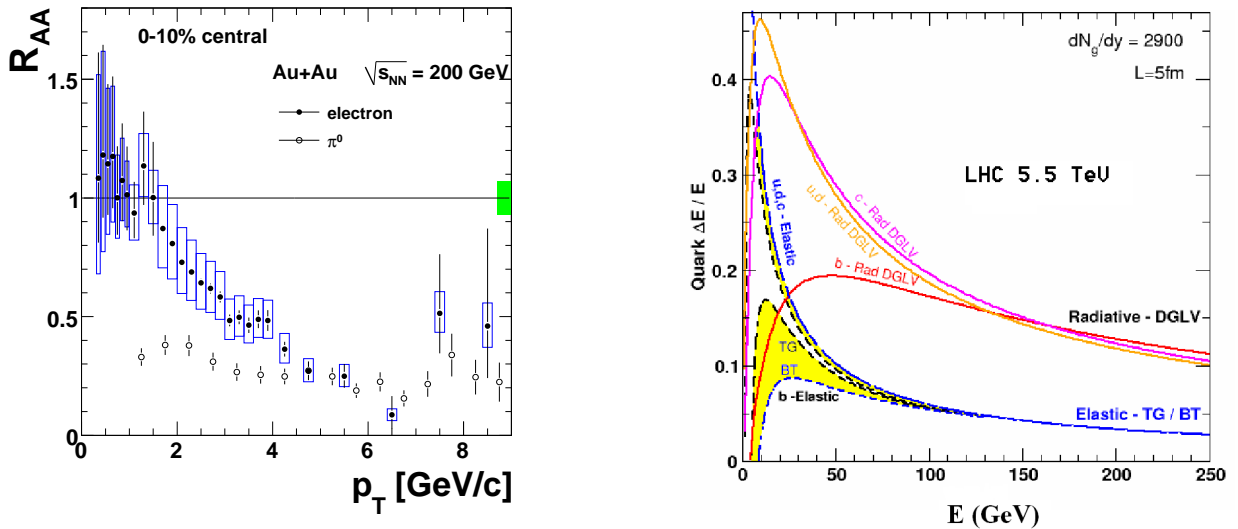

Figure 6.2: (left) The measured single particle suppression for non-photonic electrons (mainly from semi-leptonic decay of charm and bottom mesons) and π^0s from PHENIX Collaboration [7]. (right) The calculated radiative (solid curves) and collisional (dashed curves) energy loss in $\Delta E / E$ for various quark flavors at the LHC from Ref [98].
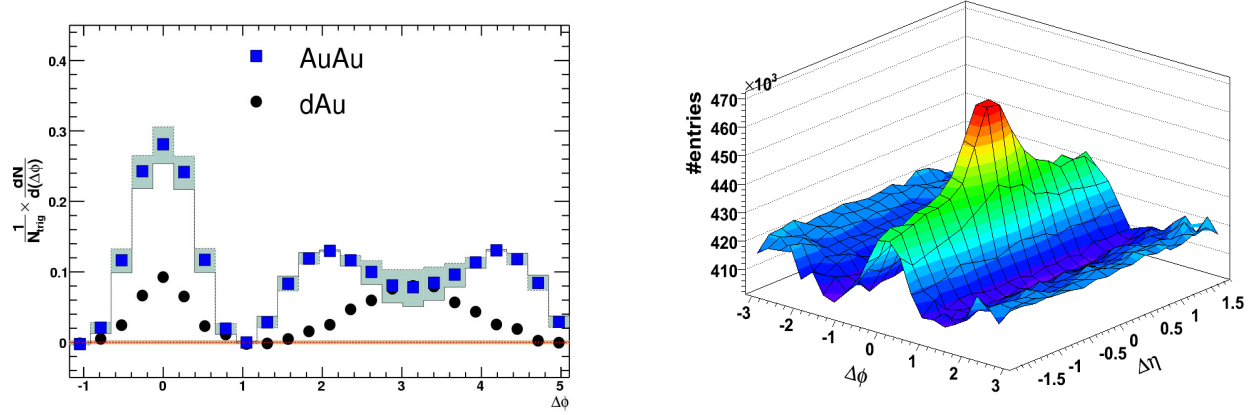
61

Figure 6.3: (left) Lower-p_T azimuthal correlations in central Au+Au showing a large yield at $\Delta\phi \sim \pi \pm 1.1$ rad [102]. (right) $\Delta\phi$ x $\Delta\eta$ correlations showing an extended "ridge" in $\Delta\eta$ [103]. The p_T ranges are $3 < p_T < 4$ GeV for trigger hadrons and $p_T > 2$ GeV for associated hadrons.

of single, non-photonic electrons, dominantly from charm and bottom quark decays, has been observed (see the left panel of Fig. 6.2) [7, 99]. Since the heavy quark mass kinematically suppresses forward gluon radiation (a phenomenon known as the "dead cone"), heavy quark energy loss was expected to be much less than that for light quarks [100]. A comparison of the fractional energy loss from collisions and radiation of different quark species expected at the LHC [98] is shown in the right panel of Fig. 6.2. Unfortunately, interpretation of the single, non-photonic electron suppression is not straightforward. Large uncertainties arise in calculating the charm cross-section at next-to-leading-log (NLL). Therefore, a theoretical understanding of the relative contribution of charm and bottom at a fixed electron p_T is not well constrained. Experimentally several early measurements of the charm-to-bottom ratio exist [101], but suffer from large statistical and systematic uncertainties.

Since these initial discoveries of energy loss of high-p_T particles, measurements sensitive to the medium's response have been made utilizing jets as probes of the medium. As shown in the left panel of Fig. 6.3, azimuthal correlations between 3-4 GeV trigger hadrons with associated hadrons with $p_T > 2$ GeV in Au+Au show a yield peaked at $\Delta\phi \sim \pi \pm 1.1$ rad as a "shoulder", non-existent in p+p and d+Au [19]. One possible explanation of this additional yield at these large angles is the existence of a Mach cone generated by a supersonic jet traversing the medium [104, 105]. The Mach angle is fixed by the speed of sound in the medium and, therefore, should not depend on the p_T of the particles, consistent with recent RHIC data [106]. The "shoulder" position shows a common centrality dependence at different collision energies and for different colliding species. Because the medium is similar for the energies and species considered, this indicates that the effect is a universal property of the produced medium, like the speed of sound, which would be similar across energies and geometries. Three-particle correlations, which are sensitive to differences between conical emission and bent/deflected jets, are consistent with conical emission[107, 108].

The right panel of Fig. 6.3 shows two-particle correlations in $\Delta\phi$ and $\Delta\eta$, which reveal an extended "ridge" in η associated with the trigger jet [103]. Such a structure is unique to $A + A$ collisions as it is not seen in $p + p$. In fact, this ridge may extend over at least 4 units in $\Delta\eta$ [109]. Despite the increasing number of confirming experimental measurements, the interpretation of
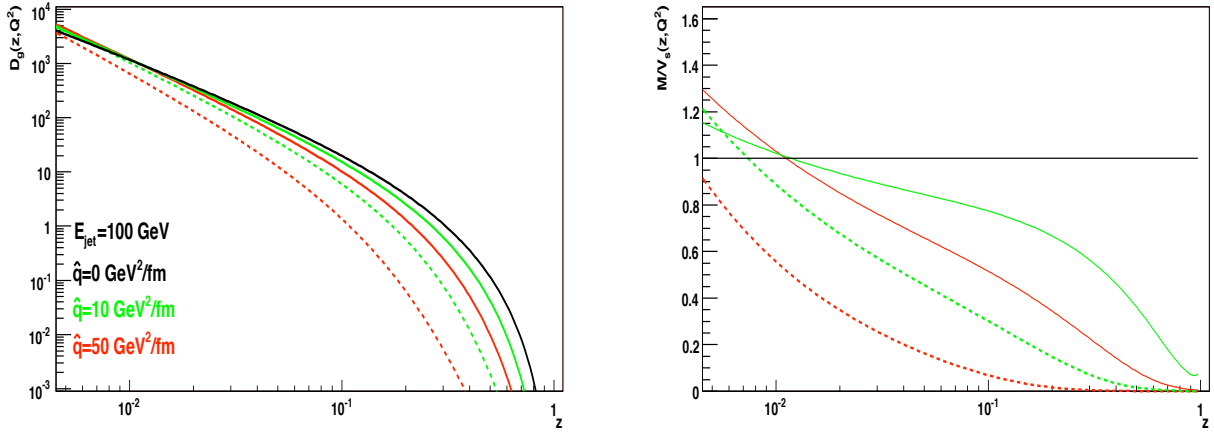
Figure 6.4: (left) Gluon to pion fragmentation functions in vacuum (black), in medium with $\hat{q} = 10 \, \text{GeV}^2/\text{fm}$ (green) and $\hat{q} = 50 \, \text{GeV}^2/\text{fm}$ (red) for 100 GeV jets passing through 2 fm of medium (solid) and 6 fm of medium (dashed). (right) The ratio of the in-medium modified fragmentation functions to the vacuum [111].

this observation is still debated. It should be noted that these results on the medium response are statistically determined from correlations rather than event-by-event. No direct observation of a cone or a ridge has been made in a single event.

With all of these exciting discoveries there are surprisingly few details that are currently understood about the energy loss mechanism. Debate continues about the dominance of gluon radiation over elastic scattering at momentum scales relevant to RHIC measurements. Within a given model, experimental data can tightly constrain the transport coefficient or the color charge density of the medium [23]. However, models still vary greatly between each other, *e.g.* estimates of the transport coefficient differ by a factor of $\sim$10. This is due to the fact that R_{AA} shows little sensitivity to the underlying energy loss mechanism; its observed value can be reproduced by almost all existing models [96].

Understanding energy loss is also experimentally challenging because two-particle correlations are "energy-loss biased". That is, a high-p_T particle has a higher probability of being detected if it loses relatively little energy due to fluctuations in the number of scatterings (punch-through) or traversing a short path length in the medium by being emitted tangentially. Requiring two high-p_T particles exacerbates this single particle bias by requiring a second high-p_T particle from the recoil jet in the same event. Some combination of these effects probably dominates high-p_T two-particle correlations [96].

These experimental constraints can be overcome at the LHC where copious high-E_T jets will be available that should be visible above the background. This will allow, for the first time, direct jet reconstruction in a heavy ion environment on an event-by-event basis. By fully reconstructing the jet, more energy than just that of the leading particle, including some part of the lost energy, will be measured. This will significantly reduce the energy loss biases. Even so, it has been argued that the fraction of energy lost outside the cone can be used to understand models of energy loss [110].

Once full jet reconstruction is available, jet tomography will be performed. Energy loss via gluon bremsstrahlung will be tested by studying the effects of energy loss on fragmentation func-
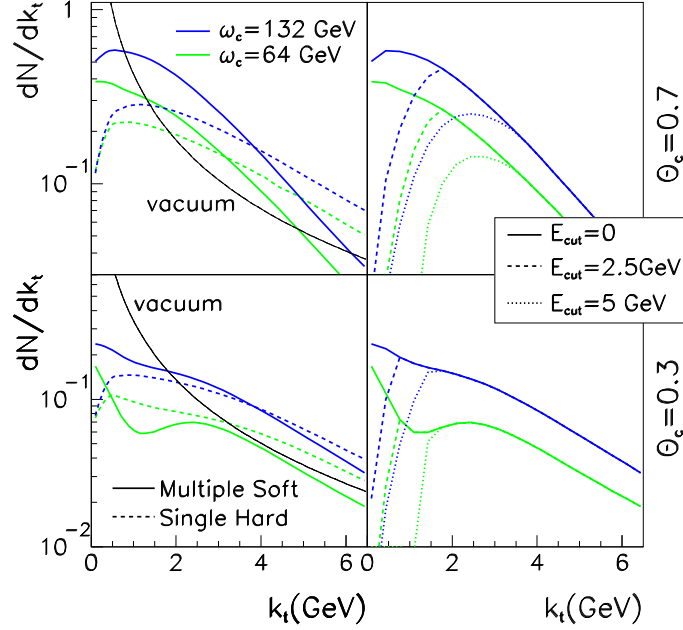
Figure 6.5: Distribution of gluon transverse momentum with respect to the jet axis, k_t (j_T in the text), for different energy (E_{cut}) and angular cuts (θ_c) of the gluons [28]. The vacuum distribution is shown in the thin solid lines. The different colored lines indicate two different medium transport properties (ω_c). Dashed lines indicate medium response and different energy cuts. Hard, in-medium gluon radiation results in increased yield at large k_t (j_T).

tions, $D(z)$. Here, z is the longitudinal momentum fraction of a jet carried by a fragment. An example of a modification of the $D(z)$ in medium [111] is shown in Figure 6.4. The characteristic pattern for energy loss is the suppression of high-z (high-p_T) fragments whose lost energy is transported to lower-z (lower-p_T) fragments. The ratio of the modified $D(z)$ to the vacuum $D(z)$ is below 1 at high z and above 1 at low z.

Another tool to study gluon bremsstrahlung is by measuring the hard radiation from the interaction of the jet with the medium. This is done via the j_T distribution. Here, j_T is defined as the transverse momentum of a fragment with respect to the jet axis. The high-j_T distribution is dominated by parton splitting in the fragmentation chain and should be enhanced by the additional hard radiation from jet-medium interactions. An example of the possible modification of the j_T distribution [28] is shown in Figure 6.5. The plot shows different j_T distributions (labeled as k_t) for gluons from jet fragmentation and energy loss with different gluon energy cuts and different maximum angles from the original parton. Even with a 5 GeV cut on the gluons, which cuts away much of the underlying event background, additional gluons are measured at large j_T resulting from the hard gluon radiation in the jet.

The most insightful single measurement for energy loss might be the jet R_{AA}. If all of the lost energy was recoverable by jet reconstruction, the jet spectrum should scale with N_{coll} like the direct photon spectrum (see Figure 6.1). Consequently, any energy lost not recoverable by full jet reconstruction, will result in the softening of the jet spectrum and so the jet $R_{AA} < 1$. This may be
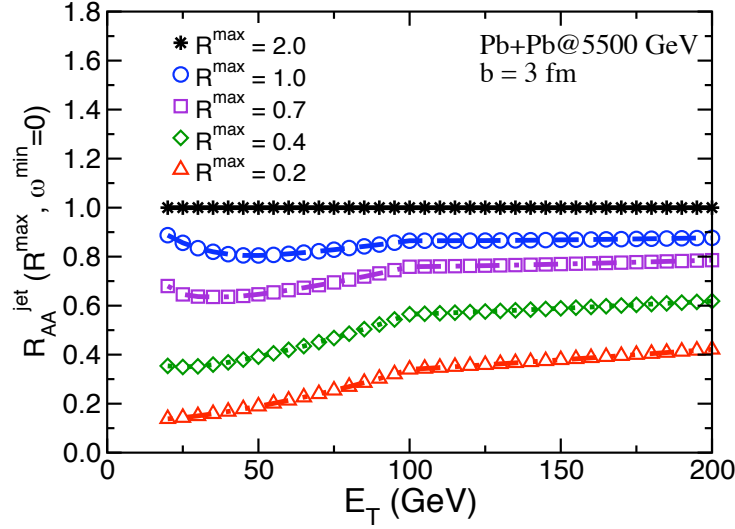
Figure 6.6: Differential jet R_{AA} calculations from Ref. [110] where energy radiated outside the cone is recovered with larger cone radii.

from collisional energy loss resulting in energy imparted to the medium and, thus, not radiated within the jet cone. It could also occur from the loss of energy which is radiated outside the jet cone. Still further, if energy loss is non-perturbative [112], the jet fragments and radiation may be indistinguishable from the underlying event and would result in no jet being reconstructed. An example of the potential power of measuring the jet R_{AA} is shown in Figure 6.6. Here the jet R_{AA} is measured for different cone radii. The full energy of the jet is only recovered when $R = 2.0$ and a clear suppression is observed for all other cone radii.

Multiple sets of measurements are therefore necessary to understand all of the details of energy loss. The sensitivity to the jet R_{AA} is shown in Figure 6.15 and discussed in Section 6.4.2. The performance for measuring fragmentation functions, $D(z)$, and j_T distributions is detailed in Section 6.5. Additionally, jet shapes are another observable to j_T and $D(z)$ that is discussed in Section 6.6. Di-jet $\Delta\phi$ and p_{out} distributions are outlined in Section 6.7. Finally, a first attempt at tagging heavy flavor jets with high-$p - T$ muons is presented in Section 6.9. These observations jet reconstruction opens up new avenues of studying energy loss at the LHC.

6.2 ATLAS calorimeter and jet measurements

The ATLAS calorimeter, as outlined in Chapter 2, is uniquely suited to perform full jet measurements and, thus, to make important and unique contributions to the understanding of jet energy loss and medium response to jets. The calorimeter (see Fig. 2.3) is nearly hermetic, covering 2π in azimuth, with the barrel and end-caps covering $|\eta| < 3.2$, and the forward calorimeters (FCAL) covering $3.2 < |\eta| < 5$. An active pre-sampling layer in front of the electromagnetic calorimeter improves the energy resolution for electromagnetic showers that originate in the inner e detector. The calorimeter is radially segmented with three electromagnetic and three hadronic measure-

ments over most of the coverage of the calorimeter. The radial segmentation of the calorimeter provides improved separation between electromagnetic and hadronic showers and is helpful in Pb+Pb collisions where the soft hadron background ranges out faster with depth than electromagnetic showers. In particular, because of the 2 T magnetic field, soft particles impact the front of the calorimeter at a shallow angle and deposit a large fraction of their energy into the first layers of the electromagnetic calorimeter. On average 60% of the background energy is deposited within the pre-sampler and first electromagnetic layer with the result that the second and third electromagnetic layers are less sensitive to soft hadron background.

As noted in Section 2.1, the fine η segmentation of the first electromagnetic layer ($\Delta\eta \approx 0.003$ in the barrel) is particularly valuable for carrying out jet measurements. The typical energy deposit in one of the cells in the first electromagnetic layer in a central HIJING [113] Pb+Pb event is $\approx$ 30 MeV while the peak energy deposit for a 1 GeV photon is typically a factor of 10 larger. Thus, electromagnetic showers from neutral hadrons and or prompt photons can be easily distinguished from the Pb+Pb underlying event (see Section 8.2).

6.3   Jet reconstruction in Pb+Pb collisions with ATLAS

The goal of the heavy ion jet analysis is to use algorithms developed for p+p measurements so that the calibrations obtained from p+p data can be used for Pb+Pb measurements with only modest adjustments. Currently, two complementary jet reconstruction algorithms are being explored: a seeded cone algorithm [114, 115] and an implementation of the k_T algorithm [116, 117, 118] optimized for fast execution time (Fast-k_T [119]). The cone and k_T algorithms differ significantly in the way they find jets, in their sensitivity to jet shape, and in the way they are adapted to the underlying event in Pb+Pb collisions. The use of multiple jet algorithms with different sensitivity to jet shape provides essential control over systematics in Pb+Pb jet measurements, especially as we do not know *a priori* the nature of the underlying event or the effects of jet quenching on the jet shape.

6.3.1   Seeded cone algorithm

The seeded cone algorithm operates on calorimeter towers. Towers are defined from energy sums of all the calorimeter layers within $\Delta\eta$x$\Delta\phi$=0.1x0.1. The towers within a given radius $R = \sqrt{\Delta\phi^2 + \Delta\eta^2}$ of the seed tower are clustered and iterated on until a convergence of the 4-vector of the jet is reached. For this algorithm, the underlying event background must be subtracted prior to reconstructing the jets. An η-dependent average cell energy, $\langle E_T^{\text{cell}}\rangle(\eta)$ is calculated for each layer of the electromagnetic and hadronic calorimeter. The $\langle E_T^{\text{cell}}\rangle(\eta)$ values are obtained excluding cells from high-E_T towers and the neighboring regions to prevent jets from biasing the background estimates. After the $\langle E_T^{\text{cell}}\rangle(\eta)$ values have been subtracted from all calorimeter cells, the resulting background-subtracted tower energies are input into the seeded cone algorithm to reconstruct jets. In this analysis, a cone of $R = 0.4$ and a seed tower energy threshold of 5 GeV are used. An example of the results of the background subtraction procedure is shown for a single event in Fig. 6.7.

The iterative cone jet algorithm will produce a candidate jet only when the transverse energy inside the cone is a local maximum in (η, ϕ). However, in the presence of heavy ion background, not all such maxima are true jets. Our studies of the behavior of the ATLAS seeded cone algorithm
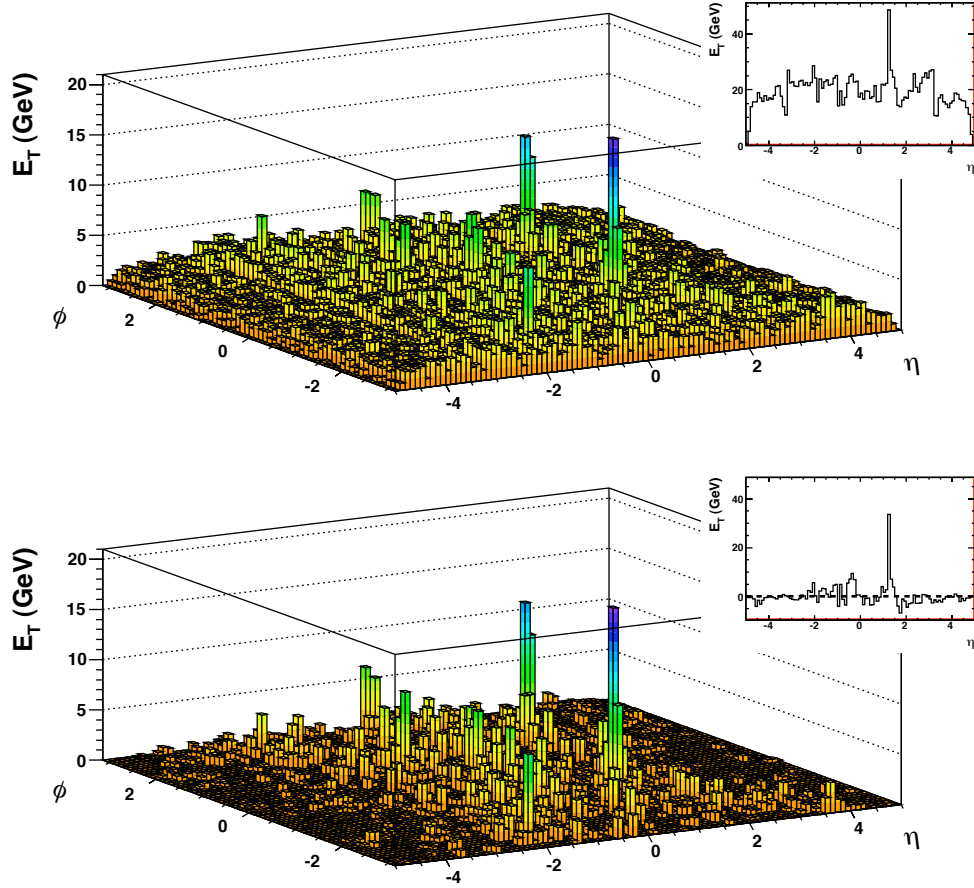
Figure 6.7: (top) Tower energies for a PYTHIA [44] di-jet event embedded into a HIJING event without quenching. (bottom) Tower energies in the same event after layer- and η-dependent subtraction of $\langle E_T{}^{\text{cell}} \rangle$ to remove the underlying event. The background-subtracted tower energies are then used as input to the seeded cone algorithm. The inset figures show the η-dependence of the energy in the towers integrated over $-0.5 < \phi < -1.5$ rad, which picks out the jet at $\phi \sim$-1 rad The large background from the underlying event is suppressed by the background subtraction.

indicate that it is not particularly sensitive to fluctuations in the number of soft particles in the cone but is sensitive to hard or semi-hard particles in the underlying event, particularly correlated particles arising from mini-jets and charm or bottom hadrons. Figure 6.8 shows an example of such a jet compared to a real jet from PYTHIA. The "raw" candidate jets returned by a standard cone algorithm, therefore, need to be subjected to background discrimination before they can be accepted as true jets. The HIJING generator without quenching produces a large number of mini-jets and heavy quarks, thereby generating an underlying event for which correlated fluctuations are relatively common. Thus, it provides a valuable testing ground for procedures to reject fake jets.

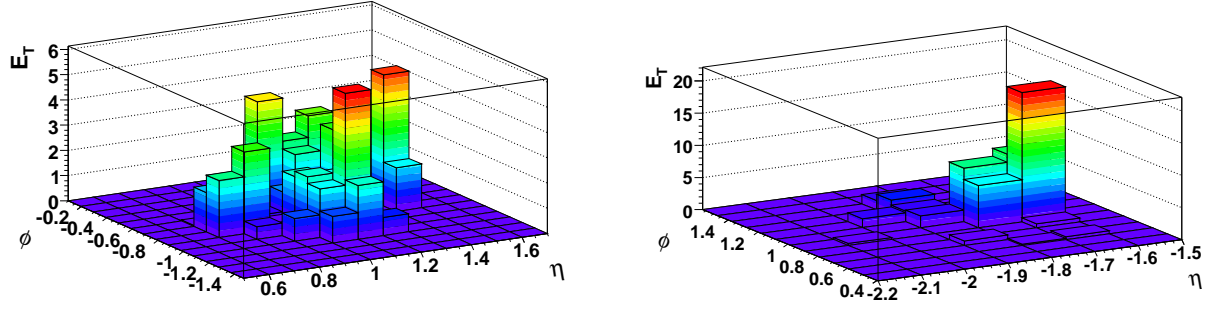The characteristics of the raw fake jets returned by the cone algorithm were studied using a

Figure 6.8: Demonstration of difference between false and true candidate jets returned by the iterative cone algorithm. (left) E_T distribution in $\Delta\eta \times \Delta\phi = 0.1 \times 0.1$ towers for a false jet resulting from nearby above-average E_T towers. (right) A similar distribution for a real jet (with an unusual fragmentation pattern).
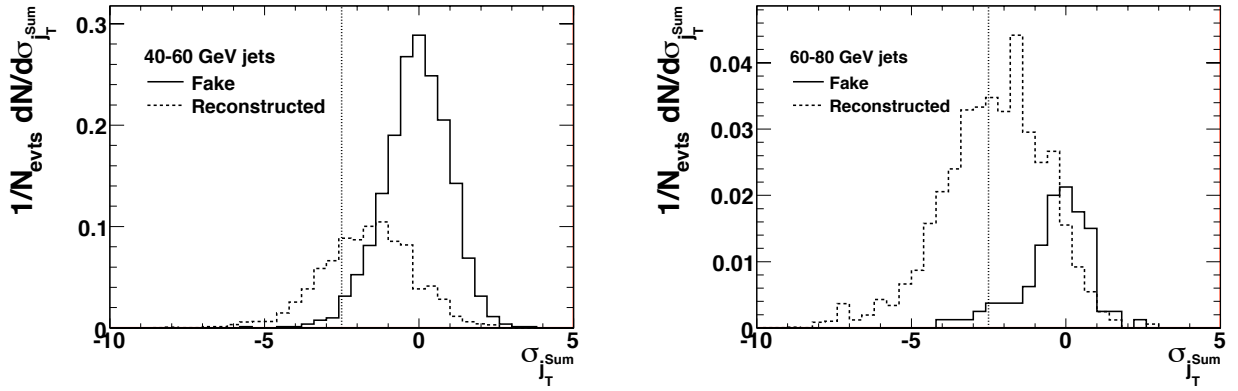

Figure 6.9: Comparison of the E_T-dependent $\sigma_{j_T^{Sum}}$ cut (see Eq. 6.3) for two different jet energies 40-60 GeV (left) and 60-80 GeV (right). Jets with $\sigma_{j_T^{Sum}} > -2.5$ are removed.

separate sample of HIJING events generated without quenching but with a cut on the maximum p_T, $p_T < 10$ GeV, of outgoing partons in hard scattering processes and a suppression of the longitudinal string (dipole) radiation. In this sample of events, all jets reconstructed with $E_T \gg 10$ GeV are fake jets returned by the cone algorithm. Several variables sensitive to the energy profile in the jet were evaluated. The most useful variable of those studied for rejecting fake jets was found to be j_T^{Sum}, which is defined as

$$j_T^{Sum} = \sum_{cell} E_T^{cell} \sin R_{cell} \quad , \tag{6.2}$$

where $R_{cell} \equiv \sqrt{\Delta\phi^2 + \Delta\eta^2}$ is the jet cone angle between the cell and the jet axis. This variable assigns higher weights to cells with larger energy or cells at large angles from the jet axis. For real jets, j_T^{Sum} depends both on the jet energy and on the angular distribution of fragments in a jet, but in a non-trivial way due to the narrowing of the jet cone with increasing energy. For fake jets we find that j_T^{Sum} is roughly proportional to the E_T of the false jet. The dependence of the separation

between real and false jets on jet E_T is removed by making an E_T-dependent cut:

$$\sigma_{j_T^{\text{Sum}}} = \frac{j_T^{\text{Sum}}(E_T) - \langle j_T^{\text{Sum}} \rangle (E_T)}{\sigma(E_T)}, \qquad (6.3)$$

where $\langle j_T^{\text{Sum}} \rangle (E_T)$ and $\sigma(E_T)$ are the E_T-dependent average value and width, respectively, for the *fake* jet j_T^{Sum} distribution. Figure 6.9 shows the distribution of $\sigma_{j_T^{\text{Sum}}}$ for false (solid) jets and real (dashed) jets. The false jet distributions are centered at 0 and have widths of 1 as seen from Eq. 6.3. With increasing jet energy the separation of the real and fake jets increases. A cut of $\sigma_{j_T^{\text{Sum}}} > -2.5$ rejects most of the fake jets, but also produces an E_T-dependent efficiency loss that is particularly severe at low E_T. Such a cut can be tuned to optimize between the desired purity and efficiency and also on the characteristics of the background. We note that the actual Pb+Pb background is likely to have substantially lower level of correlated fluctuations than produced by HIJING without quenching. The background rejection technique described here can, then, be used with a less restrictive cut on the discriminator variable and with a corresponding improved efficiency at low E_T.

6.3.2 k_T algorithm

The k_T algorithm is an infrared and collinearly safe jet algorithm. It is motivated by reconstructing back along the chain of fragmentation. The merging criteria for constituent, in this case calorimeter towers, i and j is

$$\min\left(E_{Ti}^2, E_{Tj}^2\right) \frac{R^2}{D^2} < E_{Ti}^2 \qquad (6.4)$$

where R is the angle between the constituents and D is a parameter of the algorithm which, similar to the cone radius, sets the size of the jets that will be reconstructed. Essentially all constituents with $R < D$ will be combined but softer constituents with $R > D$ can also be combined. This tends to make k_T jets have a non-conical shape. For the studies presented $D = 0.4$ was chosen. A particular advantage of this algorithm is that no fixed geometry (e.g. a cone) is imposed on the reconstructed jet. In the case of the Fast-k_T algorithm [119], the underlying event is handled in a completely different way from the cone algorithm. Following Cacciari and Salam [119], the jet reconstruction is performed directly on heavy ion events without background subtraction. In addition to real jets, the background towers are clustered into soft jets as shown in Fig. 6.10 for a HIJING [113] embedded PYTHIA [44] event. There are two jets from the embedded PYTHIA event which are clearly visible above the heavy ion background. The different shaded regions denote the jet candidates in this event (bottom left panel), most of them are jets primarily composed of background. The bottom right panel shows, for each jet, the ratio of maximum to average tower energy, E_T^{max}/E_T^{avg}, within the jet, plotted as function of the jet η. Clearly, this variable distinguishes between the PYTHIA jets and background jet candidates. It should be noted that this ratio for a jet with a Gaussian distribution in R is $1/\sigma$, where σ is the width of the energy profile in R. Therefore the background jets are much wider than the signal jets, as expected, and have lower values of E_T^{max}/E_T^{avg}. The η dependence of the ratio is parameterized as $r(\eta)$ and shown as the solid line in the lower right panel of Fig. 6.10. The difference between the actual E_T^{max}/E_T^{avg} and the parameterization is calculated for each jet candidate. This results in a difference distribution with a mean (μ) and a root-mean-square (RMS). A cut

$$(E_T^{max}/E_T^{avg} - r(\eta)) < \mu + 2 \times RMS \qquad (6.5)$$

69
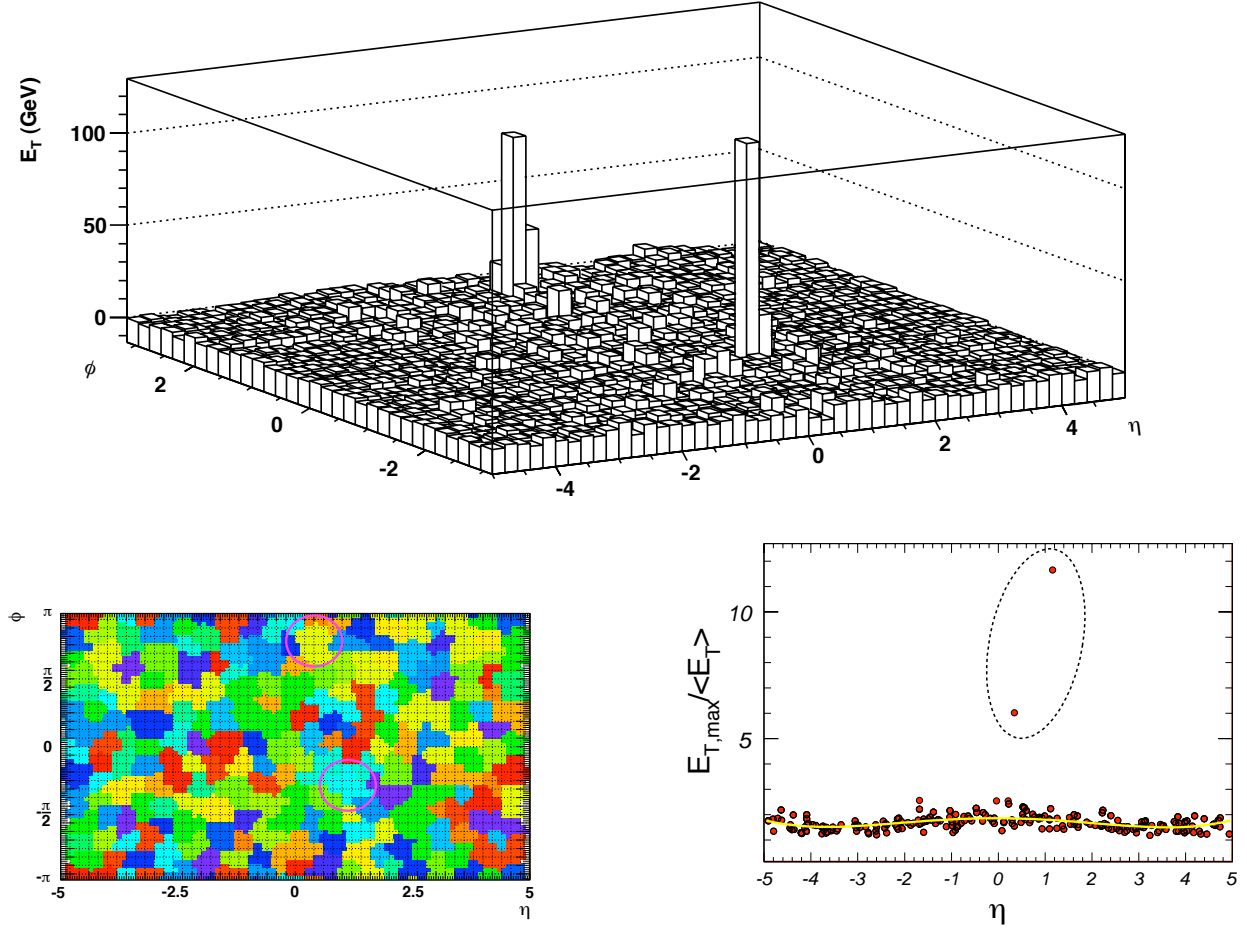
Figure 6.10: (top) Tower energies from a single PYTHIA di-jet event embedded in an event from unquenched HIJING with $dN_{ch}/d\eta = 2650$ at mid-rapidity and run with the Fast-k_T algorithm. (lower left) Each of the different, colored patches represent a jet defined by the algorithm. Every tower, even those with energy predominantly from the underlying event, is incorporated into a jet. (lower right) Distribution of maximum-to-average tower energy in reconstructed jets for this event. The two embedded PYTHIA jets, indicated by the circled points in the lower right plot and areas in the lower left plot, are distinguishable from the fake, background jets in this variable.

1 selects background jets. These jets are then used to estimate the underlying event background
2 which is subsequently subtracted from the real jets.

b (fm)	$\langle N_{coll} \rangle$	$dN_{ch}/d\eta|_{|\eta|<0.5}$
2	2030	$2673 \pm 5\ (\approx 2650)$
4	1563	$2174 \pm 5\ (\approx 2150)$
6	1017	$1587 \pm 5\ (\approx 1600)$
8	536	$1017 \pm 5\ (\approx 1000)$
10	206	$534 \pm 4\ (\approx\ 550)$

Table 6.1: Fixed impact parameter values used to produce HIJING events and their corresponding average number of collisions $\langle N_{coll} \rangle$, and mid-rapidity ($|\eta| <$0.5) primary charged particle multiplicity. It should be noted that, even if the error on the mean multiplicity is 4–5, the sample RMS for the multiplicity is about 100–150.

6.4 Jet reconstruction performance

6.4.1 Method of evaluation

The performance of the seeded cone and k_T algorithms was evaluated through an extensive simulation study. In the simulation, a merged event is constructed by embedding a PYTHIA di-jet event into a simulated Pb+Pb HIJING event without quenching and without a hard scattering cut which would remove mini-jets. In heavy-ion collisions, the performance of the jet reconstruction algorithm is very sensitive to fluctuations in the underlying background. Thus mini-jets, heavy quarks, and other correlated sources produce many fake jets at low E_T. The HIJING events likely represent an upper limit of the event multiplicities (in $dN_{ch}/d\eta$) comparing to other models at the LHC (see Fig. 2.5). These simulations therefore represent a "worst case scenario" for the underlying background in Pb+Pb collisions.

Merging jets into background events occurs after each event is passed through a full GEANT4 simulation of the ATLAS detector. The merged events are then passed through the reconstruction chain and data analysis software. The resulting jets from the merged events are matched to the truth jets, which are defined as the jets found with the same jet algorithm with the PYTHIA final state particles as input. A match is found if the reconstructed jet and truth jets are close in angular space ($R = \sqrt{\Delta\phi^2 + \Delta\eta^2} < 0.5$). If multiple reconstructed jets are matched to the same truth jet, the jet with the smallest R with respect to the truth jet is chosen to be the matched jet. In determining efficiencies and fake rates all reconstructed and truth jets are considered and not, for instance, only the highest energy jets in the event. The performance of each jet algorithm is evaluated based on a few key quantities: energy resolution, energy scale, efficiency and fake rate. These quantities are evaluated at the truth jet E_T, η, and ϕ unless otherwise specified.

In order to evaluate the centrality dependence of performance quantities in this and other physics studies, HIJING events were generated at a set of fixed impact parameters. For these impact parameters, the mid-rapidity ($|\eta| < 0.5$) charged particle multiplicity ($dN_{ch}/d\eta$) was evaluated with the results shown in Table 6.1. When discussing the centrality dependence of jet reconstruction performance and other results in other chapters, we will quote $dN_{ch}/d\eta$ since such a quantity is, in principle, less subject to the assumptions of the HIJING model. We note, however, that the correlated semi-hard production in HIJING has a greater impact on jet performance than fluctuations in the soft background so different models for Pb+Pb events producing the same $dN_{ch}/d\eta$ will not necessarily give the same jet performance.
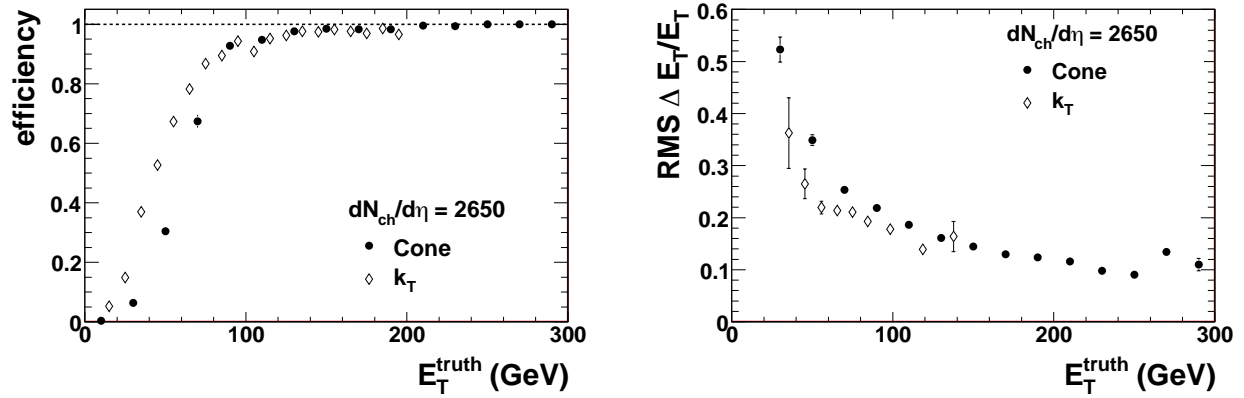
71

Figure 6.11: Comparison of efficiency (left) and E_T resolution (right) for the cone (closed) and k_T (open) algorithms for reconstructing jets in $dN_{ch}/d\eta = 2650$.

6.4.2 Performance results

Figure 6.11 shows the comparison of the jet performance for cone and k_T jets for the highest multiplicity environment simulated. The efficiency is shown in the left panel. There are differences at low-E_T, primarily due to how the fake background is handled. In the case of the cone algorithm the j_T^{Sum} cut represents a strict cut on the fake jets at the expense of reconstruction efficiency. The fake jet rejection for the k_T algorithm is loose in order to have as high efficiency as possible for all jets. For the comparison to be most fair additional fake jet rejection should be applied after k_T jet reconstruction which will naturally reduce the reconstruction efficiency. Still, the efficiencies converge to better than 95% at $E_T > 120$ GeV.

The jet energy resolution, shown in the right hand panel of Figure 6.11, is defined as the root-mean-square of the distribution of $\Delta E_T / E_T = \left(E_T^{truth} - E_T^{reco} \right) / E_T^{truth}$. A better resolution for the k_T algorithm is observed. However, the k_T jet relative jet energy scale is -20% for 50 GeV jets compared to -2% for the cone algorithm. This large deviation for the k_T jets is due to the fact that the periphery of the jets get incorprated by the neighboring background jets that subsequently are removed by the fake jet rejection. Therefore, some fraction of the energy of the jet is lost to the background. There is also a E_T dependence since the shape of the jet changes with the E_T. Because of this issue we have focused more on the cone algorithm than the k_T algorithm.

The jet performance results have been studied as a function of background multiplicity. Figure 6.12 shows the jet reconstruction efficiency for seeded cone jets as a function of E_T^{truth} and as a function of HIJING multiplicity. There is little to no dependence of the efficiency on multiplicity. This result is a combination of two effects. First, the shape of the efficiency curve is most influenced by the 5 GeV tower E_T seed cut in cone algorithm. A lower seed cut would result in higher efficiency at lower jet E_T but would generate more background jets. Second, for the results presented in Fig. 6.12 the same background rejection cuts have been applied for all centralities. For actual data analysis, the cuts would depend on centrality becoming less severe for more peripheral collisions. Thus, the results in Fig. 6.12 represent worst-case results for non-central collisions.

Figure 6.13 shows the energy and position (in ϕ) resolution as a function of truth jet E_T for cone jets for several Pb+Pb multiplicity bins. Both energy and position resolution of cone jets improve with increasing jet energy and for lower multiplicity environments. Although not shown, the
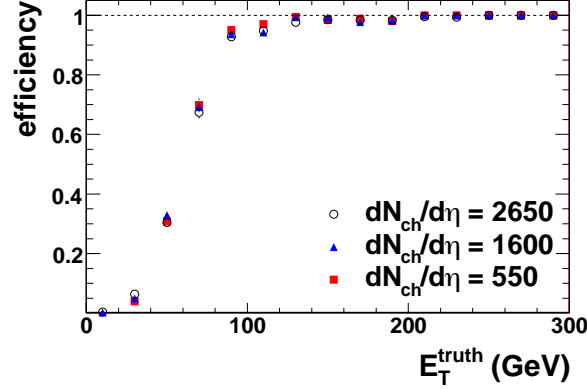
Figure 6.12: Jet reconstruction efficiency for jets reconstructed with the seeded cone as a function of input jet E_T and as a function of HIJING Pb+Pb multiplicity.
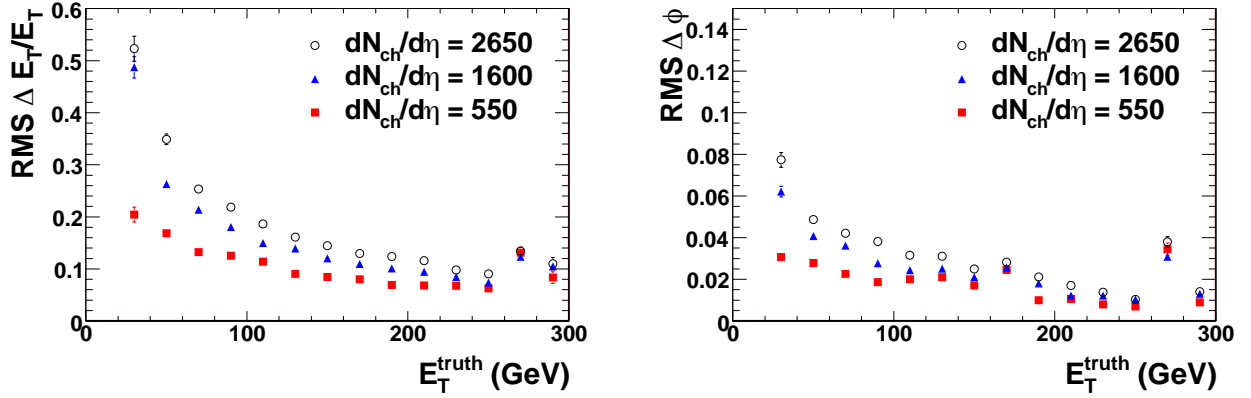

Figure 6.13: (left) Jet energy resolution as function of truth jet E_T for three multiplicity bins for seeded cone jet algorithm. (right) The azimuthal angular resolution of the seeded cone jets as function of truth jet energy.

position resolution in η is comparable to that in ϕ for all multiplicities. We note that many physics models predict that $dN_{ch}/d\eta$ for the most central Pb+Pb events is closer to $dN_{ch}/d\eta = 1600$ than 2650 (see Fig. 5.1), for which case we should expect a significant improvement of the resolution in the real data.

The pseudo-rapidity dependence of the jet performance has also been evaluated. Figure 6.14 shows the jet energy resolution for seeded cone jets with $E_T^{truth} > 50$ GeV and for three different multiplicity bins. The points with $|\eta| < 3.2$ are obtained from jets reconstructed in the barrel and the end-cap calorimeters while the filled points with $|\eta| > 3.2$ are from jets reconstructed in the forward calorimeters, an analysis which has only been carried out for the most central Pb+Pb sample. The improvement in energy resolution as η increases in the barrel and end-cap regions is due to the decrease in the underlying HIJING background. In the most forward rapidity region, the energy resolution deteriorates due to larger segmentation of the forward calorimeters. However, due to a lower underlying background, the resolution is comparable to that for mid-rapidity. In summary, over the entire η coverage of the calorimeter, 20-30% jet E_T resolution is
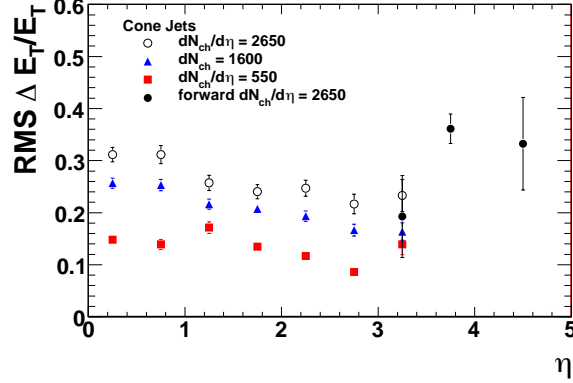
Figure 6.14: Jet energy resolution for $E_T > 50$ GeV seeded cone jets as a function of η for HIJING Pb+Pb events of different centrality, $dN_{ch}/d\eta|_{|\eta|<0.5}$.

$dN_{ch}/d\eta$	efficiency	B/(S+B)	$\sigma_{\Delta E_T / E_T}$
2650	70%	$\ll 1\%$	25%
1600	70%	$\ll 1\%$	21%
550	70%	$\ll 1\%$	15%

Table 6.2: Relevant jet reconstruction quantities for 70 GeV seeded cone jets reconstructed in different $dN_{ch}/d\eta$ backgrounds: efficiency, fake fraction, and jet energy resolution.

1 obtained in the highest occupancy environment.

2 The upper panel of Figure 6.15 compares the reconstructed cone jet spectrum with the in-
3 put and fake jet spectra. Even without correcting for efficiency and energy resolution, the re-
4 constructed spectrum already matches the input spectrum above 80 GeV quite well. The fake jet
5 spectra before and after the rejection cuts are shown by the dashed line and squares, respectively.
6 These rates fall much faster than the input jet spectrum given by PYTHIA. The impact of these
7 performance results on physics results can be seen in the lower panel of Fig. 6.15 which shows the
8 ratio of reconstructed and input jet spectra without correction. Above 80 GeV the required correc-
9 tions are of order 20%, much smaller than the factor of two jet suppression predicted by Lokhtin
10 (see Fig. 6.6). We note, for completeness, that no adjustment of the jet energy scale after back-
11 ground subtraction has been applied. Distortions of the jet energy scale due to the background
12 subtraction are included in Fig. 6.15. Based on these results, we expect the systematic errors in the
13 measurement of the jet spectrum to be sufficiently controlled that the spectrum can provide direct
14 sensitivity to collisional energy loss and large-angle radiative energy loss.

15 A summary of important performance variables, jet reconstruction efficiency, fake rate, and E_T
16 resolution, are listed in Table 6.2 for 70 GeV reconstructed seeded cone jets in three multiplicity
17 bins.
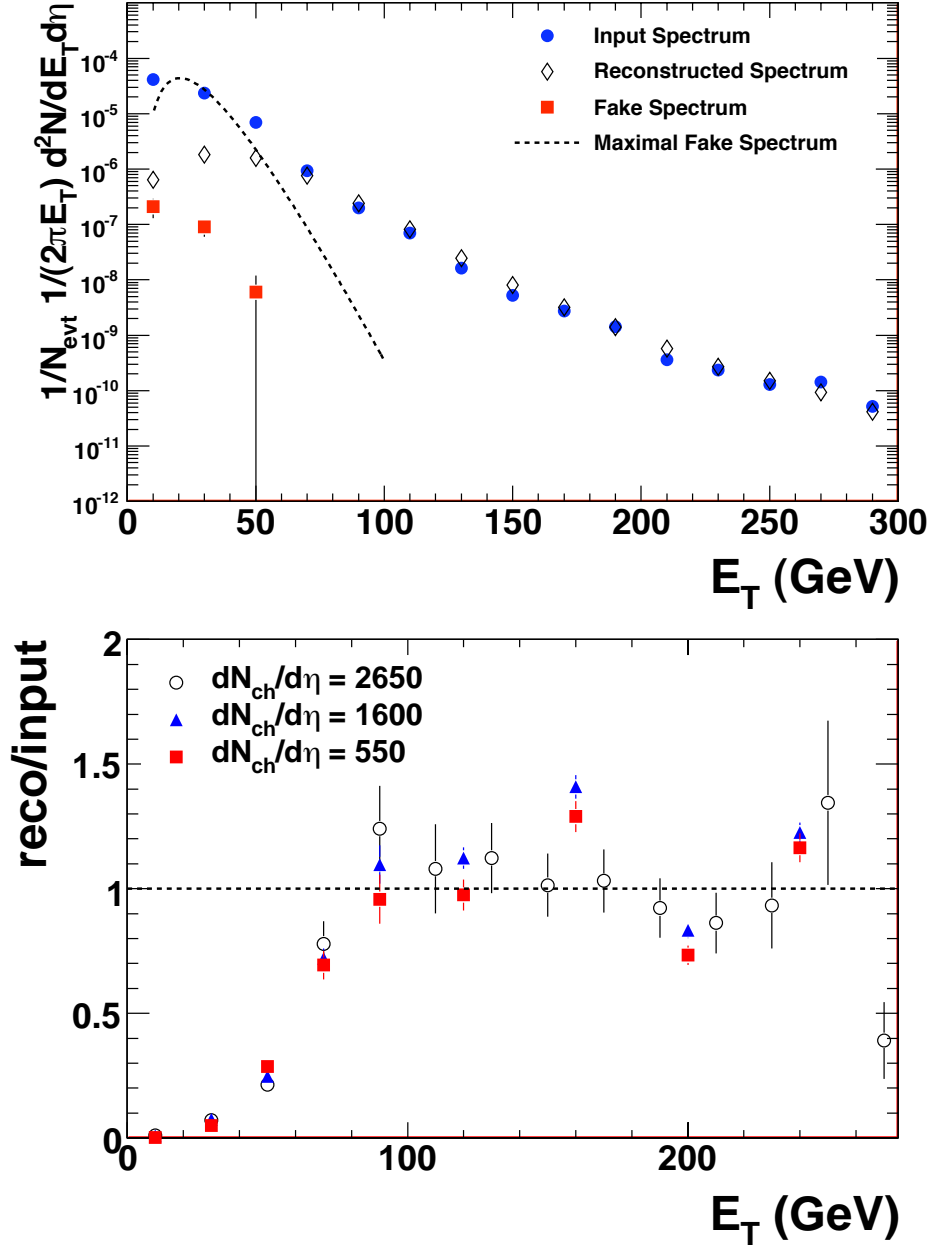
Figure 6.15: (top) Input (filled circles), raw reconstructed (diamonds), and fake (squares) spectra for cone jets in central ($dN_{ch}/d\eta$ = 2650) Pb+Pb collisions. The reconstructed spectrum is not corrected for efficiency or energy resolution. The dashed line represents the absolute fake jet rate from pure HIJING events prior to background jet rejection (see text for details). (bottom) Ratio of reconstructed to input jet spectrum for three different Pb+Pb collision centralities without efficiency and resolution corrections to the reconstructed spectra.

6.5   Jet Fragmentation

Full jet reconstruction provides new variables sensitive to in-medium energy loss that are currently not available at RHIC. The first of these is the transverse momentum of fragments with respect to the jet axis, j_T (see Fig. 6.5),

$$
\begin{aligned}
j_T &= |\hat{p}_{jet} \times \vec{p}_{frag}| \\
&\approx p_{T,frag} \sin R \quad ,
\end{aligned}
\tag{6.6}
$$

where $\hat{p}_{jet}$ is the jet direction, $\vec{p}_{frag}$ is the three momentum vector of the fragment, $p_{T,frag}$ is the particle transverse momentum with respect to the beam, $R = \sqrt{\Delta\phi^2 + \Delta\eta^2}$ is the jet cone variable, and the approximation is at mid-rapidity. The j_T distribution has a soft core governed by non-perturbative physics and a power law tail resulting from hard radiation of the parton shower. Jet in-medium energy loss is expected to modify the distribution of hard fragments associated with the jet and can be detected as a modification of the j_T distribution [28].

Another observable of interest is the modification of the jet fragmentation function. The fragmentation variable, z, is the longitudinal fraction of the jet momentum carried by the fragment (see Fig. 6.4),

$$
\begin{aligned}
z &= \frac{\hat{p}_{jet} \cdot \vec{p}_{frag}}{|\vec{p}_{jet}|} \\
&\approx p_{T,frag}/E_{T,jet} \cos R.
\end{aligned}
\tag{6.7}
$$

The interaction of the jet with the medium is expected to soften the fragmentation function by reducing the number of fragments at large z and increasing the number of fragments at small z (see Ref. [111] for a recent analysis).

The reconstructed fragmentation function, $D(z)$, and the j_T distribution are obtained using charged tracks reconstructed from the silicon detectors (Pixel and SCT) in the ATLAS Inner Detector (see Chapter 4). Fake stiff tracks are rejected by projecting the track into the middle layer of the electromagnetic calorimeter and requiring a p_T-dependent energy cut on the calorimeter tower to which the track points. If a track projects into a calorimeter tower which is part of a reconstructed jet, it is included in the inclusive distribution. Background distributions are constructed using tracks that match to HIJING particles[1]. These background distributions are subtracted from the inclusive distributions. The resulting distributions for charged tracks with $p_T > 2$ GeV matched to R=0.4 cone jets with $E_T > 70$ GeV in events with $dN_{ch}/d\eta$=2650 are shown in Fig. 6.16. A p_T-independent 70% tracking efficiency (see Fig. 4.2) correction is all that is applied. The open diamonds are the reconstructed distributions and they compare well to the input (PYTHIA) distributions in solid circles. The input distributions were constructed by including any charged primary particle with $p_T > 2$ GeV that is within an R=0.4 of a truth jet.

Despite not correcting for the jet position and energy resolution and scale, good agreement between the input and reconstructed fragmentation function is seen. However, differences between the reconstructed and input j_T distributions are observed at low and high j_T. This difference is a result of the position resolution of the reconstructed jet. To show this, jets were reconstructed

---

[1] This is a provisional strategy that obviously cannot be used on the real data. In the real experiment background distributions should be estimated using tracks outside the jet regions.
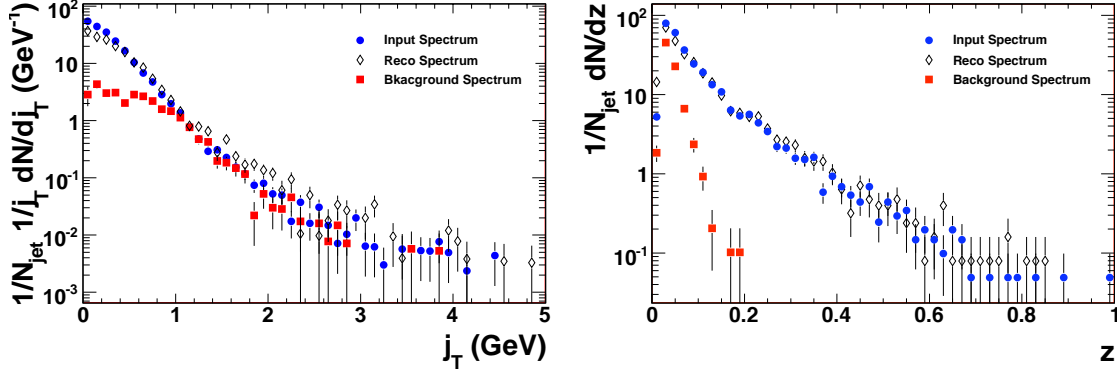
Figure 6.16: Reconstructed distribution (diamonds) of j_T (left) and z (right) for tracks with $p_T >$ 2 GeV matched to jets with $E_T > 70$ GeV after the subtraction of background distributions and after the correction on tracking efficiency (background distributions shown in red squares). They compare well to the input PYTHIA distributions (blue circles). The input jets were embedded in $dN_{ch}/d\eta$=2650 HIJING events.

with a cone radius R=0.2, which has an intrinsically better position resolution since background fluctuations in the tail of the jet are excluded. The jet positions reconstructed with R=0.2 were used with the tracks matching the R=0.4 cone jets. The resulting fragmentation function and j_T distribution are shown in Fig. 6.17. Good agreement is seen between the input and reconstructed j_T distribution.

To begin to test these variable's sensitivity to the effects of jet quenching, $D(z)$ and j_T distributions from PYTHIA and PYQUEN [120] **not** embedded in heavy ion events are reconstructed. PYQUEN was run for the most central collisions (b=0 fm) and the default parameters were used [2], which are estimates for LHC heavy ion beam energies. In the top panel of Fig. 6.18 one can see the comparison between distributions from the reconstructed events from PYQUEN and PYTHIA. As expected, the high-z (high-p_T) fragments are suppressed and the low-z fragments are enhanced. It is interesting to note that, contrary to other energy loss models [121], the high j_T fragments are suppressed as well. This could be due to the fact that PYQUEN quenches the radiated gluons as well. In any case, the quenching modifications observed for both distributions are much larger than difference between the input and reconstructed distributions. This is clearly visible from the comparison in the lower panels of Fig. 6.18. If jet quenching is as predicted by PYQUEN, ATLAS will have good sensitivity to measure energy loss effects using these distributions.

---

[2]initial temperature $T_0 = 1$ GeV, proper time of quark-gluon plasma formation $\tau_0 = 0.1$ fm/c, number of active quark flavors in quark-gluon plasma $n_f = 0$
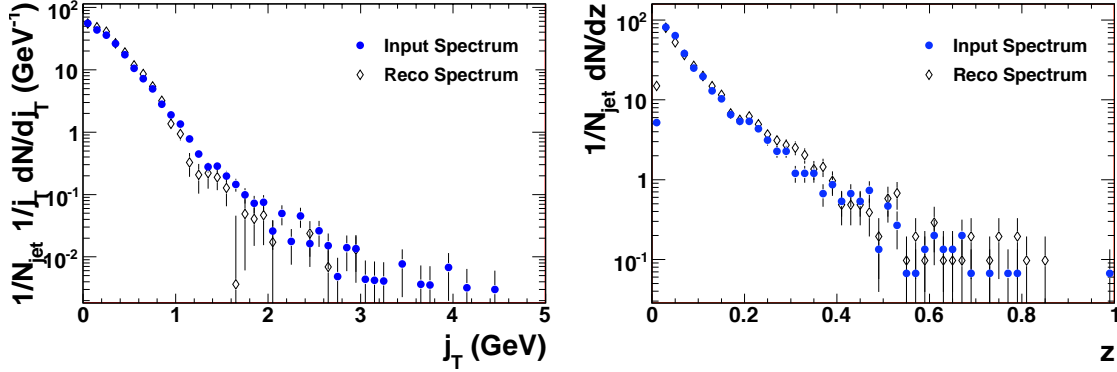
Figure 6.17: j_T (left) and z (right) distributions using the R=0.2 cone jet positions.

6.6 Jet shapes

A suitable variable to measure the jet energy flow within the jet is the jet shape. The integral and differential jet shapes are defined as

$$\Psi(r, R_{cone}) = \frac{\int_0^r E_T(\rho)\mathrm{d}\rho}{\int_0^{R_{cone}} E_T(\rho)\mathrm{d}\rho} \tag{6.8}$$

$$\psi(r, R_{cone}) = \frac{\mathrm{d}\Psi(r, R_{cone})}{\mathrm{d}r} \tag{6.9}$$

Such distributions are expected to be modified within the heavy ion environment [110].

Reconstructed jet shapes are constructed by summing calorimeter cells in an annulus at a distance r from the jet axis. The left panel of Fig. 6.19 shows the comparison between input PYTHIA jet shapes determined using primary generated particles and reconstructed jet shapes. The jets used are the same as previous sections: jets with $E_T > 70$ GeV and without any jet-level cuts, *i. e.* no efficiency, E_T scale or resolution, and position resolutions. The truth jets are much narrower than the calorimeter jets because of the segmentation of the calorimeter. To evaluate the accuracy of the measurement of jet shapes in the heavy ion collisions, jet shapes in the most central collisions ($dN_{ch}/d\eta = 2650$) are compared to those in peripheral collisions ($dN_{ch}/d\eta = 550$). From the right panel of Fig. 6.19 one can see that the jet shapes determined in the most central collisions are in a good agreement with jet shapes determined in the most peripheral collisions. The small underestimation of the energy at low r in the most central collisions is due to the jet position resolution.

To study the sensitivity of reconstructed jet shapes to quenching, PYQUEN is utilized. In Fig. 6.20 the differential and integral jet shapes computed for quenched (PYQUEN) and unquenched (PYTHIA) jets are presented at the generator and reconstruction level. The flow of the energy can be seen better from the differential jet shape. For quenched jets, the energy is transported from the center of the jet ($\psi_{PYQUEN}(r = 0) < \psi_{PYTHIA}(r = 0)$) to the jet periphery($\psi_{PYQUEN}(r \sim R) > \psi_{PYTHIA}(r \sim R)$). The upper plots of the Fig. 6.20 compare generated quenched and unquenched events. The lower plots then compare the situation after the GEANT simulation and reconstruction. One can see that differences between quenched and unqueched jets are visible including the
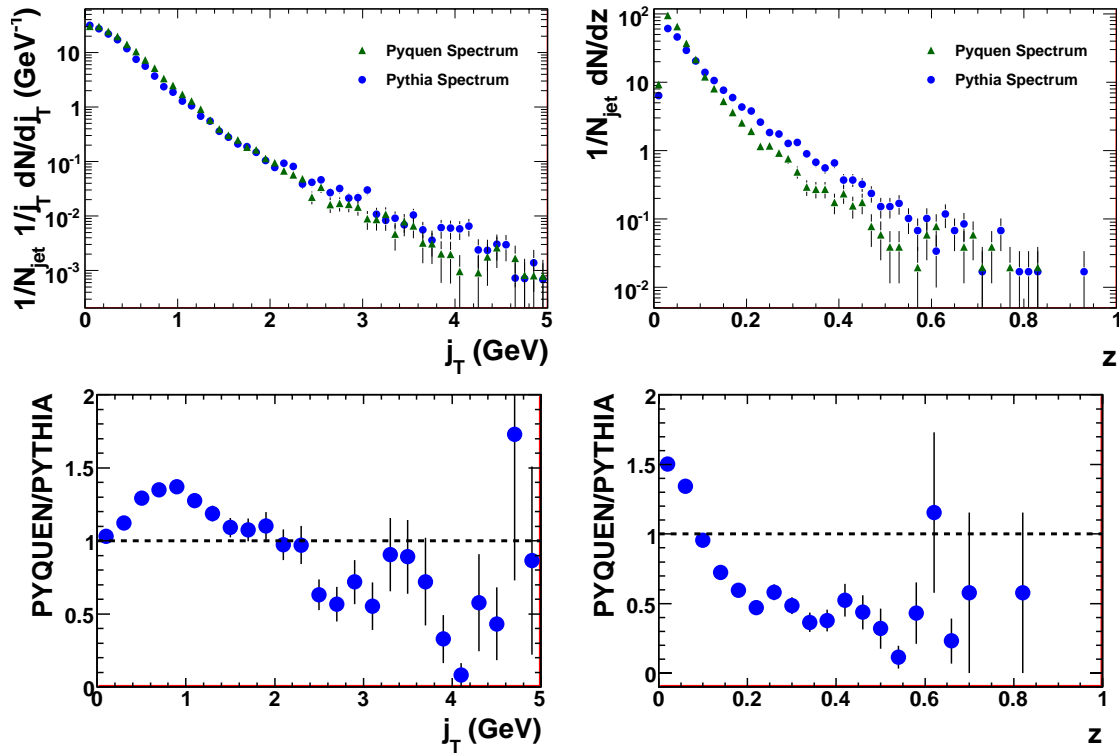
78

Figure 6.18: (upper) Reconstructed PYQUEN and PYTHIA j_T (left) and z (right) distributions. (lower) PYQUEN to PYTHIA ratio for reconstructed events.

detector response.

6.7 Di-jet correlations

The large η acceptance of the ATLAS calorimeter system provides nearly complete acceptance for di-jets making possible a variety of correlation measurements. Primary partons traversing the medium are also expected to multiple scatter off other partons in the medium as a consequence of energy loss [33]. Therefore, angular correlations between the back-to-back di-jets should be broadened in central Pb+Pb collisions relative to p+p collisions [27]. The left panel of Fig. 6.21 shows the conditional yield of detecting a second, associated jet (B) given a leading jet (A) as a function of their relative azimuth, $|\Delta\phi|$ in central Pb+Pb collisions. This study uses the same set of jets as in previous sections: seeded cone jets with $E_T > 70$ GeV and no efficiency and energy resolution corrections are applied. The same set of PYTHIA jets are embedded in another set of HIJING events with an addtional $Q^2 < 100$ GeV^2 cut to remove mini-jet production which reduces the correlated underlying event background and therefore fake jet rate. The distributions show a clear peak at $|\Delta\phi| = \pi$, indicating the back-to-back emission of di-jets, and very little background at other $|\Delta\phi|$. Integrating the distribution gives a 60% probability for detecting a jet with $E_T > 70$ GeV that is associated with a leading jet with $E_T > 100$ GeV. This high coincidence
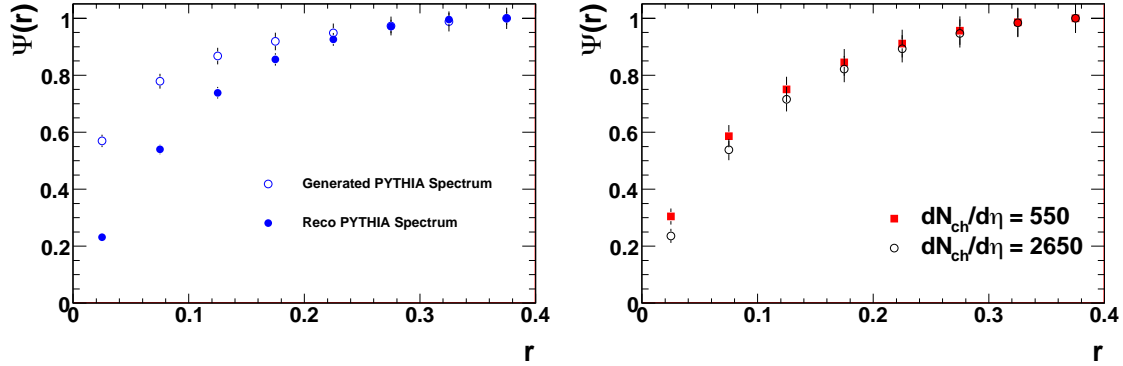
Figure 6.19: (left) Integral jet shape for reconstructed (closed) vs. input (open) p+p events. (right) Integral jet shape reconstructed in the most central collisions (open circles) vs. jet shape reconstructed in the most peripheral collisions (red squares).

rate is due to the large detector acceptance and accurate measurements for single jets.

A more sensitive probe of multiple scattering might be the p_{out} distribution which measures the momentum acoplanarity of the associated jet compared to the leading jet. The variable p_{out} is defined as

$$p_{out} = E_T^B \sin R. \tag{6.10}$$

where R is the angle between the jets. The distribution is shown in the right panel of Fig. 6.21.

These distributions are of interest because of their possible in-medium modifications. If energy loss is due to gluon bremsstrahlung, the parton will multiple-scatter through the medium. The multiple-scattering will manifest itself as broadening of the di-jet $\Delta\phi$ and p_{out} distributions compared to p+p collisions [33].

6.8 Medium Response

At RHIC, the studies of the medium response to jet energy loss are important tools to understand properties of the produced medium. In principle, such studies can also be explored with ATLAS. However, ATLAS's abilities for measuring medium response are difficult to quantify as there is no consensus on the mechanism of medium response, and thus no model implementations of this effect exist that could be used to generate LHC events. Still, if a ridge exists and is associated with a high-E_T jet and extends to ±4 units in $\Delta\eta$, the ATLAS calorimeter, covering $|\eta| < 5$, will certainly encompass the entire ridge. Furthermore, a possible Mach cone and ridge associated with di-jets can be studied on an event-by-event basis as opposed to statistically averaging over many events as has been done at RHIC.

It will be important to establish that the Mach cone or ridge is associated with jet production. Therefore, one possible way to measure these structures is to trigger on a fully reconstructed (high-p_T) jet and to correlate neutral clusters and/or charged hadrons both in the same hemishpere (in azimuth) as the jet and in the opposite hemisphere of the jet. If the a Mach cone is observed, then the Mach angle, and therefore the speed of sound of the medium, could be extracted from these
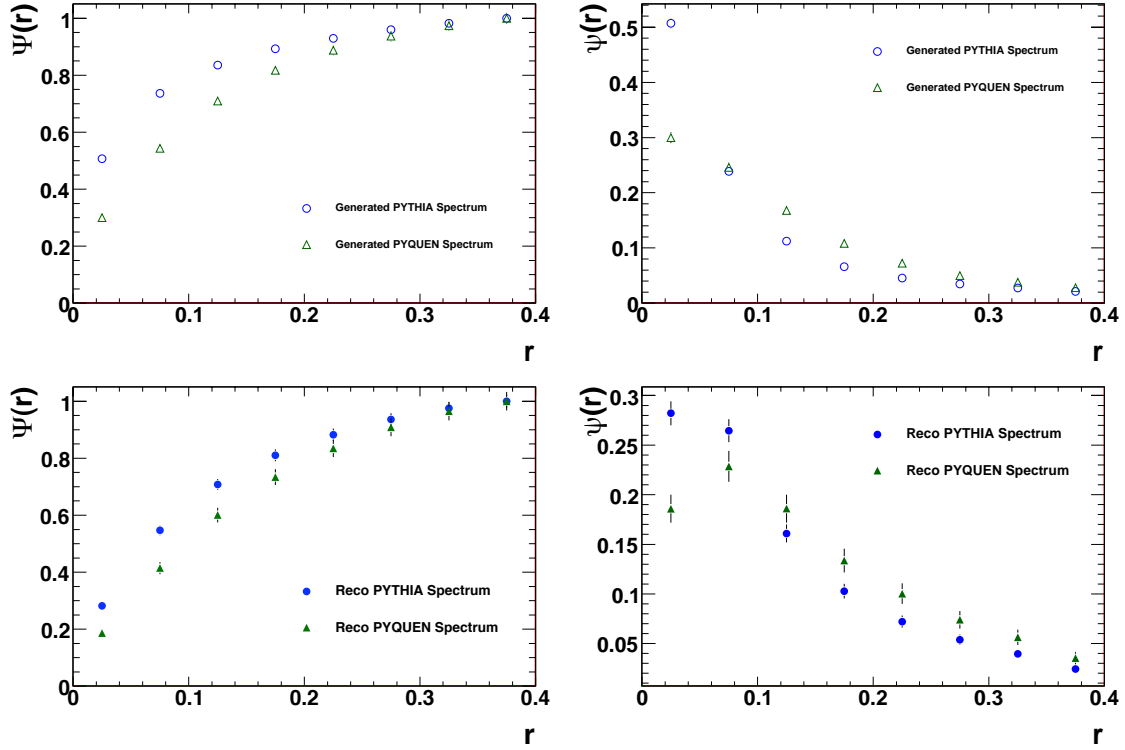
Figure 6.20: Integral and differential jet shape for PYQUEN (closed) and PYTHIA (open) generated (upper) and reconstructed (lower) events.
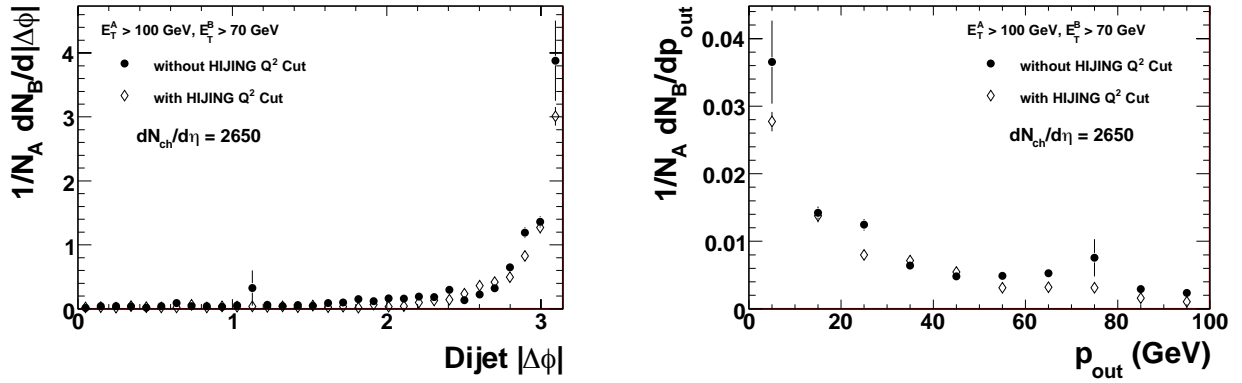

Figure 6.21: Conditional yield for finding an associated jet above 70 GeV (B) given a leading jet above 100 GeV (A), plotted as a function of (left) di-jet $|\Delta\phi|$ and (right) p_{out} (see Eqn. 6.10).

correlations.

6.9 Heavy quark jet reconstruction

To understand heavy quark energy loss, it will be important to identify bottom and charm jets. Fortunately, the excellent jet reconstruction capability of the ATLAS detector and excellent capabilities for tagging heavy quark mesons and associated semi-leptonic decay muons make the direct study of the heavy-quark energy loss feasible. Once the high energy jets are reconstructed, two tagging methods can be applied to identify the flavor of the reconstructed jets: 1) tagging charm and bottom mesons directly via their displaced decay vertices and associating these heavy mesons to reconstructed jets; 2) associating semi-leptonic decay muons directly to reconstructed jets. A first attempt of the latter approach is described in this section.

At leading order, most of the muon-tagged jets come from hard-scattering processes that lead to di-jet events. The reconstructed jet and muon could either belong to the same truth jet, or they belong to different jets of the di-jet. Indeed, due to the weak decay of light hadrons in flight, a portion of the muons may not be associated with heavy quark jets. In addition, only a fraction of the heavy quark jets contribute to high p_T muons via the semi-leptonic decay of heavy quark mesons. Based on these considerations, the performance of muon tagging for heavy quark jets has been quantified by the two most important parameters. The first parameter is the purity of heavy quark jets in the tagged jet sample, and the second parameter is the tagging efficiency for jets that are known to come from heavy quarks.

To estimate the purity of heavy quark jets in the tagged jet sample, PYTHIA minimum bias events were generated with the requirement that each event contains at least one muon with $p_T > 5$ GeV and one jet with $E_T > 35$ GeV. The resulting events were then embedded into central HIJING Pb+Pb events ($dN_{ch}/d\eta = 2650$ at mid-rapidity) generated as described in Section 6.4.1. The jets were reconstructed with the seeded cone jet algorithm. Single muon candidates were reconstructed using the standard tracking and muon identification software in ATLAS [122]. Details of the muon reconstruction are given in Chapter 7.

The purity of heavy quark jets in the tagged jet sample is defined as the ratio of the number of jets of interest, *i.e.* those from heavy quarks, and the total number of jets. To identify the heavy quark jets, the jets reconstructed from the merged event are first matched to the truth jets, which are obtained by applying the seeded cone algorithm to the final state particles in the input PYTHIA event. The matching criterion that requires the three-dimensional opening angle, θ, between the reconstructed and truth jet momentum vectors is smaller than to satisfy 0.2 rad. Input (truth) jets are tagged as bottom jets by tracing the PYTHIA ancestry information back to the original string. If it is a bottom string and the truth jet in question has more than 50% of the bottom quark energy, the truth jet is considered to be a bottom jet. Otherwise, the truth jet, and hence the matched reconstructed jet, is either a charm jet or light quark jet.

The purities of the muon-tagged jets are shown in the left panel of Fig. 6.22 as a function of the azimuthal angle difference between the muon and tagged jet. The red circles show the bottom-tagged purity; about 40% of the tagged jets come from bottom quarks. The blue squares show that the heavy flavor-tagged purity is about 70%. This suggests 30% of the tagged jets come from charm quarks and remaining 30% of the tagged jets come from light quarks and gluons. To summarize, the jets tagged by muon with $p_T > 5$ GeV contains approximately equal number of bottom, charm and light quark/gluon jets.

The purity of heavy quark jets in the tagged jet sample also depends strongly on the trigger muon p_T. This is shown on the right panel of Fig. 6.22. The red circles are bottom-tagged purity
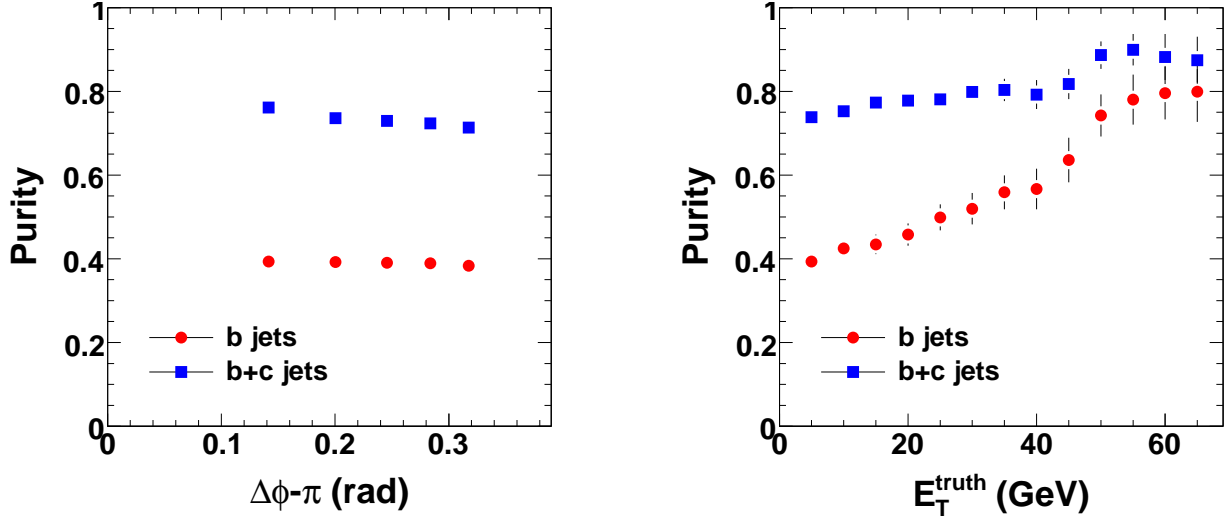
Figure 6.22: Bottom jet (red circles) and heavy flavor (blue squares) tagging purity as a function of azimuthal angle difference between the tagged jet and muon at the away-side ($\Delta\phi \sim \pi$) requiring a muon with $p_T > 5$ GeV (left) and as a function of truth muon E_T (right).

and the blue squares show the heavy flavor-tagged purity. For muons at $p_T > 60$ GeV, approximately 80% of all tagged jets are bottom-jets.

Further improvement is possible if we consider the correlation between muon p_T and jet E_T. Since heavy quark jets have much harder fragmentation functions, *i.e.* the leading heavy meson contributing to the muon carries most of the energy of the jets, the muon p_T and jet p_T should be much closer to each other than for muons from light hadron decays. Thus a high E_T jet correlated with a low p_T muon is more likely a gluon or light quark jet.

The minimum bias PYTHIA events used for the purity study contain a limited number of bottom jets. For an accurate estimation of the tagging efficiency for bottom jets at ATLAS, a separate set of PYTHIA events containing bottom jets was generated, requiring at least one muon with $p_T > 5$ GeV, and at least one jet with $E_T > 35$ GeV. These events were embedded into central ($dN_{ch}/d\eta = 2650$) HIJING Pb+Pb events, and analyzed using the same procedure applied to minimum-bias PYTHIA events. The same criteria for matching the reconstructed jets with truth bottom jets are applied. Figure 6.23 shows the azimuthal correlation between reconstructed jets ($E_T > 35$ GeV) and muons ($p_T > 5$ GeV) for the bottom (blue) and non-bottom (red) jet samples. The muons either come directly from the tagged bottom jet themselves (peak around $\Delta\phi \sim 0$), or they corresponds to muons from a bottom jet recoiling from another bottom jet (peak around $\Delta\phi \sim \pi$). For the non-bottom jet sample, fewer jets are measured, however a correlation with muons is still observed.

The narrow azimuthal correlation between the tagged jets and the muon can be used to improve the purity of the bottom jets by making a matching cut in $\Delta\phi$. The tagging efficiency is defined as the probability for a bottom jet to be within the matching cut. The efficiency for tagging the bottom jet with the muon is shown in the right panel of Fig. 6.23. A cut of 0.16 rad gives a 70% tagging efficiency while relaxing the cut to 0.32 rad gives an efficiency of 80%.

Using high-p_T muons to tag heavy flavor jets will be an important tool in studying the heavy
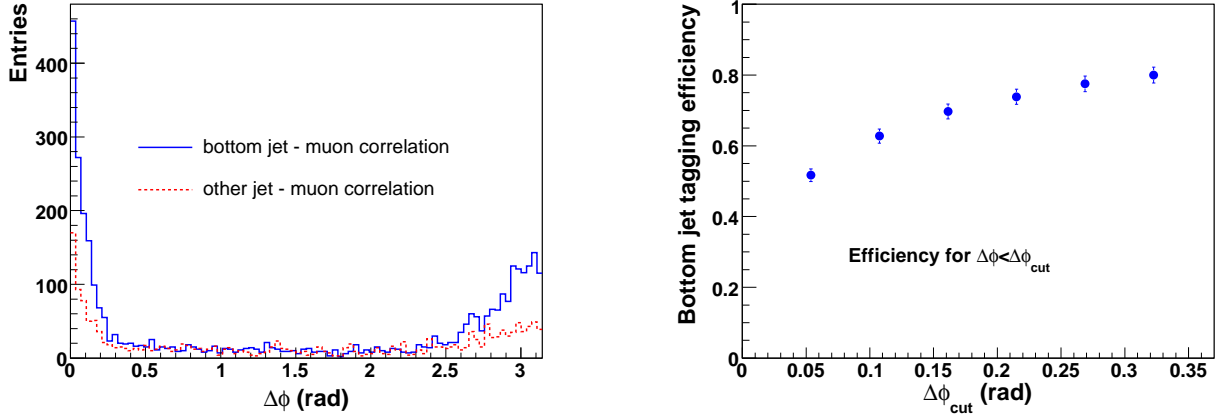
Figure 6.23: (left) Azimuthal correlation between the reconstructed jets and the muons. The solid line and dashed line are for tagged bottom jets and other jets, respectively. (right) Jet tagging efficiency as a function of angular cuts ($\Delta\phi < \Delta\phi_{cut}$).

flavor energy loss. A clear correlation in muon-jet $\Delta\phi$ is observed from heavy flavor jets. By cutting on this muon-jet $\Delta\phi$ and the muon p_T it is possible to tune the purity of the heavy flavor sample and the tagging efficiency.

6.10 Jet Triggering

The full details of triggering on jets is given in Chapter 9. However, it is necessary to give some words on the effects of the trigger on the performance outlined in this chapter. Generally, triggering on jets requires the calorimeteric energy in some region to be above a predefined threshold. This is the case in ATLAS as well. Such a jet trigger is unavoidably complicated by the physics of heavy ion collisions. First, there are fluctuations in the underlying event which produce false positive signals which can add to the bandwidth. Second, the modification of the jets because of energy loss have yet unknown effects on the energy distribution within those jets. Such modifications may make triggering using a simple threshold biased towards those jets which lose little energy. The overall strategy will be to first obtain a list of jets through the trigger, evaluate any biases that exist, and refine the trigger thresholds and strategy.

ATLAS employs a three-level trigger. Level-1 identifies "regions of interest" (ROI) that will be subsequently analyzed in later stages of the trigger. Because the bandwidth out of the level 1 trigger is about a factor of 10 below the expected Pb+Pb minimum bias collisions rate, no rejection is necessary at Level-1. At Level-2, the ROIs are analyzed and further criteria are applied to obtain a rejection. A cone algorithm with a maximum of 3 iterations is used for jet reconstruction of the 0.4x0.4 (in $\Delta\eta \times \Delta\phi$) ROI. At this stage, background subtraction, based on the total event E_T information from the Level-1 Missing E_T trigger, will be performed. The third level of triggering, the event filter, will perform the full offline-like reconstruction of the complete event to make the final rejection on events.

Since an ROI from Level-1 is necessary despite no requirement of rejection, a set of jet thresholds must be defined. These thresholds must result in a low fake rate and high efficiency for jets.

The severest limit on the threshold is the requirement that no more than 32 ROI be in the event. If there are more than 32, the readout of the ROIs are truncated. The first attempt at evaluating the appropriate threshold and its effect on the jet trigger efficiency can be seen in Figure 9.4. In the higher levels of triggering, techniques that were outlined in this chapter will be used to reconstruct jets. We can expect that the efficiency for triggering on jets will be similar to that of the cone jet reconstruction (see Figure 6.12). In fact, the similarity between this and the Level-1 jet reconstruction efficiency in Figure 9.4 are similar especially for more peripheral collisions.

The potential biases from triggering will be evaluated by comparing samples of jets from minimum bias and triggered events. This comparision will not only yield valuable information on the physics of jet energy loss but also provide the data on which to base a more appropriate trigger for jets in heavy ion collisions.

6.11   Summary

- Utilizing the large acceptance, finely-segmented ATLAS calorimeter, jets in a heavy ion environment can be measured with high efficiency and excellent position/energy resolution over a broad range in energy ($E_T > 40$ GeV), pseudo-rapidity (± 5) and multiplicities (at least up to $dN_{ch}/d\eta = 2650$). These unprecedented reconstruction capabilities for full jets will significantly reduce the energy-loss biases intrinsic in leading hadron and di-hadron correlation analyses at RHIC.

- The full jet and di-jet measurements possible with the ATLAS detector will provide direct constraints on the mechanisms for energy loss and jet-medium interactions. In particular, the jet fragmentation (via $D(z)$) and the jet shape (via the j_T distribution, $\psi(r)$, di-jet $\Delta\phi$ and p_{out}) can be reliably quantified. These measurements are sensitive to jet energy loss and medium response.

- Combining the jet reconstruction with the muon identification capability of the ATLAS detector allows the study of heavy quark energy loss, which will be of particular use to quantify the role of radiative and collisional energy loss.

- Full jet reconstruction combined with the direct photon capability of the ATLAS calorimeter (described in detail in the Chapter 8) provides a means to probe the properties of the medium using γ-jet correlations.

- All of the measurables described here will be studied as a function of global variables, such as centrality and the angle with respect to the reaction plane.

- In tandem, these techniques will allow ATLAS to undertake a comprehensive program of tomographic studies of the energy loss and the properties of the medium produced in Pb+Pb collisions at the LHC.

Chapter 7

Quarkonia and Z Measurements

This Chapter describes the physics importance of quarkonia and Z measurements in Pb+Pb collisions at the LHC, and the ATLAS capabilities for performing these measurements.

7.1 Physics motivation

The measurement of quarkonia production in heavy ion collisions provides a powerful tool for studying the properties of hot and dense matter created in such collisions. If this matter is deconfined, color screening prevents various quarkonia states from being formed when the color screening length becomes smaller than the quarkonium size [123]. Since the color screening length is related to the temperature of the matter created in heavy ion collisions, one can use the observation of suppression of different quarkonia states as a thermometer. Thus, it is important to measure simultaneously different quarkonia states, since they are predicted to dissociate at different temperatures [124, 125, 35]. Ref. [35] in particular makes predictions for six separate states based on a potential model fit to lattice calculation data, as shown in Table 7.1:

State	χ_c	ψ'	J/ψ	Y'	χ_b	Y
T_{dis}	$\leq T_c$	$\leq T_c$	$1.2T_c$	$1.2T_c$	$1.3T_c$	$2T_c$

Table 7.1: Predictions for quarkonia dissociation temperatures, where T_c denotes the critical temparature, from Ref. [35]
.

The suppression of quarkonia due to Debye screening was expected to be the platinum signature of the production of a Quark-Gluon Plasma in relativistic heavy ion collisions. However, the quantitative agreement between J/ψ suppression measured by the NA50 experiment at CERN [126, 127], and the PHENIX collaboration at RHIC [128] cannot currently be understood simply by Debye screening. Recent results from the PHENIX experiment are shown in Fig. 7.1, along with NA50 and NA60 data from SPS. The exact interpretation of both results is still being debated, and information about other quarkonia states is necessary in order to clarify the situation. At the LHC, the higher collision energy and luminosity will allow the study of the Y family in addition to charmonium states. As a result, it will be possible to measure a much wider variety
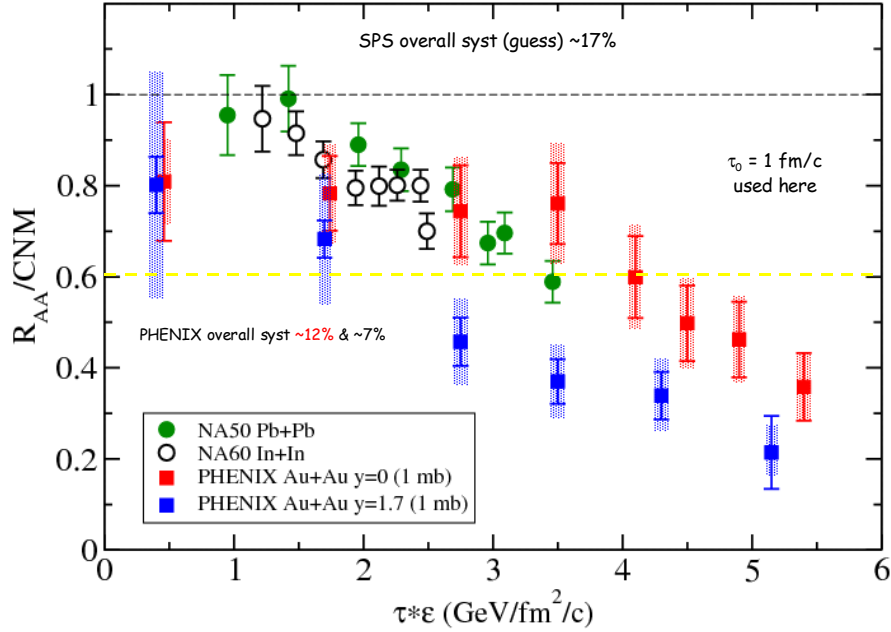
Figure 7.1: $J/\psi\ R_{AA}/CNM$ vs. $\tau\varepsilon$ in A+A collisions, where CNM is the cold nuclear matter suppression. PHENIX Au+Au measurements for mid (forward) rapidity data are shown with red (blue) squares [128]. NA50 Pb+Pb [129] and NA60 In+In results [130] are shown by green and open black circles, respectively.

1   of bottom (*b*) and charm (*c*) quarkonia states with different binding energies and thus different
2   expected dissociation temperatures.
3   Z bosons will be copiously produced at the LHC, and can serve as an important test of the
4   standard model, and as also a useful probe for understanding properties of the hot and dense
5   nuclear matter created in high energy heavy ion collisions. In p+p collisions, the measurement of
6   production cross sections multiplied by the leptonic branching fractions for Z and W bosons can be
7   used for precise determinations of several Standard Model (SM) parameters, and places stringent
8   constraints on manifestations of Beyond the Standard Model (BSM) physics. As an example, the
9   precise determination of the total widths of the Z and W bosons provides an important test of
10 the standard model because these widths are sensitive to new (and possibly undetected) decay
11 modes. Both W and Z production and their subsequent decays provides stringent tests of QCD.
12 Calculations of higher-order corrections to the simple, color-singlet final states of W and Z decays
13 is very advanced, with a residual theoretical uncertainty smaller than 1% [131].
14   The rapidity distribution (*dN/dy*) of Z's is considered to be a precision test of our knowledge
15 of parton distribution functions (PDF) [132, 133]. As such, Z's are especially important at the LHC
16 because, at least in early runs, there will be no p+A or d+A collisions, which are typically seen
17 as very useful for understanding so-called "cold nuclear matter effects". Z's are rather straight-
18 forward to observe in Pb+Pb collisions via the di-muon decay channel (BR=3.366 +- 0.007%), and
19 possibly the di-electron channel. In these leptonic modes, the Z decay products interact only

weakly with the surrounding matter, and thus leave the interaction zone without rescattering. This allows Z's to be a tool to study PDF modification in nuclear matter, as well as other initial state effects.

The Z is also a useful probe for understanding properties of hot and dense nuclear matter created in high energy heavy ion collisions. The production of Z bosons in association with jets is also an important signal, and a useful complimentary measurement for jet-jet and photon-jet studies. Z-jet correlations were measured at Tevatron (see e.g. [134, 135, 136]). In heavy ion collisions such correlations can provide valuable information about jet modification in hot and dense nuclear matter created in high energy heavy ion collisions, since Z bosons and its decay muons are transparent to strong interactions.

Finally, from the experimental perspective, precise measuremens of the properties of the Z boson provide strong constraints on the detector performance. Its mass, width and leptonic decays can be exploited to measure the energy and momentum scale, its resolution, and the lepton identification efficiency very precisely.

In this Chapter, we present the capabilities of ATLAS for measuring the Υ and J/ψ quarkonia families via di-muon decays in heavy ion collisions. The simulation results for expected acceptance, reconstruction efficiency, mass resolution, rates and background estimates for Υ and J/ψ states in Pb+Pb collisions at LHC are shown. Studies of Z boson decays in the di-muon channel in Pb+Pb collisions are also described, and the results on the mass resolution, expected acceptance, efficiency and rates are presented. In addition, the prospects for studying quarkonia and Z bosons via their di-electron decay channel are outlined.

7.2 $\Upsilon \rightarrow \mu^+\mu^-$ measurements

7.2.1 Υ mass resolution

In order to study the Υ mass resolution, 50000 single Υ's were generated, simulated, and reconstructed with Athena 12.0.3 and default cuts. A sub-sample of these, constituting 5000 Υ's, were then merged into simulated central ($b = 2$ fm, $dN_{ch}/d\eta = 2650$) Pb+Pb HIJING events in order to study how the Υ mass resolution ($\sigma(\Upsilon)$) is affected by the high multiplicity environment of heavy ion collisions. These resolutions were obtained from fits in the 9.2-9.8 GeV mass region. The Υ mass resolution in Pb+Pb collisions as a function of Upsilon η and p_T is shown in Fig. 7.2 and Fig. 7.3, respectively. For comparison, in Fig. 7.2, the mass resolution is displayed also for single Υ's. There is no significant deterioration of mass resolution in central Pb+Pb collisions compared to single Υ's, similarly as was observed in the earlier analysis [137]. The best mass resolution is achieved in the barrel region ($|\eta| < 1$), and is approximately 120 MeV, whereas there is essentially no dependence of $\sigma(\Upsilon)$ on p_T, which can be expected on kinematic grounds, due to the large Υ mass.

7.2.2 Υ reconstruction efficiency

6000 single Υ's merged with PYTHIA p+p events were used as a baseline for this study. To study the degradation of reconstruction efficiency in Pb+Pb collisions, single Υ's were merged also with 3000 mid-central ($b = 6$ fm, $dN_{ch}/d\eta = 1600$) HIJING events. The product of acceptance and reconstruction efficiency, $A\varepsilon$, in central ($b = 2$ fm) Pb+Pb collisions has been studied as a function
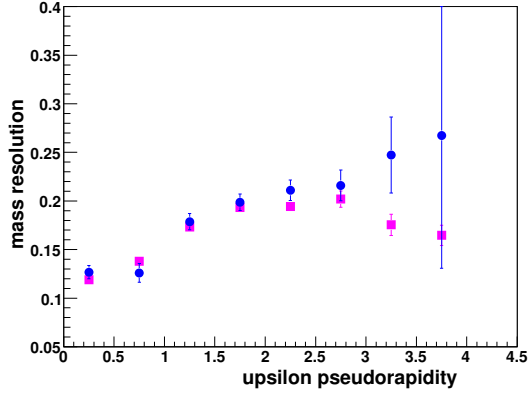
Figure 7.2: Y mass resolution in central Pb+Pb collisions as a function of η (blue circles). For comparison, mass resolution for single Y is shown by magenta squares. Error bars show statistical errors only.
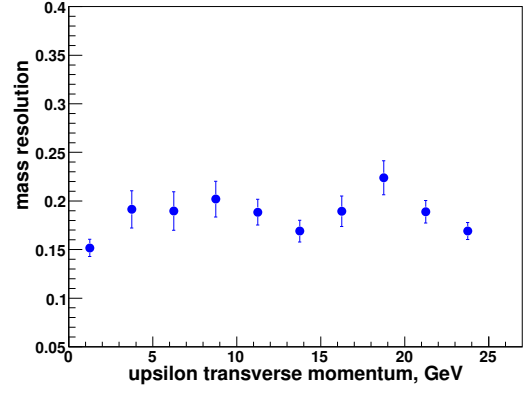

Figure 7.3: Y mass resolution in central Pb+Pb collisions as a function of p_T. Error bars show statistical errors only.
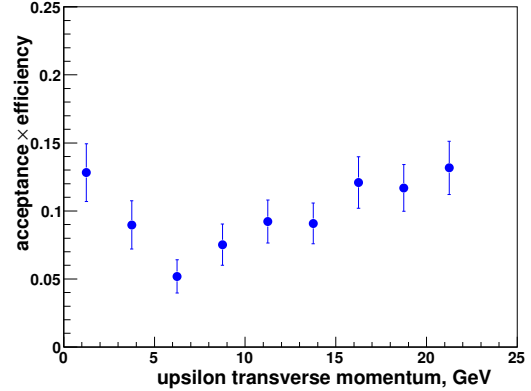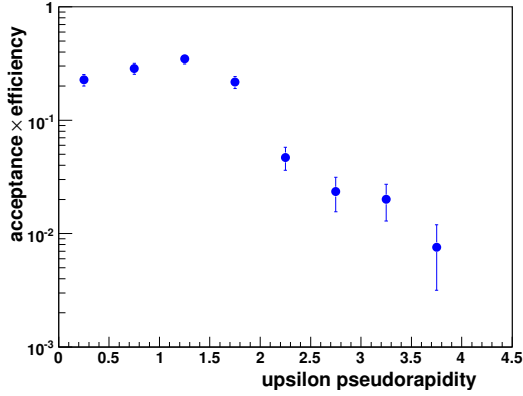

Figure 7.4: Y acceptance times efficiency as a function of $|\eta|$ (left) and p_T (right) for central (b=2 fm) Pb+Pb collisions. Error bars show statistical errors only.

1 of η and p_T (Fig. 7.4). The value of $A\epsilon$ integrated over p_T and η for these events is 10.5% $\pm$ 0.1%.
2 For comparison, $A\epsilon$ integrated over p_T and η in p+p collisions is 12.3% $\pm$ 0.1%. Thus, the efficiency
3 in central Pb+Pb relative to pp collisions is $\approx$ 85%. In mid-central ($b = 6$ fm) Pb+Pb collisions the
4 integrated $A\varepsilon$ is 10.8% $\pm$ 0.1%. These results agree with those obtained from the previous analysis
5 using different cuts and samples [137].

6   Figure 7.4 (left) shows that, due to their large mass, Y's can be reconstructed out to $|\eta| \approx 4$,
7 even outside of the nominal spectrometer acceptance of $|\eta| < 2.7$. However, for $\eta > 2$ the Y
8 acceptance drops quickly, falling below 1% for $|\eta| > 3.5$. Figure 7.4 (right) shows that there is a
9 relatively weak dependence of $A\varepsilon$ on the Y transverse momentum.

7.2.3 Expected Υ rates and backgrounds

Backgrounds and expected Υ yields were estimated using PYTHIA. In order to make predictions for Pb+Pb collisions, it is assumed that the number of both high-p_T muons and Υ's scales with the number of binary collisions N_{coll}, while the backgrounds are assumed to scale as the square root of the signal yield. The number of binary collisions (N_{coll}) was taken from a Glauber calculation [138]. For minimum bias collisions the predicted value of N_{coll} is 400, while for the 10% most central collisions $N_{coll} = 1670$.

Various sources of background muons include: 1) muons from open charm and beauty decays, 2) muons from hadron in-flight decays before absorption in the calorimeter, and 3) punch-through hadrons which can be reconstructed as muons. The main source of 2) and 3) are pions and kaons.

In order to estimate contributions from heavy quark decays, PYTHIA predictions of decay muon spectral shapes were used, with cross-sections calculated in [27]. In order to estimate the contribution from charged light meson decays and punch-through hadrons, single pions and kaons were propagated through the full generation, simulation, and reconstruction chain in Athena. Reconstructed muons from these single π and K events were then used to calculate p_T and η spectral shapes for background muons coming from hadron decays and punch-through hadrons, with multiplicities normalized using cross-sections listed in [27]. To imitate background in Pb+Pb collisions, all multiplicities were scaled with the number of binary collisions, and then combined with appropriately-scaled Υ's, and run together through the full simulation chain.

The expected di-muon invariant mass distribution as obtained from this Monte Carlo study is shown in Fig. 7.5. The statistical errors correspond to a conservative 0.5 nb^{-1} integrated Pb+Pb luminosity and a 100% efficient muon trigger. It is observed that the signal-to-background ratio is close to 1. This plot includes acceptance and efficiency corrections and was plotted with muons from the barrel region only ($|\eta| < 1$). The average Υ mass resolution in this region is 120 MeV, and about 4 k Υ are expected to be reconstructed. As one can see, the Υ and Υ' states can be clearly separated. However, the extraction of a separate Υ'' yield is more challenging.

In addition to the standard selection of fully reconstructed muons in the Inner Detector and in the Muon Spectrometer, a looser selection allowing one of the muons of the pair to be tagged has been used [137]. The tagging strategy recovers low p_T muons as a track segment in two of the three muon stations. For this study 30000 $\Upsilon \rightarrow \mu^+\mu^-$ were generated with PYTHIA and processed with Athena, release 14.2.23. This release includes a more recent version of the tracking as well as tagging tools. Figure 7.6 shows the transverse momentum and rapidity distributions dN/dp_T and dN/dy of the $\Upsilon \rightarrow \mu^+\mu^-$. The generated distributions are in full black, whereas the reconstructed distributions are in dotted blue for the standard and in dashed red for the tagged muon strategies. Switching from Athena release 12 to release 14, the overall acceptance and reconstruction efficiency with the standard selection increases from 12.8% to 17.2%, largely due to the use of the NewT package instead of xKalman for the reconstruction in the Inner Detector. The improvement factor due to tagging is 35%, the acceptance and reconstruction efficiency increasing from 17.2% to 23.2%, which corresponds to 35k $\Upsilon \rightarrow \mu^+\mu^-$ events expected in one month of 0.5 nb^{-1} of integrated luminosity of Pb+Pb running. The rate improvement is more important in case of charmonium measurements, as it will be shown later. Note that restricting tagging to muons with $|\eta| < 2$ has only a small effect on the overall mass resolution.
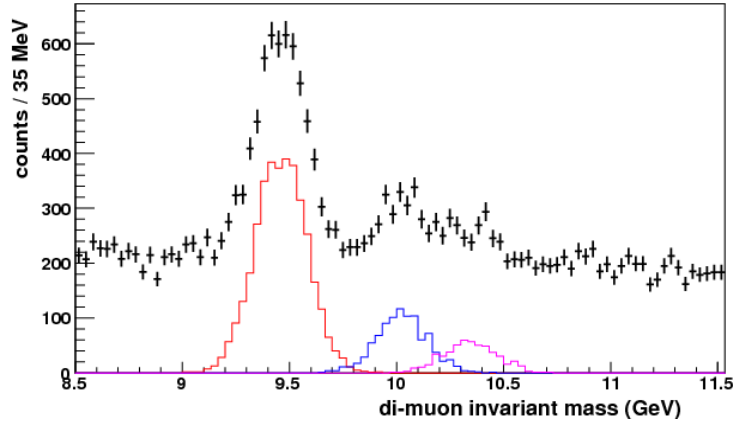
Figure 7.5: Di-muon invariant mass distribution as expected for one month of data, taking into account acceptance and efficiency, for decay muons in the barrel region only ($|\eta| < 1$). Error bars show statistical errors only. Solid color histograms represent expected yields from the three Y states, and black crosses show the sum of signal and background.

Figure 7.6: dN/dp_T (left) and dN/dy (right) distributions for $Y \rightarrow \mu^+\mu^-$ (color online). The generated distributions are in full black, the reconstructed distributions are in dotted blue for the standard selection with a muon-p_T >3 GeV, and in dashed red for the tagged muon selection with a muon-p_T >3 GeV.

7.3 Charmonium measurements
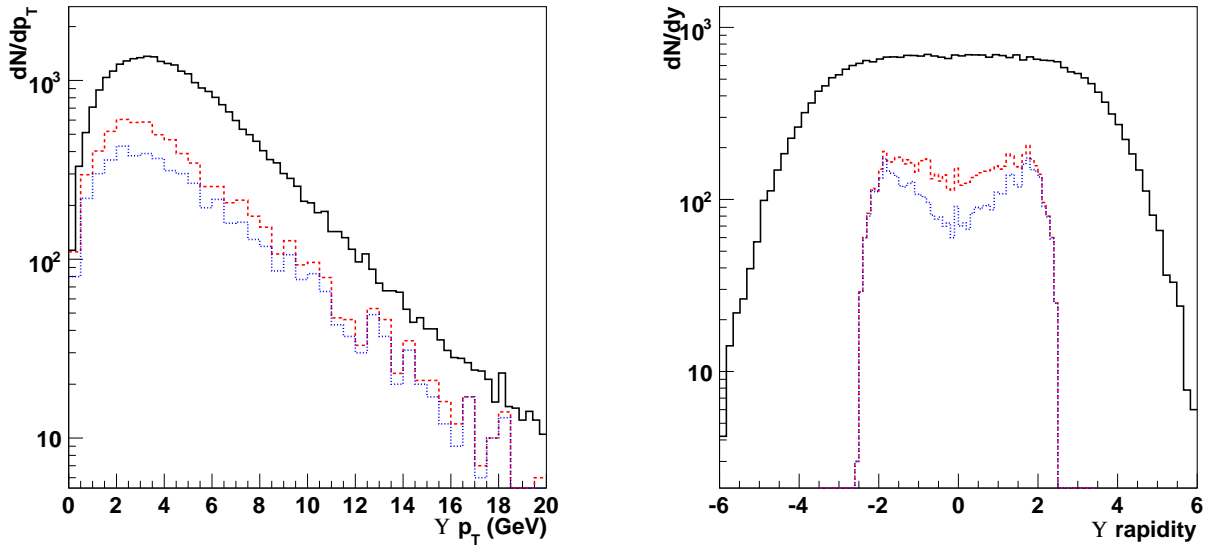
In addition to the Y family, it is important to measure charmonium states, in particular the J/ψ and ψ'. This measurement will give us additional valuable information about quarkonia color screening, and will provide a direct connection to lower energy RHIC and SPS data.

A basic difference in the experimental study of Y and J/ψ production is that, because of its mass, the Y can be measured over its full p_T spectrum starting at p_T=0, even at low η. Indeed, even if the Y is produced at rest, the decay muons have in general enough energy to traverse the calorimeters and reach the Muon Spectrometer. The situation is different for muons from J/ψ decays, which in most cases need an additional p_T from the parent particle, or a Lorentz-boost, to reach the Muon Spectrometer. As a consequence, a full p_T analysis of the $J/\psi \rightarrow \mu^+\mu^-$ channel (which is important because quarkonia suppression may depend on the resonance transverse momentum) is only possible in the forward regions where, however, the background is largest.

On the other hand, the $J/\psi \rightarrow \mu^+\mu^-$ production has a much larger cross-section than Y production, which allows stricter cuts to be applied to reduce the background. The cross-section for the process $J/\psi \rightarrow \mu^+\mu^-$ is $B_r d\sigma/dy(Pb + Pb \rightarrow J/\psi \rightarrow \mu^+\mu^-)$=49 mb and $B_r d\sigma/dy(Pb + Pb \rightarrow \psi' \rightarrow \mu^+\mu^-)$=879 μb [27]. Another advantage is that the reconstructed di-muon mass resolution ($\sim$70 MeV from a full-simulation study) is sufficient to separate J/ψ from ψ' even in the forward regions of the detector, which is not the case for the Y resonances.

The acceptance and efficiency values have been calculated using Athena, release 14.2.23, for 164000 $J/\psi \rightarrow \mu^+\mu^-$ events. The dN/dp_T and dN/dy distributions for the $J/\psi \rightarrow \mu^+\mu^-$ are displayed in Fig. 7.7. The generated distributions are in full black, the reconstructed distributions are in dashed-dotted black for the standard strategy with a muon-p_T >3 GeV, in dotted blue with a muon-p_T >1.5 GeV, and in dashed red for the tagged muon strategy with a muon-p_T >1.5 GeV. The combined acceptance and reconstruction efficiency for a muon-p_T > 3 GeV is 0.075% (0.051% without tagged muons). Due to the low mass of the J/ψ, the acceptance is mainly for $|\eta| > 1.5$, and the low-p_T range of J/ψ is not accessible for a muon-p_T cut at 3 GeV as used for the Y. However, with a muon-p_T cut at 1.5 GeV and a tagged muon strategy, the J/ψ can be measured from p_T=0 with the acceptance increased up to 0.785% (0.301% without tagged muons). Note, that a minimum energy of 3-4 GeV is needed for the muon to reach the Muon Spectrometer, corresponding to a p_T of 3-4 GeV at η=0. A Lorentz-boost is necessary for a muon-p_T of 1.5 GeV.

The signal-to-background ratio for J/ψ measurements is correspondingly 0.5 and 0.2 for the muon-p_T cut of 3 and 1.5 GeV [137]. The number of $J/\psi \rightarrow \mu^+\mu^-$ events expected in one month of 0.5 nb^{-1} of integrated luminosity of Pb+Pb running is, after background subtraction and with tagged muon strategy, 19 k and 192 k for a muon-p_T cut of 3 and 1.5 GeV.

Evidently, the choice of the strategy is therefore more important for the J/ψ than for the Y studies. An additional way to increase the J/ψ statistics is to reduce the toroidal field of the Muon Spectrometer as it improves the low-p_T muon acceptance. It has also the advantage to make easier a low p_T muon trigger but at the expense of a slightly worse mass resolution [137]. A study of a trigger based on a low muon-p_T cut for $|\eta|$ >1.5 is under way.

Finally, it should be noted that tagging displaced vertices provides a tool to discriminate prompt J/ψ from those originating from B-meson decays. The ratio between prompt and decay J/ψ could be studied as a function of the event centrality.
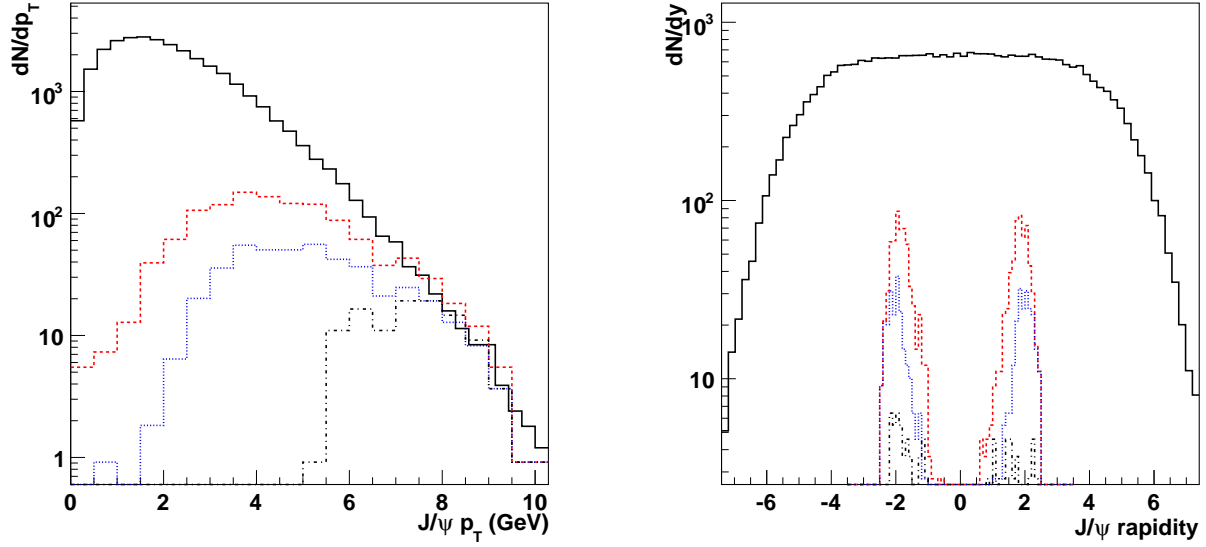
Figure 7.7: dN/dp_T (left) and dN/dy (right) distributions for $J/\psi \rightarrow \mu^+\mu^-$ (color online). The generated distributions are in full black, the reconstructed distributions (x 5) are in dashed-dotted black for the standard selection with a muon-p_T >3 GeV, in dotted blue for the standard selection with a muon-p_T >1.5 GeV and in dashed red for the tagged muon selection with a muon-p_T >1.5 GeV.

7.4 Z **boson measurements**

7.4.1 Z **Measurements**

Z's will be primarily measured via their di-muon decay channel. In order to understand how useful the Z measurement can be in heavy ion collisions at LHC, it is essential to understand the relevant efficiencies and expected rates in Pb+Pb collisons. Studies of Z measurements in p+p collisions have already been made by ATLAS collaboration in both di-electron and di-muon channels (see e.g. [43] and references therein). In this report, we are studying Z measurements in Pb+Pb collisions only in the di-muon channel.

In order to study the effects of the high-multiplicity environment, typical of high energy heavy ion collisions, on the Z measurement, we have generated single Z's with a flat distribution in pseudorapidity (from -5 to 10) and transverse momentum (from 0 to 25 GeV). These Z's were merged to central (impact parameter $b = 2$ fm) HIJING Pb+Pb events, and reconstructed using the standard ATLAS software (in this case, Athena version 12.0.3). The same Z's were also merged to minimum bias p+p PYTHIA events and reconstructed in a similar fashion. The results of these two simulations were then compared in order to determine how the ATLAS detector performance is affected by high multiplicity of Pb+Pb collisions. Comparison with single Z's has not been done, since the reconstruction software requires a proper determination of the event vertex, which is impossible in single-particle events.
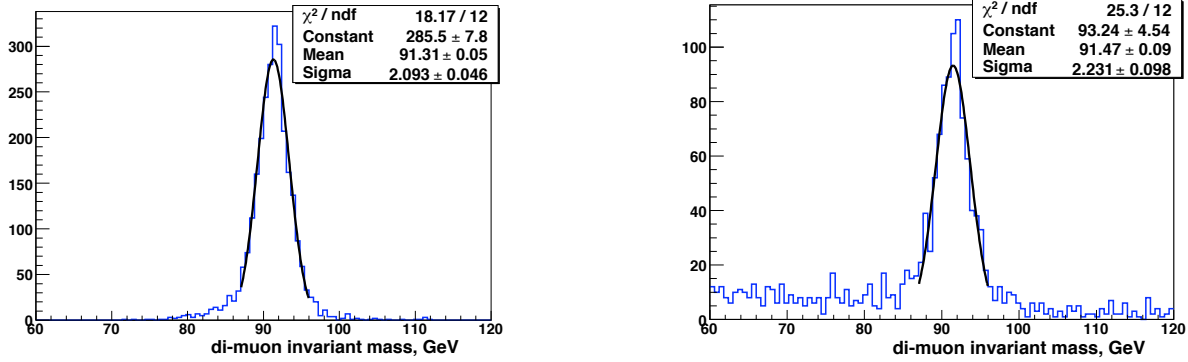
93

Figure 7.8: (left) Di-muon invariant mass distribution for Z bosons embedded in p+p collisions. (right) Di-muon invariant mass distribution for Z bosons embedded in central Pb+Pb collisions.

7.4.2 Z **mass resolution**

The di-muon invariant mass distributions in p+p and Pb+Pb events with embedded Z's are shown in Fig.7.8. It is observed that the Z mass resolution is only weakly affected by the high multiplicity background in Pb+Pb collisions. The observed difference is within one sigma of the fit error. The combinatorial background observed in Fig.7.8(right) for Pb+Pb collisions is almost entirely produced by combination of one of the muons from Z decay and another muon from the background Pb+Pb HIJING events.

7.4.3 **Acceptance and efficiency**

The Z acceptance multiplied by the reconstruction efficiency ($A\epsilon$) in p+p collisions is shown in Fig.7.9(left) as a function of pseudorapidity and transverse momentum. Fig.7.9(right) compares the Z $A\epsilon$ for p+p and central Pb+Pb collisions as a function of pseudorapidity. The latter plot was produced by projecting the former on vertical axis. The value of $A\epsilon$ is almost constant with pseudorapidity up to $\eta \sim 3.5$ and then falls quickly at larger pseudorapidities. It is also essentially independent of transverse momentum.

Reconstruction efficiency in central Pb+Pb collisions relative to the reconstruction efficiency in p+p collisions is $\sim 90\%$ and is shown as a function of pseudorapidity in Fig.7.10. It is observed that the relative efficiency is essentially flat as a function of pseudorapidity. The sample of Z's embedded into central Pb+Pb collisions was smaller than that used for p+p collisions, and was a subset of the latter. This explains the values above 1.0 at high pseudorapidity.

7.4.4 **Expected rates and yields**

The Z production cross section at 5.5 TeV is estimated to be approximately $\sigma_Z = 0.65$ nb [132]. Assuming an integrated yearly luminosity for Pb+Pb of $L = 0.5$ nb^{-1}, a ratio of Pb+Pb to p+p cross-sections ~ 100, and the number of binary collisions in minimum-bias Pb+Pb events as $N_{coll} = 400$ [138], we can calculate that ~ 13000 Z will be produced in one year of running using the following formula:
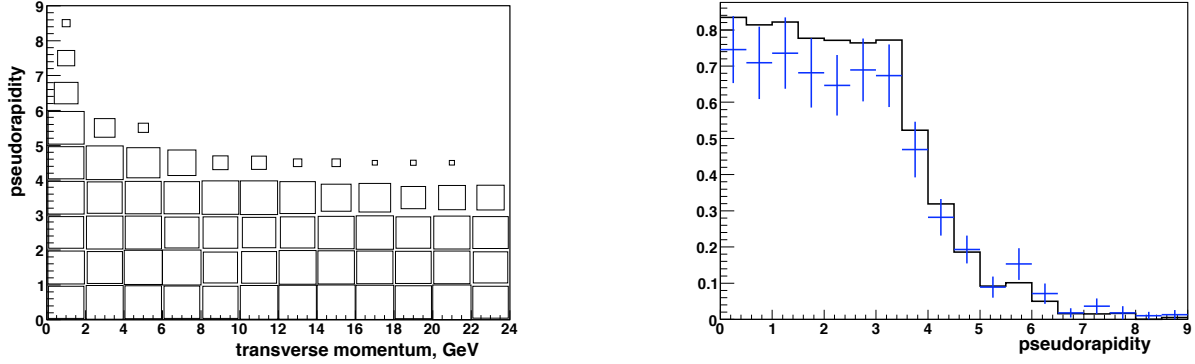
Figure 7.9: (left) *Z* acceptance times reconstruction efficiency (*Aε*) for p+p collisions as a function of *η* and transverse momentum. The largest-size boxes correspond to efficiency of about 75%. (right) *Aε* for p+p collisions (black histogram) and for central Pb+Pb collisions (blue markers) as a function of pseudorapidity.
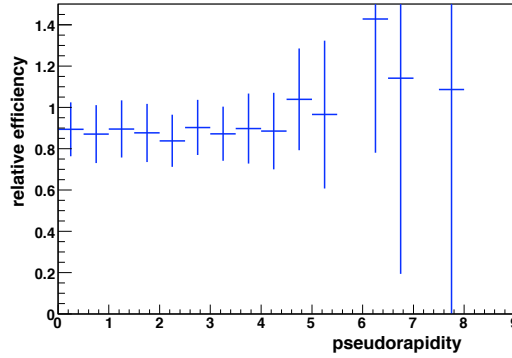

Figure 7.10: Ratio of the *Z* reconstruction efficiency in central Pb+Pb collisions to that found in p+p collisions as a function of pseudorapidity.

$$N_{Z^0}^{A+A} = L \frac{\sigma_{A+A}}{\sigma_{p+p}} N_{coll} \sigma_{Z^0}$$

This number has to be corrected for acceptance and efficiency, and the latter depends quite strongly on the pseudorapidity distribution of *Z* produced in Pb+Pb collisions at 5.5 TeV. We have used several different pseudorapidity distributions in order to estimate the integrated value of *Aε*. The rapidity distribution of *Z* produced in p+p collisions at 14 TeV has been predicted in Ref. [133] and is shown in Fig.7.11(right). PYTHIA predicts a similar shape, but a much wider pseudorapidity distribution, which is shown in Fig.7.11. Note that the rapidity distribution (magenta curve) is different in shape from the pseudorapidity distribution (black curve and blue markers). Both PYTHIA and distributions from [133] are almost flat in rapidity, but differ in their overall width.

The integrated value of *Aε*, calculated using the pseudorapidity weight from PYTHIA, is 31%. If the PYTHIA distribution is forced to the same width as the distribution from [133], the
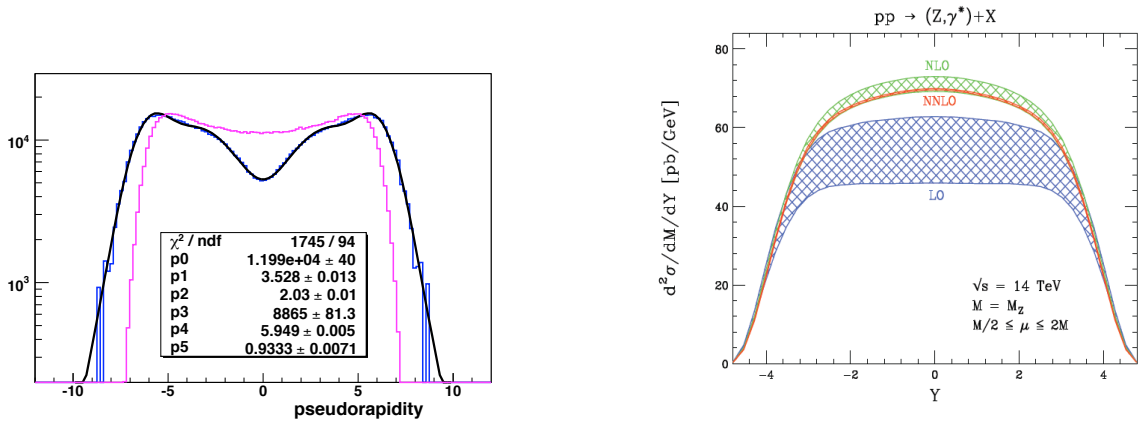
Figure 7.11: (left) Pseudorapidity (black curve) and rapidity (magenta histogram) distributions of Z predicted by PYTHIA for p+p collisions at 5.5 TeV. (right) Rapidity distribution of Z predicted by [133].

integrated $A\epsilon$ becomes significantly larger, namely $\sim 59\%$. If a flat rapidity distribution (from -4 to 4) is used, the integrated $A\epsilon$ is found to be $\sim 67\%$. This is straightforward to understand if one takes into account that the Z acceptance drops sharply above $\eta =\sim 3.5$ (as shown in Fig.7.9).

Thus, we can expect to reconstruct from 4 to 8 thousand Z's in one year of heavy ion running depending on the exact rapidity distribution of Z's. The latter number is probably more realistic, because it is based on the NLO pQCD prediction of the rapidity width of the Z boson production.

7.5 Perspective for observing quarkonia and Z bosons decaying into $e^+ e^-$

For the studies with central Pb+Pb collisions, the TRT has not been considered because of its large occupancy (see Chapter 2). Nevertheless the TRT can be used fully in peripheral collisions, and partially in central ones when selecting inside the TRT in-time signals along the extrapolated trajectory from track reconstruction in the PIXEL and SCT detectors. This should improve tracking and resolution . The TRT can also identify low p_T electrons from Y and $J/\psi \to e^+ e^-$ on a statistical basis without a full reconstruction inside the TRT. Some preliminary analysis has been done in [137] and will be continued.

It is also planned to pursue the study of Z bosons decaying into two electrons. For this purpose we can apply a standard selections of high-p_T electron identification and isolation. It is expected that the capability of measuring this decay channel should be not significantly worse as compared to p+p collisions [39] similarly as it was observed in the case of the di-muon channel.

7.6 Summary

Quarkonia dissociation in heavy ion collisions can be studied with the ATLAS detector at the LHC for both the charmonium and bottomonium family in the di-muon channel.

- The Y reconstruction efficiency in heavy ion collisions is not affected by the high multiplicity environment, and it is the same as that for single Y's even in the most central Pb+Pb collisions.

- The Y mass resolution is good enough to separate Y and Y′ states when limiting the muon acceptance to $|\eta| < 2$. Separation for Y″ states is less clear, but also possible in the barrel region ($|\eta| < 1$).

- The J/ψ and ψ' can be studied with large statistics. The background can be reduced to an acceptable level. The choice of selection criteria makes sure that the performance is only slightly affected by the presence of the soft heavy-ion background.

- It is expected to record about 35 k Y's and about 19 to 190 k J/ψ's, depending on the strategy used, in one month of running in full ATLAS acceptance.

This chapter has also presented the ATLAS performance for Z boson measurement in Pb+Pb collisions.

- The relative Z reconstruction efficiency is 90% in Pb+Pb collisions compared to p+p collisions.

- The Z mass resolution is only weakly-affected by the high-multiplicity environment in Pb+Pb collisions, compared to p+p collisions. The observed difference in width is less than 10% and is compatible with no change.

- The integrated acceptance times efficiency ($A\epsilon$) in Pb+Pb collisions depends strongly on the width of the Z rapidity distribution in Pb+Pb collisions at 5.5 TeV. It could range from $\sim 30\%$ to $\sim 60\%$, and we expect 4 to 8 thousand Z bosons to be reconstructed in one year of running.

The prospects for studying quarkonia and Z bosons via their di-electron decay channel are also outlined.

Chapter 8

Direct Photons & Photon-Jet Correlations

This chapter describes the physics need for direct photon and γ-jet measurements with ATLAS, the techniques available in ATLAS for photon detection, and its capabilities for photon physics and γ-jet correlations, both with and without isolation. The ability to efficiently separate photons and neutral hadrons without an isolation cut over a broad acceptance is a unique strength of ATLAS. In addition to providing an optimal window on jet energy loss, this particular aspect of the analysis provides the unique capability to measure non-isolated photons from fragmentation or from the medium.

8.1 Physics motivation

The main goal of LHC heavy ion program is to understand the properties of the quark-gluon plasma (QGP) created in Pb+Pb collisions. In ATLAS, this relies primarily on jet-tomography: a parton created in a hard collision interacts with the QGP medium, essentially probing the QGP in analogy with positron-emission tomagraphy in biology. By crossing symmetry, this can provide much the same information as the idealized experiment of scattering a quark or gluon off of a pre-existing plasma.

There are two types of hard processes that can be used for this jet-tomography, the most commonly occuring is di-jet production from $2 \to 2$ parton scattering. This approach suffers from two drawbacks. First, the kinematics of the hard parton collision, i.e. the energy or transverse momentum of the hard scatter, is unknown except as a convolution over all possibilities. Second, it is challenging to define and reconstruct jets in Pb+Pb collisions: jets are not only strongly modified by the QGP medium, but also susceptible to fluctuation of the large underlying event background, which distorts the jet energy scale and energy resolution. Despite these difficulties and their associated model-dependence, significant information can be extracted from a comparison of di-jets in Pb+Pb collisions with those in p+p collisions. Chapter 6 discusses jet reconstruction and the use of di-jets.

The second, better albeit less abundant, type of hard process for use in jet-tomography is one which produces a hard photon in coincidence with a single parton. These processes, known as "γ-jet" events, are a particularly useful probe because the medium is nearly transparent to photons. Therefore the γ's can be used to measure the original energy and direction of the away-side jets, which should be strongly modified by the medium. They not only provide a model independent

way for calibrating the jet energy scale and resolution in heavy ion collisions, but also help to extend the jet reconstruction to lower E_T where the jet reconstruction efficiency degrades due to the large underlying event (as shown in Fig. 6.12). The measurement of γ-jet correlation should also be able to eliminate the energy loss bias intrinsic to the jet-jet coincidence measurements where there is no absolute calibration of jet energy (since both jets can be modified by the medium). Thus, the study of γ-jet events provides direct access to the average behavior as well as fluctuations of the energy loss process.

In addition to serving as controlled measurement for jet energy loss, and as calibration tool for jet reconstruction, direct γ at intermediate and low p_T can directly probe the properties of the QGP in further ways. The medium itself may respond to the passage of the parton, for instance with shock-wave induced "Mach cones" which probe the speed of sound in the medium [96, 139]. Furthermore, recent theoretical calculations [140] suggest that a dominant fraction of direct γ at $p_T < 50$ GeV may come from medium-induced bremsstrahlung processes (such as $q \rightarrow q + \gamma$) or in-medium flavor conversion processes (such as $q + g \rightarrow q' + \gamma$). Measurements of these semi-hard final state direct γ can provide independent insights on microscopic properties, such as the degrees of freedom and coupling strength, of the QGP.

"Direct" photons, in this document, refer to those photons that are produced during the initial creation and later stage evolution of the fireball, which should be distinguished from "decay" photons from the electromagnetic decays of hadrons. To leading order in pQCD, most direct photons come from γ-jet events generated by the initial hard-scattering processes such as QCD Compton scattering ($qg \rightarrow \gamma q$) and annihilation ($q\bar{q} \rightarrow \gamma g$) processes, and these photons are called "prompt" photons. The main difficulty facing the γ-jet analysis is the relatively small production rate. The relative cross-section of γ-jet events compared to jet-jet events is shown in Fig. 8.1, and is typically down by a factor of 1000–3000 for E_T below 200 GeV at LHC energies. Clusters from electromagnetically decaying neutral hadrons, such as $\pi^0, \eta \rightarrow \gamma\gamma$, create a large background to the direct photon sample, as can also be seen in Fig. 8.1. A more detailed description of the results in Fig. 8.1 is given below during the discussion of the related Fig. 8.11.

As an alternative way to illustrate the relative abundance between direct photon and neutral hadron background, we plot in Figure 8.2 the direct γ to ($\pi^0 + \eta$) ratio as function of transverse energy from a next-to-leading order (NLO) calculation for p+p collision at $\sqrt{s} = 5.5$ TeV. It is performed using the INCNLL code [141] with the CTEQ6m parton distribution [142] and the KKP fragmentation function [143]. Both figures provide us the expected signal to background ratio before any trigger or offline cuts and without any medium effects. Our goal is to evaluate the influence of the high occupancy environment in Pb+Pb events, as well as the analysis cuts, to the γ, and γ-jet studies. We haven't evaluated the influences of the triggers, which we defer to future studies. However, we expect the rate of Pb+Pb collisions is sufficiently low (a few kHz) that the event rejection only takes place at event filter state (high level trigger or HLT). This is expected to significantly minimize any Level-1 and Level-2 trigger biases by detailed analysis in HLT (see Chapter 9.

The main challenge for the γ-jet analysis is to derive an algorithm which can effectively reject the decay photons while maintaining a reasonable fraction of direct photons. In this section, the performance of ATLAS detectors for single γ and for γ-jet measurements is evaluated. Two methods are described to reject decay photons. In the first, a shower shape cut based on the highly

99
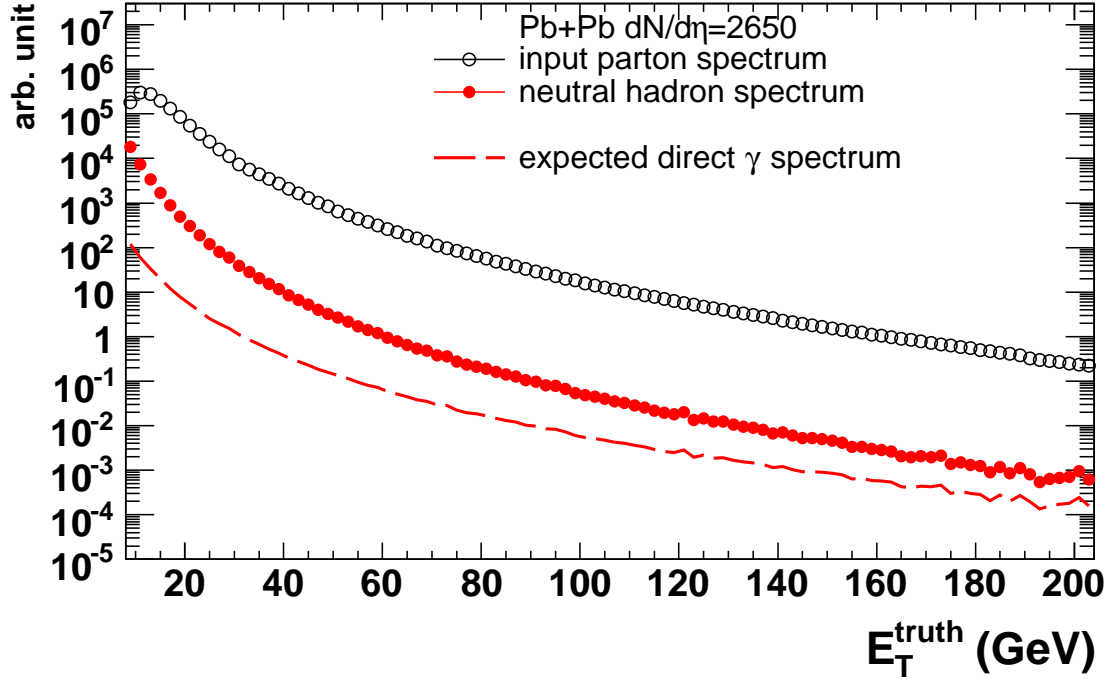
Figure 8.1: The relative rates for production of photons from γ-jet events and hadrons from di-jet events, before any cuts. The spectra shown are for input jets (open circles), input $\pi^0 + \eta$ (red solid circles), and expected direct γ (dashed line).

Figure 8.2: Next to leading order pQCD calculation of the direct γ to neutral hadron ratio as function of transverse energy for p+p collisions at $\sqrt{s} = 5.5$ TeV (using the INCNLL code with the CTEQ6m parton distribution function and the KKP fragmentation function). The η yield is estimated to be 50% of that for π^0.

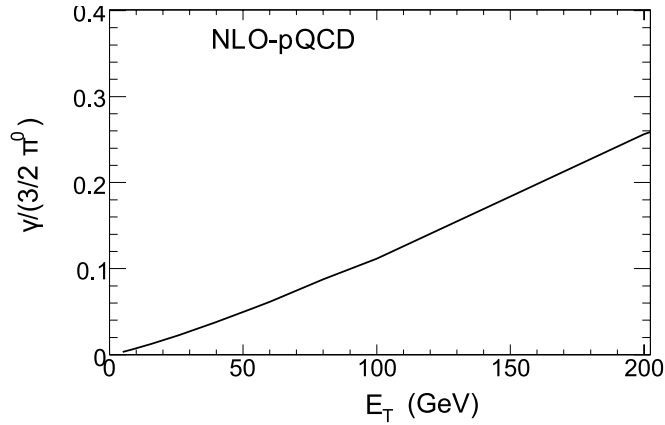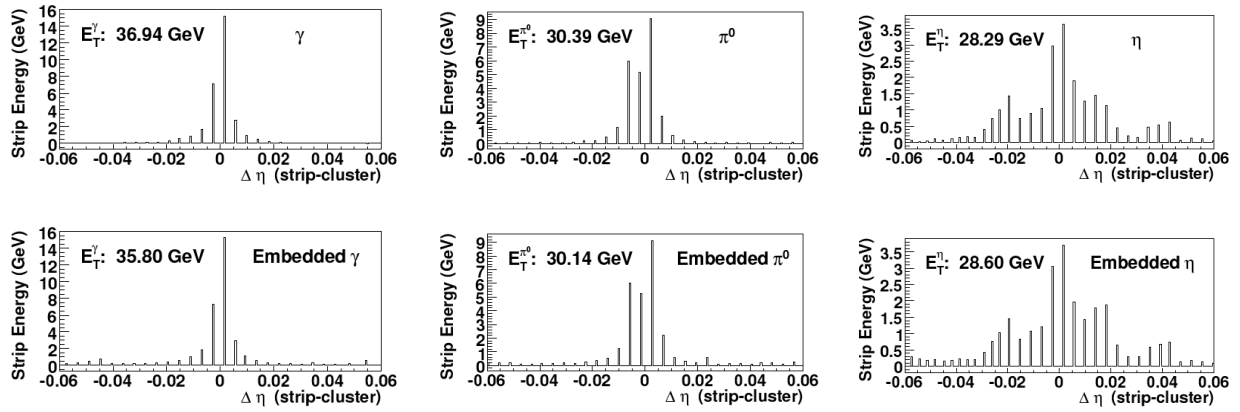Figure 8.3: The energy deposition in the strip layers around the direction of (upper left) a single photon, (upper middle) a single π^0 and (upper right) a single η as well as for (lower row) the identical particles embedded in a central ($b = 2$ fm) Pb+Pb event. The energy values are the reconstructed energies.

segmented first layer of the calorimeters provides a factor of 3–5 rejection [1]. An additional factor of 10 rejection can then be achieved by a set of isolation criteria. The largest rejection power is then obtained by combining the shower shape and isolation cuts, which are largely orthogonal to each other. Future prospects and comparisons to ALICE and CMS are discussed in the end.

8.2 Photon identification

The design of the ATLAS electromagnetic calorimeter is optimal for direct photon identification. The first layer of the electromagnetic calorimeter, which covers the full azimuth and $|\eta| < 2.4$, has very fine segmentation along the η direction (ranging from 0.003–0.006 units). This layer provides detailed information on the shower shape, which allows a direct separation of γ's, π^0's, and η's on a particle-by-particle level. Deposited energy distributions for a typical single γ, single π^0, and single η meson are shown in the upper row of Fig. 8.3. Characteristically different shower profiles are seen. The energy of a single photon is concentrated across a few (typically 3) strips, with a single maximum in the center, while the showers for $\pi^0 \to \gamma\gamma$ and $\eta \to \gamma\gamma$ are distributed across more strips, often with two or more peaks. The broad shower profile for π^0 and η reflects the overlap of showers for two or more decay photons, which are typically separated only by a few strips. The strip size of 0.003 units roughly corresponds to the minimum opening angle between two decay photons for a 90 GeV π^0. The opening angle for an η meson with the same energy is about four times larger. Even when the two peaks are not resolved, the multi-photon showers are measurably broader on a statistical basis. Thus the strip layer allows the rejection of π^0 and η decay photons over a very wide energy range.

In Pb+Pb collisions, the shower profiles at the strip layer could, in principle, be distorted by

---

[1]We use the standard ATLAS egamma variables as described in CSC note [43], but the cuts are specifically tuned for Heavy ion analysis.

the high occupancy environment. To study such occupancy effects, single γ's, π^0's and η's have been embedded in Pb+Pb events generated with HIJING. The official ATLAS detector simulation, digitization and data analysis procedures have been used to simulate and analyze the merged events and to reconstruct the embedded photons and mesons. The lower row of Fig. 8.3 shows the strip layer energy distributions surrounding the direction of single particles embedded in central Pb+Pb events. The γ, π^0 and η in these plots are the same ones used in the upper row of plots. Despite the large number of low-energy particles produced in Pb+Pb events, the underlying event only introduces, typically, around a hundred MeV background for each strip. In comparison, a single photon typically deposits 40-50% of its total energy in the strip layer. Since the energy deposited in each strip by a high energy single γ, π^0 and η is typically several GeV, the shower shape for the embedded particle is almost unchanged by the background. One expects the rejection to work down to very low energy (about 10 GeV), and the performance for the background rejection and identification efficiency should not depend strongly on the event centrality.
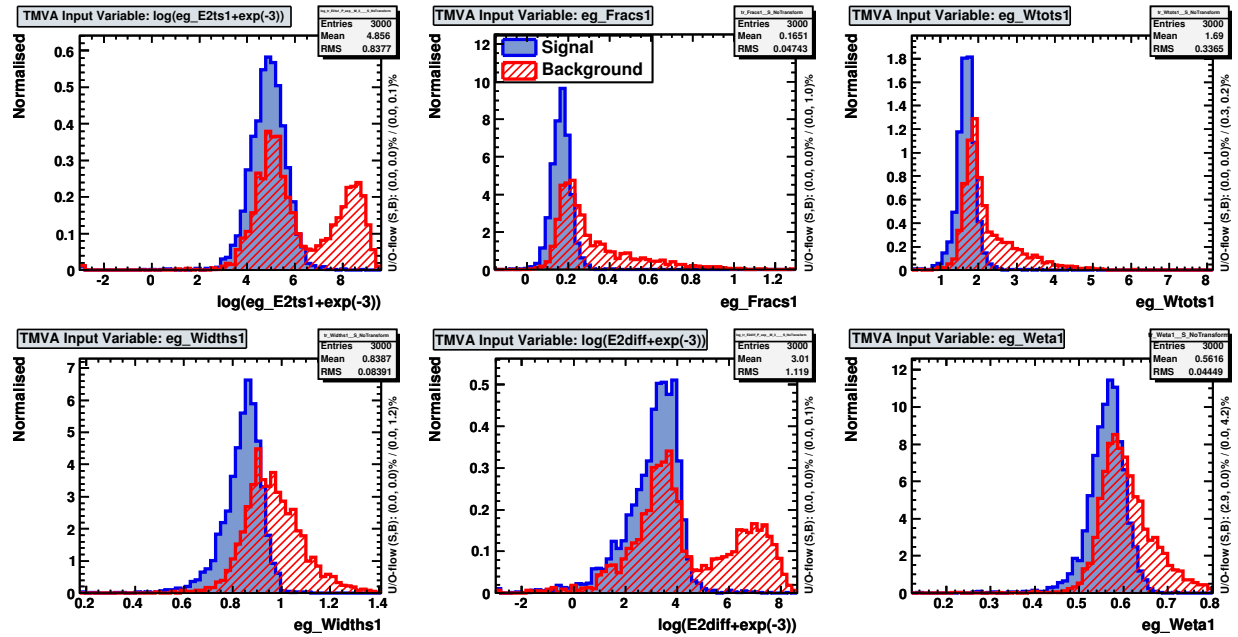

Figure 8.4: Distributions of shower-shape variables for single signal photons and for background clusters from single neutral mesons for the six variables listed in the text. The photons and mesons have $|\eta| < 0.75$ and $45\,\text{GeV} < E_T < 70\,\text{GeV}$.

To distinguish direct photons from neutral hadrons, a set of cuts has been developed based on the shower shape in the strip layer. These cuts reject those showers that are anomalously wide or exhibit a double peak around the maximum. In total, six variables from the ATLAS-standard egamma package are used to define the cuts:

- 1: (eg_Fracs1) The fraction of energy outside the shower core, i.e $(E(\pm7) - E(\pm3))/E(\pm7)$, where $E(\pm n)$ is the energy deposited in $\pm n$ strips around the strip with the highest energy;

- 2: (eg_Widths1) The uncorrected RMS width of the cluster calculated in 3 strips;

102

- 3: (`eg_Wtots1`) The RMS width of the cluster calculated in 20 strips;

- 4: (`eg_Weta1`) The "corrected" RMS width of the cluster calculated in 3 strips, where an attempt is made to correct for the effect of a possible non-normal incidence of the photon using the different longitudinal layers to estimate the angle of incidence;

- 5: (`eg_E2ts1`) The height of the second highest peak, summed over 3 strips (Note: Plotted as log(eg_E2ts1 + exp(-3)));

- 6: ("E2diff"$\equiv$`eg_E2tsts1-eg_E2mins1`) The difference between the height of the second highest peak (in 1 strip) and the minimum energy found in between the two peaks (Note: Plotted as log(E2diff + exp(-3))).

Figure 8.4 shows the distribution of these six variables for the case of a particular bin in η and E_T. It is clear that these variables can be used to discriminate between the signal and the background. The cuts on these variables have been tuned as function of photon energy and pseudo-rapidity. In general, better rejection can be achieved using a tighter cut, but at the expense of reduced efficiencies. The performance has been quantified via photon efficiency (ϵ_γ) and relative rejection ($R_{\rm rel}$). The former is defined as the fraction of photons passing the cuts. The latter is defined simply as the ratio of the efficiencies for γ and neutral hadrons (labeled as bkg),

$$R_{\rm rel} = \frac{\epsilon_\gamma}{\epsilon_{bkg}} \quad . \tag{8.1}$$

The relative rejection basically reflects the gain on the signal (direct photon yield) relative to background (neutral hadron yield). The absolute rejection can also be used, which is defined as

$$R_{\rm abs} = \frac{1}{\epsilon_{bkg}} \quad , \tag{8.2}$$

thus $R_{\rm abs} \approx R_{\rm rel}$ if the efficiency for direct photons is close to one.

In this analysis, two sets of cuts have been developed based on the previously mentioned 6 egamma variables: a "loose" cut set and a "tight" cut set. The performance for these two sets is summarized in Fig. 8.5 for the loose cuts and in Fig. 8.6 for the tight cuts. For single particle (reconstruction of single γ vs single π^0 or η meson), the performance is comparable with the CSC note [43]. The variations from point to point are not due to statistical fluctuations, which typically are smaller than the symbol size, but are caused by the fact that the cuts are currently tuned by hand bin-by-bin in E_T. The loose cuts give a factor of 1.5–3 relative rejection with a photon efficiency of about 90%; the tight cuts give a factor of 3–5 relative rejection with an efficiency of about 50%. The efficiency is tuned to be roughly independent of E_T, η, and centrality. The corresponding rejection factors were found to vary weakly with the E_T, η, and centrality. The η dependence (not shown) is roughly $\pm 25\%$ relative to the η-averaged value with the best performance near midrapidity. These results suggest that the best performance can be achieved for 30–50 GeV photons.

The identified photons are well reconstructed, even in heavy ion collisions. Figure 8.7 shows the position resolution in ϕ and η averaged over the entire acceptance as a function of E_T. The resolution is shown for single photons (labeled as $dN_{ch}/d\eta = 0$) and for photons embedded in Pb+Pb collisions for three different centralities, indicated by their midrapidity particle densities. For E_T around 100 GeV, the η resolution is about 0.0003, while the ϕ resolution is about 0.0006 (0.6 mrad). Figure 8.8 shows the relative resolution for E_T, again averaged over the acceptance, which is about 2% at an E_T of 100 GeV.

Figure 8.5: (left) Photon identification efficiency and (right) relative rejection factor for neutral hadrons for the loose cut set for single particles (open circles) and single particles embedded in central ($b = 2$ fm, $dN_{ch}/d\eta = 2650$) Pb+Pb collisions (filled triangles). These are averaged over the entire range $|\eta| < 2.4$.
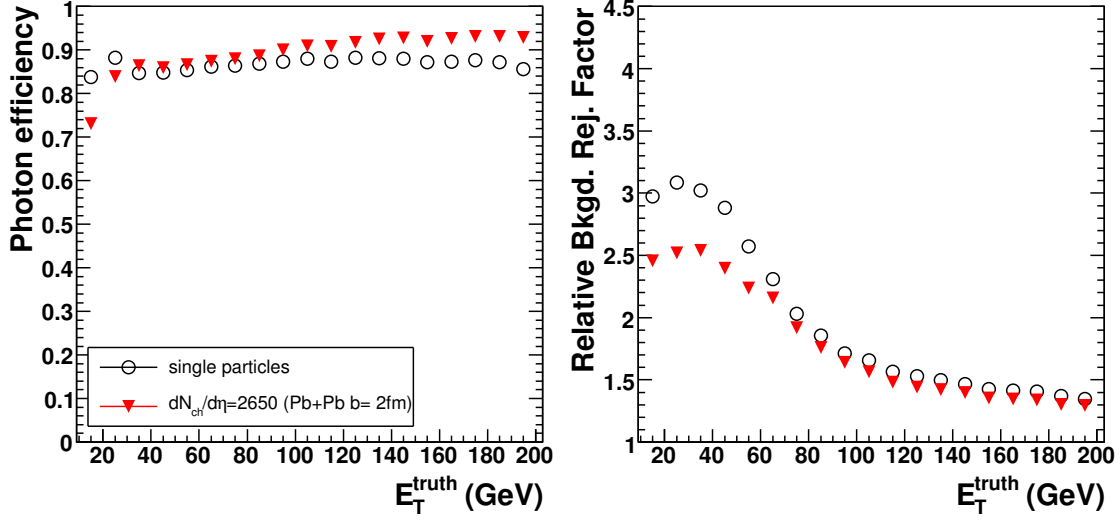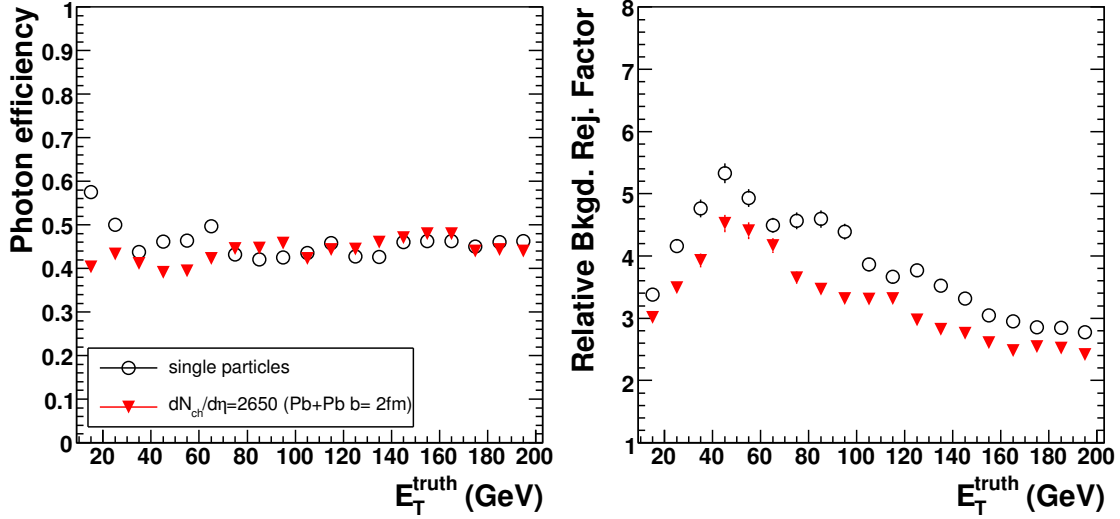

Figure 8.6: (left) Photon identification efficiency and (right) relative rejection factor for neutral hadrons for the tight cut set for single particles (open circles) and single particles embedded in central ($b = 2$ fm, $dN_{ch}/d\eta = 2650$) Pb+Pb collisions (filled triangles). These are averaged over the entire range $|\eta| < 2.4$.

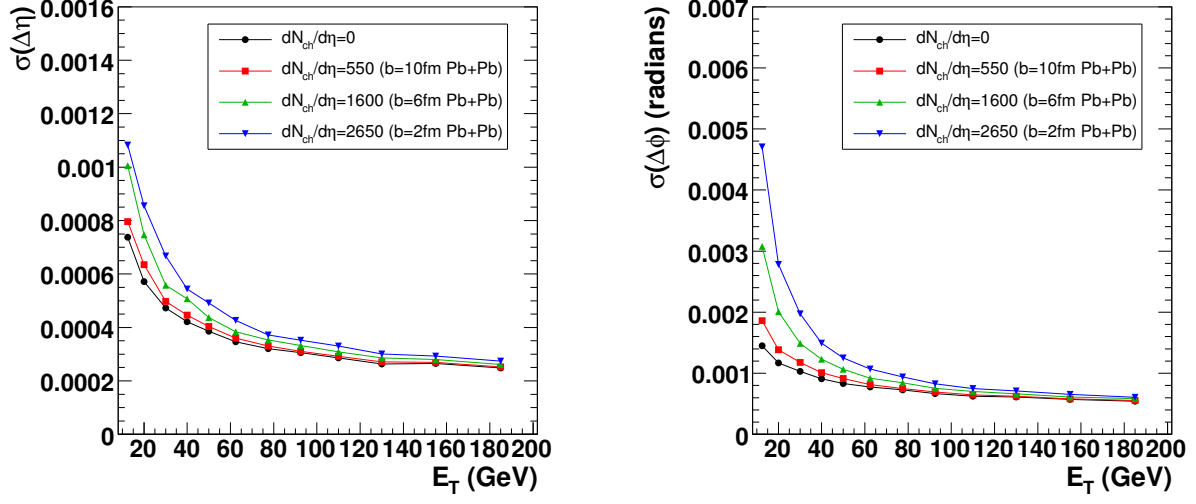Figure 8.7: Angular resolution, (left) pseudo-rapidity and (right) azimuthal angle, vs. E_T for single photons and single photons embedded in Pb+Pb HIJING events.
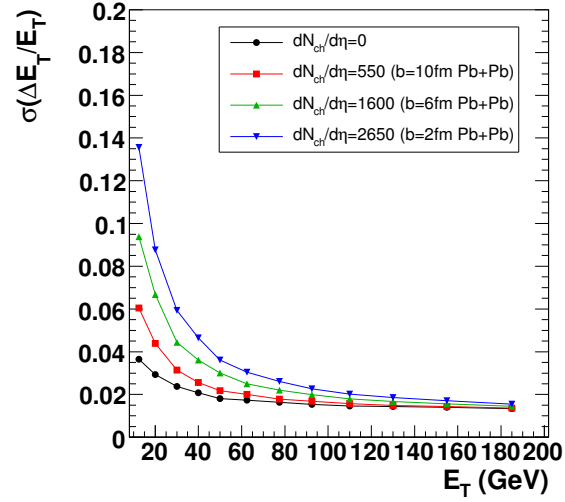

Figure 8.8: Relative energy resolution vs. E_T for reconstructed single photons and those embedded in Pb+Pb HIJING events.

8.3 Isolation cuts

One difference between direct photons and decay photons is that the direct photons are usually isolated but decay photons come from hadrons that are the fragments of jets: e.g. jet$\rightarrow \pi^0 \rightarrow \gamma\gamma$. The decay photons typically merge into one cluster, but they have other hadrons in the neighboring angular space coming from the same original jet. Thus the direct photons can be distinguished from decay photons based on a set of isolation criteria. The isolation cuts are defined by using the charged tracks and total tower E_T in a cone around the jets. These cuts are tuned to maximize the rejection while keeping reasonable efficiency. This is achieved by varying the p_T threshold for charged tracks and the isolation cone size, or by varying the energy sum threshold and corresponding cone size. In general, the isolation efficiency drops with increasing cone size and decreasing p_T threshold or total E_T sum. The rejection, on the other hand, follows the opposite trend. We determine the best cuts separately for three Pb+Pb centralities and p+p and summarize them in Table 8.1. For example the cuts for most central Pb+Pb events require that no charged track in a cone of $0.02 < R < 0.2$ has a $p_T < 2.5$ GeV, and the total energy in a cone of $R < 0.2$ surrounding the cluster should be less than 31 GeV+0.025E_γ. The requirement of $0.02 < R$ for charged tracks is necessary to avoid false rejection of genuine isolated photons due to conversions. Note that the efficiency and rejection numbers quoted in this table are for the isolation cut only, without a cluster-shape-based photon identification cut.

	b=2fm ($dN_{ch}/d\eta = 2650$)	b=6fm ($dN_{ch}/d\eta = 1600$)
Track-based cut	$0.02 < R < 0.2$	$0.02 < R < 0.25$
	$p_T < 2.5$ [GeV]	$p_T < 2.5$ [GeV]
Energy-based cut	$R < 0.2$	$R < 0.2$
	$\sum E_T < 31 + 0.025E_\gamma$ [GeV]	$\sum E_T < 17.2 + 0.025E_\gamma$ [GeV]
Efficiency	0.60	0.70
Absolute rejection at 50 GeV	8	10
	b=10fm ($dN_{ch}/d\eta = 550$)	p+p
Track-based cut	$0.02 < R < 0.35$	$0.02 < R < 0.5$
	$p_T < 2.0$ [GeV]	$p_T < 1$ [GeV]
Energy-based cut	$R < 0.2$	$R < 0.2$
	$\sum E_T < 5.6 + 0.025E_\gamma$ [GeV]	$\sum E_T < 0.9 + 0.025E_\gamma$ [GeV]
Efficiency	0.70	0.91
Absolute rejection at 50 GeV	14	16

Table 8.1: The isolation cuts used in this analysis for three Pb+Pb centrality bins and p+p collisions. The track-based cut requires all charged tracks in the specified cone should have energy below the p_T threshold. The magnetic field also imposed a lower limit of about 0.5 GeV. Similarly, the energy-based cut requires the total energy in the cone surrounding the cluster should be less than the threshold. The efficiency and rejections are for all direct photon samples (without photon identification cut).

The performance of the isolation cuts for p+p and central Pb+Pb events is summarized in Fig 8.9. In central collisions (corresponding to b=2fm in HIJING), the efficiency is about 65% and the absolute rejection is about 8 for $E_T > 50$ GeV. In p+p collisions, the efficiency is about 90%

with an absolute rejection factor of about 16 above 50 GeV. Fig. 8.10 shows the corresponding performance for mid-central and peripheral Pb+Pb events. The increase of rejection with E_T is mainly due to the increase of jet multiplicity and jet energy which makes the isolation cut more effective.

Figure 8.9: The photon efficiency and absolute rejection for background neutral hadrons for the isolation cuts (see Table. 8.1) as a function of energy in (left) p+p and (right) central Pb+Pb events.

8.4   Combined photon identification and isolation cuts

The combined performance for direct γ identification using both the shower shape and isolation cuts is summarized in Fig 8.11. In this study, about 140k PYTHIA di-jets are generated and embedded into the Pb+Pb HIJING events, similar to what was done for jet reconstruction in Chapter 6. To speed up the simulation, these di-jet events were generated with seven $\sqrt{Q^2}$ cuts in the 10–100 GeV range each with comparable statistics, which were then combined into a single jet spectrum by weighting them with the corresponding di-jet cross-section. PYTHIA also provides the spectra of π^0 and η mesons from jet fragmentation. After applying the γ-identification and isolation cuts, we obtain the spectrum of remaining neutral mesons that survive the cuts, which are the background for the direct photons.

To compare with the direct photon yield passing the same set of cuts, the NLO pQCD calculation of Fig. 8.2 is used to generate a realistic hadronic background. The expected direct photon yield is obtained by multiplying the expected spectra of π^0 and η mesons with the ratio $\gamma/(\pi^0 + \eta)$, which is then multiplied by the measured photon identification efficiency to obtain an estimated reconstructed photon spectrum. Figure 8.11 shows the spectra of jets (open circles), $\pi^0 + \eta$ (solid squares), $\pi^0 + \eta$ passing the cuts (solid circles), expected γ (solid line), and expected γ passing the cuts (dashed line). As the figure shows, above 60 GeV, the cuts suppress the yield of background neutral hadrons below the direct photon yield.
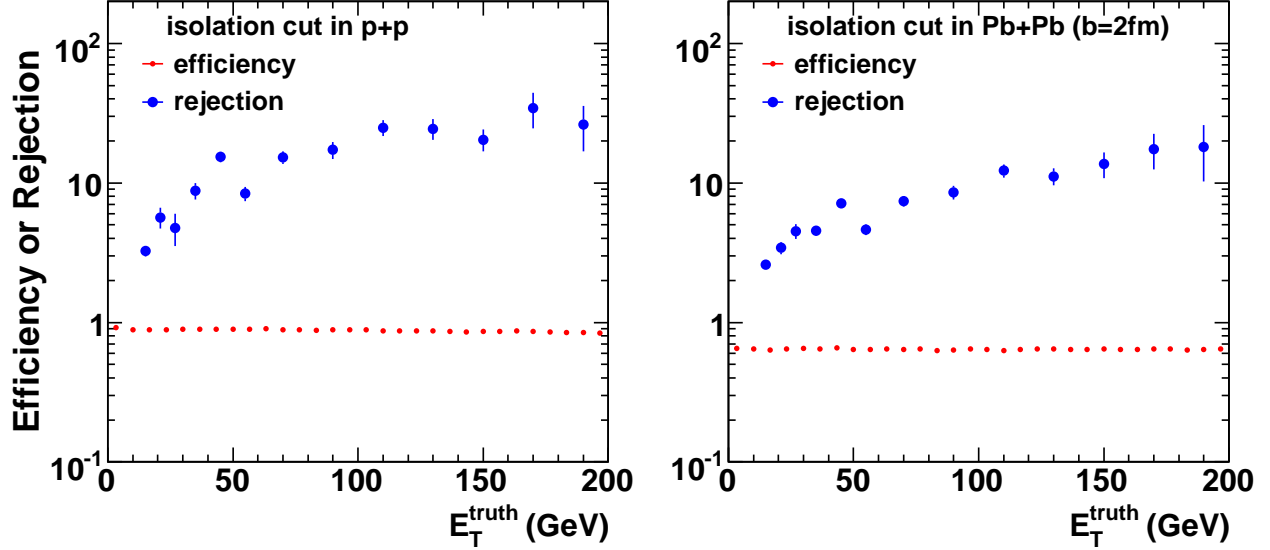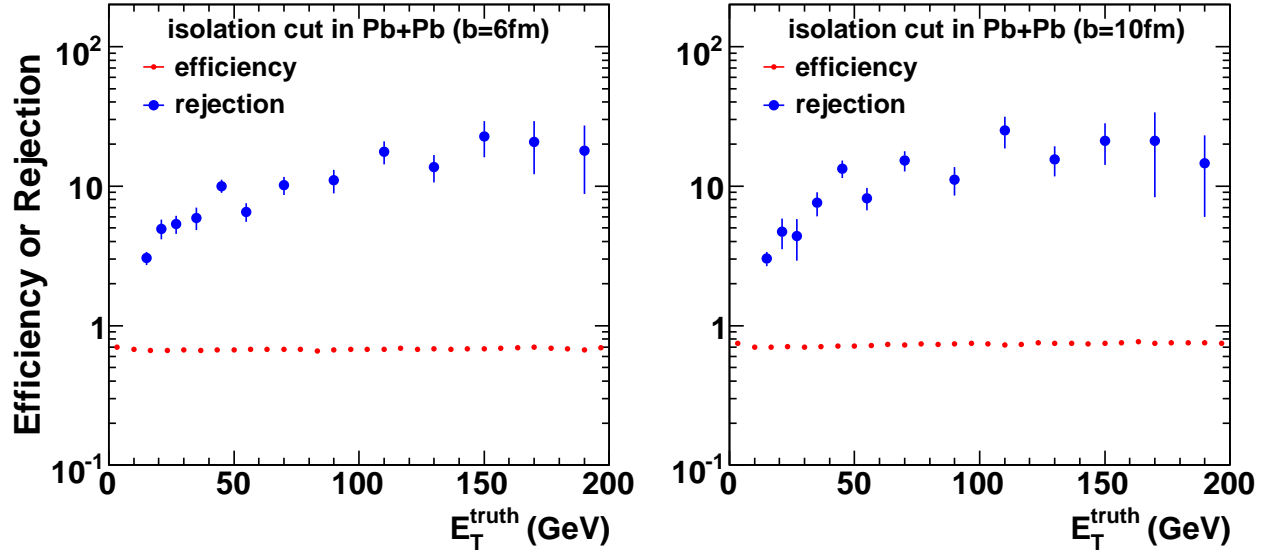
Figure 8.10: The photon efficiency and absolute rejection for background neutral hadrons for the isolation cuts (see Table. 8.1) as a function of energy in (left) b=6 fm and (right) b=10 fm Pb+Pb events.
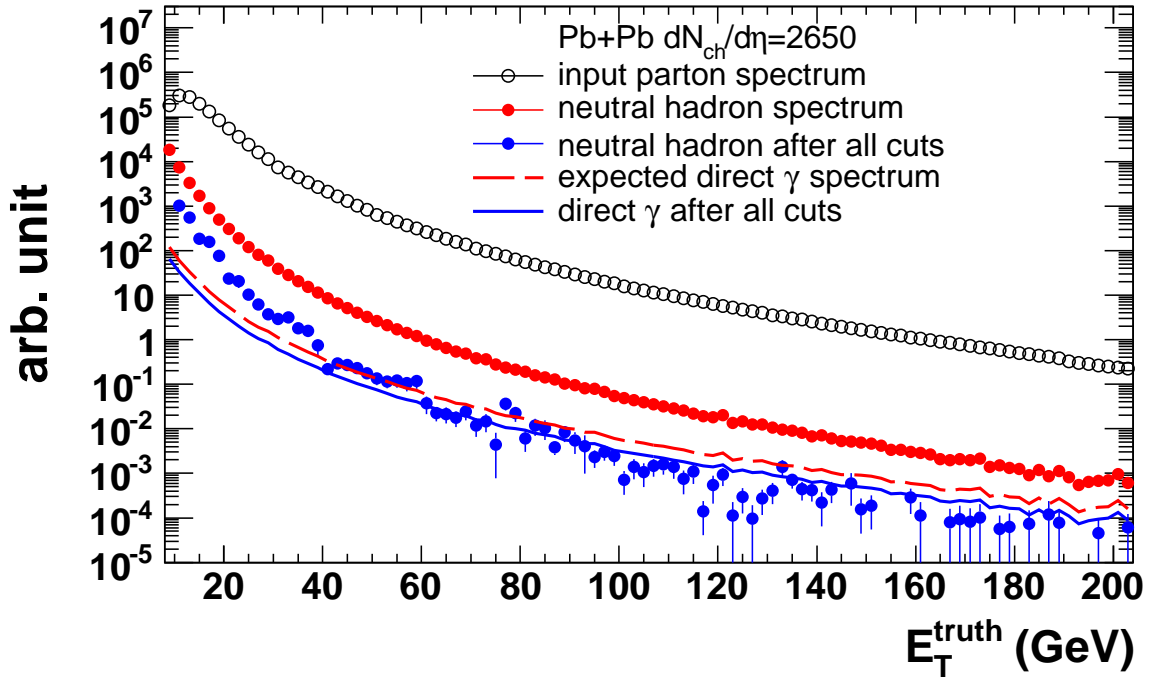
Figure 8.11: The performance of the shower shape cuts and isolation cuts on PYTHIA di-jets embedded into $b = 2$ fm Pb+Pb events. The spectra shown are for input jets (open circles), input $\pi^0 + \eta$ (red solid circles), remaining $\pi^0 + \eta$ (blue solid circles), expected direct γ (dashed line) and direct γ surviving all cuts (solid line).

Figure 8.12 shows the ratio of direct photons to remaining neutral hadrons passing the cuts as function of photon energy in central Pb+Pb events. Assuming no suppression for neutral hadrons, $S/B = 1$ is reached for 100 GeV photons (left plot). By assuming a factor of 5 suppression of high p_T yields for π^0 and η (see Section 1.4, Fig. 1.5 and Ref. [16]), the S/B is improved by a factor of 5, which leads to a $S/B \sim 1$ for 30 GeV photons. This should be compared with the original S/B, which is less than 0.1 below 100 GeV according to the NLO pQCD calculations shown in Fig. 8.2. Note that the improvement of S/B towards high E_T is partly due to the increase of $\gamma/(\pi^0 + \eta)$ ratio.

Figure 8.12: The ratio of direct photons over background neutral hadrons passing the loose shower shape cuts only (solid squares), isolation cuts only (open circles) and combined cuts (solid circles) in central Pb+Pb events, assuming (left) no suppression for hadrons, and (right) a factor of 5 suppression for hadrons.

The centrality dependence of the direct photon performance is summarized in Fig. 8.13. The S/B ratio is the best in p+p collisions, which is about factor of 4–5 larger than that for most central Pb+Pb events. However, by taking into account the benefit one gains from the likely hadron suppression, we expect to achieve a similar level of performance that is approximately independent of the event centrality.

8.5 Rate estimate

The number of expected direct photons observed per year is based on the following assumptions:

- 3 weeks/year running at 60% up time, which gives 0.5 nb^{-1} integrated luminosity for minimum bias Pb+Pb collisions;

- Estimation of the direct photon yield based on the next to leading order pQCD calculation shown in Fig. 8.2;

- Photon reconstruction efficiency of 50% passing the shower shape and isolation cuts;
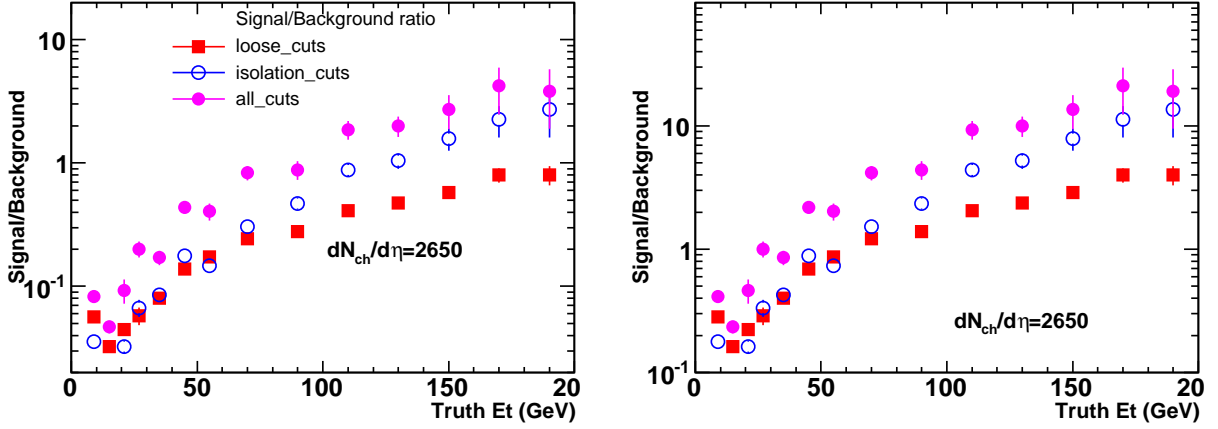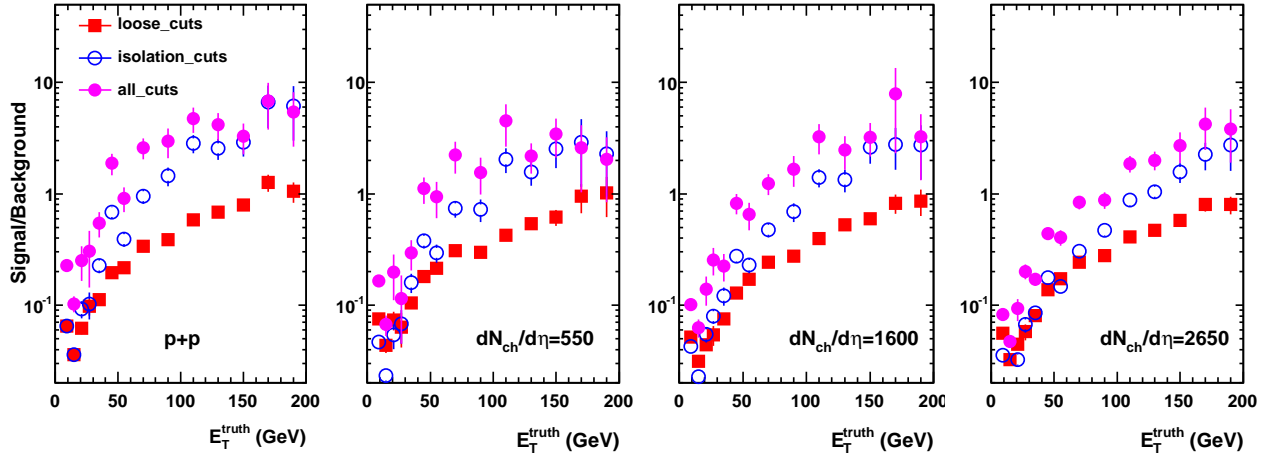
Figure 8.13: The ratio of direct photons over background neutral hadrons passing the loose shower shape cuts only (solid squares), isolation cuts only (open circles) and combined cuts (solid circles) for different occupancies under the assumption that the nuclear modification factor $R_{\mathrm{AA}} = 1$, for all centralities.

- π^0's and η's are suppressed by a factor of 5 in central Pb+Pb collisions.

- Triggering strategy in Pb+Pb collisions as described in Chapter 9.

Based on these assumptions, 200k (10k) γ will be measured above 30 GeV (70 GeV) per LHC year with $S/B > 1$ ($S/B > 4$).

Figure 8.14 shows the estimated statistical error bars for a direct photon spectrum after a nominal heavy ion run for a variety of centralities, showing the ability to measure direct photons out to 200 GeV. We assume that the analyzed sample of the most central events ($dN_{ch}/d\eta = 2650$), mid-central events ($dN_{ch}/d\eta = 1600$), and peripheral events ($dN_{ch}/d\eta = 550$) will constitute 0-10%, 10-30% and 30-100% of the total inelastic cross-section, respectively. Note that we haven't performed the subtraction of the remaining decay background, which will necessarily lead to additional efficiency loss and sizable systematic uncertainties, especially for low p_T where the S/B is still low. For Figure 8.14, we simply assumed 100% efficiency for such background subtraction procedure. We defer evaluation of the efficiency and systematic uncertainty associated with background subtraction to a future study.

8.6 γ-jet correlations

Once the direct photons are cleanly identified, the away-side jet can be reconstructed and it is feasible to study the correlation between the γ and jet. A first attempt at measuring such a coincidence has been made. A set of PYTHIA γ-jet events was generated and embedded into the same set of HIJING events without quenching used for the jet performance study. Jet reconstruction was performed using the seeded cone algorithm with $R = 0.4$ and 5 GeV seed towers as described in Chapter 6. The photons were measured using the photon identification and isolation cuts outlined earlier.
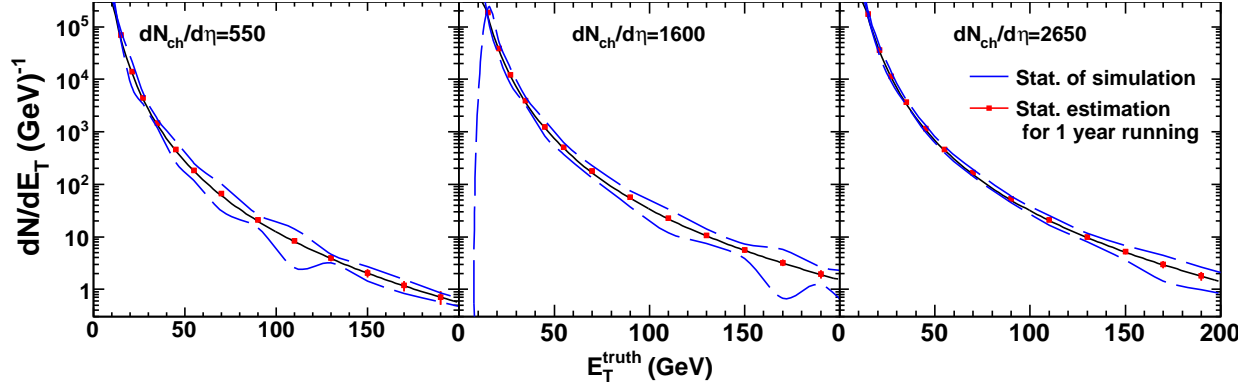
Figure 8.14: Simulated photon spectrum expected after the application of cuts for (left panel) peripheral, (middle panel) mid-central, and (right panel) central Pb+Pb collisions. The error is the expected statistical error calculated based on direct photon yield folded with efficiency. The potential systematic error associated with rejecting remaining decay background is not evaluated yet. The blue dashed lines indicated the statistical uncertainty due to the simulation.

Two different energy ranges for γ-jet correlations are shown in Figure 8.15. The left-hand plot shows the $\Delta\phi$ correlation between isolated photons from 40–60 GeV with jets from the same energy interval while the right-hand plot shows photons and jets from 60–80 GeV. The filled symbols indicate the result for the standard fake jet rejection cut on $\sigma_{j_T^{Sum}}$ which was used in the jet performance study (see discussion in Chapter 6 and Figure 6.9). A clear away-side jet signal around $\Delta\phi = \pi$ is visible above the low, flat background in both cases. The open symbols in the figure show the results with a relaxed, looser, cut which lets in fake jets. The pedestal level indicates the upper limit of fake jets, since their distribution is expected to be random (i.e. flat) in $\Delta\phi$. This type of comparison will allow a data-driven determination of the optimal fake jet rejection criterion as well as a confirmation of our understanding of the efficiency and purity of the cut and the expected background. A S/B ratio can be defined by fitting a gaussian plus flat background to plots such as those in Fig. 8.15. The γ-jet S/B as a function of the fake jet rejection cut is shown in Fig. 8.16.

A more complete study would require evaluation and subtraction of the residual background contamination in the triggering direct photons. Nevertheless, our initial results indicate that it is indeed possible to tag away-side jets. Especially above 50 GeV where the direct photon background and fake jet contamination are small. These γ-jet correlations will be an essential physics measurement, allowing us to understand the energy loss and fragmentation behavior of partons in the medium as well as the response of the medium to a hard parton. In addition, they could be used to improve jet energy scale calibration, to reject background jets and to improve the reconstruction efficiency by testing for a coincidence with isolated photons. However, more studies are needed to quantify such physics potentials.
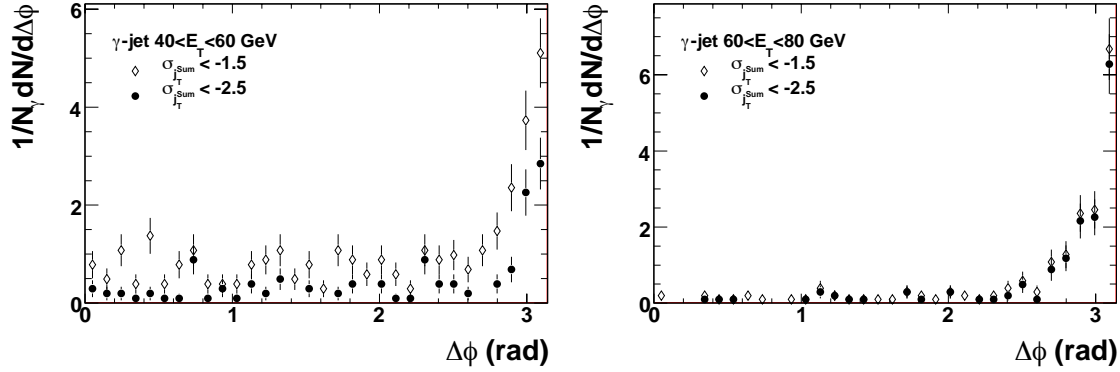
Figure 8.15: Correlations in $\Delta\phi$ for γ-jet pairs where both the photon and the jet have 40-60 GeV (left) and 60-80 GeV (right) in E_T. Two different fake-jet-rejection cuts are used: tight (filled symbols) and loose (open symbols).
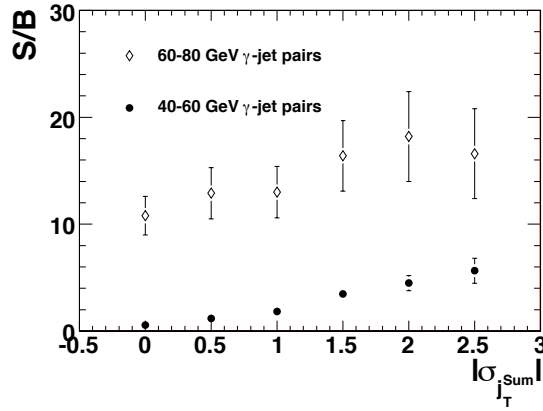
Figure 8.16: The resulting γ-jet signal-to-background in the peak region for both sets of E_T bins.

8.7 Unique ATLAS capabilities

ATLAS's large acceptance allows full jet reconstruction in 2π and up to 10 units in pseudo-rapidity ($|\eta| < 5$) with $> 50\%$ efficiency for jets above 50 GeV in central Pb+Pb collisions (see Fig.6.12). The results presented in this chapter show that ATLAS can reconstruct a highly-pure sample of direct photons above $E_T = 20$ GeV over nearly 5 units in pseudo-rapidity ($|\eta| < 2.4$) with a constant 50–60% efficiency even for central Pb+Pb collisions with $dN_{ch}/d\eta = 2650$. Combined with the measurement of global properties of the collision (as discussed in Chapter 5), this should allow a detailed study of γ-jet tomography as a function of centrality and angle relative to the reaction plane in a broad E_T and η range.

ATLAS's sophisticated calorimeter system provides γ and γ-jet capabilities which are competitive, and often superior, compared to ALICE and CMS. Compared to ALICE, the advantage of the ATLAS detector lies in its large detector acceptance (see Figure 8.17) coupled with its high rate

triggering capability. Compared to CMS, which also has a large acceptance calorimeter and a similar trigger system, the advantage of the ATLAS design is its longitudinally segmented calorimeter, and especially the finely-segmented strips in the first layer. This will allow the discrimination between γ's and neutral hadrons independent of the isolation cuts. In the case of γ-jet, this should allow ATLAS to extend the measurements down to $E_T = 20$ GeV.

One area where the ATLAS calorimeter provides capabilities completely unmatched by the other LHC experiments is the measurement of medium induced photons over the full experimental acceptance. Recent theoretical calculation constrained by existing photon data have suggested that direct photons coming from final-state sources — such as fragmentation, in-medium gluon conversion and medium-induced bremsstrahlung — can dominate the direct photon yield up to $p_T = 50$ GeV [140]. These are compelling phenomena to address since their production rate directly reflects the interaction of quarks and gluons as they propagate through the medium.

Fragmentation and medium-related photons are not straightforward to measure in general, as they are produced close to the primary jet, and thus can not be extracted using isolation cuts. Fortunately, the first layer of the ATLAS electromagnetic calorimeter, as discussed in section 8.2, has sufficiently fine segmentation in η that it can resolve fragmentation photons even within jets. Fig.8.6 suggests that even without isolation, a tight γ identification cut can provide a unbiased, centrality-independent relative rejection factor of 3 to 5 against the hadronic decay background with about 50% efficiency for the photons. Assuming the yield of medium-induced photons is roughly equal to that of prompt photons, as suggested by recent NLO calculations, a S/B of about 0.3 will be achieved at around $E_T = 50$ GeV in central Pb+Pb collisions. This will allow a statistical subtraction of the hadronic background and facilitate the first measurement of medium-induced photons in heavy ion collisions over a large acceptance, and thus down to very low x.

8.8 Summary

This chapter has presented the ATLAS performance for direct photon identification and γ-jet correlation measurements.

- The first layer of the ATLAS electromagnetic calorimeter provides an unbiased relative rejection factor against background neutral hadrons of either 1.5–3 (loose shower shape cuts) or 3–6 (tight shower shape cuts).

- The loose γ identification cuts can be combined with isolation cuts which can provide an additional factor of about 10 relative rejection. This results in a total relative rejection of about 20 even in central Pb+Pb collisions.

- The photon efficiency is constant at 60% down to $E_T = 20$ GeV for central Pb+Pb allowing the study of medium modification for low-E_T jets.

- Identified direct photons can improve the reconstruction efficiency and S/B significantly for jets below 80 GeV, relative to the performance for jet reconstruction without tagging.

- If the medium induced direct photon yield is as large as suggested by some theoretical calculations [140], then the tight shower shape cuts alone may provide good rejection against hadron decays within jets to allow the study of fragmentation photons, in-medium gluon conversion and medium-induced bremsstrahlung. This is a unique capability of ATLAS.

113
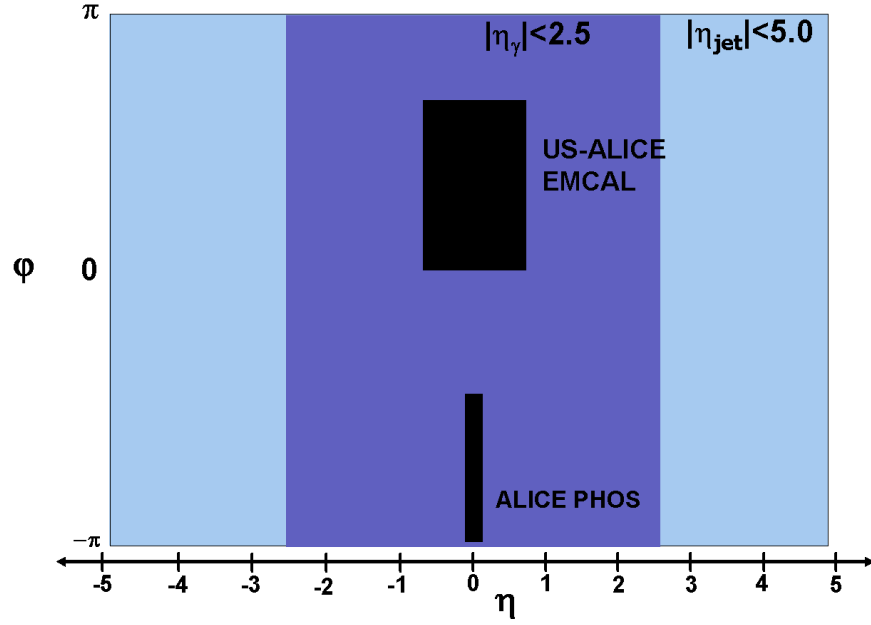
Figure 8.17: Comparison of acceptance for γ-jet physics between ATLAS and ALICE, CMS acceptance is comparable to ATLAS.

- Based on the Monte-carlo estimation of the background, the expected luminosity could provide 200k photons above 30 GeV with $S/B > 1$, and 10k above 70 GeV per LHC year with $S/B > 4$ [2].

---

[2]Determining the S/B is necessarily data-driven, current estimate could be affected by the uncertainty in the efficiency, background subtractions, and multiplicity of the Pb+Pb collisions.

Chapter 9

Trigger & DAQ

The ATLAS data acquisition system is well suited to carrying out the measurements described in this proposal both in terms of readout capability and triggering. This chapter briefly summarizes the design of the ATLAS data acquisition system (DAQ), discusses the conditions under which the DAQ system will operate during Pb+Pb running, and describes the strategy for minimum-bias and rare process triggering during heavy ion data-taking.

9.1   ATLAS data acquisition system

ATLAS has implemented a traditional collider data acquisition system [144] (see diagram in Fig. 9.1) utilizing a three-level trigger system that can, in principle, sample every bunch crossing at 40 MHz while reducing the rate of recorded events to a few hundred Hz, limited by an aggregate data rate of 300 MByte/sec. Data from all detector channels are sampled and stored in either analog or digital form at the bunch crossing frequency.

The ATLAS Level-1 trigger [145] uses data from the electromagnetic and hadronic calorimeters, the Muon trigger chambers, trigger scintillators, and (for Pb+Pb operation) the ZDC to make a decision to keep or reject data from a bunch crossing within 2.5 μs of crossing. Data from events selected by the Level-1 trigger – up to a maximum rate of 75 kHz – are partially read out and processed by the Level-2 trigger processor farm. Events selected by the Level-2 trigger up to a maximum rate of 1 kHz are completely read out and then subjected to offline style analysis in the ATLAS "Event Filter" farm. Event Filter reduces the event rate to approximately 200 Hz with an average processing time of the order of four seconds. Events selected by Event Filter algorithms are transmitted to the ATLAS Tier 0 system for recording and immediate analysis.

During high luminosity (10^{34} cm^{-2}s^{-1}) p+p operation of the LHC there will be $\sim$ 20 minimum-bias p+p collisions per bunch crossing. Under these conditions the total data volume read out from a single crossing is expected to be $\sim$ 1 MByte. The ATLAS DAQ system is designed to have sufficient throughput to read high-luminosity events out to the Event Filter farm at the maximum 1 kHz rate. These performance specifications will be used below to evaluate the DAQ performance under Pb+Pb conditions. The data from the ATLAS calorimeters provides the bulk of the estimated p+p events size as no zero suppression is applied in the calorimeter readout.

The ATLAS Level-2 and Event Filter systems – together referred to as the "High Level Trigger" (HLT) – were designed to find jets, photons, muons, and other desired signatures of interesting
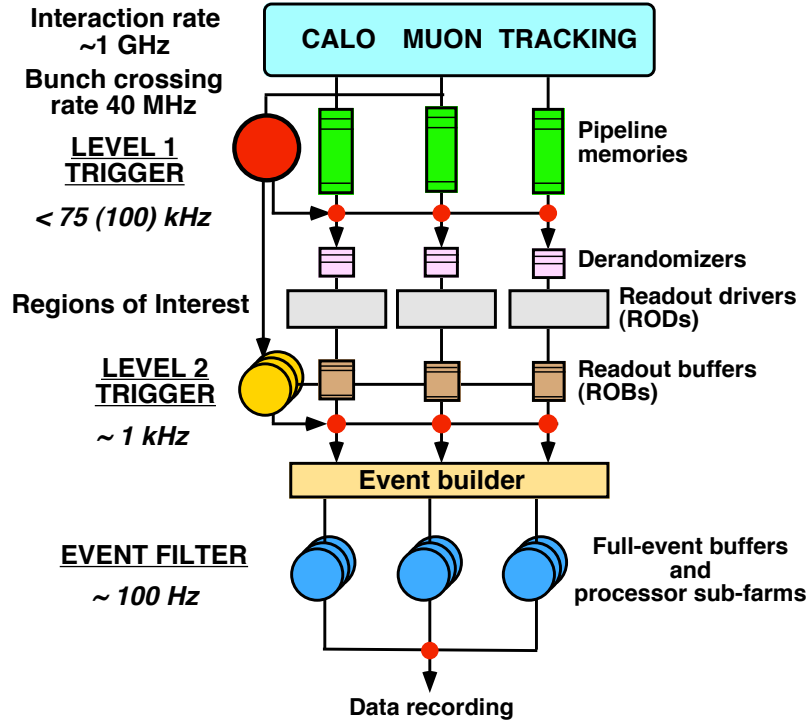
Figure 9.1: Schematic of the ATLAS data acquisition system.

physics in "Regions of Interest" (ROIs) identified by the Level-1 trigger. Each jet, photon, and muon candidate satisfying a Level-1 trigger criterion has a corresponding geometrical region that guides subsequent Level-2 and Event Filter analysis. This refines the Level-1 trigger decision and ultimately determines whether data from a given crossing are transmitted to the Tier 0 system for archiving. The combination of Level-1 trigger/ROI, Level-2 trigger algorithm, and Event Filter algorithm that select a specific physics pattern are collectively referred to as a "trigger slice." [NEED DISCUSSION OF HI EFFECT ON SLICES?]

9.2 Pb+Pb conditions

Based on the maximum anticipated Pb+Pb luminosity of 1×10^{27} cm^{-2}s^{-1} [146] and assuming a Pb+Pb total cross-section of 7.7 b [138], we expect a maximum Pb+Pb hadronic collision rate of 7.7 kHz. This rate is a factor of 10 below the maximum Level-1 trigger rate so the full minimum-bias Pb+Pb rate can be sampled by the Level-2 trigger. Nonetheless, the Level-1 trigger will be used to find jets, photons, and muons at Level-1 to provide regions of interest for Level-2 and Event Filter processing.

We have estimated an average minimum-bias event size of 5 MByte for Pb+Pb collisions using HIJING followed by complete GEANT4 simulations of the detector response. The modest increase in event size from p+p to Pb+Pb collisions is largely due to the fact that the calorimeter readout has no zero suppression. The increased event size will reduce the maximum rate at which events

DAQ Stage	Input Rate (Hz)	Max. Output Rate (Hz)	Max. Rejection
Level-1	$< 8 \times 10^3$	75×10^3	none
Level-2	$< 8 \times 10^3$	900	9
Event Filter	900	50	16

Table 9.1: Estimated maximum minimum-bias Pb+Pb event rates through different components of the ATLAS DAQ system and resulting upper limits of rejection required in each stage of trigger system.

can be transferred to the Event Filter farm. The specification for the ATLAS Event Builder which performs the complete readout of all events selected by the Level-2 trigger is that it should be able to read an aggregate data rate of 4.5 GBytes/s. Based on the above heavy ion event size we estimate a maximum output rate from Level-2 to be 0.9 kHz during Pb+Pb operation. The specification for the maximum archiving bandwidth from ATLAS is 300 MByte/s. Based on the estimated event size, this gives an archiving rate of approximately 60 events/s. These numbers are summarized in Table 9.1.

9.3 Pb+Pb minimum bias triggers

A well-understood minimum bias trigger is essential to the success of the heavy ion program. The uncertainty in the fraction of total inelastic cross section sampled by this trigger translates directly into an uncertainty on centrality variables (e.g. N_{part}, N_{coll}, or b) which gets significantly worse in more peripheral events. The RHIC program showed clearly that a variety of triggering schemes should be used, with careful offline cuts and various extrapolation techniques, to reduce this uncertainty. Doing this, all of the RHIC experiments kept uncertainties down to a few percent, even with triggers having less than 90% efficiency [NEED REF].

Multiple triggers are available for use as Pb+Pb minimum-bias triggers. The ZDC, described in the previous chapter, will provide a trigger whose efficiency is expected to be better than 90%. The ATLAS Minimum Bias Trigger Scintillators (MBTS) were designed to increase the efficiency for triggering on minimum-bias collisions in p+p collisions. Covering a pseudorapidity range of $2.4 < |\eta| < 3.8$, the MBTS has similar acceptance as multiplicity and trigger detectors used in RHIC experiments and will provide a Pb+Pb minimum-bias trigger with nearly 100% efficiency in Pb+Pb collisions. However, the MBTS is not expected to survive beyond early low luminosity runs due to radiation damage. The ATLAS Level-1 trigger has implemented a sum of the total transverse energy, ΣE_T, in the electromagnetic, hadronic, and forward calorimeters. A detailed study of the performance of the ΣE_T trigger including calorimeter suggests that the ΣE_T trigger would have an efficiency of 85% for a noise trigger rate of less than 10% of the true Pb+Pb minimum-bias trigger rate.

Beam-gas and halo events and other backgrounds will be removed in the HLT, which has more than sufficient capacity given that it is designed for 75 kHz input rate and the maximum heavy ion rate will be only about 10% of that. Various algorithms involving silicon spacepoints and tracks are being optimized for early p+p running[REF?], and we expect to be able to adapt these for heavy ion running. While the large occupancy will challenge these algorithms for more central events, these events are highly unlikely to ever arise from backgrounds, and so a simple threshold

on the MBTS total energy should be sufficient to tag them as good events. Conversely, the lower multiplicities will have a larger background contamination but in these the p+p algorithms should work properly.

9.4 Rare signal triggers

As noted in Section 9.2, no Level-1 trigger rejection is required during Pb+Pb running. However, we cannot simply skip Level-1 because it provides input for Level-2, so we will use the Level-1 trigger to find jet, photon, and muon ROIs that will be the starting point for later trigger processing.

The rare triggers of interest in Pb+Pb collisions include: jets, high-p_T photons/electrons, single muons/dimuons and Z's. Each of these triggers depends either on a calorimeter based trigger (jets, photons, electrons) and/or a muon trigger. We describe the Level-1 trigger strategy for each of these separately. Our studies of the performance of Level-2 and Event Filter algorithms on Pb+Pb events are not yet complete, but we expect the efficiency and resolution of the combined Level-2/Event Filter algorithms to be similar to the results presented in Chapters 6-8 as the algorithms are similar to the offline algorithms used in the presented physics studies.

9.5 Pb+Pb jet and photon triggers

9.5.1 Level-1

The ATLAS Level-1 trigger is designed to trigger on jets using an overlapping tiling of trigger towers of size $\Delta\eta \times \Delta\phi = 0.2 \times 0.2$ whose energies are calculated in the calorimeter readout electronics using a combination of analog and digital sums. The Level-1 jet sums are generated for tiles that cover $\Delta\eta \times \Delta\phi$ regions of 0.4×0.4, 0.6×0.6 and 0.8×0.8. In the forward region ($|\eta| > 2.9$) 16 tiles with size of 2.0×0.4 are used. The ATLAS jet trigger allows for 8 possible thresholds (resp. 4 for forward region) on each of the different tile sizes. Tiles that provide a local maximum E_T and pass at least one of the jet trigger E_T thresholds are candidate JET ROIs. The ROIs are tagged according to which threshold they satisfy and the list of generated ROIs is available for readout by the Level-2 trigger.

Because of the large background in heavy ion events, only the 0.4×0.4 tiles will be useful. As noted above, the primary role of the jet Level-1 trigger for heavy ion operation is to provide the ROIs for use in the HLT. The specification for the Level-2 readout of Level-1 jet trigger ROIs allows a maximum sustained rate of 32 JET ROIs to be read out per event. If the number of ROIs reaches this limit the recording stops. Thus, the loose thresholds can cause an effecting loss of a part of calorimeter. We need to optimize thresholds to accept as many interesting events as possible staying below the maximum allowed.

We have simulated the response of Level-1 trigger for PYTHIA di-jet events embedded into Pb+Pb HIJING events of different centralities. The left panel of Figure 9.2 shows the integral distribution of transverse energy in the 0.4×0.4 ROIs in terms of the number of ROIs per event satisfying a given $E_T^{4\times4}$ threshold. Three different centrality bins have been used: the most central ($dN/d\eta = 2700$, $b = 2$ fm), semi-peripheral ($dN/d\eta = 1700$, $b = 6$ fm), and peripheral collisions
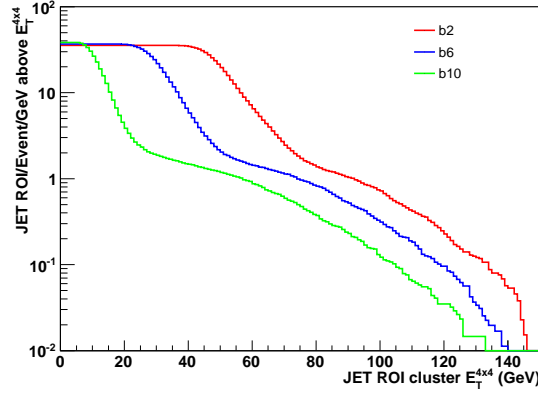
Figure 9.2: *Left:* Level-1 jet 0.4×0.4 ROI E_T distributions in reconstructed PYTHIA jets embedded to HIJING Pb+Pb events for three centrality bins - the most central ($dN/d\eta = 2700$, $b = 2$ fm), semi-peripheral ($dN/d\eta = 1700$, $b = 6$ fm), and peripheral collisions ($dN/d\eta = 460$, $b = 10$ fm). The distribution shows a number of ROIs per event satisfying a given threshold (x-axis). *Right:* A fraction of saturated events for a given threshold on JET ROI $E_T^{4\times4}$ (x-axis) in minimum bias Pb+Pb events.

1 ($dN/d\eta = 460$, $b = 10$ fm). Because of the baseline shift in the $E_T^{4\times4}$ energies resulting from the
2 Pb+Pb underlying event, the distribution shifts to larger energies for more central collisions.
3   In a current version of the trigger firmware it is not possible to set the threshold for JET ROIs
4 in correlation with the centrality measured by total E_T trigger. Therefore, the baseline strategy is
5 to set a single threshold for JET ROI. The rejection that is needed from Level-1 to Event Filter is
6 only a factor of 9. This implies that we can send some small fraction of saturated events directly
7 form Level-1 to Event Filter. The threshold thus has to maximize the efficiency and minimize the
8 number of events that are saturated. The right panel of Figure 9.2 shows a fraction of saturated
9 events for a given threshold on JET ROI $E_T^{4\times4}$ in minimum bias Pb+Pb events (without embedded
10 PYTHIA jets). One can see that selecting the threshold e.g. $E_T^{4\times4}$ =45 GeV gives small number of
11 saturated events, precisely 0.5×10^{-2}. These by-passed events fill the whole available input band-
12 width of Event Filter by 5 %. The efficiency for such a choice of the threshold is approaching 100%
13 above 70 GeV, below 70 GeV the efficiency is steeply decreasing namely for peripheral events. To
14 improve the jet trigger efficiency we can use JET ROIs in combination with other trigger objects as
15 we will discus further. The trigger information from the forward region provided by 16 tiles (each
16 having size of 2.0×0.4) will be directly transferred to the Level-2 trigger.
17   In addition to the jet regions of interest described above, the ATLAS Level-1 trigger also pro-
18 vides the ability to trigger on photons and τ's using information from the calorimeter. The di-
19 agram in Figure 9.3 illustrates the function of the photon trigger. The photon trigger starts with
20 electromagnetic towers of size $\Delta\eta \times \Delta\phi = 0.1 \times 0.1$. The largest energy tower pair within a 0.2×0.2
21 region with E_T greater than one of eight thresholds, satisfying a cut on the electromagnetic energy
22 in a surrounding "isolation" ring and cut on the total hadronic energy in a 0.4×0.4 region be-
23 hind candidate ROI becomes an electromagnetic ROI (EM ROI). The isolation cut and the cut on
24 hadronic energy are optional. The integral distribution of EM ROI E_T above a given E_T^{EM} threshold
25 is shown in the left panel of Figure 9.4. Because the EM ROIs cover a much smaller $\Delta\eta \times \Delta\phi$
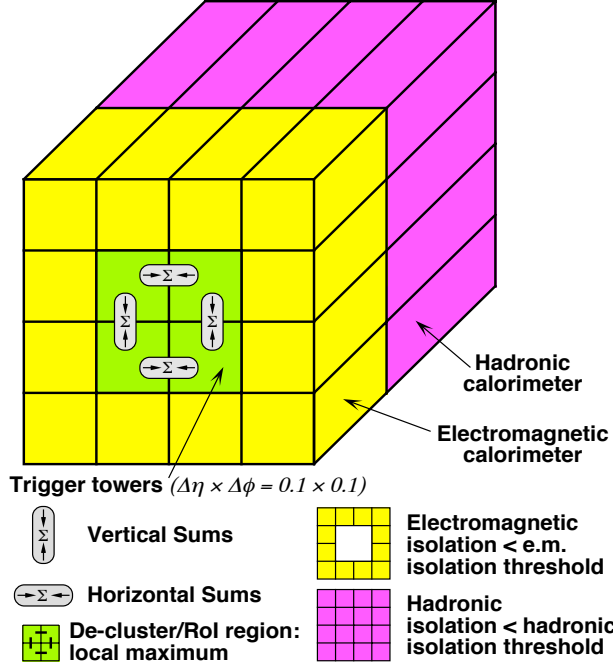
Figure 9.3: Diagram illustrating the Level-1 electromagnetic ROI algorithm

Figure 9.4: *Left:* Level-1 EM ROI E_T distributions in reconstructed PYTHIA jets embedded to HIJING Pb+Pb events for three centrality bins - the most central ($dN/d\eta = 2700$, $b = 2$ fm), semi-peripheral ($dN/d\eta = 1700$, $b = 6$ fm), and peripheral collisions ($dN/d\eta = 460$, $b = 10$ fm). The distribution shows a number of ROIs per event satisfying a given threshold (*x*-axis). *Right:* The efficiency of the jet trigger with EM/Tau ROIs included for three different centrality bins.

1 region, the baseline shift is much smaller in the E_T^{EM} distributions compared to the $E_T^{4 \times 4}$ distribu-
2 tions. Similarly to JET ROIs the limit on the maximal number of EM ROIs exists which is 64. To
3 avoid the saturation a threshold of 9 GeV is sufficient in the whole range of centrality. This thresh-
4 old is reasonably low and provides good ability to trigger on photons or electrons. The Level-1
5 calorimeter trigger also implements a Tau region of interest similar to the EM ROI but including
6 the hadronic layers. To avoid the saturation the threshold of 14 GeV on Tau ROI is sufficient.
7   In fact, we obtain this sufficient rejection simply with a cut on E_T of EM/Tau ROI without the
8 use of the isolation cut. By avoiding the isolation cut at Level-1 we avoid having to accommodate
9 the effect of the underlying event in the isolation ring, *and* we can use the Level-1 EM/Tau trigger
10 to reduce an inefficiency in the Level-1 jet trigger. A fixed threshold on JET ROI E_T can cause
11 that some jets will be excluded at Level-1. However, a significant fraction of such jets will have a
12 neutral hadron with sufficient energy that it could be selected by the EM/Tau trigger – which is
13 much less sensitive to the fluctuations in the underlying event.
14   The efficiency of the jet trigger with EM/Tau ROIs included for three different centrality bins
15 is shown in the right panel of Figure 9.4. The threshold for the JET ROI is 45 GeV, the threshold

for EM ROI and Tau ROI is 9 GeV and 14 GeV respectively. For this study the embedded PYTHIA jets with energy of the initial parton in the range of $70 - 140$ GeV were used. Each jet identified by the Level-1 trigger was matched to an offline reconstructed jet found using the modified cone algorithm described in Chapter 6. The matching criterion in searching for the closest offline jet was $\Delta R = 0.2$. One can see that above 50 GeV the efficiency is above 90%.

We should bear in mind that this initial study represents the worst case scenario because we can request the firmware modification of the trigger system that would allow for a centrality dependent trigger on rare signals. However such a modification is non-trivial and requires intervention of experts.

9.5.2 Level-2 and Event Filter

The Level-2 trigger will provide the first real rejection during Pb+Pb data-taking. The Level-2 trigger has access to all of the data generated by the Level-1 trigger including JET and EM ROIs and the ΣE_T from the calorimeters (see Section 9.3), which allows characterization of Pb+Pb collision centrality. This ΣE_T value will be used to estimate the energy of the underlying event contributing to the overall jet energy.

For Level-2 jet reconstruction a simplified version of the offline iterative cone jet algorithm is used to refine the jet energy and position. For Pb+Pb collisions, the background subtraction based on ΣE_T will be performed. Since the p+p implementation of the Level-2 trigger uses the full set of calorimeter cells for performing the jet finding, the only additional time spent in the Level-2 jet algorithm for Pb+Pb collisions will be the step of subtracting the estimated background value from the calorimeter cells and evaluating discriminant quantities to remove false jets. Events selected as satisfying a jet Level-2 trigger will be re-analyzed in the Event Filter using more complete calibrations and corrections and using the same background subtraction procedure as used in the offline analysis. We, therefore, expect the performance of the Event Filter algorithm to be similar to the results shown in Section 6.4.2.

The thresholds that will be applied at Level-2 and in the Event Filter will depend on the actual jet production rates including the effects of shadowing and quenching, and properties of the Pb+Pb underlying event. They will also depend on the fraction of the 50 event/s recording rate allocated to jet triggers. Figure 9.5 shows a plot of the estimated number of jets per event produced in the ATLAS acceptance above a given E_T as a function of E_T assuming no quenching and neglecting shadowing. This result was obtained from the PYTHIA cross-sections used in Section 6.4.1 scaled by T_{AB}, and integrated over $|\eta| < 5$ and presented as the number of jets per minimum-bias Pb+Pb collision above a given E_T. These numbers are uncertain to at least a factor of two because of NLO contributions not accounted for by the K-factor in PYTHIA, shadowing of nuclear PDFs not included in PYTHIA, unknown effects related to jet quenching (see Fig. 6.6), and other effects. However, Fig. 9.5 shows clearly that the jet rates in Pb+Pb collisions at the LHC will be high, with more than one $E_T > 100$ GeV jet in a thousand Pb+Pb events. If we suppose that 20% of the recording bandwidth is dedicated to jet triggers, at full luminosity a jet E_T threshold of > 100 GeV would be required to reduce the 7.7 kHz minimum-bias rate to 10 Hz. However, at lower luminosities – either during a first LHC Pb+Pb run or later in stores – a trigger as low as 50 GeV could be utilized. In fact, a mixture of jet thresholds will be used with scaledowns to collect statistics over the entire E_T range.
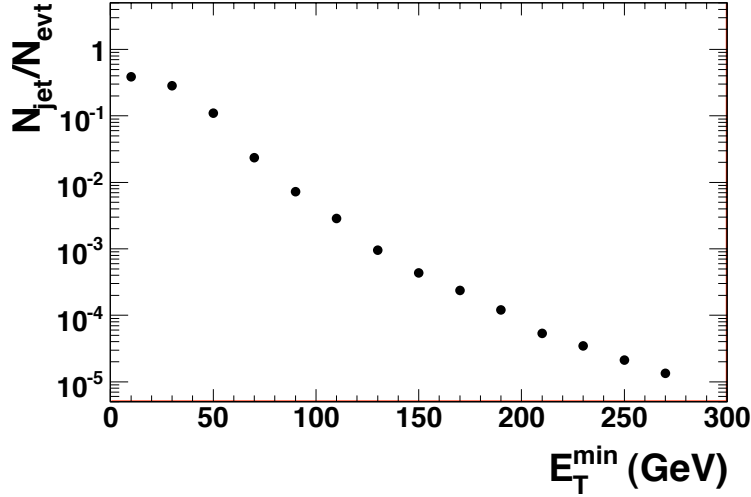
121

Figure 9.5: Estimated number of jets per event in the ATLAS acceptance above a given E_T in minimum-bias Pb+Pb collisions.(see text for details).

9.5.3 Pb+Pb muon triggers

Muon triggering is provided by Resistive Plate Chambers (RPC) in the barrel region and Thin Gap Chambers (TGC) in the end-caps. The ATLAS Level-1 Muon trigger system is designed to select events with single muons passing one or more p_T threshold or events containing two muons passing one or more of the thresholds. In the current offline implementation of muon trigger emulation, di-muon triggers do not have invariant mass cut; the only requirement is that an event has two muons with p_T above the applied threshold.

The Level-1 muon trigger efficiency was studied using PYTHIA simulated p+p events containing Y's that were merged with minimum bias Pb+Pb HIJING events. The default p+p trigger thresholds were used with the lowest threshold corresponding to $p_T \approx 6$ GeV/c. The trigger efficiency was defined as the number of events in which an Y was reconstructed and trigger fired, divided by the number of events in which an Y was reconstructed. The results for the Level-1 efficiency are shown in Fig. 9.6 as a function of Y p_T. As shown in the figure, the trigger efficiency is rather low, especially if the Ys are required to pass a Level-1 di-muon trigger. However, this low efficiency results primarily from the default muon p_T threshold of 6 GeV/c. Due to the Y decay kinematics the probability to have both muons with $p_T > 6$ GeV/c is very low.

Since rejection is not needed at Level-1, we will use multiple strategies to achieve higher Y trigger efficiency. First we can lower the p_T cut on the muons down to a minimum of 3.5 GeV/c. By reducing the cut we will improve the likelihood that both muons are found by the Level-1 trigger allowing a real invariant mass cut on be applied at Level-2. Second, we will accept some rate (yet to be determined) of single muon triggers through to the Event Filter where the full offline muon reconstruction can be performed. Assuming that the rejection provided by the single muon trigger at 6 GeV/c is sufficient to allow all selected events through to the Event Filter, the resulting Y efficiency would be approximately that of the single muon curve shown in Fig. 9.6. Ultimately, a combination of single and di-muon triggers with a variety of p_T thresholds will be used at Level-1 to seed Level-2 and Event Filter algorithms – similar to the jet and photon
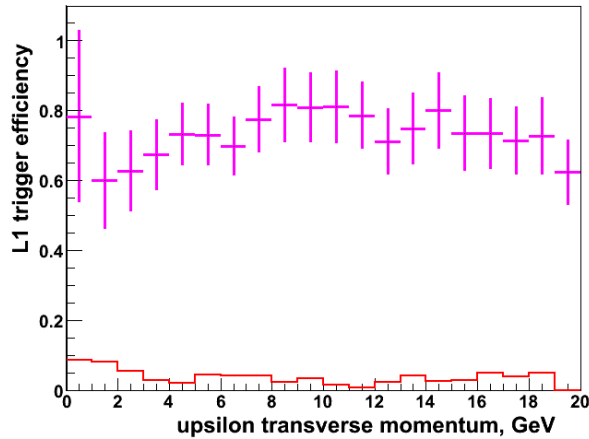
Figure 9.6: Level-1 Y trigger efficiency as a function of Y p_T obtained using PYTHIA p+p events with forced Y production merged into minimum bias Pb+Pb HIJING and using default p+p muon trigger thresholds. Magenta points show single muon trigger efficiency (any Level-1 single muon trigger fired), while red histogram shows di-muon trigger efficiency (two muons passing trigger thresholds). Error bars show statistical errors only.

trigger schemes described above. The combined performance of the resulting muon trigger slices is underway. We note that the single muons found at Level-1 can also be correlated with jets at Level-2 and in the Event Filter to select heavy flavor jets for archiving [REF TO HEAVY FLAVOR JET SECTION].

9.6 Summary

The ATLAS data acquisition and trigger system is well suited to carry out the Pb+Pb measurements described in this proposal. During Pb+Pb operation ATLAS will record roughly 50 Pb+Pb events per second. Multiple triggers will be used as Pb+Pb minimum-bias triggers, including a ZDC coincidence trigger, a scintillator-based coincidence trigger (MBTS), and a calorimeter ΣE_T threshold trigger. The combination of these triggers is expected to provide a minimum-bias Pb+Pb efficiency greater than 95%. For rare signals no rejection is needed at Level-1 for all expected Pb+Pb luminosities, but the Level-1 trigger will be used to find regions of interest that will be used in the Level-2 trigger and the Event Filter to select jets, photons, and muons and a fraction of minimum-bias Pb+Pb events for recording. The threshold for the jet and electromagnetic regions of interest can be set low enough to have little or no impact on the trigger efficiency for photons and electrons, and to provide a reasonable efficiency for jets. The Level-2 trigger will use fast versions of offline algorithms to reconstruct jets with background subtraction and find electromagnetic clusters. The Event Filter will run full offline analysis on the regions of interest found by Level-1 and surviving Level-2 cuts. The resulting performance for jet and photon finding in the combined Level-2 and Event Filter systems will be similar to the results presented in Chapters 6 and 8. For Y measurements, the default p+p Level-1 di-muon trigger is found to be inefficient in selecting Y's at Level-1. However, since rejection is not needed at Level-1, a combination of

single muon and di-muon triggers with lowered p_T thresholds at Level-1 will seed Level-2 and Event Filter algorithms that can select Y's based on invariant mass cuts and with better efficiency. The Level-1 single muon triggers will also provide the ability to select heavy flavor jets at Level-2 and in the Event Filter. [NEEDS SOME MORE GENERAL CONCLUSION ABOUT ATLAS HI TRIGGERING]

Chapter 10

Summary

The primary physics goals of the ATLAS Heavy Ion program outlined in the introduction and described in this proposal are to

- Carry out "day-1" measurements of global observables such as $dN_{ch}/d\eta$, $dE_T/d\eta$, $v_2(p_T,\eta)$ as a function of centrality.

- Carry out quantitative, tomographic measurements of the properties of QGP created in heavy ion collisions at the LHC using complete jets, measurements of jet fragmentation observables, photon-jet pairs, tagged heavy quarks, and heavy vector bosons.

- Probe the response of the medium to the passage of energetic jets with large-acceptance studies of $d^2E_T/d\eta\,d\Delta\phi$ and $d^3N/d\eta\,dp_T\,d\Delta\phi$ in events containing high-energy jets.

- Probe Debye screening in the QGP via measurements of Υ decays to di-muons.

- Use a future p+A program to study semi-hard and hard processes at low-x to constrain nuclear shadowing and test models of parton saturation.

This program focuses on the use of hard probes to study the properties of the QGP created in heavy ion collisions at the LHC. It necessarily includes the global measurements that will be essential for constraining theoretical interpretations of the jet and quarkonia measurements. The proposed program also takes full advantage of the strengths of the ATLAS detector, namely:

- Large acceptance, electromagnetic and hadronic calorimeters

- Fine transverse segmentation and three-fold longitudinal segmentation of electromagnetic calorimeters

- Large-acceptance silicon tracking with pixel and strip detectors

- Large-acceptance muon spectrometers

125

Bibliography

[1] *The QCD Equation of State with almost Physical Quark Masses*, M. Cheng et al., Phys. Rev. **D77**, 014511 (2008), 0710.0354.

[2] *Quantum Chromodynamics and the Theory of Superdense Matter*, E. V. Shuryak, Phys. Rept. **61**, 71 (1980).

[3] *Universal features of QCD dynamics in hadrons and nuclei at high energies*, R. Venugopalan (2007), 0707.1867.

[4] *The glasma initial state at the LHC*, T. Lappi, J. Phys. **G35**, 104052 (2008), arXiv:0804.2338.

[5] *The large N limit of superconformal field theories and supergravity*, J. M. Maldacena, Adv. Theor. Math. Phys. **2**, 231 (1998), hep-th/9711200.

[6] *Viscosity in strongly interacting quantum field theories from black hole physics*, P. Kovtun, D. T. Son, and A. O. Starinets, Phys. Rev. Lett. **94**, 111601 (2005), hep-th/0405231.

[7] *Energy loss and flow of heavy quarks in Au + Au collisions at $\sqrt{s_{NN}}$ = 200 GeV*, A. Adare et al. (PHENIX), Phys. Rev. Lett. **98**, 172301 (2007a), nucl-ex/0611018.

[8] URL `https://wiki.bnl.gov/TECHQM/index.php/Main_Page`.

[9] *Evidence for a new state of matter: An assessment of the results from the CERN lead beam programme*, U. W. Heinz and M. Jacob (2000), nucl-th/0002042.

[10] *Centrality and pseudorapidity dependence of elliptic flow for charged hadrons in Au + Au collisions at $\sqrt{s_{NN}}$ = 200 GeV*, B. B. Back et al. (PHOBOS), Phys. Rev. **C72**, 051901 (2005a), nucl-ex/0407012.

[11] *Elliptic flow in Au + Au collisions at $\sqrt{s_{NN}}$ = 130 GeV*, K. H. Ackermann et al. (STAR), Phys. Rev. Lett. **86**, 402 (2001), nucl-ex/0009011.

[12] *Comparison of chemical freeze-out criteria in heavy-ion collisions*, J. Cleymans, H. Oeschler, K. Redlich, and S. Wheaton, Phys. Rev. **C73**, 034905 (2006), hep-ph/0511094.

[13] *Quark gluon plasma and color glass condensate at RHIC? The perspective from the BRAHMS experiment*, I. Arsene et al. (BRAHMS), Nucl. Phys. **A757**, 1 (2005), nucl-ex/0410020.

[14] *The PHOBOS perspective on discoveries at RHIC*, B. B. Back et al., Nucl. Phys. **A757**, 28 (2005b), nucl-ex/0410022.

[15] *Formation of dense partonic matter in relativistic nucleus nucleus collisions at RHIC: Experimental evaluation by the PHENIX collaboration*, K. Adcox et al. (PHENIX), Nucl. Phys. **A757**, 184 (2005), nucl-ex/0410003.

[16] *High transverse momentum eta meson production in p + p, d + Au and Au + Au collisions at $\sqrt{s_{NN}}$ = 200 GeV*, S. S. Adler et al. (PHENIX), Phys. Rev. **C75**, 024909 (2007a), nucl-ex/0611006.

[17] *High-p(T) tomography of d + Au and Au + Au at SPS, RHIC, and LHC*, I. Vitev and M. Gyulassy, Phys. Rev. Lett. **89**, 252301 (2002), hep-ph/0209161.

[18] *Evidence from d + Au measurements for final-state suppression of high p_T hadrons in Au + Au collisions at RHIC*, J. Adams et al. (STAR), Phys. Rev. Lett. **91**, 072304 (2003), nucl-ex/0306024.

[19] *Modifications to di-jet hadron pair correlations in Au + Au collisions at $\sqrt{s_{NN}}$ = 200 GeV*, S. S. Adler et al. (PHENIX), Phys. Rev. Lett. **97**, 052301 (2006a), nucl-ex/0507004.

[20] *Disappearance of back-to-back high p_T hadron correlations in central Au + Au collisions at sNN = 200 GeV*, C. Adler et al. (STAR), Phys. Rev. Lett. **90**, 082302 (2003), nucl-ex/0210033.

[21] *Distributions of charged hadrons associated with high transverse momentum particles in p+p and Au + Au collisions at $\sqrt{s_{NN}}$ = 200 GeV*, J. Adams et al. (STAR), Phys. Rev. Lett. **95**, 152301 (2005), nucl-ex/0501016.

[22] *Indications of Conical Emission of Charged Hadrons at RHIC*, B. I. Abelev et al. (STAR) (2008), 0805.0622.

[23] *Quantitative Constraints on the Opacity of Hot Partonic Matter from Semi-Inclusive Single High Transverse Momentum Pion Suppression in Au+Au collisions at sqrt(s_{NN}) = 200 GeV*, A. Adare et al. (PHENIX), Phys. Rev. **C77**, 064907 (2008), 0801.1665.

[24] *Direct observation of dijets in central Au + Au collisions at s(NN)**(1/2) = 200-GeV*, J. Adams et al. (STAR), Phys. Rev. Lett. **97**, 162301 (2006), nucl-ex/0604018.

[25] *Scaling of transverse energies and multiplicities with atomic number and energy in ultrarelativistic nuclear collisions*, K. J. Eskola, K. Kajantie, P. V. Ruuskanen, and K. Tuominen, Nucl. Phys. **B570**, 379 (2000), hep-ph/9909456.

[26] *Hadron multiplicities, p_T spectra and net-baryon number in central Pb + Pb collisions at the LHC*, K. J. Eskola, H. Honkanen, H. Niemi, P. V. Ruuskanen, and S. S. Rasanen (2007), 0705.1770.

[27] *Hard probes in heavy ion collisions at the LHC: Jet physics*, A. Accardi et al. (2004), CERN Yellow Report CERN-2004-009, hep-ph/0310274.

[28] *Medium modification of jet shapes and jet multiplicities*, C. A. Salgado and U. A. Wiedemann, Phys. Rev. Lett. **93**, 042301 (2004a), hep-ph/0310079.

[29] *Modified fragmentation function and jet quenching at RHIC*, X.-N. Wang, Nucl. Phys. **A702**, 238 (2002), hep-ph/0208094.

[30] *Simulation of jet quenching and high-p_T particle production at RHIC and LHC*, I. P. Lokhtin, S. V. Petrushanko, A. M. Snigirev, and C. Y. Teplov, PoS **LHC07**, 003 (2006), arXiv:0706.0665.

[31] I.P. Lohktin, private communication.

[32] *Drag force in AdS/CFT*, S. S. Gubser, Phys. Rev. **D74**, 126005 (2006), hep-th/0605182.

[33] *Radiative energy loss and p_T-broadening of high energy partons in nuclei*, R. Baier, Y. L. Dokshitzer, A. H. Mueller, S. Peigne, and D. Schiff, Nucl. Phys. **B484**, 265 (1997), hep-ph/9608322.

[34] *Heavy Ion Collisions at the LHC - Last Call for Predictions*, e. . Armesto, N. et al., J. Phys. **G35**, 054001 (2008a), 0711.0974.

[35] *Color Screening Melts Quarkonium*, A. Mocsy and P. Petreczky, Phys. Rev. Lett. **99**, 211602 (2007), 0706.2183.

[36] *The production of J/ψ in 200-GeV/nucleon Oxygen +Uranium interactions*, C. Baglin et al. (NA38), Phys. Lett. **B220**, 471 (1989).

[37] *Two particle azimuthal correlations at high transverse momentum in Pb - Au at 158-AGeV/c*, M. Ploskon (CERES), Nucl. Phys. **A783**, 527 (2007), nucl-ex/0701023.

[38] *Two- and three-particle azimuthal correlations of high- p_T charged hadrons in Pb+Au collisions at 158-AGeV/c*, S. Kniege and M. Ploskon (CERES), J. Phys. **G34**, S697 (2007), nucl-ex/0703008.

[39] *Expected Performance of the ATLAS Experiment - Detector, Trigger and Physics*, G. Aad et al. (The ATLAS) (2009), 0901.0512.

[40] *A detailed study of high-p_T neutral pion suppression and azimuthal anisotropy in Au + Au collisions at $\sqrt{s_{NN}}$ = 200 GeV*, S. S. Adler et al. (PHENIX), Phys. Rev. **C76**, 034904 (2007b), nucl-ex/0611007.

[41] *HIJING 1.0: A Monte Carlo program for parton and particle production in high-energy hadronic and nuclear collisions*, M. Gyulassy and X.-N. Wang, Comput. Phys. Commun. **83**, 307 (1994a), nucl-th/9502021.

[42] *Geant4 - a simulation toolkit*, S. Agostinelli et al., Nucl. Instr. Meth. **A506**, 250 (2003).

[43] *Expected Performance of the ATLAS Experiment - Detector, Trigger and Physics*, G. Aad et al., p. 747 (2008a), arXiv:0901.0512 [hep-ex].

[44] *PYTHIA 6.3: Physics and manual*, T. Sjostrand, L. Lonnblad, S. Mrenna, and P. Skands (2003), hep-ph/0308153.

[45] *High-energy physics event generation with PYTHIA 5.7 and JETSET 7.4*, T. Sjostrand, Comp. Phys. Commun. **82**, 74 (1994).

[46] *Glauber modeling in high energy nuclear collisions*, M. L. Miller, K. Reygers, S. J. Sanders, and P. Steinberg, Ann. Rev. Nucl. Part. Sci. **57**, 205 (2007), nucl-ex/0701025.

[47] *Color glass condensate at the LHC: Hadron multiplicities in p+p, p+A and A+A collisions*, D. Kharzeev, E. Levin, and M. Nardi, Nucl. Phys. **A747**, 609 (2005), hep-ph/0408050.

[48] *Zero Degree Calorimeters for ATLAS* (2007), CERN/LHCC/2007-001.

[49] *Eccentricity fluctuations and elliptic flow at RHIC*, R. S. Bhalerao and J.-Y. Ollitrault, Phys. Lett. **B641**, 260 (2006), nucl-th/0607009.

[50] *Incident-energy and system-size dependence of directed flow*, G. Wang, J. Phys. **G34**, S1093 (2007), nucl-ex/0701045.

[51] *Probing small x parton densities in ultraperipheral A+A and p+A collisions at the LHC*, M. Strikman, R. Vogt, and S. White, Phys. Rev. Lett. **96**, 082001 (2006), hep-ph/0508296.

[52] *Neutron tagging of quasielastic J/psi photoproduction off nucleus in ultraperipheral heavy ion collisions at RHIC energies*, M. Strikman, M. Tverskoy, and M. Zhalov, Phys. Lett. B **626**, 72 (2005), hep-ph/0505023.

[53] *Tracking fast small color dipoles through strong gluon fields at the LHC*, L. Frankfurt, M. Strikman, and M. Zhalov (), arXiv:0811.0368 [hep-ph].

[54] *Evidence for color fluctuations in the nucleon in high-energy scattering*, L. Frankfurt, M. Strikman, D. Treleani, and C. Weiss, Phys. Rev. Lett. **101**, 202003 (2008a), arXiv:0808.0182 [hep-ph].

[55] *Large t diffractive J/ψ photoproduction with proton dissociation in ultraperipheral pA collisions at LHC*, L. Frankfurt, M. Strikman, and M. Zhalov, Phys. Lett. B **670**, 32 (2008b), arXiv:0807.2208 [hep-ph].

[56] *Fracture functions from cut vertices*, M. Grazzini, L. Trentadue, and G. Veneziano, Nucl. Phys. B **519**, 394 (1998), hep-ph/9709452.

[57] *Fracture functions: An improved description of inclusive hard processes in QCD*, L. Trentadue and G. Veneziano, Phys. Lett. B **323**, 201 (1994).

[58] *Proof of factorization for diffractive hard scattering*, J. C. Collins, Phys. Rev. D **57**, 3051 (1998), hep-ph/9709499.

[59] *Measurement of leading proton and neutron production in deep inelastic scattering at HERA*, C. Adloff et al. (H1), Eur. Phys. J. **C6**, 587 (1999).

[60] *Leading neutron energy and p_T distribution in deep inelastic scattering and photoproduction at HERA*, S. Chekhanov et al. (ZEUS), Nucl. Phys. **B776**, 1 (2007).

[61] *Measurement of Inclusive Neutron Spectra at the ISR*, J. Engler et al., Nucl. Phys. **B84**, 70 (1975).

[62] *Leading neutron spectra*, A. B. Kaidalov, V. A. Khoze, A. D. Martin, and M. G. Ryskin, Eur. Phys. J. **C47**, 385 (2006).

[63] *How to probe high gluon densities in p p collisions at the Large Hadron Collider*, H. J. Drescher and M. Strikman, Phys. Rev. Lett. **100**, 152002 (2008).

[64] *Observation of Exclusive Dijet Production at the Fermilab Tevatron p-pbar Collider*, T. Aaltonen et al. (CDF), Phys. Rev.D **77**, 052004 (2008a).

[65] *ATLAS Technical Design Report Volume 1* (1997), ATLAS Collaboration, LHCC 97-16.

[66] *Description of Global Pattern Recognition Program (XKALMAN)*, I. Gavrilenko (ATLAS) (2007), ATLAS Internal Note, ATL-INDET-97-165, 1997.

[67] T. Cornelissen, M. Elsing, S. Fleischmann, W. Liebig, E. Moyse, and A. Salzburger, Tech. Rep. ATL-SOFT-PUB-2007-007. ATL-COM-SOFT-2007-002, CERN, Geneva (2007).

[68] *Application of Kalman filtering to track and vertex fitting*, R. Fruhwirth, Nucl. Instrum. Meth. **A262**, 444 (1987).

[69] *The ATLAS Experiment at the CERN Large Hadron Collider*, G. Aad et al. (ATLAS), JINST **3**, S08003 (2008b).

[70] *Vertex reconstruction in the ATLAS experiment at the LHC*, E. Bouhova-Thacker et al. (ATLAS), ATL-INDET-PROC-2008-003.

[71] *Multiplicity distributions for jet parton showers in a medium*, N. Borghini and U. A. Wiedemann, Nucl. Phys. **A774**, 549 (2006), hep-ph/0509364.

[72] *Rapidity and angular distributions of charged secondaries according to the hydrodynamical model of particle production*, P. Carruthers and M. Doung-van, Phys. Rev. **D8**, 859 (1973).

[73] *Entropy production at high energy and mu(B)*, P. Steinberg, PoS **CPOD2006**, 036 (2006), nucl-ex/0702019.

[74] *Charged-particle pseudorapidity distributions in Au + Au collisions at $\sqrt{s_{NN}}$ = 62.4 GeV*, B. B. Back et al. (PHOBOS), Phys. Rev. **C74**, 021901 (2006a), nucl-ex/0509034.

[75] *Centrality and energy dependence of charged-particle multiplicities in heavy ion collisions in the context of elementary reactions*, B. B. Back et al. (PHOBOS), Phys. Rev. **C74**, 021902 (2006b).

[76] *The significance of the fragmentation region in ultrarelativistic heavy ion collisions*, B. B. Back et al., Phys. Rev. Lett. **91**, 052303 (2003), nucl-ex/0210015.

[77] *Importance of Correlations and Fluctuations on the Initial Source Eccentricity in High-Energy Nucleus-Nucleus Collisions*, B. Alver et al., Phys. Rev. **C77**, 014906 (2008), 0711.3724.

[78] *Differential elliptic flow prediction at the LHC from parton transport*, D. Molnar (2007), 0707.1251.

[79] *Collision geometry scaling of Au+Au pseudorapidity density from $\sqrt{s_{NN}}$ = 19.6 GeV to 200 GeV*, B. B. Back et al. (PHOBOS), Phys. Rev. **C70**, 021902 (2004).

[80] *Scaling properties in bulk and p_T dependent particle production near mid-rapidity in relativistic heavy ion collisions*, B. Alver et al. (PHOBOS), Phys. Rev. **C80**, 011901 (2009).

[81] *Common event characterization in the RHIC experiments*, A. Denisov et al. (PHENIX), Nucl. Phys. **A698**, 551 (2002).

[82] *Charged particle multiplicity near mid-rapidity in central Au+Au collisions at $\sqrt{s_{NN}}$ =56 and 130 GeV*, B. B. Back et al. (PHOBOS), Phys. Rev. Lett. **85**, 3100 (2000).

[83] *Heavy Ion Physics with the ATLAS Detector* (2004), ATLAS Collaboration, LHCC 2004-009I-013.

[84] *Highly Relativistic Nucleus-Nucleus Collisions: The Central Rapidity Region*, J. D. Bjorken, Phys. Rev. **D27**, 140 (1983).

[85] *ATLAS Experiment at the CERN Large Hadron Collider*, G. Aad et al. (ATLAS), JINST **3**, S08003 (2008c).

[86] *Methods for analyzing anisotropic flow in relativistic nuclear collisions*, A. M. Poskanzer and S. A. Voloshin, Phys. Rev. **C58**, 1671 (1998), nucl-ex/9805001.

[87] *Measurement of collective flow in heavy-ion collisions using particle-pair correlations*, S. Wang et al., Phys. Rev. **C44**, 1091 (1991).

[88] *Flow measurements via two-particle azimuthal correlations in Au + Au collisions at $\sqrt{s_{NN}}$ = 130 GeV*, K. Adcox et al. (PHENIX), Phys. Rev. Lett. **89**, 212301 (2002a), nucl-ex/0204005.

[89] *Analysis of anisotropic flow with Lee-Yang zeros*, R. S. Bhalerao, N. Borghini, and J. Y. Ollitrault, Nucl. Phys. **A727**, 373 (2003).

[90] *Genuine collective flow from Lee-Yang zeroes*, R. S. Bhalerao, N. Borghini, and J. Y. Ollitrault, Phys. Lett. **B580**, 157 (2004).

[91] *Flow analysis from multiparticle azimuthal correlations*, N. Borghini, P. M. Dinh, and J. Y. Ollitrault, Phys. Rev. **C64**, 054901 (2001).

[92] *Multiple collisions and induced gluon Bremsstrahlung in QCD*, M. Gyulassy and X.-n. Wang, Nucl. Phys. **B420**, 583 (1994b), nucl-th/9306003.

[93] *Jets as a Probe of Quark Gluon Plasma*, D. A. Appel, Phys. Rev. **D33**, 717 (1986).

[94] *Suppression of hadrons with large transverse momentum in central Au + Au collisions at $\sqrt{s_{NN}}$ = 130 GeV*, K. Adcox et al. (PHENIX), Phys. Rev. Lett. **88**, 022301 (2002b), nucl-ex/0109003.

[95] *Reaction operator approach to non-Abelian energy loss*, M. Gyulassy, P. Levai, and I. Vitev, Nucl. Phys. **B594**, 371 (2001), nucl-th/0006010.

[96] *Mach cones and dijets: Jet quenching and fireball expansion dynamics*, T. Renk (2006), hep-ph/0608333.

[97] *Jet properties from dihadron correlations in p + p collisions at $\sqrt{s}$ = 200 GeV*, S. S. Adler et al. (PHENIX), Phys. Rev. **D74**, arXiv:072002 (2006b), hep-ex/0605039.

[98] *Testing AdS/CFT Drag and pQCD Heavy Quark Energy Loss*, W. A. Horowitz and M. Gyulassy (2008), 0804.4330.

[99] *Transverse momentum and centrality dependence of high-pt non-photonic electron suppression in Au+Au collisions at $\sqrt{s_{NN}}$ = 200 GeV*, B. I. Abelev et al. (STAR), Phys. Rev. Lett. **98**, 192301 (2007), nucl-ex/0607012.

[100] *Heavy quark colorimetry of QCD matter*, Y. L. Dokshitzer and D. E. Kharzeev, Phys. Lett. **B519**, 199 (2001), hep-ph/0106202.

[101] *Measurement of Bottom versus Charm as a Function of Transverse Momentum with Electron-Hadron Correlations in p+p Collisions at sqrt(s)=200 GeV*, . A. Adare (PHENIX) (2009), 0903.4851.

[102] *Low- and intermediate-p_T di-hadron distributions in Au + Au collisions at $\sqrt{s_{NN}}$ = 200 GeV from STAR*, M. J. Horner (STAR), J. Phys. **G34**, S995 (2007), nucl-ex/0701069.

[103] *Near-side $\Delta\eta$ correlations of high-p_T hadrons from STAR*, J. Putschke (STAR), AIP Conf. Proc. **842**, 119 (2006).

[104] *Collective Flow signals the Quark Gluon Plasma*, H. Stöcker, Nucl. Phys. **A750**, 121 (2005), nucl-th/0406018.

[105] *Conical flow induced by quenched QCD jets*, J. Casalderrey-Solana, E. V. Shuryak, and D. Teaney, J. Phys. Conf. Ser. **27**, 22 (2005), hep-ph/0411315.

[106] *System size and energy dependence of jet-induced hadron pair correlation shapes in Cu + Cu and Au + Au collisions at $\sqrt{s_{NN}} = 200$ GeV and 62.4 GeV*, A. Adare et al. (PHENIX), Phys. Rev. Lett. **98**, 232302 (2007b), nucl-ex/0611019.

[107] *Indications of Conical Emission of Charged Hadrons at RHIC*, B. I. Abelev et al. (STAR), Phys. Rev. Lett. **102**, 052302 (2009), 0805.0622.

[108] *Identification of exotic jet topologies via three particle correlations in PHENIX*, N. N. Ajitanand (PHENIX), Acta Phys. Hung. **A27**, 197 (2006), nucl-ex/0511029.

[109] *High p_T Triggered $\Delta\eta,\Delta\phi$ Correlations over a Broad Range in $\Delta\eta$*, E. Wenger (PHOBOS) (2008), 0804.3038.

[110] *A theory of jet shapes and cross sections: from hadrons to nuclei*, I. Vitev, S. Wicks, and B.-W. Zhang, JHEP **11** (2008), hep-ph/0810.2807.

[111] *Medium-evolved fragmentation functions*, N. Armesto, L. Cunqueiro, C. A. Salgado, and W.-C. Xiang, JHEP **02**, 48 (2008b), arXiv 0710.3073.

[112] *Universal upper bound on the energy of a parton escaping from the strongly coupled quark-gluon matter*, D. E. Kharzeev (2008), arXiv:0806.0358.

[113] *HIJING: A Monte Carlo model for multiple jet production in p+p, p+A and A+A collisions*, X.-N. Wang and M. Gyulassy, Phys. Rev. **D44**, 3501 (1991).

[114] *Jets from Quantum Chromodynamics*, G. Sterman and S. Weinberg, Phys. Rev. Lett. **39**, 1436 (1977).

[115] *QCD studies using a cone based jet finding algorithm for $e^+ + e^-$ collisions at LEP*, R. Akers et al. (OPAL), Z. Phys. **C63**, 197 (1994).

[116] *Experimental Investigation of the Energy Dependence of the Strong Coupling Strength*, S. Bethke et al. (JADE), Phys. Lett. **B213**, 235 (1988).

[117] *Longitudinally invariant k_T clustering algorithms for hadron hadron collisions*, S. Catani, Y. L. Dokshitzer, M. H. Seymour, and B. R. Webber, Nucl. Phys. **B406**, 187 (1993).

[118] *Successive combination jet algorithm for hadron collisions*, S. D. Ellis and D. E. Soper, Phys. Rev. **D48**, 3160 (1993), hep-ph/9305266.

[119] *FastJet: Dispelling the N^3 myth for the k_T jet- finder*, M. Cacciari (2006), hep-ph/0607071.

[120] *Fast simulation jet quenching in ultrarelativistic heavy ion collisions*, I. P. Lokhtin and A. M. Snigirev (2006), HEP-PH/0406038.

[121] *Medium Modification of Jet Shapes and Jet Multiplicities*, C. Salgado and U. Wiedemann, Phys. Rev. Lett. **93**, 042301 (2004b).

[122] ATLAS offline reconstruction and analysis evenironment (Athena), version 12.0.6.

[123] *J/ψ Suppression by Quark-Gluon Plasma Formation*, T. Matsui and H. Satz, Phys. Lett. **B178**, 416 (1986).

[124] *J/ψ and eta_c in the deconfined plasma from lattice QCD*, M. Asakawa and T. Hatsuda, Phys. Rev. Lett. **92**, 012001 (2004), hep-lat/0308034.

[125] *Behavior of charmonium systems after deconfinement*, S. Datta, F. Karsch, P. Petreczky, and I. Wetzorke, Phys. Rev. **D69**, 094507 (2004), hep-lat/0312037.

[126] *J / psi and Drell-Yan cross-sections in Pb+Pb interactions at 158 GeV/c per nucleon*, M. C. Abreu et al. (NA50), Phys. Lett. **B410**, 327 (1997).

[127] *Observation of a threshold effect in the anomalous J/ψ suppression*, M. C. Abreu et al. (NA50), Phys. Lett. **B450**, 456 (1999).

[128] *J/ψ production vs transverse momentum and rapidity in p+p collisions at $\sqrt{s}$ = 200 GeV*, A. Adare et al. (PHENIX), Phys. Rev. Lett. **98**, 232002 (2007c), hep-ex/0611020.

[129] *A new measurement of J/ψ suppression in Pb - Pb collisions at 158-GeV per nucleon*, B. Alessandro et al. (NA50), Eur. Phys. J. **C39**, 335 (2005), hep-ex/0412036.

[130] *J/ψ production in Indium-Indium collisions at 158- GeV/nucleon*, R. Arnaldi et al. (NA60), Phys. Rev. Lett. **99**, 132302 (2007).

[131] , K. Melnikov and F. Petriello, Phys.Rev. **D74**, 114017 (2006).

[132] *Parton Distributions and the LHC: W and Z Production*, A. D. Martin, R. G. Roberts, W. J. Stirling, and R. S. Thorne (1999), hep-ph/9907231.

[133] *High-precision QCD at hadron colliders: electroweak gauge boson rapidity distributions at NNLO*, C. Anastasiou, L. Dixon, K. Melnikov, and F. Petriello (2004), hep-ph/0312266.

[134] *Measurement of Cross Sections for b Jet Production in Events with a Z Boson in pp Collisions at roots = 1.96 TeV*, T. Aaltonen et al. (2008b), arXiv:0812.4458 [hep-ex].

[135] *Measurement of differential Z/ + jet + X cross sections in pp collisions at root(s) = 1.96 TeV*, V. Abazov et al., Phys.Lett. **B669**, 278 (2008), arXiv:0808.1296 [hep-ex].

[136] *Measurement of the b Jet Cross Section in Events with a Z Boson in pp Collisions at root(s)=1.96 TeV*, A. Abulencia et al., Phys.Rev. **D74**, 032008 (2006), hep-ex/0605099.

[137] L. Rosselet, P. Nevski, and S. Timoshenko (ATLAS) (2008), ATLAS Note CERN-ATL-PHYS-PUB-2008-003.

[138] *Hard scattering cross sections at LHC in the Glauber approach: From p+p to p+A and A+A collisions*, D. G. d'Enterria (2003), nucl-ex/0302016.

[139] *Mach shocks induced by partonic jets in expanding quark-gluon plasma*, H. Satarov, M.and Stöcker and I. Mishustin, Phys. Lett. **B627**, 64 (2005), nucl-ex/0505245.

[140] *Energy loss of leading hadrons and direct photon production in evolving quark-gluon plasma*, S. Turbide, C. Gale, S. Jeon, and G. D. Moore, Phys. Rev. **C72**, 014906 (2005), hep-ph/0502248.

[141] *Prompt Photon Production at Large p_T Scheme Invariant QCD Predictions and Comparison with Experiment*, P. Aurenche, R. Baier, M. Fontannaz, and D. Schiff, Nucl. Phys. **B297**, 661 (1988).

[142] *New Generation of Parton Distributions with Uncertainties from Global QCD Analysis*, J. Pumplin et al., JHEP **07**, 012 (2002).

[143] *Testing the Universality of Fragmentation Functions*, B. Kniehl, G. Kramer, and B. Poetter, Nucl. Phys. **B597**, 337 (2001), hep-ph/0011155.

[144] *ATLAS high-level trigger, data acquisition and controls: Technical design report*, CERN-LHCC-2003-022.

[145] *ATLAS first-level trigger: Technical design report*, CERN-LHCC-98-14.

[146] *The LHC as a Nucleus-Nucleus Collider*, J. Jowett, plenary talk at the Quark Matter 2008 conference (2008).